PREDICTING THE DYNAMIC BEHAVIOR OF FRANCIS TURBINE GENERATING UNITS

Thèse N° 7131

Joao GOMES PEREIRA JUNIOR

2019

EPFL
ÉCOLE POLYTECHNIQUE
FÉDÉRALE DE LAUSANNE

Knowledge emerges only through invention and re-invention,
through the restless, impatient, continuing, hopeful inquiry human
beings pursue in the world, with the world, and with each other.

O conhecimento emerge apenas através da invenção e da reinvenção,
através da inquietante, impaciente, contínua e esperançosa investigação
que os seres humanos buscam no mundo, com o mundo e uns com os outros.

— Paulo Freire

To my family . . .

Acknowledgements

A PhD research work in EPFL usually takes about four years. It is a long journey that requires the support from a large number of people, institutions, and often, industrial partners. For this reason I would like to take this opportunity to acknowledge all the support I received, for without it I would never be able to achieve this academic degree.

I would like to start by thanking my PhD thesis director, Prof. François Avellan, for giving me the opportunity to work under his direction, first as a master student and later as a PhD student. I would like to thank him for his guidance and for giving me the opportunity to participate in research projects of the highest standards. Professor Avellan is known worldwide for being an expert in hydraulic turbines, but his ability in cooking a great paella also deserves recognition. I would like to thanks Christophe Nicolet, who also provided me guidance during both my master and PhD. Also, I would like to express my gratitude and appreciation to Loïc Andolfatto, who taught me a lot about what a PhD degree is about and how to properly write and present a research work.

Among the PhDs and post-docs with whom I shared my time at LMH, I would like to thanks Arthur Favrel for his collaboration in almost all the research papers I have published, and also for the beers we shared. Together with Loïc, looking good in mustaches, the site tests in Canada will always be a great memory from these years. I also want to thank all those with whom I shared my office: Matthieu Dreyer, Christian Landry, João Delgado, Elena Vagnoni and also David Valentin for a short time. Among those, special thanks to Elena, as we were office mates for years and for her support during the last and hardest moments of the thesis. Thanks Christian Landry for the last minute help with the translation of my thesis abstract, and for the endless support with SIMSEN software. By the way, I am serious when I say endless, as you know already it won't stop with the end of the thesis!

With João Delgado, Elena, Sebastian Leguizamon, Alexis, Federico and David Valentin - the « latinos » group in LMH - mutual understanding was always easier! I am glad I had you guys around. To my partners during lunchtime in HEP, including Pascal, Outi, Ebrahim and Siamak, it was always a pleasure to share this part of the day with you. Thanks Siamak for all the interesting, but sometimes awkward, conversations we had. I believe one day you will understand the real value and appreciate the taste of a good beer. Thanks Pascal for sharing your passion for novelties in science and answering our questions regarding Switzerland.

Acknowledgements

me to clean my mind and to be more productive once I was back to work. Nothing could make more sense than delivering my thesis after a long distance regatta in Venice: *on ne lache pas!*

Finally, I will take the liberty to write a few words in Portuguese for my family and wife.

Aos meus pais, João e Angelita, muito obrigado por todo apoio e educação que me deram durante toda minha vida. Agradeço também às minhas irmãs, Janaína e Juliana, que também sempre me deram todo apoio que precisei e ainda preciso. Obrigado também às minhas tias, tios e primas. Nunca vou conseguir expressar com palavras toda minha gratidão e alegria de ter vocês como minha família. Para minhas pequenas e amadas sobrinhas, Mariana e Heloísa, sejam bem vindas ao time!

Para terminar, gostaria de agradecer à minha esposa, Clarissa V. Büttow, por ter me acompanhado durante todo meu doutorado. Agradeço pelo seu companheirismo, pelas risadas nas horas mais calmas e pelo seu apoio nos momentos mais difíceis. Espero que você também tenha todo o apoio que vai precisar durante o seu doutorado que se inicia. Naquilo que é do meu alcance, poderá sempre contar comigo!

Lausanne, 06 August 2019   J. G.

Abstract

To reduce CO_2 emissions and tackle global warming, an increasing amount of electrical power consumed around the world must be obtained from renewable sources. Among these sources, hydropower has not only the advantage of leaving a very small carbon footprint, but also the ability to be flexible and compensate for the intermittent nature of other sources like solar and wind. For these qualities, a large number of new hydropower projects is foreseen in the near future.

Hydropower still has a large potential for new projects worldwide. Furthermore, many already existing plants have also the possibility to modernize its facilities and increase its available installed capacity. For both new plants and modernization projects, thorough investigations are necessary to decide if the project is technically viable and economically relevant. Nevertheless, in the very early design stage, some key information regarding the properties of the future generating unit is often unknown or sometimes estimated with high uncertainty levels.

One of these unknown aspects is the turbine efficiency: it can only be known with high accuracy after performing measurements on a reduced scale physical turbine model homologous to the future turbine prototype. The turbine complete characteristics of torque and discharge is also necessary for a proper dimensioning of the generating unit, as it impacts notably the overpressure in the water conduits and the overspeed of the rotating parts.

Francis turbines operating at part load and full load conditions feature the so-called cavitation vortex rope in their draft tube cone. Therefore, two additional dynamic aspects can impact the performance of a Francis turbine generating unit: (1) a possible resonance between the hydraulic circuit first eigenfrequency and the excitation frequency from the vortex rope, and (2) the occurrence of high amplitude power swings and pressure surge induced by the cavitation vortex rope in unstable full load operating conditions. Currently, these two additional aspects usually remain completely unknown until the prototype enters into operation.

This thesis objective is then to develop and validate new empirical models, testing and calculation procedures able to perform accurate predictions of a Francis turbine prototype dynamic behavior still in the early stage of a hydropower plant project. They can be used by engineers working in the design of Francis generating units to estimate with accuracy the final dynamic behavior of these units as a whole and, consequently, optimize the unit design to reduce costs

Abstract

---

and minimize risks related to the occurrence of undesired dynamic behavior of the cavitation vortex rope.

The complete database of reduced scale physical model measurements available in the Laboratory for Hydraulic Machines (LMH) at the *École Polytechnique Fédérale de Lausanne* (EPFL) is used to construct empirical models able to estimate the turbine efficiency and complete characteristics. The obtained standard error in estimating peak efficiency values is then less than 1%.

Extensive measurements and 1-D eigenvalue calculations are performed to better understand the dynamic behavior of the cavitation vortex in a specific test case. As a result, procedures to predict with accuracy part load resonance and full load instability are presented. These predictions can then be made soon after reduced scale model testing, i.e., usually years before the prototype enters into operation.

Résumé

Afin de réduire les émissions de CO_2 et lutter contre le réchauffement climatique, la production d'électricité par des sources d'énergie renouvelable doit être augmentée. Parmi ces sources, l'hydroélectricité a non seulement l'avantage d'avoir une faible empreinte carbone, mais aussi la capacité d'être flexible afin de compenser la nature intermittente d'autres sources d'énergie telles que l'énergie solaire et éolienne. Grâce à ces qualités, un grand nombre de nouveaux projets d'aménagements hydroélectriques est prévu dans un avenir proche.

L'énergie hydroélectrique a encore un grand potentiel pour des nouveaux projets dans le monde entier. En outre, de nombreuses installations existantes ont la possibilité de moderniser leurs installations et d'augmenter leur capacité installée. Tant pour les nouvelles centrales que pour les projets de modernisation, des études approfondies sont nécessaires pour déterminer si le projet est techniquement viable et économiquement intéressant. Néanmoins, souvent au début de la phase de conception, certaines informations clés concernant les propriétés de la future unité de production sont inconnues ou parfois estimées avec des niveaux d'incertitude élevés.

L'une de ces inconnues est l'efficacité de la turbine. En effet, le rendement de la turbine ne peut être estimé avec précision qu'après la réalisation de mesures sur un modèle réduit de la turbine, homologue au futur prototype. Les courbes caractéristiques de la turbine en termes de couple et de débit sont également nécessaires pour un dimensionnement adapté du groupe, car elles auront en particulier un impact sur les valeurs de survitesse de ce dernier et sur les surpressions dans les conduites.

Les turbines Francis fonctionnant à charge partielle ou à forte charge présentent un type de vortex nommé torche de cavitation dans le cône de leur aspirateur. Par conséquent, deux aspects dynamiques supplémentaires peuvent influencer la performance d'un groupe générateur doté d'une turbine Francis : (1) une possible résonance entre la première fréquence propre du circuit hydraulique et la fréquence d'excitation provenant de la torche de cavitation à charge partielle, et (2) l'occurrence de grandes oscillations de puissance et de fortes pulsations de pression induites par la torche de cavitation dans des conditions de fonctionnement instables à forte charge. Actuellement, ces deux aspects dynamiques de la turbine restent généralement inconnus jusqu'à la mise en service du prototype.

Résumé

L'objectif de cette thèse est alors de développer et valider de nouveaux modèles empiriques et des procédures expérimentales et analytiques capables d'effectuer des prévisions précises du comportement dynamique des turbines Francis à une étape avancée d'un projet de centrale hydroélectrique. Ils peuvent être utilisés par des ingénieurs participant à la conception des turbines Francis pour estimer avec précision le comportement dynamique final de ces unités et, par conséquent, optimiser la conception pour réduire les coûts et minimiser les risques liés à l'occurrence de comportements dynamiques non désirés de la torche de cavitation.

L'ensemble des mesures effectuées sur des modèles réduits disponible au sein du Laboratoire de Machines Hydrauliques (LMH) de l'Ecole Polytechnique Fédérale de Lausanne (EPFL) a été utilisé pour construire des modèles empiriques capables d'estimer le rendement des turbines Francis et ses courbes caractéristiques. L'écart-type obtenu lors de l'estimation des valeurs de rendement maximal est inférieure à 1%.

Un grand nombre de mesures expérimentales et des calculs de valeurs propres ont été effectués pour mieux comprendre le comportement dynamique de la torche de cavitation dans un cas test spécifique. Des nouvelles méthodologies permettant de prédire avec précision des conditions de résonance à charge partielle et des conditions instables à forte charge sont présentées. Ces nouvelles méthodologies peuvent être appliquées peu de temps après des essais sur modèle réduit, soit des années avant la mise en service du prototype.

Nomenclature

Acronyms

AIC	**A**kaike **I**nformation **C**riterion
BEP	**B**est **E**fficiency **P**oint
CFD	**C**omputational **F**luid **D**ynamics
EPFL	**É**cole **P**olytechnique **F**édérale de **L**ausanne
LMH	**L**aboratoire des **M**achines **H**ydrauliques
MFGF	**M**ass **F**low **G**ain **F**actor
NPSE	**N**et **P**ositive **S**uction **E**nergy
RMSE	**R**oot-**M**ean-**S**quare **E**rror
SSE	**S**um of **S**quared **E**rrors
SWSE	**S**um of **W**eighted **S**quared **E**rrors

Superscripts

T	transposed

Subscripts

0	swirl-free condition
a	active
abs	absolute
BEP	at the best efficiency point
c	cavitation
cone	draft tube cone
Gen	generator
G	proposed by Gordon
g	gross
h	hydraulic
LB	losses in the bearings
LG	losses in the generator

rb	total loss (sum of losses)
M	turbine reduced scale physical model
m	mechanical
max	minimum
min	maximum
OP	operating range
P	turbine prototype
Pen	penstock
PVC	precessing vortex core
R	relative value
Run	runaway condition
rated	rated value
ref	reference value
TR	transition zone
t	transferred
v	vapor

Latin letters

A	turbine outlet, or a given component according to the subscript, cross-section area	(m^2)
a	pressure wave speed	$(m \cdot s^{-1})$
C	flow velocity	$(m \cdot s^{-1})$
C_c	cavitation compliance	(m^2)
Cm	meridional component of the flow velocity	$(m \cdot s^{-1})$
Cu	tangential component of the flow velocity	$(m \cdot s^{-1})$
C_{xy}	coherence	(-)
D	diameter	(m)
E	specific energy	$(J \cdot kg^{-1})$
E_{pipe}	pipe wall Young modulus	(Pa)
E_w	water bulk modulus	(Pa)
e	pipe wall thickness	(m)
f_0	first eigenfrequency	(Hz)
f_{PVC}	precessing vortex frequency	(Hz)
g	gravity	$(m \cdot s^{-2})$
g_T	transformation function	(-)
H	turbine head	(m)
He	Hermite polynomial	(-)
h	local piezometric head	(m)
N	rotational speed	(min^{-1})
N_s	total number of samples	(-)
N_{Ts}	total number of samples available for one given turbine	(-)

$NPSE$	net pressure suction energy	(J·kg^{-1})
n	rotating frequency	(Hz)
p	pressure	(Pa)
P	power	(MW)
P_{xx}	power spectral density	
P_{xy}	cross power spectral density	
$\bar{p}$	mean pressure	(Pa)
p_{max}	truncation parameter	(-)
Q	discharge	$(\text{m}^3\text{·s}^{-1})$
S_h	excitation pressure head	(m)
T	torque	(N·m)
T_{aq}	measurements acquisition period	(s)
t	time	(s)
U	runner blade peripheral velocity	(m·s^{-1})
V	volume	(m^3)
W	weight value	(-)
X	input variable for the Hermite polynomials	(-)
y	year of commissioning	(-)
z	elevation level	(m)

Greek letters

α	guide vanes opening angle	(°)
β	void fraction	(-)
η	efficiency	(-)
λ	modal strength for polynomial approximations (Chapter 2), system eigenvalue (Chapter 5)	(-)
μ'	pipe bulk viscosity coefficient	(Pa·s)
μ''	cavitation vortex bulk viscosity coefficient	(Pa·s)
Π	dimensionless pressure wave speed	(-)
ρ	density	(kg·m^{-3})
σ	Thoma number	(-)
σ_{Std}	standard error of estimate	
ϕ	weighting function	(-)
χ	mass flow gain factor	(s)
χ_{nD}	local cavitation coefficient	(-)
ω	angular velocity	(rad·s^{-1})

Dimensionless numbers

c_p	pressure coefficient; $c_p = (\bar{p}(t) - p_{ref})/(\rho \cdot E)$	(-)
Fr	Froude number; $\text{Fr} = \sqrt{E/(g \cdot D)}$	(-)

n_{ED}	IEC speed factor; $n_{\mathrm{ED}} = n/\left(D \cdot \sqrt{E}\right)$	(-)
M''	cavitation volume dimensionless bulk viscosity; $\mathrm{M}'' = \mu'' \cdot f_0/\left(p_{\mathrm{cone}} - p_{\mathrm{v}}\right)$	(-)
n_{QE}	IEC specific speed; $n_{\mathrm{QE}} = n_{\mathrm{ED}} \cdot \sqrt{Q_{\mathrm{ED}}}$	(-)
Q_{ED}	IEC discharge factor; $Q_{\mathrm{ED}} = Q/\left(D^2 \cdot \sqrt{E}\right)$	(-)
S	swirl number; $S = n_{\mathrm{ED}} \cdot \left(\pi^2/8\right) \cdot \left(1/Q_{\mathrm{ED}} - 1/Q_{\mathrm{ED}_0}\right)$	(-)
$\mathrm{St}_{\mathrm{PVC}}$	Strouhal number for the precessing vortex; $\mathrm{St}_{\mathrm{PVC}} = f_{\mathrm{PVC}} \cdot D^3/Q$	(-)
T_{ED}	IEC torque factor; $T_{\mathrm{ED}} = T/\left(\rho \cdot D^3 \cdot E\right)$	(-)
Π	dimensionless pressure wave speed; $\Pi = \rho \cdot a^2/\left(p_{\mathrm{cone}} - p_{\mathrm{v}}\right)$	(-)
σ	Thoma number; $\sigma = NPSE/E$	(-)
χ_{nD}	local cavitation coefficient; $\chi_{nD} = \left(p_{\mathrm{cone}} - p_{\mathrm{v}}\right)/\left(\rho n^2 D^2\right)$	(-)

Contents

Contents

List of Figures

List of Tables

1 Introduction

1.1 Research context

According to the International Energy Agency (IEA), about 75% of the technical potential for hydropower remains undeveloped (see Table 1.1). As described in [1], to attain the objective of reducing the amount of CO_2 emissions by 50% of the emission levels in 2005, the amount of hydropower capacity and annual generation should roughly double by 2050. Consequently, a large number of new projects for the construction of hydropower plants and the modernization of old ones are expected in the next 30 years.

While working on the design of a hydropower project, engineers will have to consider a large number of aspects such as environmental impact, energy market, legal and regulatory aspects, estimates of capital and operating expenditures. They must also estimate the income that the future power plant will generate, which is a function of the total amount of kWh produced and sold over the year.

The final expenditures and income obtained with a hydropower plant will depend on dynamic properties of the hydraulic turbine expected to be installed in this given power plant generating

Table 1.1 – Regional hydro power technical potential, installed capacity and resulting undeveloped potential as of 2009 [1]

World region	Technical potential, installed capacity (GW)	2009 Installed capacity (GW)	Undeveloped potential (%)
North America	388	153	61
Latin America	608	156	74
Europe	338	179	47
Africa	283	23	92
Asia	2037	402	80
Australasia & Oceania	67	13	80
World	3721	926	75
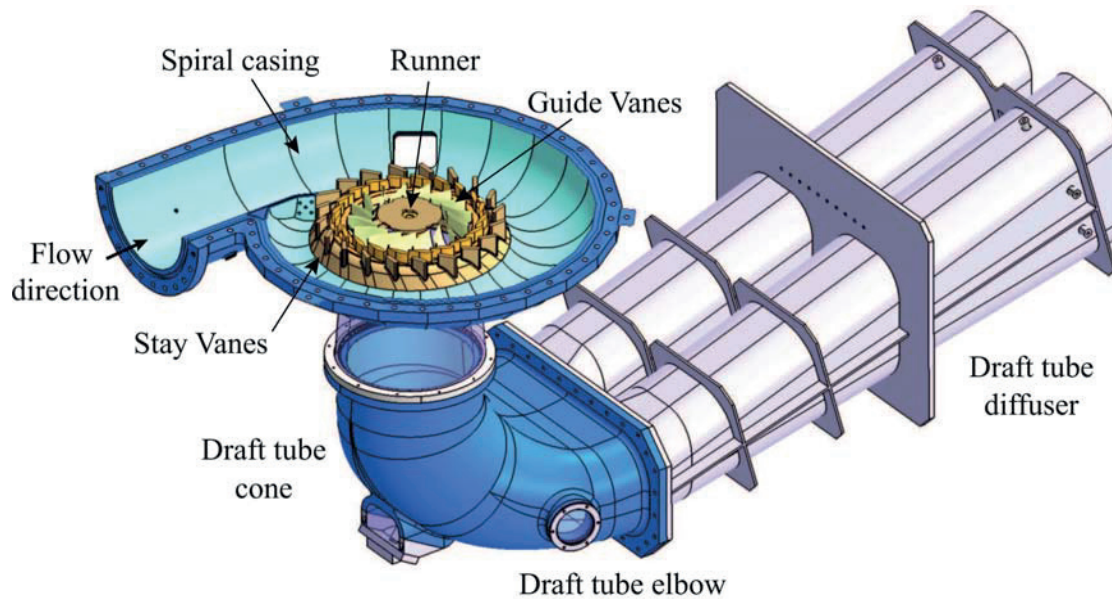
Figure 1.1 – Example of a Francis turbine, adapted from [3].

units. As in the early stages of a hydropower plant project this turbine is not yet properly defined and tested, these dynamic properties have to be estimated.

According to General Electrics, one major manufacturer of hydraulic turbines, hydropower plants featuring Francis type turbines represent about 60% of the installed capacity for hydro worldwide [2]. An example of a Francis turbine, along with the name and location of its most relevant parts, adapted from [3], is presented in Figure 1.1.

The design choices applied to a Francis turbine installed in a given hydropower plant will affect the generating unit in:

- its *global efficiency*: Francis turbines efficiency values can have large variations according to the available specific energy and the turbine discharge. These variations affect the annual amount of energy produced, influencing the plant financial revenue.

- its *behavior in transient conditions*: in an emergency shut-down situation, such as after a sudden disconnection from the power grid (load rejection), the angular momentum transmitted from the water to the turbine runner accelerates the rotating parts of the unit until a maximum value is reached, known as the turbine overspeed. After a load rejection, the water discharge is drastically reduced by the closing of the turbine guide vanes, generating a water hammer effect in the penstock. The turbine overspeed and the water hammer effect are then directly dependent on the turbine characteristic curves [4]. Consequently, if the turbine characteristic curves are not considered properly in the overall design of the generating units, this type of transient conditions can lead to catastrophic events and great loss of investments [5].

- its risk of presenting large undesired *pressure pulsations and power swings*: Francis turbines may operate outside its best efficiency point (BEP), i.e., in part load if the discharge value is lower than that at the BEP, or in full load if the discharge value is higher than that at the BEP. For both part load and full load, the swirling flow leaving the turbine runner induce the so called vortex rope. This vortex rope may lead to a hydro-acoustic resonance phenomenon at part load or reach unstable conditions at full load, both causing high pressure pulsations and power swings.

Despite being an essential part in the design of a power plant as a whole, accurate data regarding the turbine dynamic properties is not available until measurements are performed in a reduced scale physical turbine model homologous to the future turbine prototype. In reality, predicting the possible occurrence of part load resonance and unstable full load conditions is still challenging and, for most of the cases, it is a risk that is usually not assessed. When these phenomena are observed on-site, expensive mitigation measures are implemented such as air injection or limitations in the operating range, as presented in [6].

In this thesis research work a set of empirical models to predict with accuracy the turbine prototype efficiency and its complete characteristic curves of discharge and torque are presented. Additionally, methods to foresee part load resonance phenomenon and full load instability are provided. These models and methods can be used in early stages of the hydropower plant project, allowing its optimization and reducing risks.

1.2 Francis turbine efficiency and complete characteristic curves

Hydraulic turbines are designed to maximize the conversion of hydraulic power into power in the form of shaft torque. In hydropower plants, this shaft torque is transmitted to an electrical generator that transforms the mechanical power into the electrical power delivered to the power grid, as illustrated in the power plant layout of Figure 1.2. The amount of power delivered by the turbine to the generator is given as:

$$P = \eta \rho Q E \tag{1.1}$$

where η ($\cdot$) is the turbine efficiency, ρ (kg$\cdot$m^{-3}) is the water density, Q (m^3$\cdot$s^{-1}) is the discharge and $E = gH$ (J$\cdot$kg^{-1}) is the turbine specific available energy. The turbine η values are usually represented by the so-called efficiency hill chart, such as the one presented as an example in Figure 1.3. To simplify comparisons between different turbines, efficiency hill charts and turbine characteristic curves are usually presented as a function of non-dimensional factors, such as the ones for the discharge, the runner rotation speed and the torque proposed by the International Electrotechnical Commission (IEC) standard [8] and detailed in eq. (1.2).

$$Q_{\text{ED}} = \frac{Q}{D^2\sqrt{E}} \qquad n_{\text{ED}} = \frac{nD}{\sqrt{E}} \qquad T_{\text{ED}} = \frac{T}{\rho D^3 E} \tag{1.2}$$

1 Gates
2 Penstocks
3 Inlet valve
4 Turbine
5 Generator
6 Automation, control, protection
7 Medium-voltage switchgear
8 Power transformer
9 High-voltage switchgear
10 Transmission line
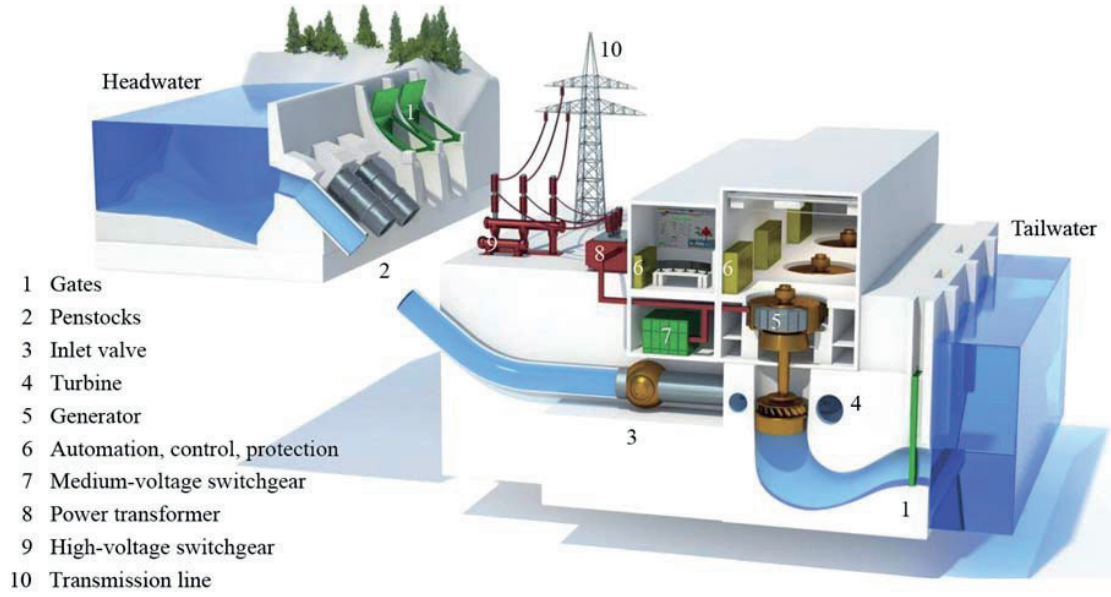
Figure 1.2 – Typical power plant layout [7].
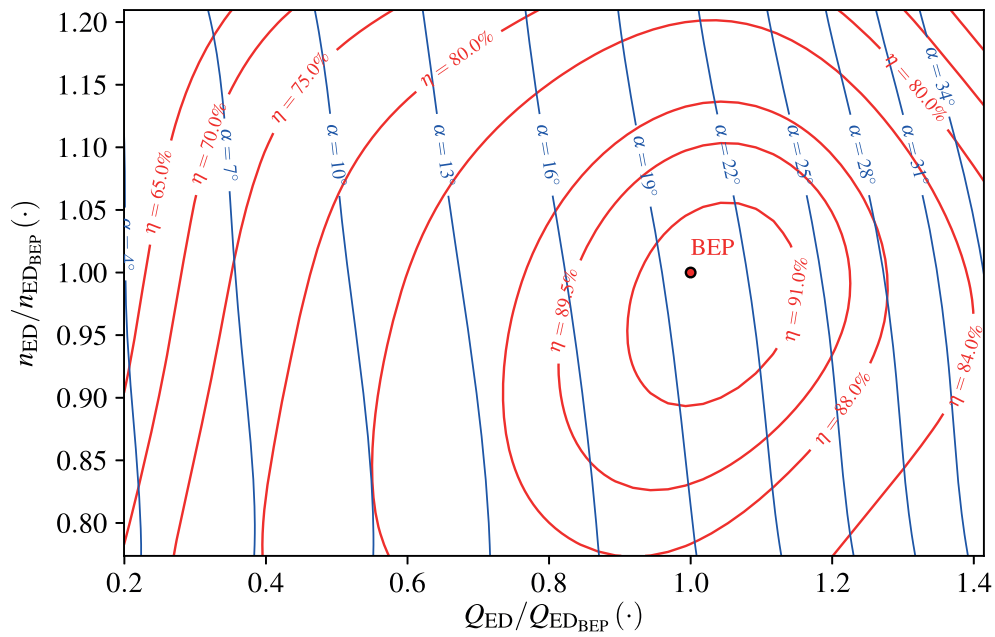
Figure 1.3 – Example of Francis turbine efficiency hill chart.

where D (m) is the runner diameter, n (s^{-1}) is the runner rotation speed and T (N·m) is the turbine torque.

The turbine efficiency is relevant when the generating unit is operating inside its designed operating range conditions and with its generator connected to the grid. Otherwise, when tran-
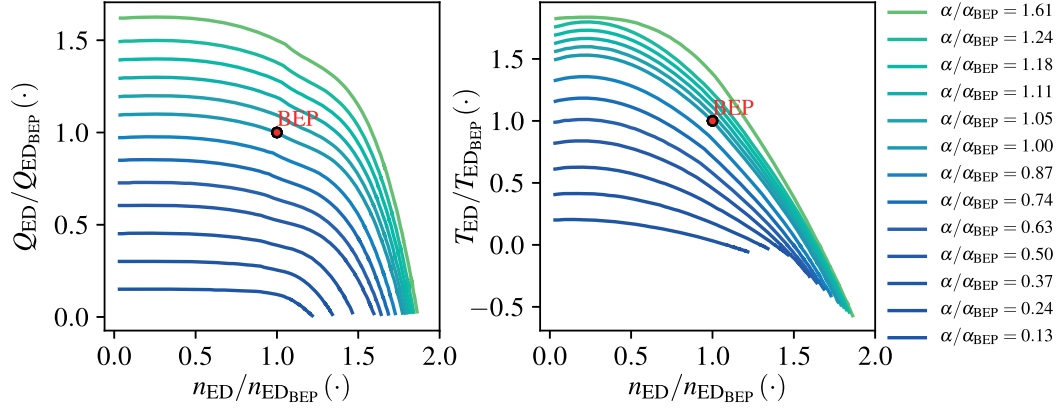
Figure 1.4 – An example of turbine Q_{ED} and T_{ED} characteristic curves for hydraulic transient simulations.

sient conditions are analyzed, broader information on the turbine dynamics is required. This broader information is usually presented in the form of discharge and torque characteristic curves. An example of turbine characteristic curves is presented in Figure 1.4. The complete characteristic curves become necessary when simulations such as for the unit start-up or an emergency shut-down are performed. The typical operating range of Francis turbines and an example of its trajectory during start-ups and emergency shut-downs inside a graph of turbine Q_{ED} characteristic curves is presented in Figure 1.5.

The efficiency and complete characteristic curves of a given turbine design are only obtained with accuracy after performing measurements in a reduced scale physical turbine model homologous to the real-scale prototype. This type of measurements are performed in a test rig following the procedures defined by the IEC standard [8], leading to efficiency values measured with 0.2% of maximum uncertainty. The Laboratory for Hydraulic Machines (LMH) at the *École Polytechnique Fédérale de Lausanne* (EPFL) features three completely modular test rigs where measurements are performed according to the IEC standard. The LMH test rigs are illustrated in Figure 1.6.

Each hydropower plant has its specific and site related conditions of available energy and water discharge. Francis turbines are then designed for these specific conditions, aiming to maximize the plant energy production. Consequently, every turbine prototype has its unique efficiency hillchart and characteristic curves.

Performing reduced scale model tests during the early stage of a power plant project is not feasible, forcing engineers to make assumptions on these turbines efficiency and characteristic curves. In some cases, as in the large-scale assessment of hydroelectric potential presented in [10], the turbine efficiency is assumed as constant, which is far from reality as illustrated in the example of hill chart of Figure 1.3. The use of 3-D Computational Fluid Dynamics (CFD)
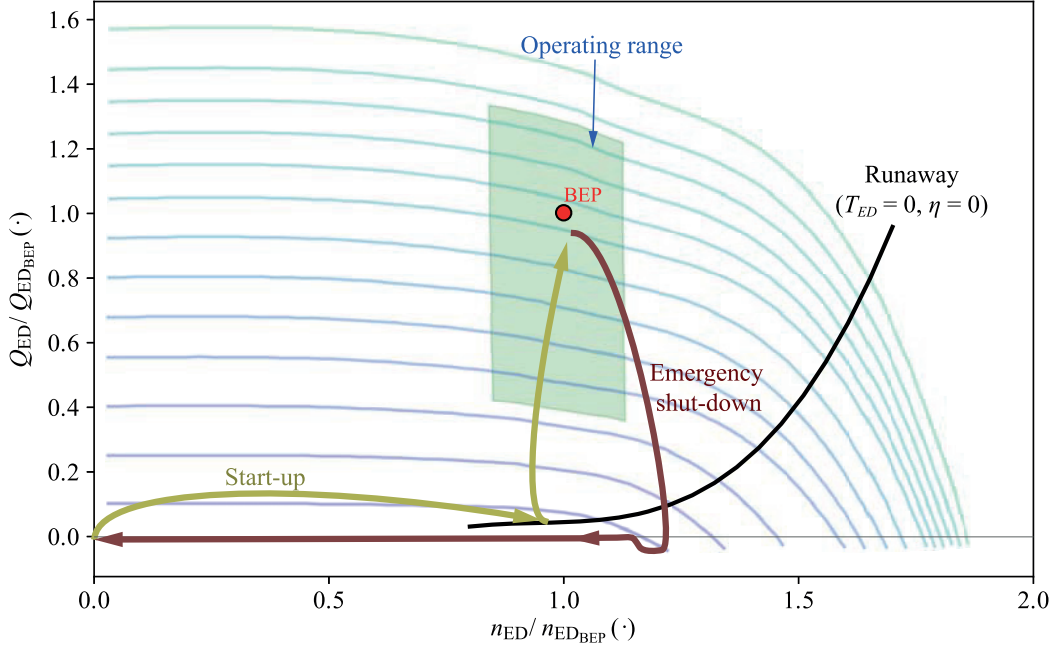
Figure 1.5 – A qualitative example of turbine typical operating range conditions and trajectory during start-ups and emergency shut-downs.

simulations — another option to define a turbine design, to estimate its efficiency and provide the complete turbine characteristic curves — is complex and very time consuming, becoming more suitable in later stages of the project when a final design must be defined. Examples of 3-D CFD simulations for Francis turbines are presented in [11–14]. Analytical models, such as those presented in [15, 16], can provide estimates of efficiency values and are much faster than CFD simulations. They are, on the other hand, much less accurate, as they have to simplify complex phenomena such as flow turbulence and instabilities.

A more suitable and more accurate option in the early stage is then the use of empirical models. These models are intended to make predictions based on actual measurements and, consequently, less focused on replicating all the complex physical phenomena occurring in each part of the turbine. A very complete empirical model for different turbine types is presented by Gordon in [17]. Gordon makes uses of a turbine efficiency database constructed by himself, from a number of different sources, to generate empirical models for the efficiency estimation. He provides an empirical model able to estimate with accuracy the peak efficiency value η_{BEP} of turbine prototypes commissioned until the year of 1999.

This thesis work proposes improvements in the empirical models proposed by Gordon for Francis turbine prototypes efficiency estimation, as well as new models to generate the turbine complete characteristic curves of torque and discharge. Inside the RENOVHydro project, these empirical models are used in an optimization loop where a large number of options for the

IEC 60193 Testing Facilities at LMH
Performance Accuracy < 2‰

	PF1	PF2	PF3
Maximum Head:	100 m	120m	100 m
Maximum Discharge:	1.4 m^3s^{-1}	1.4 m^3s^{-1}	1.4 m^3s^{-1}
Generating Power:	300 kW	300 kW	300 kW
Pumping Power:	900 kW	1000 kW	2 × 400 kW
Maximum Speed:	1500 rpm	2500 rpm	2500 rpm
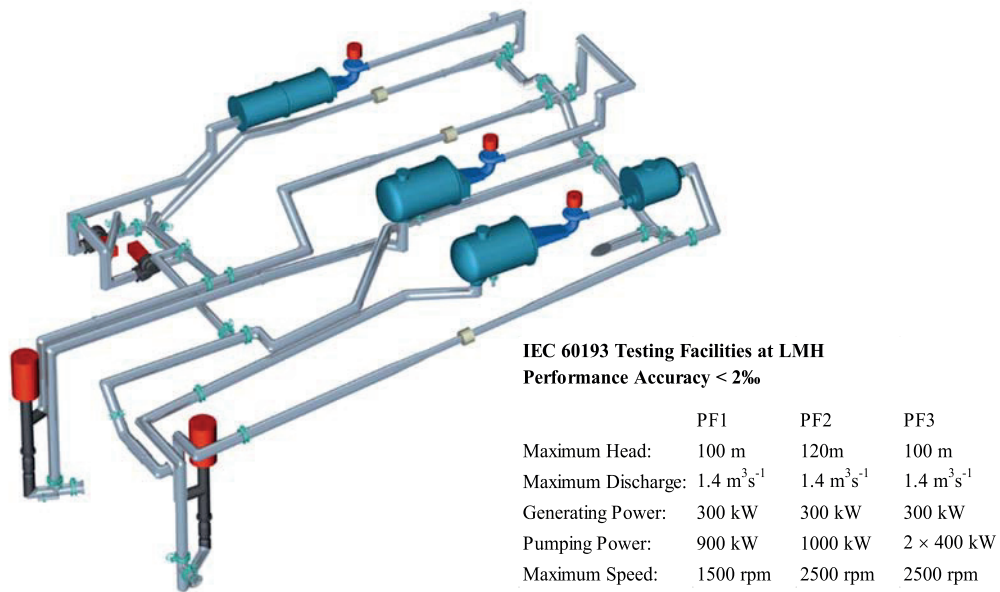
Figure 1.6 – LMH test rigs for reduced scale physical model measurements [9].

civil works, electrical equipment and hydro-mechanical equipment are tested according to the installation site and the energy market. As a result, a set of best design options with higher return on investment is provided. The RENOVHydro methodology is intended to be applied in the near future in a number of power plants renovation projects in Switzerland.

1.2.1 Part load resonance and full load stability

Francis turbines feature fixed runner blades. As a result, they are designed to operate with maximum efficiency only in a given condition of available specific energy and discharge. When Francis turbines are required to operate away from this condition, a swirling flow leaves the runner blades and enters the draft tube cone. Once the intensity of this swirling flow — given by the flow swirl number (see [18–20]) — becomes high enough, the so-called vortex rope flow instability takes place in the turbine draft tube cone. In cases where the pressure in the vortex rope core becomes lower than the vapor pressure, a cavitation volume becomes visible. Images of a cavitating precessing vortex rope in a part load operating condition and of an axisymmetric cavitating vortex rope in a full load operating condition are presented in Figure 1.7.

The precessing movement of the vortex rope in part load conditions induces pressure fluctuations in the draft tube cone that can be decomposed into a synchronous component and a convective component (see [21, 22]). The synchronous component of these pressure fluctuations acts as an excitation source for the whole hydraulic system, pulsating at the same frequency as the precession movement, usually between 20% and 40% of the runner rotation frequency [23]. This excitation frequency may, in some cases, match the first eigenfrequency

of the complete hydraulic system of the Francis generating unit, leading to resonance and large pressure and power oscillations [24–27].

The hydroacoustic parameter of the vortex rope known as the mass flow gain factor (MFGF) — defined as $\chi = -\frac{\partial V_c}{\partial Q}$ where V_c is the cavitation volume and Q the turbine discharge (see [28, 29]) — has a positive sign in part load conditions and a negative sign in full load conditions. Consequently, the dynamic response of the cavitation volume with respect to oscillations in discharge is different in part load and in full load conditions: the MFGF has a stabilizing effect in part load and a destabilizing effect in full load operating conditions. In full load, this destabilizing effect can lead to an unstable self-excited condition where unacceptable oscillations of power and pressure are observed on the turbine [26, 30–33].

The occurence or not of pressure surges in turbine prototypes depend on the eigenvalues of the complete hydraulic system which may contain, for instance, surge tanks, pressurized pipes of different lengths and diameters, other turbines or pumps. To calculate these eigenvalues, 1-D hydro-acoustic numerical models are typically used to take into account the influence of all the hydro-mechanic components contiguous to the turbine [34–37]. In [38], Nicolet presents mathematical models to simulate the dynamic behavior of various different components of a hydropower generating unit. More recently, Alligné et al. proposed in [39] a 1-D model to simulate a cavitating draft tube, derived from flow momentum and continuity equations. Other examples of 1-D numerical models to simulate the dynamic behavior of the cavitation vortex rope are given by Dörfler in [40] and by Couston and Philibert in [41].

To predict pressure surges generated by the cavitating vortex rope in turbine prototypes, either by resonance phenomena in part load or by self-excitation in full load, 3-D CFD numerical simulations are performed in [42–48] and experimental investigations are presented in [19, 20, 25, 31, 49–53]. Favrel et al. presented in [54] a complete procedure to predict part load resonance in Francis turbines prototypes making use of 1-D eigenvalue calculations and experimental modal analysis in a test rig featuring the reduced scale physical turbine model. The proposed procedure was able to predict the occurrence of part load resonance in a given power plant test case. However, resonance occurred in a power output slightly lower than the predicted value. This small deviation is explained by the use of the Thoma number as a similarity parameter between the reduced scale model and the turbine prototype, leading to non-similar pressure levels in the draft tube cone.

Koutnik et al. presented in [30] numerical simulations reproducing the transition from a stable to an unstable full load condition in a pump-storage power plant. By testing different possible values of MFGF, Koutnik et al. were able to simulate in time domain the full load instability onset, reproducing the power and pressure oscillations observed in measurements. Nevertheless, the exact determination of MFGF values and its transposition from reduced scale model to prototype scale remains challenging.
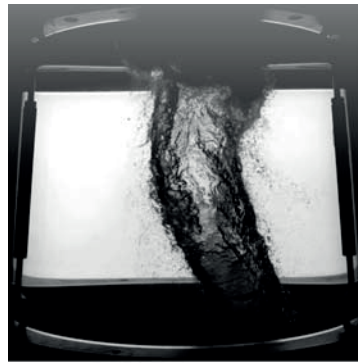
(a) Precessing vortex rope in part load.
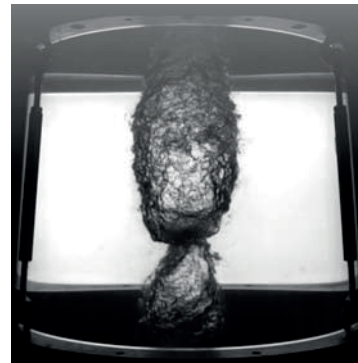
(b) Axisymmetric vortex rope in full load.

Figure 1.7 – Cavitating vortex rope visualization.

1.3 Thesis objective

This thesis main objective is to provide empirical models and calculation procedures to accurately predict the dynamic behavior of a Francis turbine prototype in the early stages of a hydropower plant project. This dynamic behavior comprises the turbine efficiency, its complete characteristic curves of torque and discharge, and the hydro-acoustic properties of the cavitation vortex rope that may lead to pressure pulsations in both part load and full load operating conditions. The proposed empirical models and calculation procedures can help the design and the engineering of hydropower units to better estimate the generating unit performance and evaluate the risk of having undesired power swings. The earlier this type of information is available, the lower are the costs of performing project adaptations, leading to an optimized final design of the power plant generating unit.

To accomplish this objective, two main courses of action are taken: (1) the reduced scale physical turbine model measurements database available at EPFL is used to construct empirical models for the turbine efficiency and characteristic curves estimation; (2) extensive measurements are performed in both the reduced scale physical model and the prototype of a given turbine to define methodologies to predict part load resonance and unstable full load operating conditions.

The resulting empirical models lead to accurate predictions of turbine efficiency and characteristic curves. With these predicted characteristic curves, transient numerical simulations can be performed to provide accurate estimates of penstock overpressure and turbine overspeed.

With improvements in the procedure proposed by Favrel et al. in [54], the operating conditions leading to part load resonance are predicted with higher accuracy. Unstable full load conditions for the same test case is also correctly predicted from eigenvalue calculations.

1.4   Thesis structure

Apart from this introduction, this thesis is presented in five chapters:

- **Chapter 2** – A procedure to construct surrogate functions based on the combination of bi-variate Hermite Polynomials is detailed. These surrogate functions are an essential part of the empirical model for the turbine efficiency estimation presented in Chapter 3. The generated surrogate functions are applied in this paper to estimate the efficiency and the discharge of a given turbine prototype during on-site measurements. The same turbine test case is taken in Chapters 4 and 5, where part load resonance and full load instability is analyzed. Chapter 2 consists of the paper manuscript titled "*Monitoring a Francis turbine operating conditions*", published in the Journal of Flow Measurement and Instrumentation.

- **Chapter 3** – Empirical models to estimate a Francis turbine prototype efficiency and characteristic curves are developed making use of the database of reduced scale physical turbine model measurements available as EPFL. The empirical models take only a limited amount of data input from the turbine, such as the runner diameter, the specific speed and the year of commissioning, so they can be applied in the very early stage of a generating unit design. Efficiency values are predicted with good accuracy: the error in peak efficiency estimation is expected to be lower than 1%.

- **Chapter 4** – An improved method to predict part load resonance in a turbine prototype is presented, leading to higher accuracy than the one presented in [54]. The method requires measurements performed on a reduced scale physical model and eigenvalue calculations to identify the pressure wave speed value inside the turbine model draft tube cone. This wave speed value is transposed to the prototype scale and eigenvalue calculations of the prototype and its contiguous hydraulic circuit are used to estimate its first eigenfrequency value. Estimated and measured resonance conditions on the prototype are presented, showing good agreement. This Chapter consists of the paper manuscript titled "*Procedure for predicting part load resonance in Francis turbines hydropower units based on swirl number and local cavitation coefficient similitude*", submitted to the Journal of Mechanical Systems and Signal Processing.

- **Chapter 5** – Similarities between a surge phenomenon observed in a turbine prototype and in its homologous reduced scale model in full load operating conditions are presented. They show that the turbine reduced scale model properly reproduces the physical mechanism behind the full load instability observed in prototypes. Eigenvalue calculations are then performed to take into account all the hydro-acoustic parameters leading to unstable full load conditions. A given MFGF value is identified on the reduced scale model and transposed to the prototype scale. Eigenvalue calculations of the prototype generating unit correctly predicted a transition from stable to unstable conditions on the prototype. Finally, 1-D transient simulations are performed to take into account changes in the pressure wave speed value inside the cavitating draft tube

cone, replicating the behavior of the turbine prototype in stable and in unstable conditions. This chapter consists of the paper manuscript titled "*Prediction of unstable full load conditions in a Francis turbine prototype*", submitted to the Journal of Mechanical Systems and Signal Processing.

- **Chapter 6** – Examples are provided showing applications of the present research work in the very early design stage of a Francis generating unit, i.e., before reduced scale model measurements are performed. The results obtained in the previous chapters are applied, demonstrating applications in real test cases where dynamic performance predictions are validated by measurements. Turbine characteristic curves generated with the empirical model are used in transient simulations, allowing the estimation of the water hammer overpressure in the penstock and the turbine runner overspeed values during an emergency shut-down. Additionally, making use of the hydro-acoustic parameters of the cavitating vortex rope presented in Chapter 4, the hydropower projects with higher risk of exhibiting part load resonance phenomenon are identified.

2 Surrogate functions based on Hermite Polynomials

This chapter corresponds to the following research paper sent to the Journal of Flow Measurements and Instrumentation, directly accepted by the editor for publication without modifications:

The author's contribution: The author contributed with the post-processing of all the measurements data, the generation of figures, graphs and by writing the paper. He also participated in the prototype measurements campaign and in the generation of algorithms to construct the surrogate functions.

Abstract

Francis turbines are designed for a specific set of operating conditions that is particular to each hydropower plant site. It allows this type of turbine to extract as much hydraulic power as possible, as long as they are operating in the right conditions. For this reason, power plant operators must know in advance what are the best conditions for operating their generating units and, naturally, in which exact conditions these units are actually operating. Detailed information about the turbine behavior in any operating condition can be obtained by performing measurements in a reduced scale physical model of the turbine prototype. These tests provide what is known as the turbine hill chart: a two-dimensional graphical representation of the most relevant turbine properties showing, for instance, the power output, the discharge, the efficiency and the cavitation conditions. This paper presents a method to monitor the operating conditions of a Francis turbine by locating it on the hill chart. To do so, it requires the generation of polynomial bi-variate functions based on Hermite polynomials that can calculate the turbine discharge and efficiency from its guide vanes angle and power output. A test case is presented with a turbine prototype of 444 MW of rated power operating

through a wide range of operating conditions. The validation is done by comparisons between the measured and estimated values of gross head, leading to similar values.

2.1 Introduction

Hydraulic turbines are required to operate in a wide range of conditions and to adjust its power output to the variations of water availability, energy demand and energy generation from other resources. Depending on factors such as the available specific energy and discharge, the turbine may operate in non-optimal conditions, affecting their performance and shortening their lifespan.

Francis turbines feature fixed blades, preventing them to better adapt to available energy and discharge variations, resulting in efficiency loss and the generation of a vortex swirling flow at part load conditions [55] and full load conditions [31]. Additionally, cavitation may happen when the counter-pressure provided by the downstream reservoir water level is low. This cavitation can cause pressure pulsations and induce wear and tear and vibration, increasing the risk of failure as discussed in [56] and [57]. General information about cavitation generation and its impacts in a Francis turbine can be found in [58], [59] and [60].

To mitigate the drawbacks of these harsh operating conditions and to optimize the exploitation of generating units containing Francis turbines, two different steps are required. The first step is to investigate how the machine behaves in every possible operating condition of interest, generating a picture that is unique for each turbine design. The second step is to monitor online, through measurements, where exactly inside this larger picture the turbine is actually operating.

This general picture is known as the turbine hill chart. It provides all the necessary information regarding efficiency, cavitation, vortex-rope presence and power generation, for instance. The complete hill chart of a turbine prototype can be obtained through measurements on a homologous reduced scale model using a test rig specially designed for this purpose. Measurements on the reduced scale physical model are performed with a high level of accuracy that usually cannot be achieved in the prototype.

This paper proposes then a monitoring system technique based in this two steps approach. It takes only two direct measurements on the prototype to estimate in what conditions, inside the hill chart, the turbine is operating. For the generation of the complete hill chart, it requires continuous functions to interpolate the measurements on the scaled model. These functions are generated through a combination of Hermite polynomials and modal strengths.

The proposed monitoring technique differs from others like the one presented by Valero et al. [61], as it is focused on physical quantities that can be transposed, such as the discharge and the efficiency. For its simplicity, it can make it easier to put into practice plant optimization models as those proposed by [62], [63] and [64].

A test case is presented where the methodology is applied and the operating conditions are estimated. For the validation, calculated values of gross head are compared with measurements showing good agreement. The results obtained suggest us that the methodology can provide reliable online estimations of the operating conditions of the prototype.

2.2 Model tests and hill chart generation

Performing tests on reduced scale physical model of hydraulic turbines is a mandatory phase for the most important hydropower projects as it provides detailed information on the turbine that cannot be accurately calculated. These tests are performed in accordance with the IEC standard [8], where the procedures to assure a high level of measurements accuracy and the general rules to transpose the results from the model to the prototype scale are presented. The IEC standard [65] also proposes transposition procedures, but in a more refined manner as it takes into account, for instance, the differences of surface roughness between model and prototype.

To simplify comparisons between homologous turbines with different diameters and rotating speeds, the IEC standard propose the use of non-dimensional discharge and speed factors, Q_{ED} and n_{ED} respectively. They are defined as:

$$Q_{ED} = \frac{Q}{D^2\sqrt{E}} \qquad n_{ED} = \frac{nD}{\sqrt{E}} \qquad E = gH \tag{2.1}$$

where Q is the discharge, D is the turbine reference diameter, n is the runner rotation frequency, E is the turbine specific energy, g is the local gravity acceleration and H is the turbine head.

All these measurements and non-dimensional factors can then be used to generate the turbine hill chart. A turbine hill chart can be considered as a dashboard where the plant operator can catch at a glance a great number of relevant information about the turbine and decide in which conditions the turbine is supposed to operate.

An example of hill chart having Q_{ED} and n_{ED} in its x and y axes is presented in Figure 5.8. This hill chart contains measurements that were performed in a reduced scale model from where all the data is interpolated to create the isolines and zones that are shown. It presents isolines of turbine hydraulic efficiency η, guide vanes opening angle α and mechanical power provided by the turbine P_m. It also presents the best efficiency point (BEP) and four different zones:

- The inlet cavitation zone, corresponding to the rated level of the downstream reservoir;

- The interblade cavitation (see [66]), also corresponding to the rated level of the downstream reservoir;

- The rated operating zone where the turbine must operate according to the specifications;
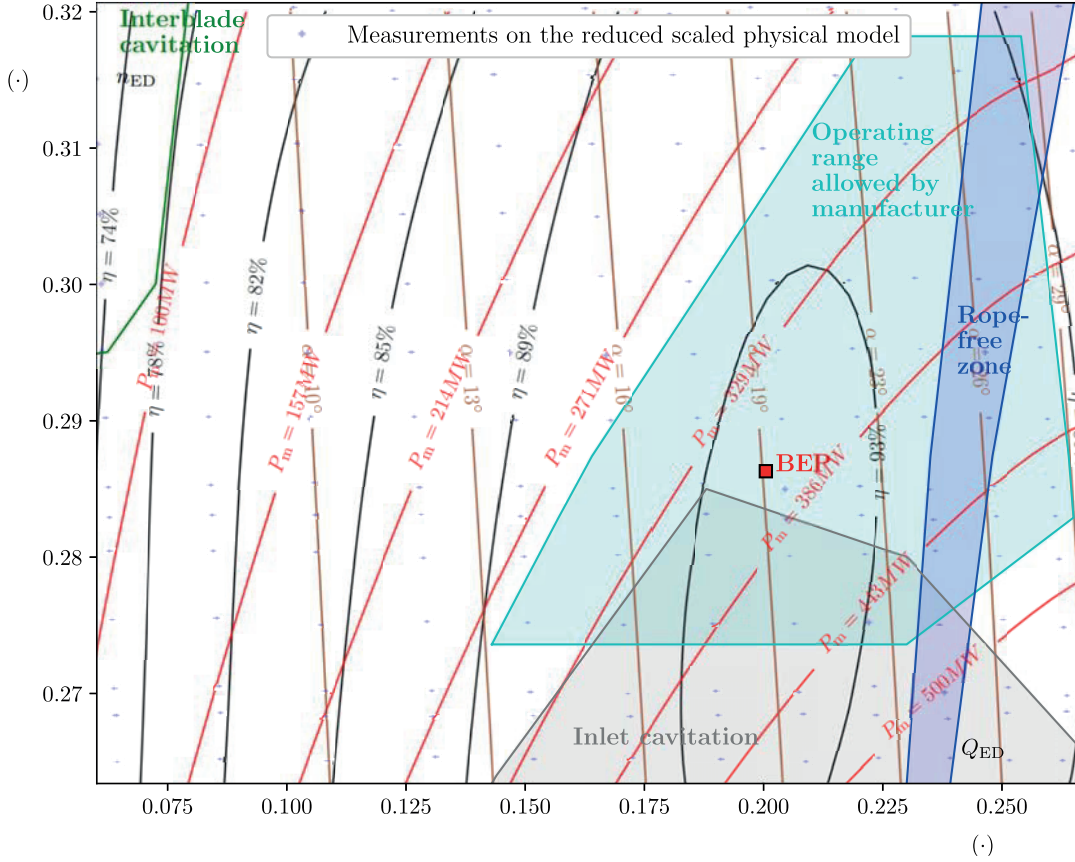
Figure 2.1 – Example of the Q_{ED}, n_{ED} hill chart featuring efficiency isolines, the BEP, the operating range, the rope-free and cavitation zones limits of a Francis turbine.

- The vortex rope-free zone.

The hydraulic efficiency and mechanical power are defined as in Equation 2.2. The values shown in this hill chart are already transposed to the prototype scale.

$$\eta = \frac{P_{\mathrm{m}}}{P_{\mathrm{H}}} \qquad P_{\mathrm{m}} = P_{\mathrm{h}} - P_{\mathrm{rb}} \qquad P_{\mathrm{h}} = \rho Q E \tag{2.2}$$

where P_{h} is the hydraulic power and P_{rb} is the sum of the power losses inside the turbine, combining the specific hydraulic energy loss, the leakage flow loss and the disc friction power loss.

2.3 Hermite polynomials interpolation method

The measurements on the reduced scale physical model provide information only on a finite number of points of the complete hill chart. An interpolation method is then required to cover the complete range where the turbine operates.

It is assumed that any variable of interest, such as the discharge or the efficiency, can be represented through a continuous bivariate function covering all this domain of possible operating conditions. With this assumption, the Weierstrass approximation theorem can be used [67]. This theorem states that every continuous function defined on a closed interval can be uniformly approximated by a polynomial surrogate function. Therefore, this paper uses surrogate functions that are generated as a combination of Hermite polynomials [68], similarly to the methodology proposed by Andolfatto et al in [69].

The Hermite polynomials $He_{n,m}$, with $n, m \in \mathbb{N}$, form a complete basis of functions inside the Hilbert space that are orthogonal with respect to the scalar product defined as:

$$\langle He_{i,j}, He_{k,l} \rangle = \int_{\mathbb{R}^2} He_{i,j}(\mathbf{X}) \cdot He_{k,l}(\mathbf{X}) \cdot \frac{1}{2\pi} \exp\left(-\frac{\mathbf{X}^2}{2}\right) d\mathbf{X} \tag{2.3}$$

with $\mathbb{R}$ being the set of real numbers, $\mathbf{X}$ being an input vector, $He_{i,j}$ and $He_{k,l}$ being any Hermite polynomial.

Hermite polynomials can be recursively defined as:

$$\begin{cases} He_{n+1,1} = a_n \cdot X_1 \cdot He_{n,1} + b_n \cdot He_{n-1,1} \\ He_{n+1,m} = He_{m-1,m} \cdot He_{n-m+2,1} \\ He_{n+1,n+2} = a_n \cdot X_2 \cdot He_{n,n+1} + b_n \cdot He_{n-1,n} \end{cases} \tag{2.4}$$

With the boundary conditions:

$$\begin{array}{ccc} He_{0,1} = 1 & He_{1,1} = X_1 & He_{1,2} = X_2 \\ a_n = \sqrt{\frac{1}{n+1}} & b_n = -\sqrt{\frac{n}{n+1}} & m \in [\![2, n+1]\!] \end{array} \tag{2.5}$$

where X_1 and X_2 are the input variables inside the vector $\mathbf{X}$. This definition for the Hermite polynomials is known as the probabilistic form of the family. Each Hermite polynomial $He_{n,m}$ can be represented with only one index by applying the change from m, n to p as defined in Equation 2.6. The graphical representation of Hermite polynomials $\text{He}_p = He_{n,m}$ with index p varying from zero to 14, corresponding to a fourth degree polynomial, is shown in Figure 2.2.

$$\begin{array}{c} \text{He}_{p \in \mathbb{N}} = He_{n,m} \\ \forall n \in \mathbb{N}, \forall m \in [\![1, n+1]\!], p = \frac{n(n+1)}{2} + m - 1 \end{array} \tag{2.6}$$

It is then possible to define surrogate functions in the form:

$$\hat{f} = \sum_{p=0}^{p_{max}} \lambda_p \text{He}_p(\mathbf{X}) \tag{2.7}$$

meaning that the surrogate function $\hat{f}$ approximates a given function f using only a truncated
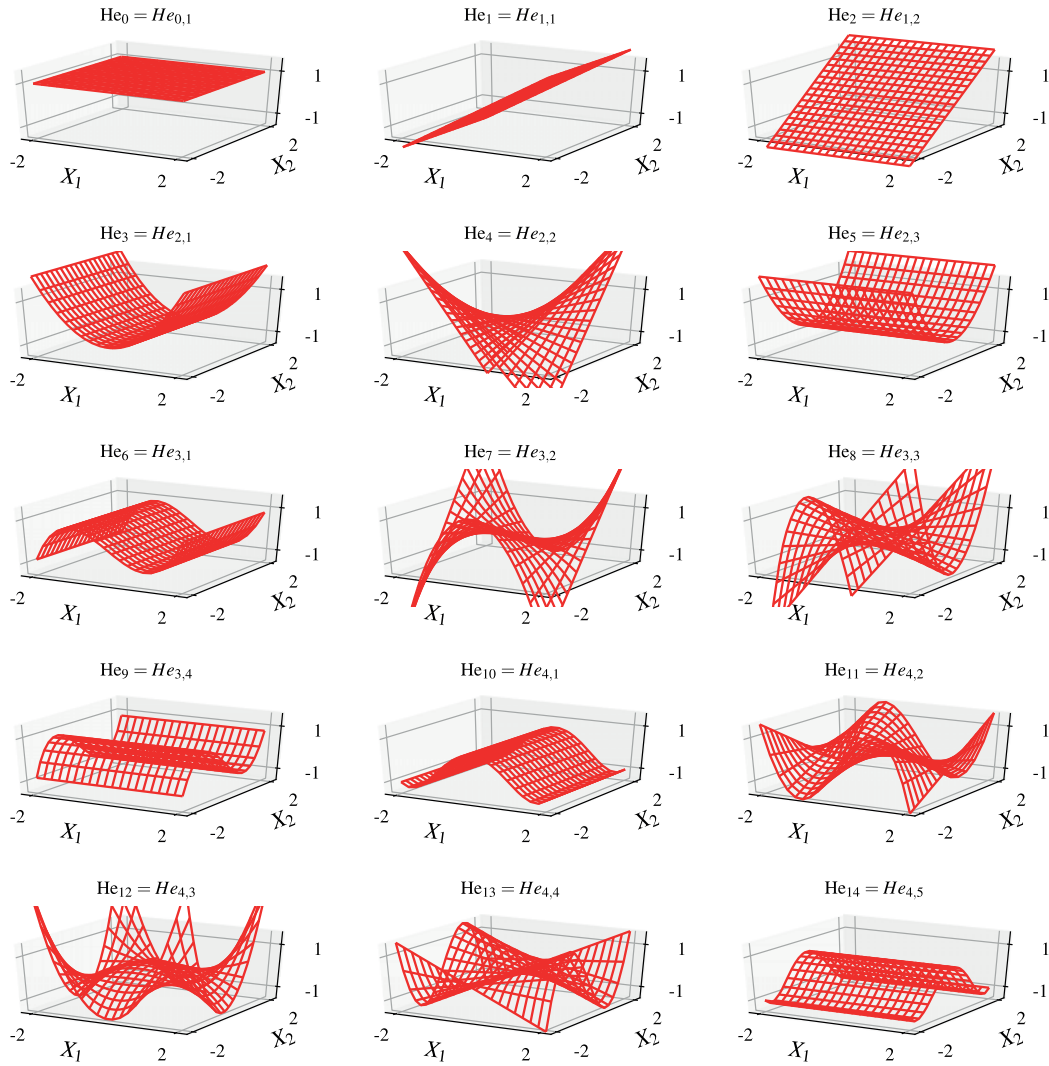
Figure 2.2 – Graphical representation of Hermite polynomials with index p from zero to 14.

basis of Hermite polynomials. The truncation parameter $p_{\max}$ and the coefficients $\lambda_p \in \mathbb{R}$, known as the modal strengths, must be chosen properly aiming to minimize the deviations between the function $\hat{f}$ and its target function f.

The explicit form of the target function f is, for the case discussed in this paper, unknown. Although, it is assumed that the performed measurements provide points on the surface given by f. In this case, one way to define the vector $\boldsymbol{\lambda}$ containing the modal strengths and to minimize the error between $\hat{f}$ and f is by using the least-squares method. The vector of modal strengths is then defined as:

$$\boldsymbol{\lambda} = \begin{bmatrix} \lambda_1 & \lambda_2 & \dots & \lambda_{p_{\max}} \end{bmatrix}^T = \left(\mathbf{He}^T \mathbf{He} \right)^{-1} \mathbf{He}^T \mathbf{f} \tag{2.8}$$

where:

$$\mathbf{f} = \begin{bmatrix} {}^{(1)}f & {}^{(2)}f & \dots & {}^{(N_s)}f \end{bmatrix}^T \tag{2.9}$$

$$\mathbf{He} = \begin{bmatrix} \mathrm{He}_0\left({}^{(1)}\mathbf{X}\right) & \mathrm{He}_1\left({}^{(1)}\mathbf{X}\right) & \dots & \mathrm{He}_{p_{\max}}\left({}^{(1)}\mathbf{X}\right) \\ \mathrm{He}_0\left({}^{(2)}\mathbf{X}\right) & \mathrm{He}_1\left({}^{(2)}\mathbf{X}\right) & \dots & \mathrm{He}_{p_{\max}}\left({}^{(2)}\mathbf{X}\right) \\ \vdots & \vdots & \ddots & \vdots \\ \mathrm{He}_0\left({}^{(N_s)}\mathbf{X}\right) & \mathrm{He}_1\left({}^{(N_s)}\mathbf{X}\right) & \dots & \mathrm{He}_{p_{\max}}\left({}^{(N_s)}\mathbf{X}\right) \end{bmatrix} \tag{2.10}$$

and the superscript ${}^{(k)} \forall k \in [\![1, N_s]\!]$ indicates the number of the measurement sample and N_s is the total number of samples.

Hermite polynomials are defined with respect to a standard normal Gaussian distribution. For this reason, its input variables are expected to have zero mean, zero correlation between them and to remain mostly inside the interval $[-1, 1]$. These conditions are usually not fulfilled among the measurements that are performed on the turbine. For this reason, a *transformation function* can be applied to map the measurements into a new set of variables that adapts better to these requirements.

As the modal strengths are calculated based only on the available measurement samples, the truncation parameter $p_{\max}$ must be chosen wisely to avoid polynomial approximations that either underfits or overfits the data. Underfitting happens when $p_{\max}$ is too low, leading to large deviations between the measurements and $\hat{f}$. Overfitting is observed when $p_{\max}$ is too high, reducing the error between $\hat{f}$ and the available measurements to a minimum, but leading to large deviations if points outside the original training set of points are evaluated.

There are different criteria that can help to identify a polynomial approximation that is underfitting or overfitting the training database. One of them is the Akaike Information Criterion

(AIC) [70], that can be applied here as:

$$\text{AIC} = N_s \left(\log \sigma_{\text{Std}}^2 + 1 \right) + 2 \left(p_{\max} + 1 \right) \tag{2.11}$$

where σ_{Std}^2 is the variance of the error inside the available points. As it can be seem in equation 2.11, the AIC will be high either if the model underfits the training data (high variance) or if it overfits the training data (high $p_{\max}$). Consequently, while comparing different $p_{\max}$ options for the same approximation, those with a good compromise between number of parameters and error will have a low AIC.

As the dimensionality of the approximation can sometimes be close to the number of available samples N_s, a correction for the AIC can be employed, as proposed in [71]. The corrected AIC, namely AICc, is employed in this paper as:

$$\text{AICc} = \text{AIC} + \frac{2 \left(p_{\max} + 1 \right) \left(p_{\max} + 2 \right)}{N_s - p_{\max} - 2} \tag{2.12}$$

2.4 Methodology

To find the exact location inside the hill chart where a Francis turbine prototype is operating, two measurements input are required. In any typical hydropower plant, the guide vanes angle α and the active power output from the generator P_{a} can be measured with accuracy and low cost. This pair of measurements is then proposed in this paper.

The guide vanes angle is not usually measured directly during a normal plant operation, but it can be easily obtained through kinematic relations between the guide vane opening angle and the servomotor stroke. Speed governors usually keep this parameter under constant monitoring.

Procedures to measure P_{a} are described in the IEC standard [72]. The relation between P_{a} and the mechanical power provided by the turbine P_{m} can be written as:

$$P_{\text{a}} = P_{\text{m}} - P_{\text{LB}} - P_{\text{LG}} \tag{2.13}$$

where P_{LB} includes the power losses in all the bearings and P_{LG} all the losses in the generator. These losses are usually calculated with precision by the manufacturers and they can be verified by the calorimetric method [73].

Assuming that the power losses are known, explicit relations between α, P_{a} and the remaining operating variables that are shown in the hill chart can be derived. For this purpose, surrogate functions as in Equation 2.7 can be generated and a transformation functions g_{T} can be defined to transform α and P_{a} into X_1 and X_2, the two terms of the input vector **X**.

In this paper, two surrogate functions are chosen: one for the discharge, $\hat{f}_Q$, and another for the turbine efficiency, $\hat{f}_\eta$. The methodology to obtain the discharge Q and the efficiency η of the prototype is summarized in the diagram of Figure 2.3. The methodology can be divided in two main parts:

1. *identification procedure*: where the transformation function g_T and the surrogate functions $\hat{f}_Q$ and $\hat{f}_\eta$ are defined according to the measurements performed on the reduced scale physical model;

2. *exploitation procedure*: where the actual turbine prototype discharge and efficiency are estimated online from the generating unit α and P_a.

Once the prototype discharge and and efficiency are known:

- the turbine available specific energy E is calculated as:

$$E = \frac{P_m}{\eta \rho Q} = \frac{P_a + P_{LB} + P_{LG}}{\eta \rho Q} \tag{2.14}$$

- knowing that the rotating speed and diameter of the prototype are fixed, n_{ED} and Q_{ED} are calculated as in Equation 5.4;

2.5 Application

2.5.1 Test case description

The operating conditions of a Francis turbine prototype of IEC specific speed $n_{QE} = 0.131$ (or $N_q = N Q^{0.5} H^{-0.75} = 43.5$, where N is the rotation speed in min^{-1}) are estimated with the proposed monitoring methodology. Measurements on its homologous reduced scale physical model were performed previously, providing the data to build the hill chart of Figure 5.8.

The reduced scale physical model features a runner of 0.35 m diameter and the measurements were performed at 800 min^{-1} rotation speed. A total of $N_s = 329$ operating points were investigated, with guide vanes opening angle varying from $5°$ to $32°$, covering any possible condition of interest for the prototype operations.

General information related to the generating unit containing the turbine prototype is presented in the Table 2.1. The local gravity g is calculated according to the IEC standard [72], based on the location of the turbine. Also according to [72], ρ is calculated based on the mean water temperature. Field acceptance tests performed previously yield an energy energy loss coefficient K defined as:

$$K = \left(g H_g - E \right) \left(\frac{Q^2}{2 A^2} \right)^{-1} \qquad A = \frac{\pi D^2}{4} \tag{2.15}$$
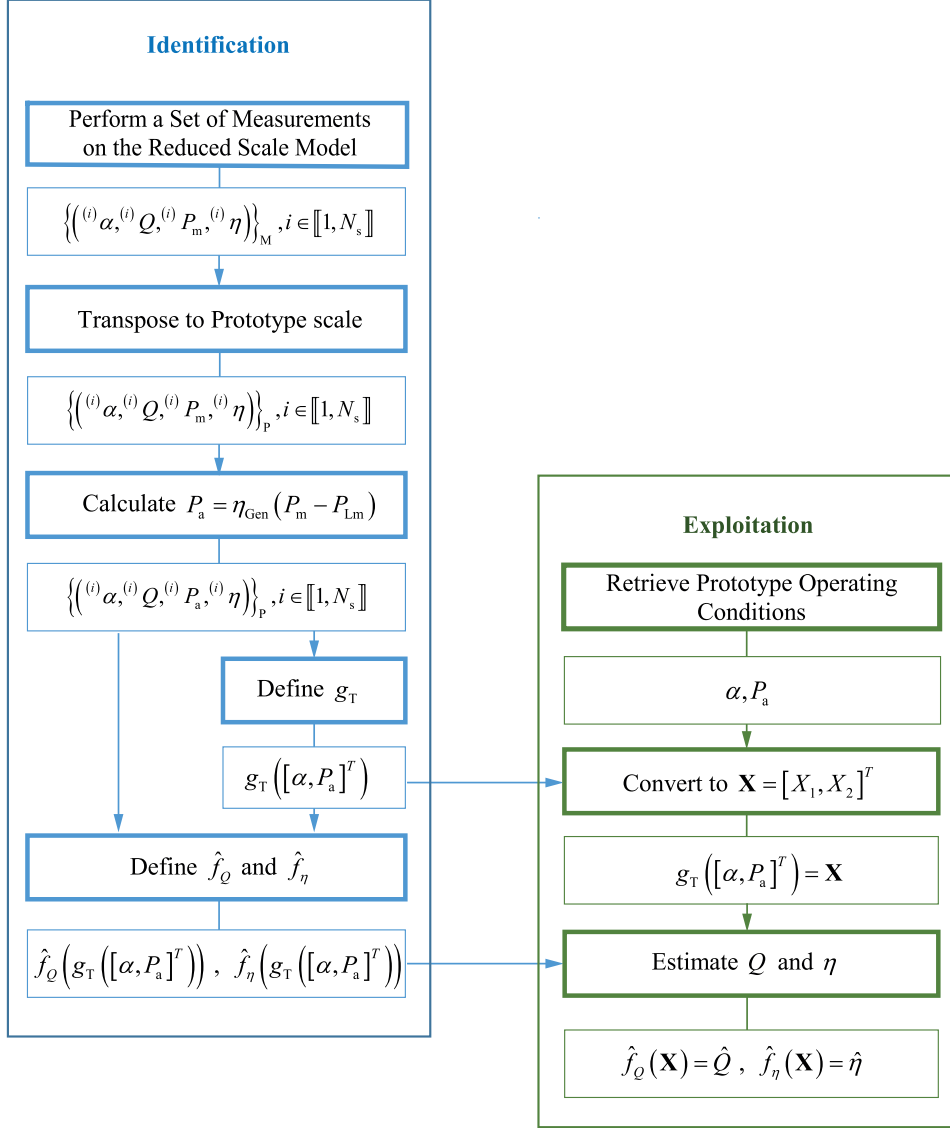
Figure 2.3 – Procedure for the parameters identification and determination of the turbine prototype efficiency and discharge.
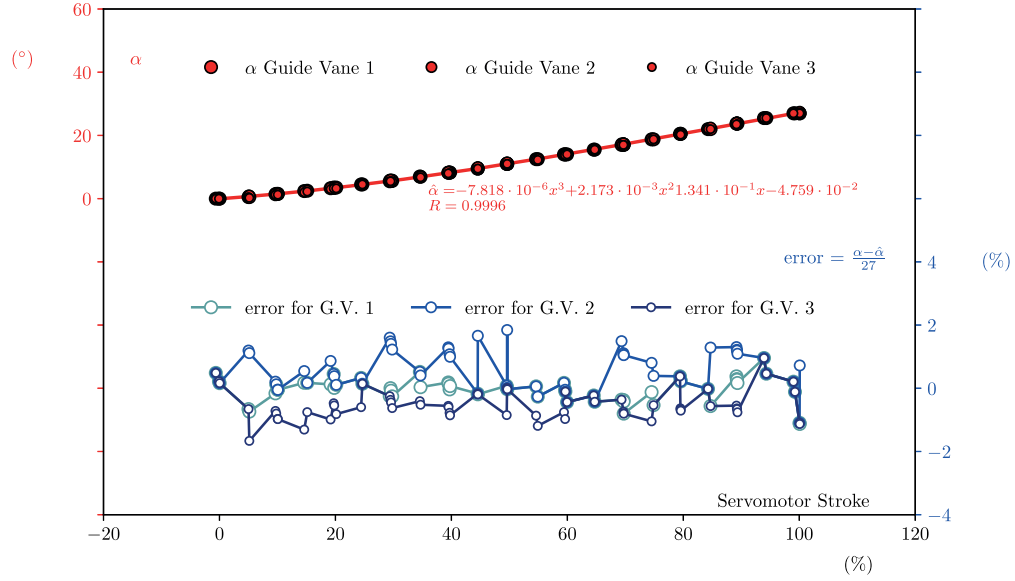
Figure 2.4 – Calibration curve for the guide vane angle according to the servomotor stroke. Measurements are performed at three different guide vanes and the relative error between them and the best fit curve is also presented.

where gH_g is the specific potential energy of the power plant and H_g is the plant gross head equal to the difference between the headwater and the tailwater reservoir levels. The table also provides the generator efficiency η_Gen, allowing P_LG to be calculated as:

$$\eta_\mathrm{Gen} = \frac{P_\mathrm{a}}{P_\mathrm{m} - P_\mathrm{LB}} \qquad P_\mathrm{LG} = P_\mathrm{a}\left(\frac{1}{\eta_\mathrm{Gen}} - 1\right) \tag{2.16}$$

The calibration curve of the guide vane angle as a function of the servomotor stroke is presented in Figure 2.4. The guide vane angle of three different guide vanes is measured and a best fit polynomial curve is generated. The error between the measurements and the best fit curve is also shown in Figure 2.4.

A total of 17 measurements were performed at different operating conditions on the prototype. Each measurement is performed after the stabilization of the temperature of the bearings and keeping a constant guide vanes opening during approximately 6 minutes for each operating condition. The guide vanes opening angle, the active output power from the generator and the plant gross head were constantly recorded. The downstream reservoir remained close to the rated level, keeping the cavitation properties as in Figure 5.8.

2.5.2   The transformation function

The transformation function g_T described in Equation 2.17 transforms the opening angles α and the active power P_a into the input variables for the Hermite polynomials X_1 and X_2.

Table 2.1 – Test case data of the prototype generating unit.

Rated active power output	P_{rated}	443.7 MW
Rated head	H_{rated}	170.7 mwc
Rated discharge	Q_{rated}	$288 \ \text{m}^3 \cdot \text{s}^{-1}$
Rotation speed	N_{P}	$128.6 \ \text{min}^{-1}$
Reference diameter	D_{P}	5.4 m
Generator efficiency[a]	η_{Gen}	98.5 %
Bearing losses[a]	P_{LB}	350 kW
Local gravity[b]	g	$9.8096 \ \text{m} \cdot \text{s}^{-1}$
Water density[b]	ρ	$999.92 \ \text{kg} \cdot \text{m}^{-3}$
Energy loss coefficient[c]	K	0.156

[a] Estimated values.
[b] According to (International Electrotechnical Commission, 1991).
[c] Estimative based on previous tests on this generating unit.

It performs a translation and a normalization of both α and P_{a}, whereas the translation and normalization parameters for P_{a} requires knowing its related α value.

$$
g_{\text{T}}\left(\begin{bmatrix} \alpha \\ P_{\text{a}} \end{bmatrix}\right) = \underbrace{\begin{bmatrix} \frac{2}{\alpha_{\max}-\alpha_{\min}} & 0 \\ 0 & \frac{2}{\text{UP}(\alpha)-\text{LP}(\alpha)} \end{bmatrix}}_{\text{Normalization}} \underbrace{\begin{bmatrix} \alpha - \overline{\alpha} \\ P_{\text{a}} - \overline{P}_{\text{a}}(\alpha) \end{bmatrix}}_{\text{Translation}} = \begin{bmatrix} X_1 \\ X_2 \end{bmatrix} \tag{2.17}
$$

where $\alpha_{\min}$ is the minimum guide vanes opening inside the database of measurements performed in the reduced scale physical model, $\alpha_{\max}$ is the maximum value and $\overline{\alpha}$ is the mean value between $\alpha_{\min}$ and $\alpha_{\max}$.

The functions $\text{LP}(\alpha)$ and $\text{UP}(\alpha)$ are third degree polynomial functions that best fits, respectively, the lowest and the highest values of P_{a} according to the tested opening angle α. Their coefficients are defined by minimizing L_{LP} and L_{UP} defined as:

$$
L_{\text{LP}} = \sum_{k=1}^{N_s} {}^{(k)}W_{\text{LP}}\left({}^{(k)}P_{\text{a}} - \text{LP}\left({}^{(k)}\alpha\right)\right)^2 \tag{2.18}
$$

$$
L_{\text{UP}} = \sum_{k=1}^{N_s} {}^{(k)}W_{\text{UP}}\left({}^{(k)}P_{\text{a}} - \text{UP}\left({}^{(k)}\alpha\right)\right)^2 \tag{2.19}
$$

where:

$$
{}^{(k)}W_{\text{LP}} = \begin{cases} 1, & \text{if } {}^{(k)}P_{\text{a}} - \text{LP}\left({}^{(k)}\alpha\right) > 0 \\ 10^4, & \text{if } {}^{(k)}P_{\text{a}} - \text{LP}\left({}^{(k)}\alpha\right) \leq 0 \end{cases} \tag{2.20}
$$
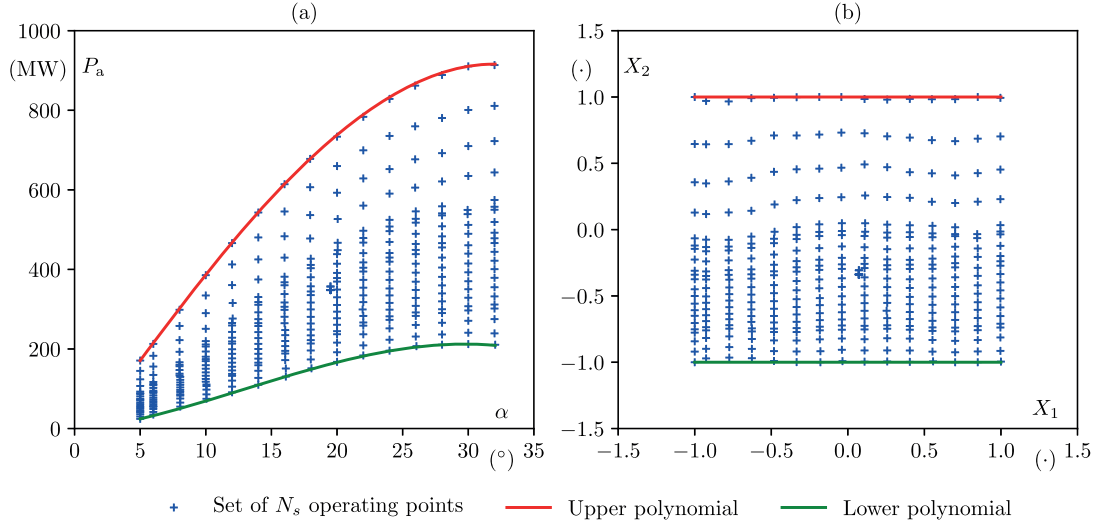
Figure 2.5 – (a) The values of α and P_a for the N_s operating points tested on the model. (b) Corresponding values of the transformed variables X_1 and X_2.

Table 2.2 – Mean, standard deviation and correlation of the input variables

	$\alpha\left(^\circ\right)$	$P_a\left(\text{MW}\right)$	$X_1\left(\cdot\right)$	$X_2\left(\cdot\right)$
Mean	18.05	311.31	0.00	-0.29
Standard deviation	8.36	182.12	0.62	0.50
Correlation coefficient	$\text{corr}\left(\alpha, P_a\right) = 0.70$		$\text{corr}\left(X_1, X_2\right) = 0.04$	

$$^{(k)}W_{\text{UP}} = \begin{cases} 10^4, \text{ if } {}^{(k)}P_a - \text{UP}\left({}^{(k)}\alpha\right) > 0 \\ 1, \text{ if } {}^{(k)}P_a - \text{UP}\left({}^{(k)}\alpha\right) \le 0 \end{cases} \tag{2.21}$$

Finally, the function $\overline{P}_a\left(\alpha\right)$ is a moving average for P_a, calculated as:

$$\overline{P}_a\left(\alpha\right) = \frac{\text{UP}\left(\alpha\right) + \text{LP}\left(\alpha\right)}{2} \tag{2.22}$$

The resulting transformation of the N_s values of α and P_a into the transformed variables X_1 and X_2 is shown in Figure 2.5. The mean and the standard deviation values of both the original and transformed variables are presented in the table 2.2. Additionally, the correlation between α and P_a and the correlation between X_1 and X_2 is also given. The presented values confirm that X_1 and X_2 are in agreement with the conditions where the Hermite Polynomials are defined.

2.5.3 Surrogate functions for the discharge and efficiency

By applying the methodology for the generation of surrogate functions, the discharge function $\hat{f}_Q$ and the turbine efficiency function $\hat{f}_\eta$ can be defined as:

$$\hat{f}_Q(\alpha, P_a) = \sum_{p=0}^{p_{Q\max}} \lambda_{Q_p} \mathrm{He}_p(g_T(\alpha, P_a)) = \sum_{p=0}^{p_{Q\max}} \lambda_{Q_p} \mathrm{He}_p(\mathbf{X}) = \hat{Q} \tag{2.23}$$

$$\hat{f}_\eta(\alpha, P_a) = \sum_{p=0}^{p_{\eta\max}} \lambda_{\eta_p} \mathrm{He}_p(g_T(\alpha, P_a)) = \sum_{p=0}^{p_{\eta\max}} \lambda_{\eta_p} \mathrm{He}_p(\mathbf{X}) = \hat{\eta} \tag{2.24}$$

where $\hat{Q}$ and $\hat{\eta}$ are the estimated values for the prototype discharge and efficiency, respectively. Possible values for the truncation parameters $p_{Q\max}$ and $p_{\eta\max}$ varying from 3 to 135 are evaluated and their AICc, maximum absolute error, mean absolute error and standard error are presented in Figure 2.6(a) and Figure 2.7(a). For both discharge and efficiency, the surrogate functions with the lowest truncation parameter values present high error values, indicating underfitting. On the contrary, those with truncation parameter values close to 135 present an increase in their AICc, indicating a higher risk of overfitting. Those are them the extreme options that must be avoided.

For both discharge and efficiency, a 3-D visualization of four surrogate functions with different truncation parameters are also presented in Figures 2.6 and 2.7. These four options of surrogate function are presented with the superscripts ^{A}, ^{B}, ^{C} and ^{D}.

The surrogate functions $\hat{f}_Q^A$ and $\hat{f}_\eta^A$ have large deviations between their estimations and the available measurements and are an example of underfitting. The functions $\hat{f}_Q^B$ and $\hat{f}_\eta^B$ have enough Hermite polynomials to properly fit the measurements with low error, also featuring low AICc. The functions $\hat{f}_Q^C$ and $\hat{f}_\eta^C$ have the lowest AICc values, indicating no overfitting or underfitting. The functions $\hat{f}_Q^D$ and $\hat{f}_\eta^D$ exhibit an increase in AICc, and their 3-D visualizations made apparent non-realistic surface undulations for a typical discharge or efficiency function, clearly indicating data overfitting.

In fact, any surrogate function with truncation parameters comprised between the options ^{B} and ^{C} can be considered as a good approximation model. For this paper, the options $\hat{f}_Q^B$ and $\hat{f}_\eta^B$ are chosen, as the resulting errors are already small and increasing the complexity of the model would only lead to a negligible reduction in error. The functions $\hat{f}_Q^B$ and $\hat{f}_\eta^B$ are also presented through the isolines in the 2-D hill charts of Figures 2.8(a) and (b).

Using the surrogate functions $\hat{f}_Q^B$ and $\hat{f}_\eta^B$ and the measured values of α and P_a of the prototype, the prototype discharge and efficiency are estimated and the results are presented in Figure 2.9. From these results, E, Q_{ED} and n_{ED} are calculated and the resulting operating conditions are presented in the hill chart of Figure 2.10.
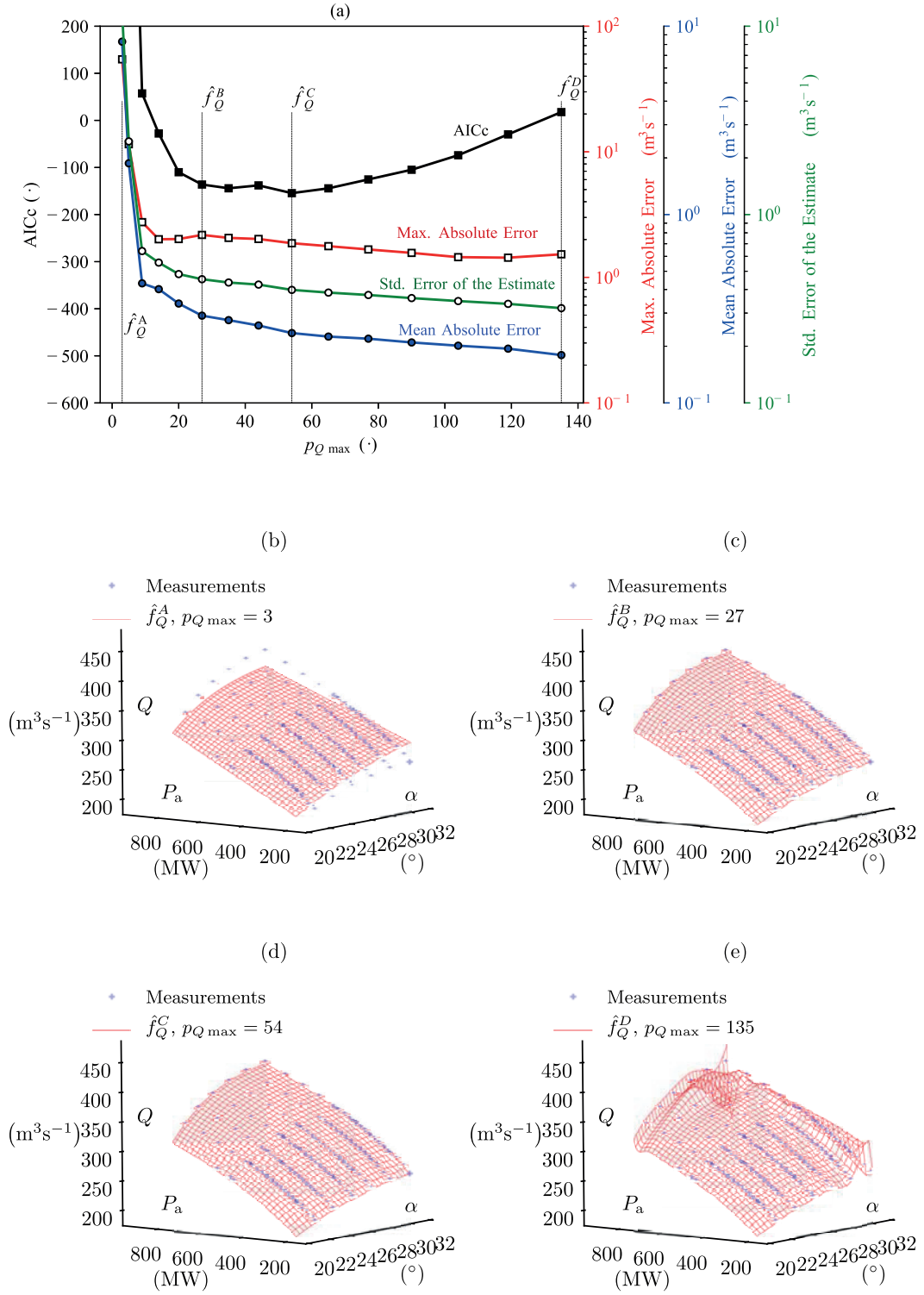
Figure 2.6 – (a) AICc, maximum absolute error, mean absolute error and standard error for $p_{Q\,\max}$ values varying from 3 to 135. (b) Example of surrogate function underfitting the available points. (c) Surrogate function with the chosen $p_{Q\,\max}$ value. (d) Function with lowest AICc. (e) Function overfitting the points.
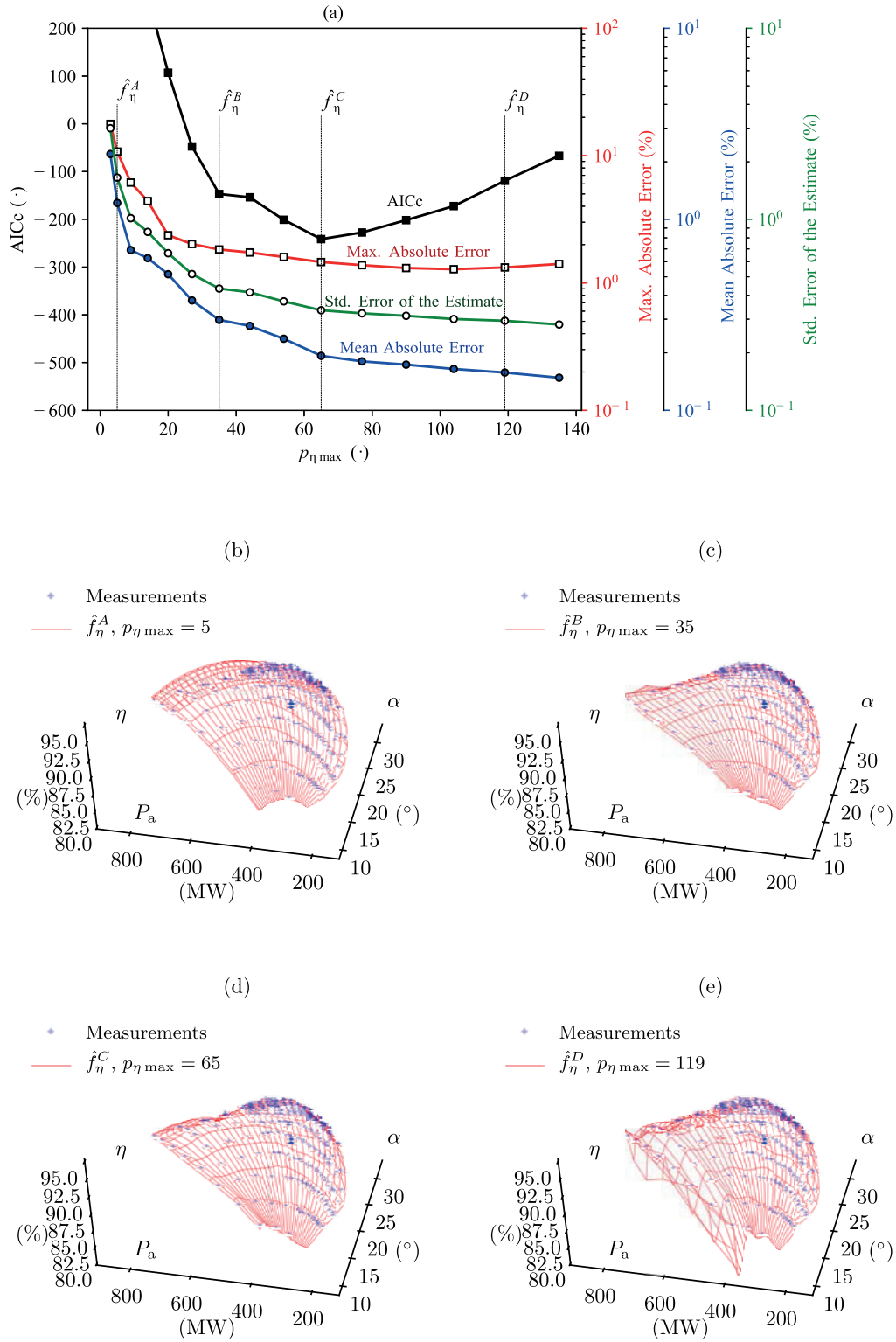
Figure 2.7 – (a) AICc, maximum absolute error, mean absolute error and standard error for $p_{\eta\max}$ values varying from 3 to 135. (b) Example of surrogate function underfitting the available points. (c) Surrogate function with the chosen $p_{\eta\max}$ value. (d) Function with lowest AICc. (e) Function overfitting the points.
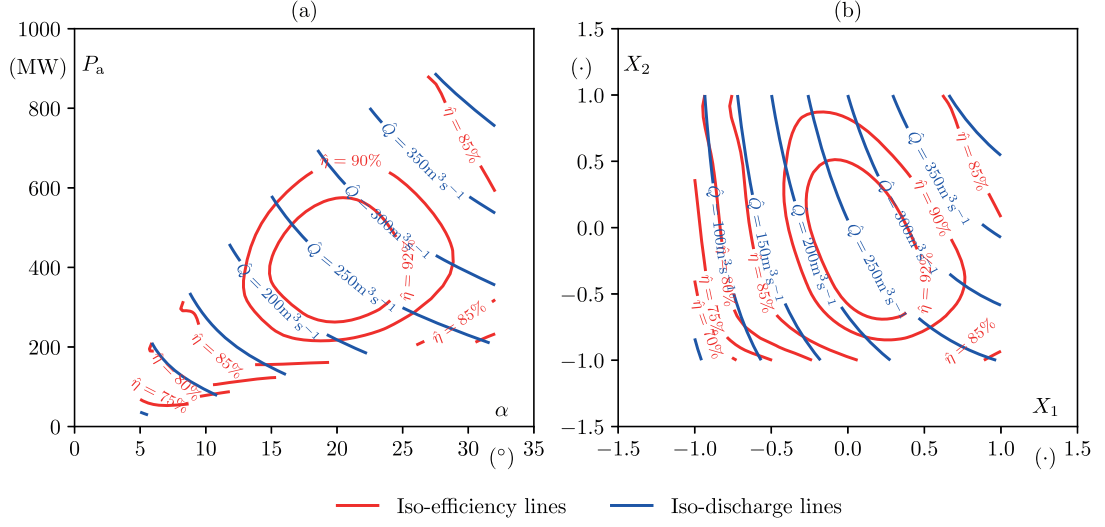
Figure 2.8 – (a) Isolines of discharge and efficiency as a function of α and P_a and (b) as a function of X_1 and X_2.

As the estimated values of prototype Q_{ED} and n_{ED} presented in Figure 2.10 illustrates, the tests started with the unit at very low discharge, so outside the rated operating range. The discharge is then increased and the unit enters in its rated range, but quickly moves into the cavitation zone. Two operating points are located at the limits of the rope-free zone. The two last ones, done at the highest discharge values, are outside the rated range and in a dangerous full load zone where a pulsating cavitation vortex rope may appear.

2.6 Validation

Because of the lack of direct measurement of the discharge, the method has been validated by comparing the gross head measured value with the gross head value resulting of the application of the present methodology. These two values are presented in Figure 2.11(a) and the error between them is shown in Figure 2.11(b)

The uncertainty bars shown in Figure 2.11 indicate the expected uncertainty using the methodology presented in this paper. It combines the following uncertainties:

- uncertainty on the discharge measurements performed on the reduced scale physical model equal to 0.10% of the maximum tested discharge;

- uncertainty on the efficiency measurements performed on the reduced scale physical model equal to 0.20%;

- uncertainty due to the polynomial approximation of the discharge and efficiency equal

(a)

(b)

- ● Prototype estimated discharge
- ─── $\hat{f}_Q^B$

- ● Prototype estimated efficiency
- ─── $\hat{f}_\eta^B$
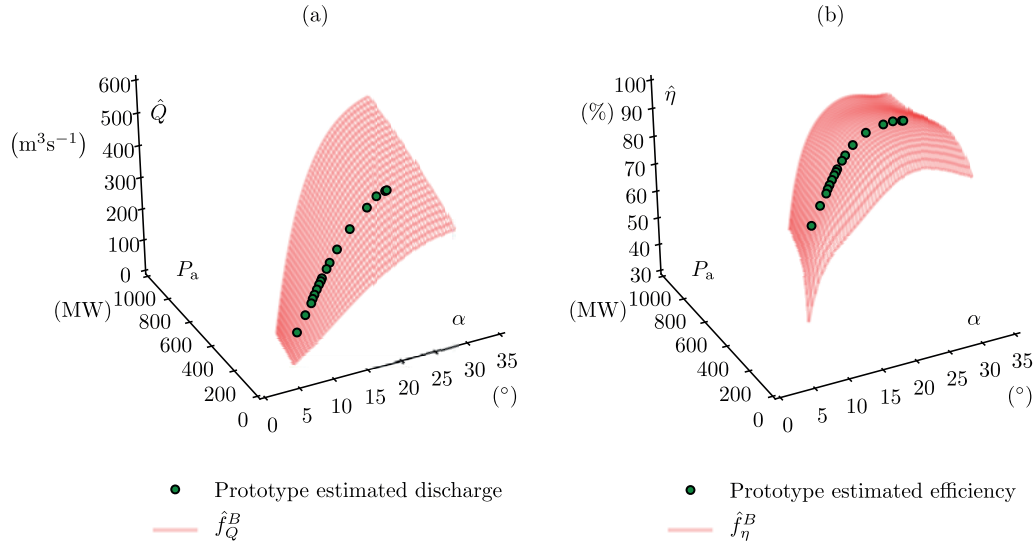
Figure 2.9 – (a) Estimated values of discharge during the site tests and the surrogate function $\hat{f}_Q^B$ and (b) the estimated values of efficiency and $\hat{f}_\eta^B$.
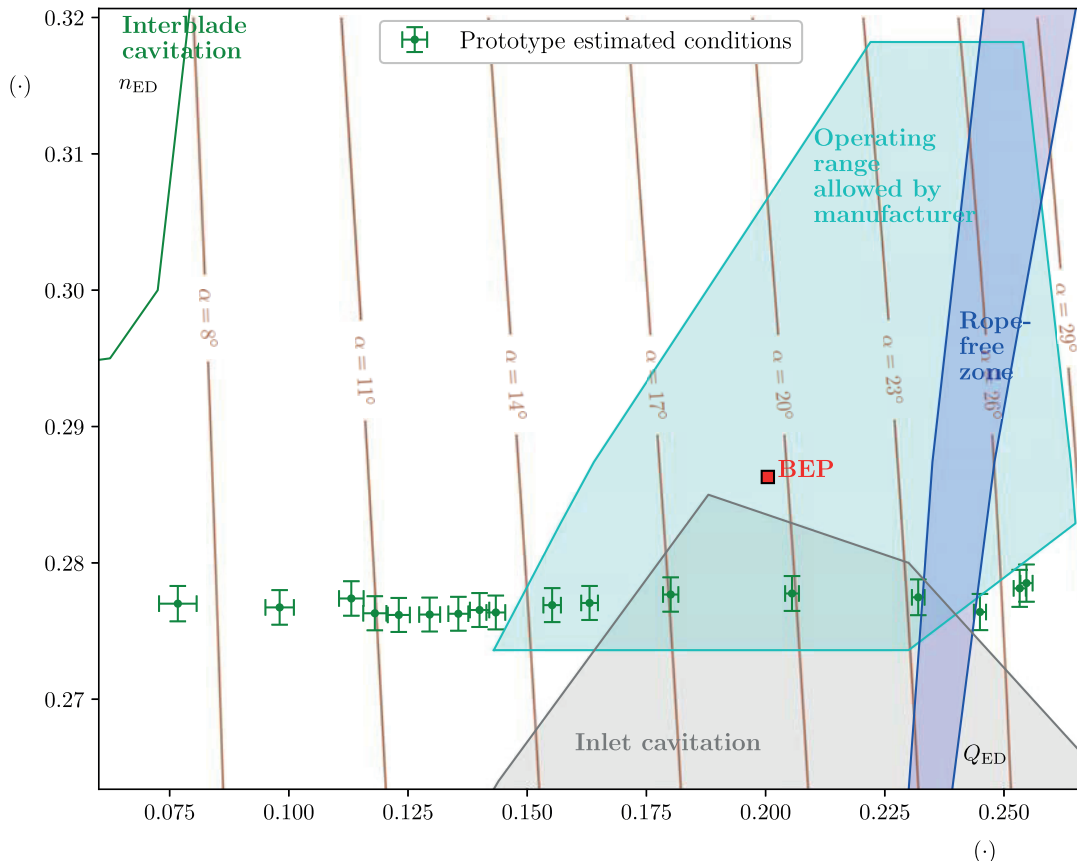
Figure 2.10 – Estimated prototype operating conditions inside its hill chart
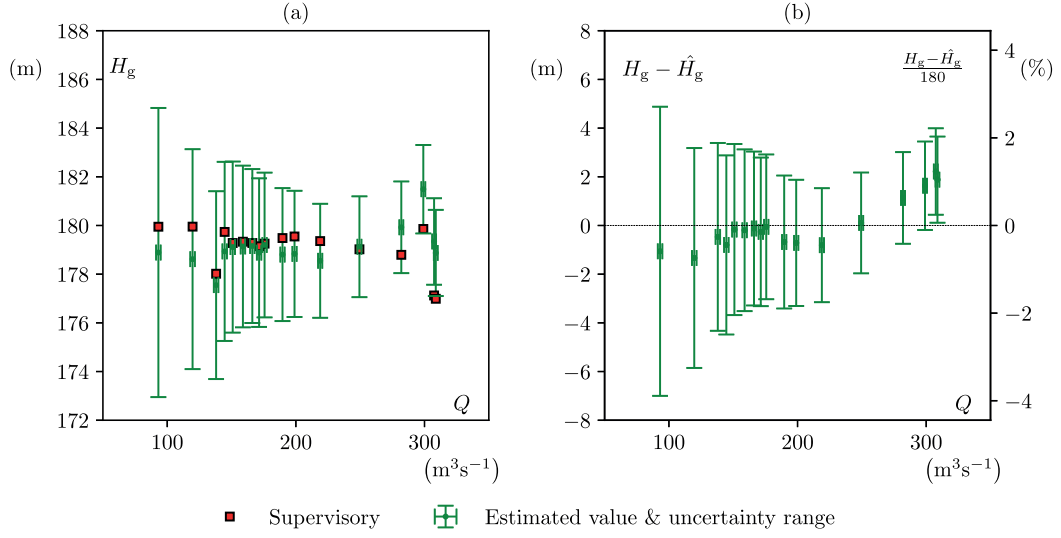
Figure 2.11 – (a) Estimate gross head and the gross head recorded by the plant supervisory. (b) Error between the two values.

to the standard error of the estimate;

- uncertainty on the prototype active power measurement equal to 0.70% of the maximum tested power;

- uncertainty on the prototype guide vanes angle measurement equal to $0.18°$, the standard error of the polynomial approximation .

A comparison between the expected uncertainty for the gross head estimates using the method presented in this paper and the expected uncertainty by doing direct measurements as described by the IEC standard [72] is presented in Figure 2.12. The presented expected uncertainty assuming the use of measurement methods in the IEC standard combine the following uncertainties:

- uncertainty on the discharge measurement equal to 1.70%, which is the expected measurement uncertainty on discharge measurements using the pressure-time method according to [72]);

- uncertainty on the prototype efficiency equal to 2.00%;

- uncertainty on the prototype active power measurement equal to 0.70% of the maximum tested power.

With the exception of the head calculated for the two highest values of discharge, all the head values provided by the supervisory are inside the calculated uncertainty range. The
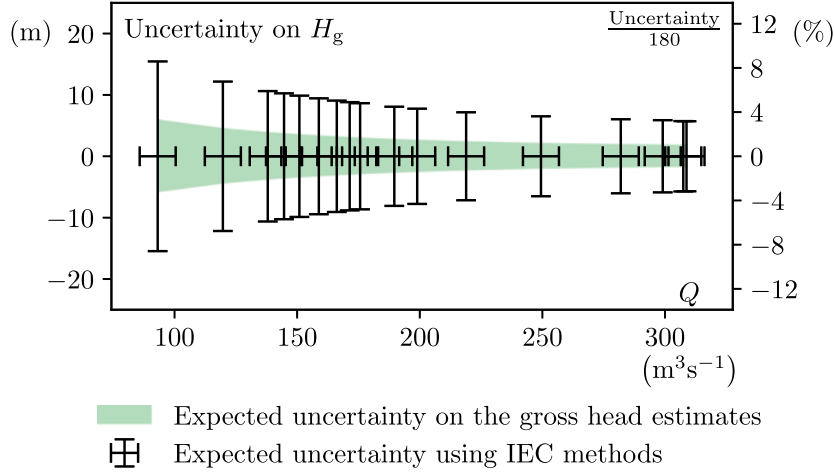
Figure 2.12 – Comparison between the expected uncertainty using the method presented in this paper and the expected uncertainty by doing direct measurements as described by the IEC standard.

maximum difference between the calculated H_g and the one provided by the supervisory is of only 2.2 mwc, representing a relative error of 1.2 %. This low deviation value suggests that the estimated values $\hat{Q}$ and $\hat{\eta}$ during the tests on the prototype are accurate.

It can also be noticed by the comparison shown in Figure 2.12 that direct measurements described by the IEC standard could possibly lead to higher values of uncertainty. In reality, sources of uncertainties due to the transposition of the results from the model to the prototype were ignored and would increase the uncertainties of the estimations using the methodology presented in this paper. A deeper and thorough investigation of this type of error propagation is outside the scope of this paper.

2.7   Conclusions

A methodology to monitor the operating conditions of a Francis turbine prototype is presented. It is based on two inputs from the generating unit, the active power and the guide vanes opening angle, and data from tests on a homologous reduced scale physical model turbine.

A test case where a 444 MW turbine prototype is operating at 17 different operating conditions is presented. For these conditions, values for the turbine discharge, efficiency, available specific energy, IEC speed factor, IEC discharge factor and the plant gross head are estimated. The estimated gross head, which requires both the turbine discharge and the efficiency as input, is then compared to the gross head obtained through direct measurements, leading to a good agreement between measurements and calculations.

Comparisons between expected uncertainties using the presented methodology and the uncertainties while using typical direct measurements are presented. The uncertainty values on the presented estimations are expected to be relatively low if the uncertainties related to the measurements transposition from scaled model to prototype are ignored.

The results lead to the conclusion that in situations where direct measurements of discharge or efficiency on the prototype are not suitable and tests on the reduced scale physical model are available, the presented monitoring methodology provides a good estimation of the turbine operating conditions. Such information is of critical relevance to optimize the operation of a hydropower plant as it can help operators to avoid operating the unit outside the range specified by the manufacturer, avoid harsh cavitation conditions, search for the best total power dispatch scheme and consequently increase the overall annual hydraulic energy harnessing. Moreover, it can work in parallel to monitoring systems more focused on vibration or pressure pulsations, providing a larger picture of the prototype behavior.

Acknowledgements

Funding

3 Estimating Francis turbines efficiency and complete characteristic curves

3.1 Introduction

The turbine efficiency η quantifies the amount of power P that is extracted from the available hydraulic power P_h. As illustrated in Figure 3.1, extracted from [74], part of the available hydraulic power is dissipated in the turbine bearings, and also due to internal flow turbulence, friction and leakages. The amount of power lost in each part of the turbine varies according to its specifc design. The expected distribution of losses in each part of a Francis turbine as a function of the specific speed ν, extracted from [75], is presented in Figure 3.2, for BEP conditions.

As presented by Gordon in [17], turbine manufacturers were able to increase turbines efficiency over the years from η_BEP values under 80% for old low head turbines to values such as η_BEP = 96% for large turbine prototypes of nowadays. This increase was made possible in part by advances in CFD simulation techniques, allowing for more optimized designs (see [75, 76, 11, 12] for instance). Better manufacturing techniques allowed the reduction in friction factors which allows efficiency increase, as demonstrated by Maruzewski et al. in [77]. Better labyrinths also allow less leakage losses, as discussed in [78], increasing the efficiency by increasing the amount of water discharge through the runner blades. A literature review of efficiency improvements in hydraulic turbines is provided by Liu et al. in [79].

Francis turbines feature fixed pitch runner blades. As a consequence, once they operate away from its BEP, a swirling flow leaves the turbine runner and a smaller amount of energy is transferred from the flow to the turbine shaft, reducing the turbine efficiency. An illustration from [74] showing typical velocity diagrams for a low and a high specific speed turbine operating at part load, and a turbine operating close to its BEP is presented in Figure 3.3.

The amount of energy transferred by the runner is mathematically modeled by the Euler equation:

$$E_\text{t} = k_{Cu\text{1e}}\left(\vec{C}_\text{1e} \cdot \vec{U}_\text{1e}\right) - k_{Cu\bar{\text{1}}\text{e}}\left(\vec{C}_{\bar{\text{1}}\text{e}} \cdot \vec{U}_{\bar{\text{1}}\text{e}}\right) - E_\text{rb} \qquad (3.1)$$
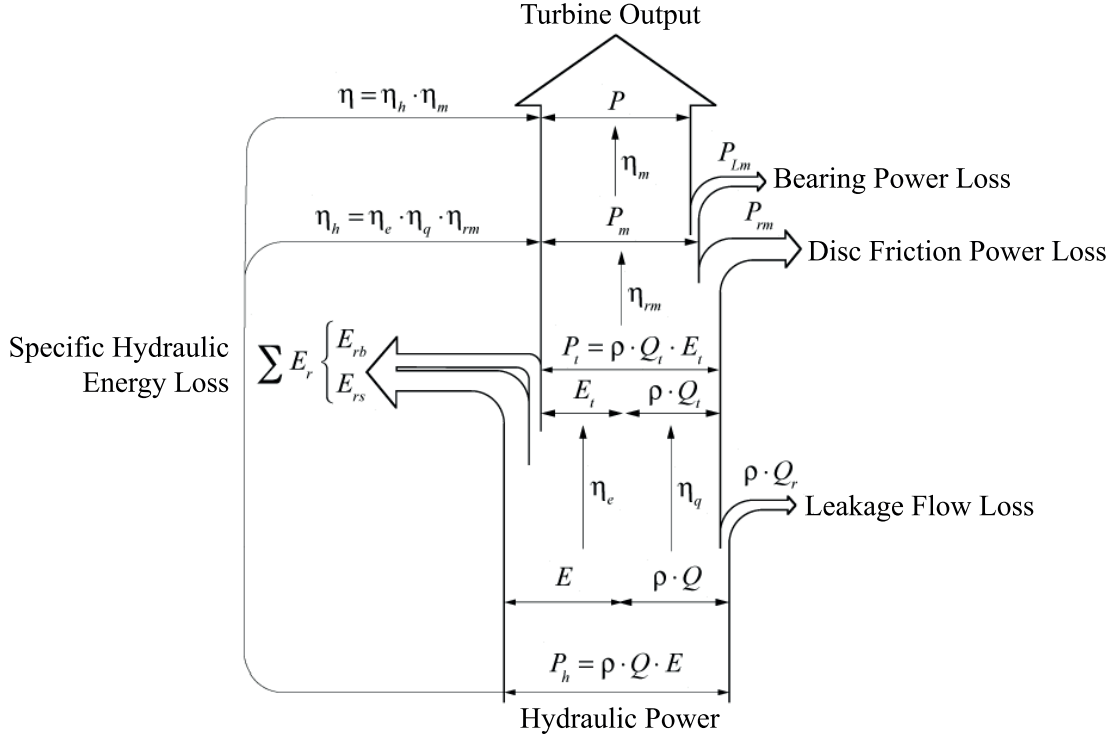
Figure 3.1 – Typical power losses in a hydraulic turbine.

where $E_{\rm rb}$ is the sum of specific energy losses due to friction and turbulence inside the runner and the indexes $_1$, $_{\bar{1}}$ and $_e$ make reference to the runner entry section, the runner outlet section and the most external streamline, respectively. The vector $\vec{C}$ is the flow absolute velocity vector, $\vec{U}$ is the runner rotating velocity vector and the coefficients k_{Cu1e} and $k_{Cu\bar{1}e}$, modeling the effect of the flow velocity profile, are defined as:

$$k_{Cu1e} = \frac{\int_{A_1}(\vec{C}\cdot\vec{U})\vec{C}\cdot\vec{n}\,dA}{Q_t(\vec{C}_{1e}\cdot\vec{U}_{1e})} \quad \text{and} \quad k_{Cu\bar{1}e} = \frac{\int_{A_{\bar{1}}}(\vec{C}\cdot\vec{U})\vec{C}\cdot\vec{n}\,dA}{Q_t(\vec{C}_{\bar{1}e}\cdot\vec{U}_{\bar{1}e})} \tag{3.2}$$

where Q_t is the discharge through the runner blades. Assumptions are usually made in order to simplify the Euler equation, such as: $E_{\rm rb} = 0$; uniform meridional flow velocty profile at the runner inlet and outlet; uniform tangential flow at the runner inlet and flow rotating as a solid body at the runner outlet. These assumptions leads to a simplified Euler equation expressed as:

$$E_t = Cu_{1e}\cdot U_{1e} - \frac{1}{2}Cu_{\bar{1}e}\cdot U_{\bar{1}e} \tag{3.3}$$

The eq. (3.3) expressed as a function of the angles α and β illustrated in Figure 3.3 becomes:

$$E_t = -\frac{U_{\bar{1}e}^2}{2} + \left(\frac{R_{1e}}{R_{\bar{1}e}}\frac{A_{\bar{1}}}{A_1}\frac{1}{\tan\alpha_{1e}} + \frac{1}{2\tan\beta_{\bar{1}e}}\right)\frac{Q_t\cdot U_{\bar{1}e}}{A_{\bar{1}}} \tag{3.4}$$
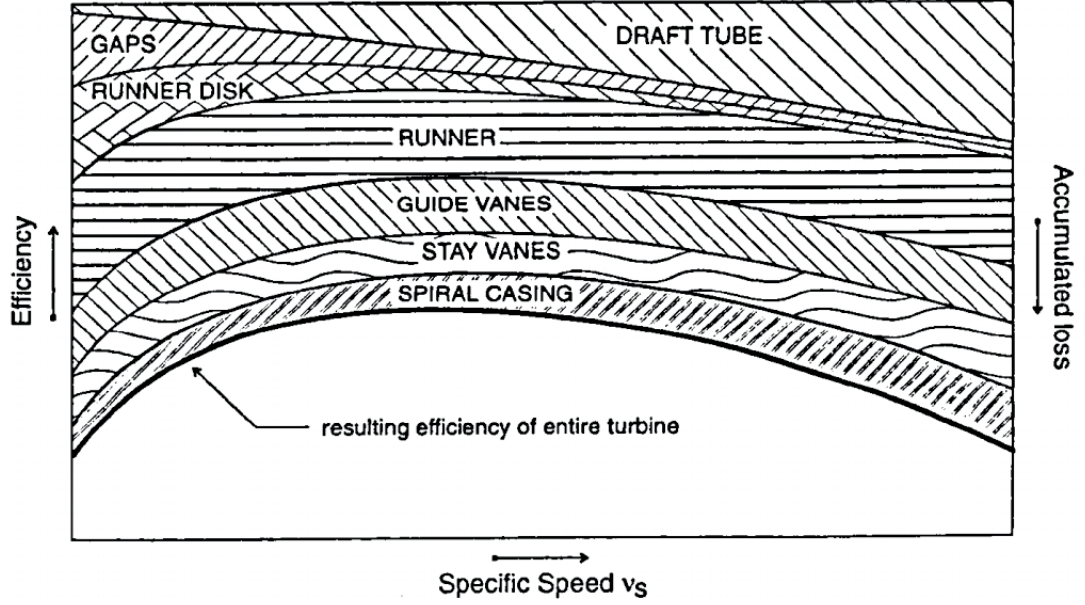
Figure 3.2 – The expected energy loss in each part of a Francis turbine as a function of the specific speed, extracted from [75].

The simplified Euler equation presented in eq. (3.4) leads to three important insights regarding the turbine efficiency:

1. No energy is transferred if $U_{\bar{1}e} = 0$, leading also to $\eta = 0$ in this condition;

2. There is a runner rotational speed greater than zero that leads to $E_t = 0$. In this condition, known as **runaway** condition, the runner rotational speed is calculated as in eq. (3.5);

$$U_{\bar{1}e_{Run}} = \frac{2 \cdot Q_t \cdot U_{\bar{1}e}}{A_{\bar{1}}} \left(\frac{R_{1e}}{R_{\bar{1}e}} \frac{A_{\bar{1}}}{A_1} \frac{1}{\tan \alpha_{1e}} + \frac{1}{2 \tan \beta_{\bar{1}e}} \right) \tag{3.5}$$

3. There is a maximum value of energy transfer $E_{t_{max}}$, expressed as in eq. (3.6).

$$E_{t_{max}} = \frac{U_{\bar{1}e_{max}}^2}{2} \qquad \text{where} \qquad U_{\bar{1}e_{max}} = \frac{U_{\bar{1}e_{Run}}}{2} \tag{3.6}$$

Even though the insights and equations derived from the simplified Euler equation (eq. (3.4)) are qualitatively relevant, the resulting values of $E_{t_{max}}$ and $U_{\bar{1}e_{Run}}$ obtained from these equations are never accurate when compared to actual measurements. In reality, E_{rb} is never zero and the flow velocity profile through the runner inlet or outlet cross-sections is never truly constant or properly expressed by a linear function.

The construction of efficiency and characteristic curves based on the Euler equation have been tried by other authors (see [16, 80]). They obtain as a result efficiency curves that are

Figure 3.3 – Typical velocity diagrams for a low and a high specific speed turbine operating at part load, and a turbine operating close to its BEP.

second degree polynomials —like the simplified Euler equation itself —which do not represent properly real efficiency curves, such as those presented in the example of hill chart of Figure 1.3. Zeng et al. in [81] used measurements from a set of 25 pump-turbines characteristic curves to construct models to predict key points in a pump-turbine characteristic curve. These key points are then connected using domain partition and surface meshes. As a drawback, the model proposed by Zeng et al. is focused on the complete characteristic curves, losing accuracy in terms of efficiency inside the typical operating range of the unit.

This thesis work provides an empirical model for Francis turbines that is also accurate in terms of turbine efficiency inside the turbine operating range. It relies more on actual measurements data than on simplified equations such as the simplified Euler equation. An example of the outcome provided by the empirical η estimation model is illustrated in Figure 3.4. To simplify the notation, in Figure 3.4 and in the following sections, the index $_R$ indicates the value of a variable made relative by its value at the BEP, such as:

$$n_{\mathrm{ED_R}} = \frac{n_{\mathrm{ED}}}{n_{\mathrm{ED_{BEP}}}} \qquad Q_{\mathrm{ED_R}} = \frac{Q_{\mathrm{ED}}}{Q_{\mathrm{ED_{BEP}}}} \qquad T_{\mathrm{ED_R}} = \frac{T_{\mathrm{ED}}}{T_{\mathrm{ED_{BEP}}}} \qquad \eta_{\mathrm{R}} = \frac{\eta}{\eta_{\mathrm{BEP}}} \tag{3.7}$$

Similar to the authors aforementioned, the empirical models presented in this Chapter make use of the turbine specific speed as an input variable. The turbine specific speed is strongly related to the installation site, more specifically the rated values of specific energy and water discharge, E_{rated} and Q_{rated}, respectively. The turbine specific speed is defined in Appendix A.1 and the typical geometry of runners for low specific speed and high specific speed turbines

are illustrated in 3.3. The specific speed n_{QE}, as defined by the IEC standard [8], is used in this paper and is calculated as:

$$n_{QE} = n_{ED_{BEP}} Q_{ED_{BEP}}^{0.5} \tag{3.8}$$

3.2 Empirical model for the efficiency estimation

3.2.1 Overall methodology

The empirical model for η estimation is constructed making use of four submodels: 1) η_{BEP} submodel; 2) operating range efficiency η_{OP} submodel; 3) runaway n_{ED} submodel and 4) efficiency in transition zones, η_{TR}, submodel. The contribution from each submodel in the construction of the estimated efficiency curve —also indicated in Figure 3.4 —is:

1. η_{BEP} submodel estimates the turbine peak efficiency by taking only easily accessible data of the turbine as an input. It takes into account the turbine year of commissioning y, its runner diameter D and its specific speed n_{QE};

2. η_{OP} submodel estimates the turbine efficiency for operating conditions surrounding the BEP, where the turbine will be normally operating. It makes use of Hermite polynomials to generate efficiency curves.

3. runaway n_{ED} submodel estimates the curve corresponding to n_{ED} values where the torque and, consequently, the efficiency is equal zero, even though the turbine rotation speed is not zero.

4. η_{TR} submodel provides estimated values of η between the operating range zone and conditions where $\eta = 0$, i.e., runaway conditions and at $n_{ED} = 0$. It takes as input the results from the previous submodels and makes use of a mixture model to combine Hermite polynomials.

The $Q_{ED_{BEP}}$ and $n_{ED_{BEP}}$ values of the Francis turbines available in the EPFL database that are used to generate the empirical submodels for η_{BEP}, η_{OP} and n_{ED} in runaway conditions, named $n_{ED_{Run}}$, are presented in Figure 3.5.

In the next subsections, from 3.2.2 to 3.2.5, the construction of these four submodels is detailed. In 3.2.6, these four submodels are combined into an unique empirical model for the turbine efficiency estimation considering any operating condition with $\eta \geq 0$.

3.2.2 Estimating the peak efficiency η_{BEP}

By performing a comprehensive research for turbine efficiency data, Gordon provided in [17] interesting insights for a methodology to predict the turbine peak efficiency η_{BEP}. His empirical
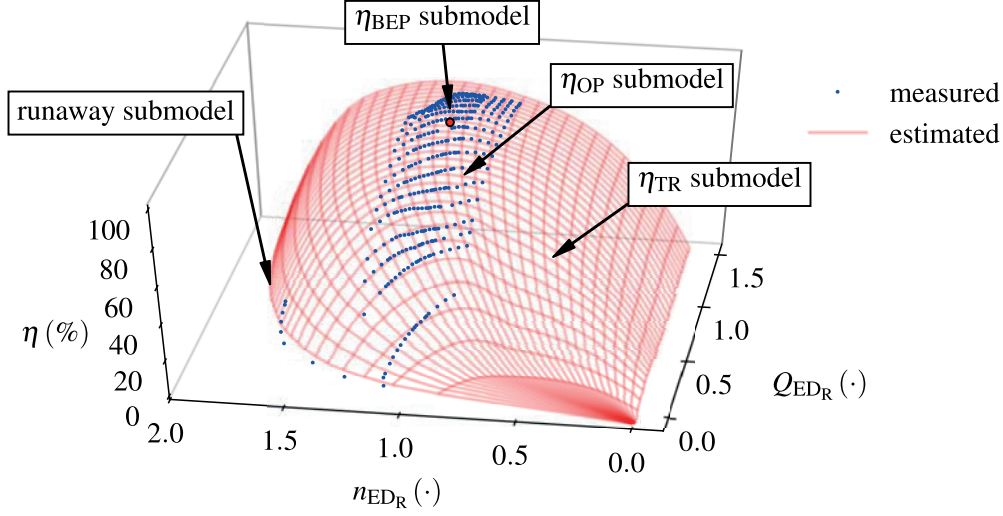
Figure 3.4 – Contributions from the four proposed submodels in the construction of the efficiency estimation curve.

formulas are able to estimate η_{BEP} values with a standard error of estimate $\sigma_{\mathrm{Std}\eta_{\mathrm{BEP}}} = 0.7\%$ when comparing measurements and estimates from turbines in his database. However, by analyzing the error between measured and estimated values of η_{BEP} among turbines available at the EPFL database, error levels tend to increase for turbines commissioned after the year 1998, as presented in Figure 3.6. Improvements on the Gordon model are then proposed to increase its accuracy.

The empirical model to estimate η_{BEP} proposed by Gordon takes one base value for the efficiency, 91.87%, and makes corrections in this value according to the turbine specific speed n_{QE}, the runner diameter D and the year in which the turbine was commissioned y. His model is expressed as:

$$\hat{\eta}_{\mathrm{BEP}_{\mathrm{G}}} = 91.87\% - \Delta\epsilon_{\mathrm{year}_{\mathrm{G}}} - \Delta\epsilon_{n_{\mathrm{QE\,G}}} + \Delta\epsilon_{\mathrm{size}_{\mathrm{G}}} \tag{3.9}$$

where the correction terms are calculated as:

$$\Delta\epsilon_{\mathrm{year}_{\mathrm{G}}} = \left(\frac{1998 - y}{187}\right)^3 \tag{3.10}$$

$$\Delta\epsilon_{n_{\mathrm{QE\,G}}} = \left[\left(\frac{n_{\mathrm{q}} - 52}{292}\right)^2\right]^{1.017} \tag{3.11}$$

$$\Delta\epsilon_{\mathrm{size}_{\mathrm{G}}} = \left(1 - 91.87 \cdot 10^{-2} + \Delta\epsilon_{\mathrm{year}_{\mathrm{G}}} + \Delta\epsilon_{n_{\mathrm{QE\,G}}}\right) \cdot \left(1 - 78.90 \cdot 10^{-2} \cdot D^{-0.2}\right) \tag{3.12}$$
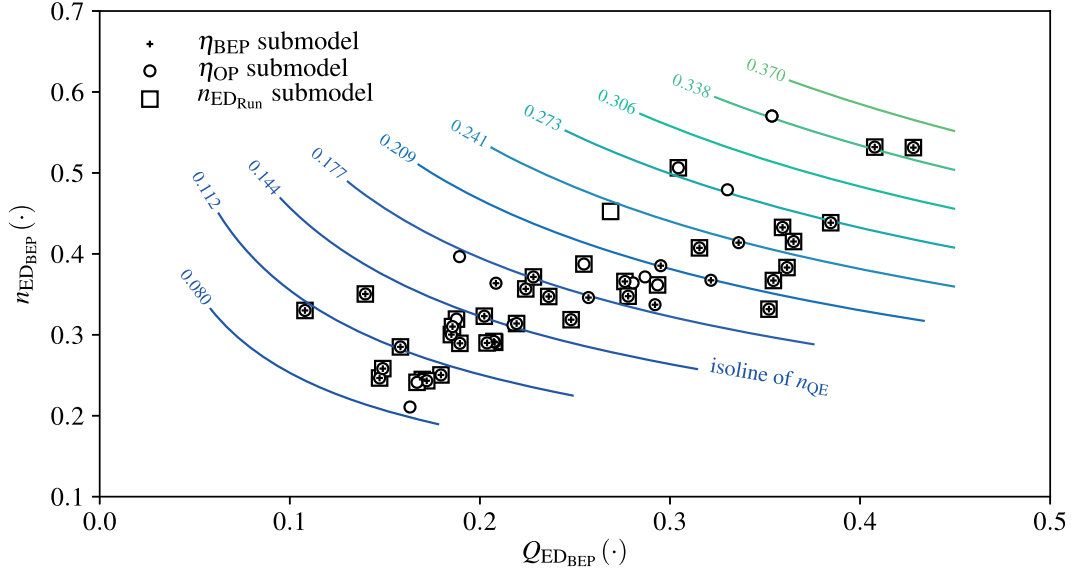
Figure 3.5 – $Q_{ED_{BEP}}$ and $n_{ED_{BEP}}$ values of the Francis turbines available in the EPFL database that are used to generate the empirical submodels for η_{BEP}, η_{OP} and $n_{ED_{Run}}$.

For $\Delta\epsilon_{n_{QE\,G}}$ calculation, Gordon considered the unit specific speed n_q (metric), where he used the prototype rated values of head and discharge. Assuming $H_{rated} = H_{BEP}$ and $Q_{rated} = 1.1 \cdot Q_{BEP}$, n_q can be calculated as:

$$n_q = \text{rpm} \cdot H_{rated}^{-0.75} \cdot Q_{rated}^{0.5} \approx 60 \cdot 1.1^{0.5} \cdot g^{0.75} \cdot n_{QE} \tag{3.13}$$

Old generating units may undergo rehabilitation and have some parts of its turbine replaced by a new one, usually with a more modern design to increase efficiency. Turbines that receive a new runner, for instance, will have an increase in efficiency, but it will probably not reach the expected efficiency value of a completely new turbine design. To overcome this issue, Manness and Doering proposed in [82] to calculate the y variable for these cases as:

$$y = \frac{\left(\text{year of } 1^{st} \text{ commissioning}\right) + 2 \cdot \left(\text{year of rehabilitation}\right)}{3} \tag{3.14}$$

Combining the η_{BEP} data provided by Gordon with that available at the LMH, all the parameters of the Gordon empirical model are recalculated. Additionally, a new formulation for $\Delta\epsilon_{year}$ is proposed, so that a maximum year value does not have to be defined. As a result, the estimated η_{BEP} values using the new parameters are calculated as:

$$\hat{\eta}_{BEP} = 98.65\% - \Delta\epsilon_{year} - \Delta\epsilon_{n_{QE}} + \Delta\epsilon_{size} \tag{3.15}$$
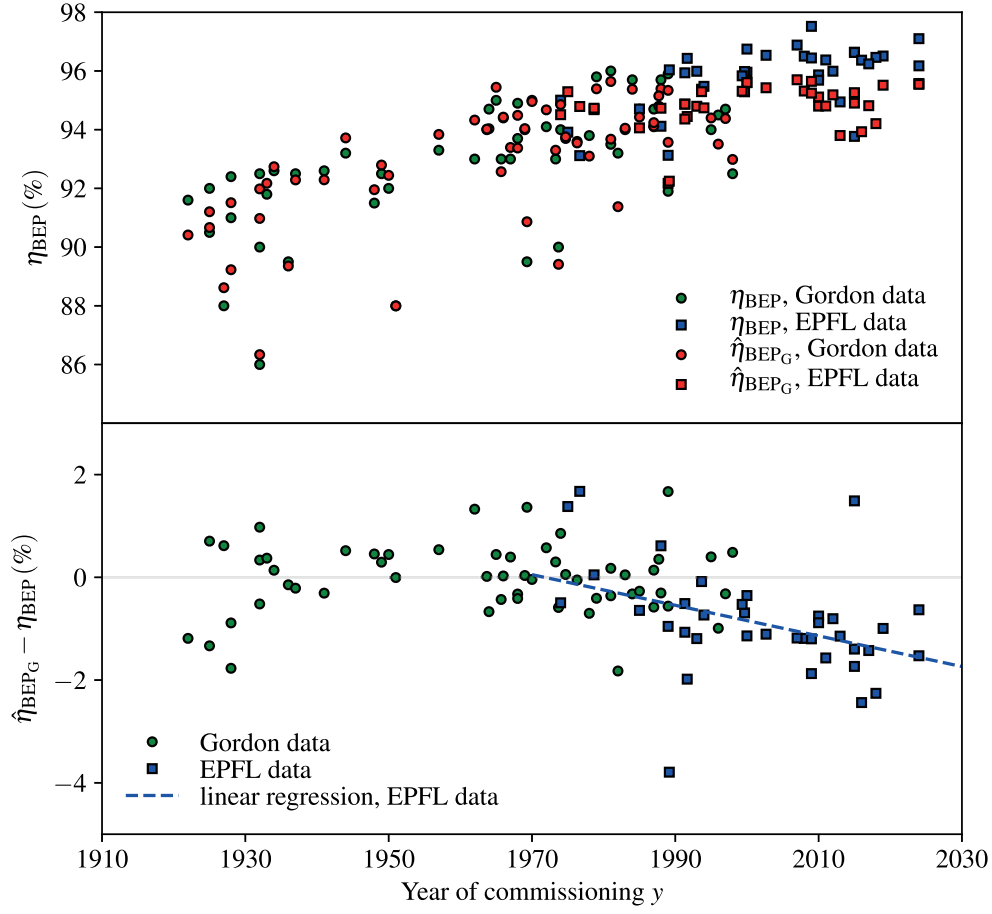
Figure 3.6 – η_{BEP} values from Gordon's database, η_{BEP} values from EPFL database and the estimated values $\hat{\eta}_{\text{BEP}}$ calculated according to the Gordon empirical model. The estimation error is also presented.

where the new correction terms are calculated as:

$$\Delta\epsilon_{\text{year}} = 1 - \frac{1}{1 + \exp\{[-1117 \cdot (y - 1746) \cdot 10^{-5}]\}} \tag{3.16}$$

$$\Delta\epsilon_{n_{\text{QE}}} = \left[\left(\frac{n_{\text{q}} - 42}{338}\right)^2\right]^{1.017} \tag{3.17}$$

$$\Delta\epsilon_{\text{size}} = \left(1 - 98.65 \cdot 10^{-2} + \Delta\epsilon_{\text{year}} + \Delta\epsilon_{n_{\text{QE}}}\right) \cdot \left(1 - 78.90 \cdot 10^{-2} \cdot D^{-0.2}\right) \tag{3.18}$$

As a result, the reference value is largely increased: from 91.87% in Gordon's model to 98.65%. Ignoring the turbine size effect, 98.65% is the expected maximum η_{BEP} value that can be
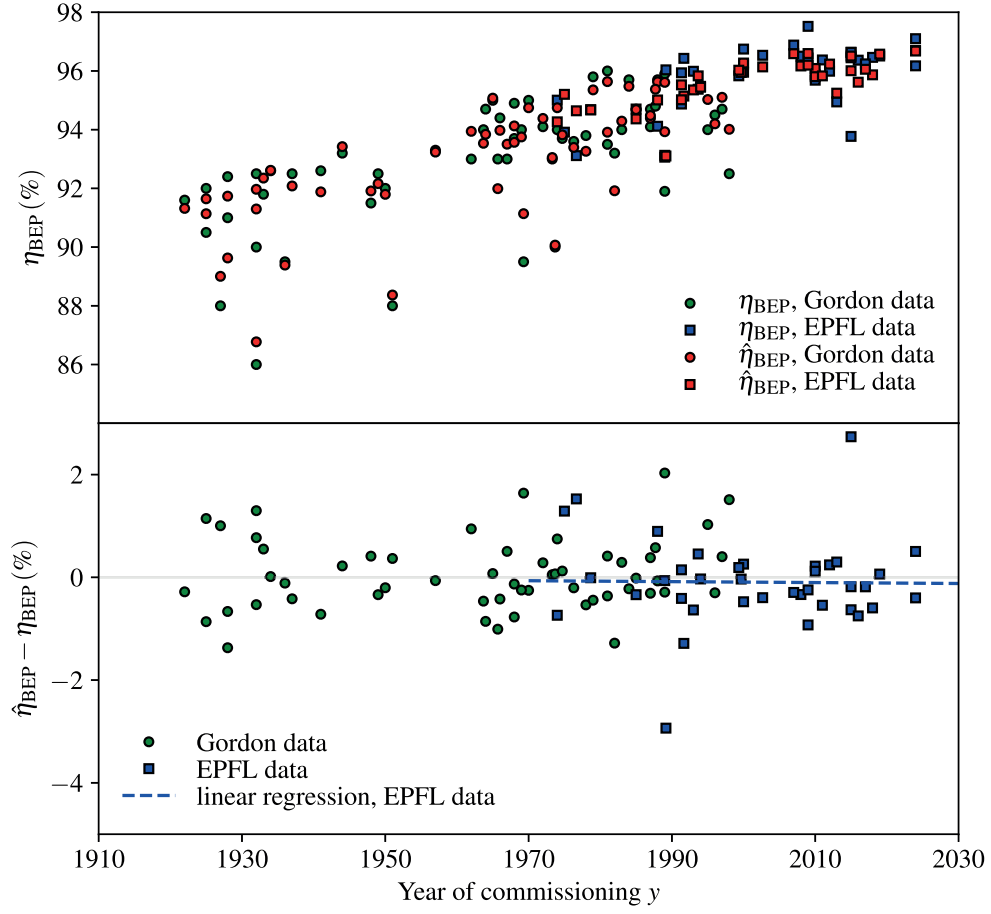
Figure 3.7 – η_{BEP} values from Gordon's database, η_{BEP} values from EPFL database and the estimated values $\hat{\eta}_{BEP}$ calculated using the updated parameters. The estimation error is also presented.

achieved for Francis turbines. Using the new parameters, η_{BEP} values are estimated with a standard error of $\sigma_{Std\eta_{BEP}} = 0.77\%$ and the more recent turbines η_{BEP} values are no longer underestimated. Results obtained with eq. (3.15) are presented in Figure 3.7.

3.2.3 Estimating the efficiency inside the operating range η_{OP}

Francis turbines are designed to operate inside a given range of head and discharge. This operating range is usually limited by conditions where damaging cavitation may occur (see [60, 56, 58, 66]), such as in full load conditions (discussed in Chapter 5) or where the turbine efficiency becomes too low.

As the water availability and power demand may have large variations during the day, a proper estimation of the turbine efficiency inside its complete operating range, η_{OP}, is necessary. As $\hat{\eta}_{BEP}$ can now be accurately estimated, the estimated efficiency inside the operating range can

be written as:

$$\hat{\eta}_{\mathrm{OP}} = \hat{\eta}_{\mathrm{R}} \cdot \hat{\eta}_{\mathrm{BEP}} \tag{3.19}$$

where the estimated relative efficiency $\hat{\eta}_{\mathrm{R}}$ must be a function, at least, of Q_{ED} and n_{ED}.

To construct a first approximation for $\hat{\eta}_{\mathrm{R}}$, a surrogate function using a combination of Hermite Polynomials is generated, following a procedure similar to the one presented in the previous Chapter. This first approximation is written as:

$$\hat{\eta}_{\mathrm{R}}\left(Q_{\mathrm{ED_R}}, n_{\mathrm{ED_R}}\right) = \sum_{p=0}^{p_{\max}} \lambda_p \mathrm{He}_p\left(g_{\mathrm{T}_0}\left(\left[Q_{\mathrm{ED_R}}, n_{\mathrm{ED_R}}\right]^T\right)\right) \tag{3.20}$$

where $p_{\max} = 9$ is chosen, so that Hermite Polynomials until the 3rd degree are considered. By using a 3rd degree function, one degree of complexity is added if compared to the simplified Euler equation and the risk of overfitting is avoided, as $p_{\max} = 9$ is still much lower than the $p_{\max}$ value used in the efficiency surrogate function constructed in Chapter 2.

The g_{T_0} function is a transformation function converting the variables $Q_{\mathrm{ED_R}}$ and $n_{\mathrm{ED_R}}$ into input variables $\mathbf{X} = \left[X_1, X_2\right]^T$ for the Hermite polynomials. The proposed g_{T_0} function for the $\hat{\eta}_{\mathrm{R}}$ approximation is expressed as:

$$g_{\mathrm{T}_0}\left(\begin{bmatrix} Q_{\mathrm{ED_R}} \\ n_{\mathrm{ED_R}} \end{bmatrix}\right) = \begin{bmatrix} a_0 & 0 \\ b_0 & c_0 \end{bmatrix}\begin{bmatrix} Q_{\mathrm{ED_R}} - \overline{Q}_{\mathrm{ED_R}} \\ n_{\mathrm{ED_R}} - \overline{n}_{\mathrm{ED_R}} \end{bmatrix} = \begin{bmatrix} X_1 \\ X_2 \end{bmatrix} \tag{3.21}$$

where $\overline{Q}_{\mathrm{ED_R}}$ and $\overline{n}_{\mathrm{ED_R}}$ are the mean values of $Q_{\mathrm{ED_R}}$ and $n_{\mathrm{ED_R}}$, respectively, considering all the N_{s} measured samples in the available database. The coefficient a_0 ensures that the variance for X_1 is equal 1 and is defined as:

$$a_0 = \left(\frac{1}{N_{\mathrm{s}} - 1}\sum_{j=1}^{N_{\mathrm{s}}}\left({}^{(j)}Q_{\mathrm{ED_R}} - \overline{Q}_{\mathrm{ED_R}}\right)^2\right)^{-0.5} \tag{3.22}$$

To ensure zero covariance between X_1 and X_2 and variance for X_2 equal 1, the coefficients b_0 and c_0 are calculated as the solution of the system:

$$\begin{cases} \frac{1}{N_{\mathrm{s}}-1}\sum\limits_{j=1}^{N_{\mathrm{s}}}\left[b_0\left({}^{(j)}Q_{\mathrm{ED_R}} - \overline{Q}_{\mathrm{ED_R}}\right) + c_0\left({}^{(j)}n_{\mathrm{ED_R}} - \overline{n}_{\mathrm{ED_R}}\right)\right]^2 = 1 \\ \sum\limits_{j=1}^{N_{\mathrm{s}}}{}^{(j)}X_1 \cdot \left[b_0\left({}^{(j)}Q_{\mathrm{ED_R}} - \overline{Q}_{\mathrm{ED_R}}\right) + c_0\left({}^{(j)}n_{\mathrm{ED_R}} - \overline{n}_{\mathrm{ED_R}}\right)\right] = 0 \end{cases} \tag{3.23}$$

This type of transformation function was first proposed by Andolfatto et al. [69]. To calculate the vector of modal strengths $\boldsymbol{\lambda} = \left[\lambda_0, \lambda_1, \lambda_2, ..., \lambda_{p_{\max}}\right]^T$ for eq. (3.20), the weighted least

squares method is applied, as in eq. (3.24)

$$\boldsymbol{\lambda}_0 = \left(\mathbf{He}^T \, \mathbf{W} \, \mathbf{He} \right) \mathbf{He}^T \, \mathbf{W} \, \boldsymbol{\eta}_{\mathrm{R}} \tag{3.24}$$

where **He** is defined as in eq. (2.10), $\boldsymbol{\eta}_{\mathrm{R}}$ is a vector containing the relative efficiency measurements as in $\boldsymbol{\eta}_{\mathrm{R}} = \left[{}^{(1)}\eta_{\mathrm{R}}, {}^{(2)}\eta_{\mathrm{R}}, ..., {}^{(N_{\mathrm{s}})}\eta_{\mathrm{R}} \right]^T$ and the **W** matrix is a diagonal matrix with elements ${}^{(j)}W$. The matrix **W** is used to avoid bias in the final result towards turbines in which more measurements were performed. For this purpose, ${}^{(j)}W$ is calculated as ${}^{(j)}W = \left({}^{(k)}N_{\mathrm{Ts}} \right)^{-1}$, where each ${}^{(k)}N_{\mathrm{Ts}}$ value corresponds to the total number of measurement samples available for a given turbine k from which the sample j is originated. As a result, the sum of all ${}^{(j)}W$ values related to the same turbine k is equal to one, giving each turbine the same importance.

All the N_{s} measurement samples of η_{R} are presented in Figure 3.8a, where the points are colored according to the turbine n_{QE} value. The resulting 3-D surface using the aforementioned first approximation is presented in Figure 3.8b. To increase the accuracy of the empirical model, another empirical relation able to adapt the $\hat{\eta}_{\mathrm{R}}$ surface according to the n_{QE} value is proposed. As a result, a function g_{T} is proposed as in eq. (3.25) and the resulting new function for $\hat{\eta}_{\mathrm{R}}$ is presented in eq. (3.26).

$$g_{\mathrm{T}}\left(\begin{bmatrix} Q_{\mathrm{ED_R}} \\ n_{\mathrm{ED_R}} \end{bmatrix}, n_{\mathrm{QE}} \right) = \begin{bmatrix} a\left(n_{\mathrm{QE}} \right) & 0 \\ b\left(n_{\mathrm{QE}} \right) & c\left(n_{\mathrm{QE}} \right) \end{bmatrix} \begin{bmatrix} Q_{\mathrm{ED_R}} - \overline{Q}_{\mathrm{ED_R}} \\ n_{\mathrm{ED_R}} - \overline{n}_{\mathrm{ED_R}} \end{bmatrix} = \begin{bmatrix} X_1 \\ X_2 \end{bmatrix} \tag{3.25}$$

$$\hat{\eta}_{\mathrm{R}}\left(Q_{\mathrm{ED_R}}, n_{\mathrm{ED_R}}, n_{\mathrm{QE}} \right) = \sum_{p=0}^{p_{\max}} \lambda_p \mathrm{He}_p\left(g_{\mathrm{T}}\left(\left[Q_{\mathrm{ED_R}}, n_{\mathrm{ED_R}} \right]^T, n_{\mathrm{QE}} \right) \right) \tag{3.26}$$

The g_{T} function of eq. (3.25) features a, b and c coefficients that are a function of n_{QE}. As a result, $Q_{\mathrm{ED_R}}$ and $n_{\mathrm{ED_R}}$ values are mapped differently in the X_1, X_2 domain, depending on the turbine n_{QE}. Two possibilities are tested:

$$\begin{cases} a\left(n_{\mathrm{QE}} \right) = a_{\mathrm{ref}} \cdot \left[k_a \cdot \log_{10}\left(n_{\mathrm{QE}} \right) + 1 \right] \\ b\left(n_{\mathrm{QE}} \right) = b_{\mathrm{ref}} \cdot \left[k_b \cdot \log_{10}\left(n_{\mathrm{QE}} \right) + 1 \right] \\ c\left(n_{\mathrm{QE}} \right) = c_{\mathrm{ref}} \cdot \left[k_c \cdot \log_{10}\left(n_{\mathrm{QE}} \right) + 1 \right] \end{cases} \tag{3.27}$$

and:

$$\begin{cases} a\left(n_{\mathrm{QE}} \right) = a_{\mathrm{ref}} \cdot \left(k_a \cdot n_{\mathrm{QE}} + 1 \right) \\ b\left(n_{\mathrm{QE}} \right) = b_{\mathrm{ref}} \cdot \left(k_b \cdot n_{\mathrm{QE}} + 1 \right) \\ c\left(n_{\mathrm{QE}} \right) = c_{\mathrm{ref}} \cdot \left(k_c \cdot n_{\mathrm{QE}} + 1 \right) \end{cases} \tag{3.28}$$

Finally, to obtain values for a_{ref}, b_{ref}, c_{ref}, k_a, k_b and k_c, a non linear least squares method is used to find the parameters that minimize the sum of weighted squared errors (SWSE), as in

Table 3.1 – Resulting SWSE values.

	Simplified method, g_{T_0}	Adaptive method, g_T	
		log type (Eq. 3.27)	linear type (Eq. 3.28)
SWSE ($\cdot$)	0.0306	0.0180	0.0170

eq. (3.29). The set of modal strengths λ is also recalculated in the same process.

$$\text{SWSE} = \sum_{j}^{N_s} {}^{(j)}W \cdot \left({}^{(j)}\hat{\eta}_R - {}^{(j)}\eta_R \right)^2 \tag{3.29}$$

where $\hat{\eta}_R$ is calculated as in eq. (3.26). To ensure a fast conversion in the calculation of the new coefficients, the initial values for a_{ref}, b_{ref}, c_{ref} and λ are assumed as a_0, b_0, c_0 and λ_0, respectively. The coefficients k_a, k_b and k_c are initially assumed as equal to zero.

In Table 3.1 the SWSE values resulting from the first approximation using eq. (3.20) and the more accurate adaptive method using eq. (3.26) are presented. For the adaptive method, SWSE results using transformation functions with coefficients a, b and c calculated as in eq. (3.27) and as in eq. (3.28) are presented. The η_R values calculated with the linear version of coefficients a, b and c, as in eq. (3.28), feature the lowest SWSE value equal to 0.0170, being then more accurate. More information regarding the expected error in η_R estimates are detailed in the Appendix A.3

Example of η_R surfaces generated with three values of n_{QE}, using linear coefficients, are presented in Figure 3.8c. A summary of all the formulae and parameters for the η_R estimation is provided in the Appendix A.2. The η_{OP} submodel is then constructed, making use of the η_{BEP} submodel and η_R values calculated with equations (3.26) and (3.28) for higher accuracy.

3.2.4   Estimating n_{ED} in runaway conditions

Zeng et al. in [81] assumed that the hydraulic moment of pump-turbines under runaway conditions is equal to a mechanical resistance approximated by the frictional loss formula of a rotating disk. Assuming that $Q_{\text{ED}_R} \propto a$, the formulation proposed by Zeng et al. is adapted to be used in Francis turbines as:

$$\frac{\hat{n}_{\text{ED}_{\text{Run}}}}{n_{\text{ED}_{\text{BEP}}}} = \frac{Q_{\text{ED}_R}^{c_0}}{a_0 \cdot Q_{\text{ED}_R} + b_0} \tag{3.30}$$

where $\hat{n}_{\text{ED}_{\text{Run}}}$ becomes a function of $n_{\text{ED}_{\text{BEP}}}$ and Q_{ED_R}, i.e., $\hat{n}_{\text{ED}_{\text{Run}}} = \hat{n}_{\text{ED}_{\text{Run}}}\left(n_{\text{ED}_{\text{BEP}}}, Q_{\text{ED}_R} \right)$. The coefficients a_0, b_0 and c_0 are determined empirically making use of the EPFL database.

To ensure that eq. (3.30) is able to generate a curve that can properly represent the measurements, it is first tested using the measurements data of each turbine separately. Examples of
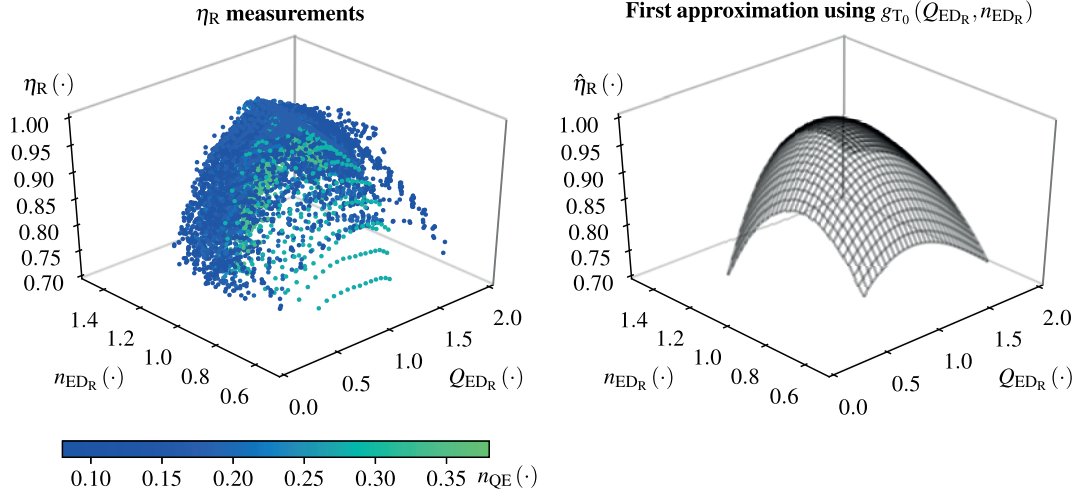
η_R measurements

(a) All the N_s measurement samples of η_R.

First approximation using $g_{T_0}(Q_{ED_R}, n_{ED_R})$

(b) First approximation of the η_R values.

Adaptive model using $g_{T_a}(Q_{ED_R}, n_{ED_R}, n_{QE})$

——— $n_{QE} = 0.10$ ——— $n_{QE} = 0.20$ ——— $n_{QE} = 0.30$
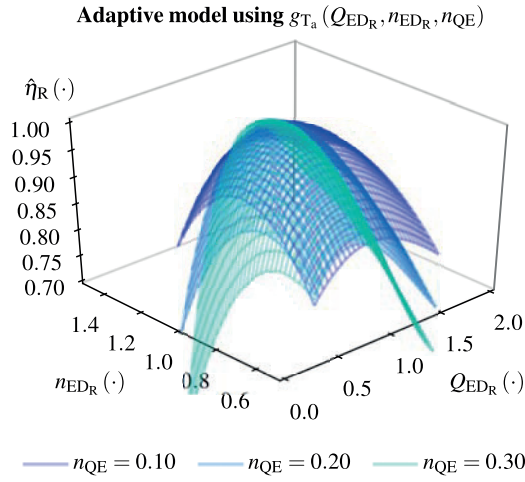
(c) Example of η_R surfaces generated with three values of n_{QE}, using linear coefficients.

Figure 3.8 – η_R measurements and results for $\hat{\eta}_R$.

$n_{ED_{Run}}$ measurements and $\hat{n}_{ED_{Run}}$ approximating curves using a_0, b_0 and c_0 coefficients of eq. (3.30) calculated individually for six turbines with different n_{QE} values are presented in Figure 3.9.

When the coefficients of eq. (3.30) are calculated individually for each turbine to best fit the measurements, the error between the measurements and the best fit curve is very small: among the 6 examples presented in Figure 3.9, the highest RMSE is $1.8 \cdot 10^{-2}$ ($\cdot$). Therefore, the same procedure undertaken previously for $\hat{\eta}_R$ can be followed: (1) find the constant coefficients a_0, b_0 and c_0 that best fits the complete available database, and (2) use them as a
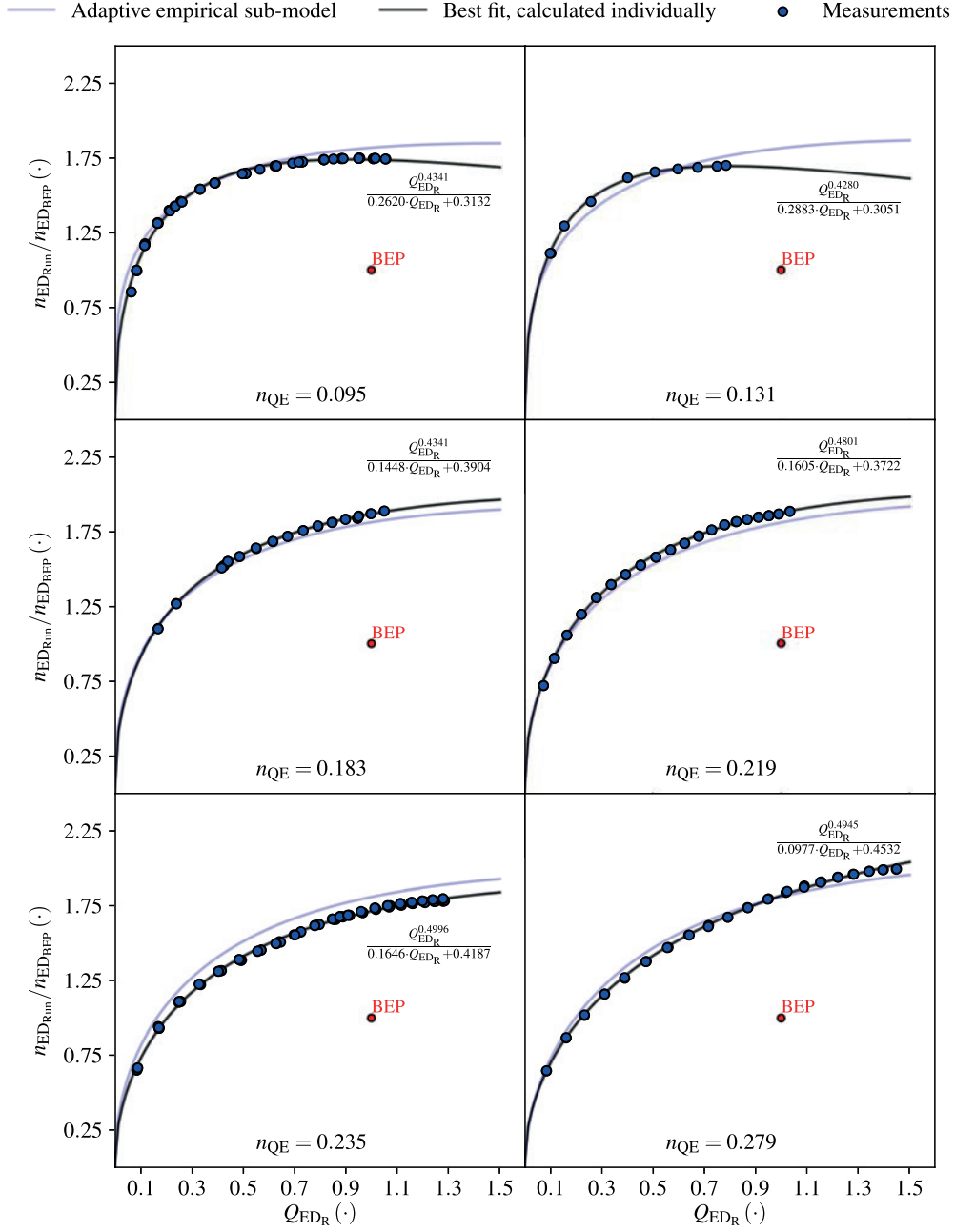
Figure 3.9 – Six examples of $n_{\mathrm{ED_{Run}}}$ measurements and approximating curves using a_0, b_0 and c_0 coefficients of eq. (3.30) calculated individually. Curves generated with the adaptive empirical submodel are also presented.

first guess for a non linear weighted least squares method where these coefficients become functions of n_{QE}. Finally, the adaptive empirical submodel of eq. (3.31) is defined to estimate

$n_{\text{ED}_{\text{R}}}$ values, while taking into account the effect of the turbine n_{QE}.

$$\frac{\hat{n}_{\text{ED}_{\text{Run}}}}{n_{\text{ED}_{\text{BEP}}}} = \frac{Q_{\text{ED}_{\text{R}}}^{c}}{a \cdot Q_{\text{ED}_{\text{R}}} + b} \qquad (3.31)$$

where a, b and c become linear functions of n_{QE}. The a, b and c functions resulting from the non linear least squares method are detailed in eq. (3.32).

$$\begin{cases} a\left(n_{\text{QE}}\right) = 1.3748 \cdot n_{\text{QE}} + 0.1501 \\ b\left(n_{\text{QE}}\right) = 0.2794 \cdot n_{\text{QE}} + 0.0861 \\ c\left(n_{\text{QE}}\right) = -0.2627 \cdot n_{\text{QE}} + 0.4628 \end{cases} \qquad (3.32)$$

Using the adaptive empirical submodel of Equations 3.31 and 3.32, the mean error $\bar{\epsilon}_{\text{Run}}$ between measured and calculated values of $n_{\text{ED}_{\text{Run}}}/n_{\text{ED}_{\text{BEP}}}$, calculated as in eq. (3.33), is equal to $5.26 \cdot 10^{-3}$ ($\cdot$). The standard deviation of the error, calculated as in eq. (3.34) is $6.41 \cdot 10^{-2}$ ($\cdot$).

$$\bar{\epsilon}_{\text{Run}} = \frac{1}{N_{\text{s}}} \sum_{j=1}^{N_{\text{s}}} {}^{(j)}\epsilon_{\text{Run}} \qquad \text{where} \qquad {}^{(j)}\epsilon_{\text{Run}} = \frac{{}^{(j)}n_{\text{ED}_{\text{Run}}}}{{}^{(j)}n_{\text{ED}_{\text{BEP}}}} - \frac{{}^{(j)}\hat{n}_{\text{ED}_{\text{Run}}}}{{}^{(j)}n_{\text{ED}_{\text{BEP}}}} \qquad (3.33)$$

$$\sigma\left(\epsilon_{\text{Run}}\right) = \sqrt{\frac{1}{N_{\text{s}} - 1} \sum_{j=1}^{N_{\text{s}}} \left({}^{(j)}\epsilon_{\text{Run}} - \bar{\epsilon}_{\text{Run}}\right)^{2}} \qquad (3.34)$$

All the $N_{\text{s}} = 1371$ available $n_{\text{ED}_{\text{R}}}/n_{\text{ED}_{\text{BEP}}}$ measurement samples for the construction of the runaway adaptive model are presented in Figure 3.10. The evolution of the estimated $\hat{n}_{\text{ED}_{\text{R}}}/n_{\text{ED}_{\text{BEP}}}$ curve for ten different values of n_{QE} is also shown.

By calculating $n_{\text{ED}_{\text{Run}}}$ as in eq. (3.31), conditions where $n_{\text{ED}} > 0$ and $\eta = 0$ are then estimated with accuracy. The $n_{\text{ED}_{\text{Run}}}$ curve defines the upper limit of n_{ED} values considered in the empirical model for η estimation.

3.2.5 Estimating the efficiency in transition zones, η_{TR}

The submodels presented previously allow the accurate estimation of the efficiency inside a typical operating range, $\eta_{\text{OP}} = \eta_{\text{BEP}} \cdot \eta_{\text{R}}$, and the n_{ED} curve where $\eta = 0$, defined as $n_{\text{ED}_{\text{Run}}}$. An additional submodel is then required to calculate η_{TR}, the turbine efficiency in conditions outside the operating range, but with $\eta > 0$.

A single surrogate function using Hermite Polynomials would, in theory, be able to accurately fit the complete domain of measured points with $\eta > 0$ and those at the runaway curve. However, this surrogate function would require polynomials of a high degree, increasing the risk of overfitting. It would create non-realistic undulations in the estimated efficiency curve,
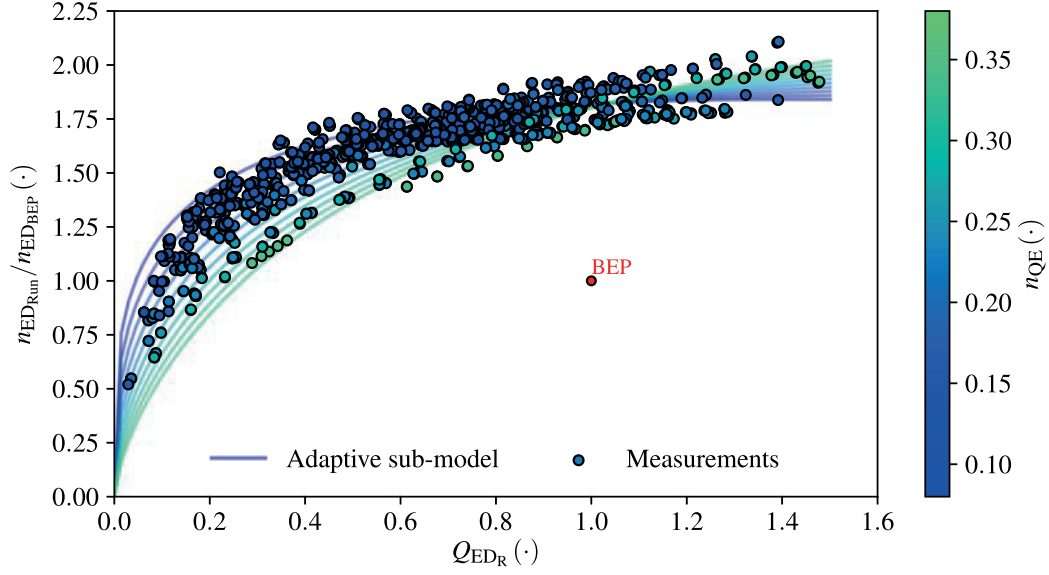
Figure 3.10 – All the available $n_{ED_R}/n_{ED_{BEP}}$ measurement samples for the construction of the runaway adaptive submodel and the evolution of the estimated $\hat{n}_{ED_R}/n_{ED_{BEP}}$ curve for ten different values of n_{QE}.

as measurements available in the transition zones are scarce.

To overcome this issue, instead of using a single Hermite Polynomial surrogate function of a high degree, $\hat{\eta}_{TR}$ is calculated by blending surrogate functions of low degree, as in 3.35. Each surrogate function $\hat{f}_i$ is multiplied by a weighting function $\phi_{TR,i} = \phi_{TR,i}\left(Q_{ED_R}, n_{ED_R}\right)$ and, for any values of Q_{ED_R} and n_{ED_R}, $\sum_i^{N_\phi} \phi_{TR,i} = 1$.

$$\hat{f}_i = \sum_{j=0}^{p_{max}} \lambda_{j,i} \mathrm{He}_j\left(\mathbf{X}\right)$$

$$\hat{\eta}_{TR} = \phi_{TR,i} \cdot \hat{f}_1 + \phi_{TR,2} \cdot \hat{f}_2 + ... + \phi_{TR,N_\phi} \cdot \hat{f}_{N_\phi} \tag{3.35}$$

$$\hat{\eta}_{TR} = \sum_{i=1}^{N_\phi} \phi_{TR,i} \cdot \hat{f}_i$$

where p_{max} is kept as $p_{max} = 9$, making $\hat{f}_i$ a third degree polynomial, similar to $\hat{\eta}_R$. For the $\hat{\eta}_{TR}$ calculation, five weighted functions are considered, i.e., $N_\phi = 5$, so that the runaway curve is separated in four zones and one last weighted function ($i = 5$) is kept for the interval where of $Q_{ED} > Q_{ED_{BEP}}$ and $n_{ED} < n_{ED_{BEP}}$.

The $\phi_{TR,i}$ functions are defined as described in Table 3.2. The variables θ_{ref}, $\Delta\theta$ and θ_{BEP} are defined as in eq. (3.36).

50

Table 3.2 – caption da table

i	$\phi_{\text{TR},i}$	θ_i
1	$\dfrac{1}{1+\exp\left\{\left[-15\cdot(\theta_i)\right]\right\}} \cdot \dfrac{1}{1+\exp\left\{\left[-15\cdot\left(\frac{\pi}{2}-\theta_i\right)\right]\right\}}$	θ_{ref}
2	$\dfrac{1}{1+\exp\left\{\left[-15\cdot\left(\theta_i-\frac{\pi}{2}\right)\right]\right\}} \cdot \dfrac{1}{1+\exp\left\{\left[-15\cdot\left(\frac{\pi}{2}+\Delta\theta-\theta_i\right)\right]\right\}}$	$\begin{cases}\theta_{\text{ref}} & \text{if } \theta_{\text{ref}} \geq 0 \\ \theta_{\text{ref}}+2\cdot\pi & \text{if } \theta_{\text{ref}} < 0\end{cases}$
3	$\dfrac{1}{1+\exp\left\{\left[-15\cdot\left(\theta_i-\left(\frac{\pi}{2}+\Delta\theta\right)\right)\right]\right\}} \cdot \dfrac{1}{1+\exp\left\{\left[-15\cdot\left(\frac{\pi}{2}+2\cdot\Delta\theta-\theta_i\right)\right]\right\}}$	$\begin{cases}\theta_{\text{ref}} & \text{if } \theta_{\text{ref}} \geq 0 \\ \theta_{\text{ref}}+2\cdot\pi & \text{if } \theta_{\text{ref}} < 0\end{cases}$
4	$\dfrac{1}{1+\exp\left\{\left[-15\cdot\left(\theta_i-\left(\frac{\pi}{2}+2\cdot\Delta\theta\right)\right)\right]\right\}} \cdot \dfrac{1}{1+\exp\left\{\left[-15\cdot\left(\frac{3\pi}{2}-\theta_i\right)\right]\right\}}$	$\begin{cases}\theta_{\text{ref}} & \text{if } \theta_{\text{ref}} \geq 0 \\ \theta_{\text{ref}}+2\cdot\pi & \text{if } \theta_{\text{ref}} < 0\end{cases}$
5	$\dfrac{1}{1+\exp\left\{\left[-15\cdot\left(\theta_i-\frac{\pi}{2}\right)\right]\right\}} \cdot \dfrac{1}{1+\exp\left\{\left[-15\cdot(-\theta_i)\right]\right\}}$	θ_{ref}

$$\theta_{\text{ref}} = \text{atan2}\left(\frac{n_{\text{ED}}-n_{\text{ED}_{\text{BEP}}}}{Q_{\text{ED}}-Q_{\text{ED}_{\text{BEP}}}}\right)$$

$$\Delta\theta = \left(\theta_{\text{BEP}} - \frac{\pi}{2}\right)\cdot\frac{1}{3} \tag{3.36}$$

$$\theta_{\text{BEP}} = \text{atan2}\left(\frac{n_{\text{ED}_{\text{BEP}}}}{Q_{\text{ED}_{\text{BEP}}}}\right)+2\cdot\pi$$

The zones where each $\phi_{\text{TF},i}$ function becomes predominant is illustrated in Figure 3.11a. A 3-D visualization of the $\phi_{\text{TR},i}$ functions is presented in Figure 3.12.

As mentioned, $\hat{\eta}_{\text{TR}}$ is intended to be used as an interpolation function to connect the $\hat{n}_{\text{ED}_{\text{Run}}}$ curve, where $\hat{\eta} = 0$, and the efficiency surface where $\hat{\eta} = \hat{\eta}_{\text{OP}}$. The function $\hat{\eta}_{\text{TR}}$ must then be constructed from points generated with the empirical models for $\hat{n}_{\text{ED}_{\text{Run}}}$ and $\hat{\eta}_{\text{OP}}$. The location of the $N_{\text{TR}} = 775$ points generated to construct the $\hat{\eta}_{\text{TR}}$ function are illustrated in the Figure 3.11b.

Using the N_{TR} generated points, a linear least squares method is applied to define the values of the modal strengths $\lambda_{j,i}$ for each function $\hat{f}_i$. A more detailed description of how the least squares method is applied to the polynomial approximation of eq. (3.35) is presented in Appendix A.4.

The $\hat{\eta}_{\text{TR}}$ function already provides an approximation of η in the complete domain where $\eta > 0$. Nevertheless, to keep the estimation of efficiency in the turbine operating range as $\hat{\eta}_{\text{OP}}$, one additional step is carried out as discussed in the following subsection.

(a)   (b)
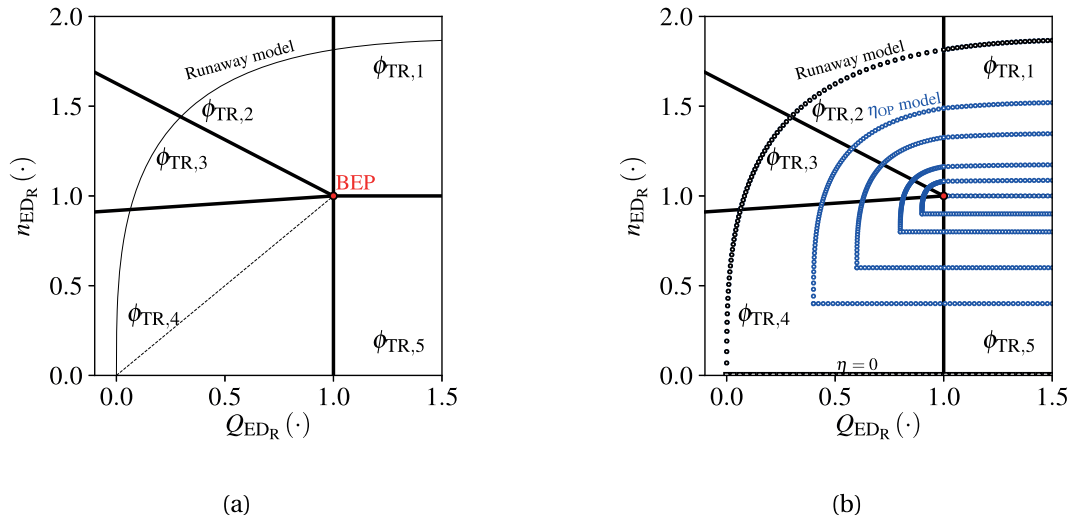
Figure 3.11 – (a) Zones where each $\phi_{\text{TF},i}$ function becomes predominant. (b) Points generated using the n_{ED} runaway model and the η_{OP} model to construct the $\hat{\eta}_{\text{TR}}$ function.
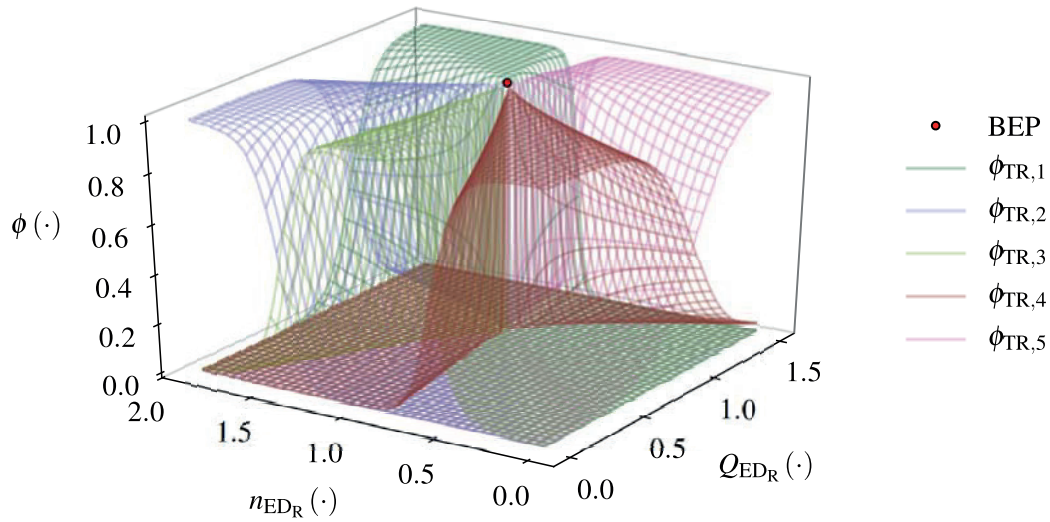
Figure 3.12 – 3-D representation of the five $\phi_{\text{TR},i}$ functions.

3.2.6   The complete efficiency empirical model $\hat{\eta}$

Finally, making use of the four aforementioned submodels to defined functions for $\hat{\eta}_{\mathrm{TR}}$ and $\hat{\eta}_{\mathrm{OP}}$, the final function for the efficiency empirical model can be written as:

$$\hat{\eta} = \phi_{\mathrm{OP}} \cdot \hat{\eta}_{\mathrm{OP}} + \sum_{i}^{N_\phi} \phi_i \hat{f}_i \tag{3.37}$$

where ϕ_{OP} is calculated as detailed in Table 3.3. The $\hat{f}_i$ functions are kept the same as in the $\hat{\eta}_{\mathrm{TR}}$ submodel. The R and R_{Run} variables are calculated as:

$$R = \sqrt{\left(n_{\mathrm{ED}} - n_{\mathrm{ED}_{\mathrm{BEP}}}\right)^2 + \left(Q_{\mathrm{ED}} - Q_{\mathrm{ED}_{\mathrm{BEP}}}\right)^2}$$

$$R_{\mathrm{Run}} = \sqrt{\left(n_{\mathrm{ED}_{\mathrm{Run}}} - n_{\mathrm{ED}_{\mathrm{BEP}}}\right)^2 + \left(Q_{\mathrm{ED}_{\mathrm{Run}}} - Q_{\mathrm{ED}_{\mathrm{BEP}}}\right)^2} \tag{3.38}$$

where the $Q_{\mathrm{ED}_{\mathrm{Run}}}$ and $n_{\mathrm{ED}_{\mathrm{Run}}}$ values lead to the same θ_{ref} value as the Q_{ED}, n_{ED} point where ϕ_{OP} is being calculated. The ϕ_i functions of the eq. (3.37) are defined as:

$$\phi_i = \phi_{\mathrm{TR},i} - \phi_{\mathrm{OP}} \tag{3.39}$$

so that $\phi_{\mathrm{OP}} + \sum_i^{N_\phi} \phi_i = 1$ for any value of Q_{ED} and n_{ED}. A 3-D visualization of the ϕ_{OP} function and the ϕ_i functions is presented in Figure 3.13.

The resulting $\hat{\eta}$ function constructed with y, D, $n_{\mathrm{ED}_{\mathrm{BEP}}}$ and $Q_{\mathrm{ED}_{\mathrm{BEP}}}$ values from eight different turbines with increasing values of n_{QE} is presented in Figure 3.14. The measured values of efficiency for these turbines are also presented. A very good agreement is then noted between the estimated and the measured η values, validating the empirical model.

Table 3.3 – Formulas for the ϕ_{OP} calculation.

Condition	ϕ_{OP}
$Q_{\mathrm{ED}} \geq Q_{\mathrm{ED}_{\mathrm{BEP}}}$ $n_{\mathrm{ED}} \geq n_{\mathrm{ED}_{\mathrm{BEP}}}$	$\dfrac{1}{1+\exp\left[-80\cdot\left(0.6\cdot\left(n_{\mathrm{ED}_{\mathrm{Run}}} - n_{\mathrm{ED}_{\mathrm{BEP}}}\right) + n_{\mathrm{ED}_{\mathrm{BEP}}} - n_{\mathrm{ED}}\right)\right]}$
$Q_{\mathrm{ED}} < Q_{\mathrm{ED}_{\mathrm{BEP}}}$ $n_{\mathrm{ED}} \geq n_{\mathrm{ED}_{\mathrm{BEP}}}$	$\dfrac{1}{1+\exp\left[-80\cdot\left(0.6\cdot R_{\mathrm{Run}} - R\right)\right]}$
$n_{\mathrm{ED}} < n_{\mathrm{ED}_{\mathrm{BEP}}}$ $\theta_{\mathrm{ref}} + 2\cdot\pi \leq \theta_{BEP}$	$\dfrac{1}{1+\exp\left[-80\cdot\left(0.6\cdot R_{\mathrm{Run}} - R\right)\right]} \cdot \dfrac{1}{1+\exp\left[-80\cdot\left(n_{\mathrm{ED}} - 0.75\cdot n_{\mathrm{ED}_{\mathrm{BEP}}}\right)\right]}$
$n_{\mathrm{ED}} < n_{\mathrm{ED}_{\mathrm{BEP}}}$ $\theta_{\mathrm{ref}} + 2\cdot\pi > \theta_{BEP}$	$\dfrac{1}{1+\exp\left[-80\cdot\left(n_{\mathrm{ED}} - 0.75\cdot n_{\mathrm{ED}_{\mathrm{BEP}}}\right)\right]}$
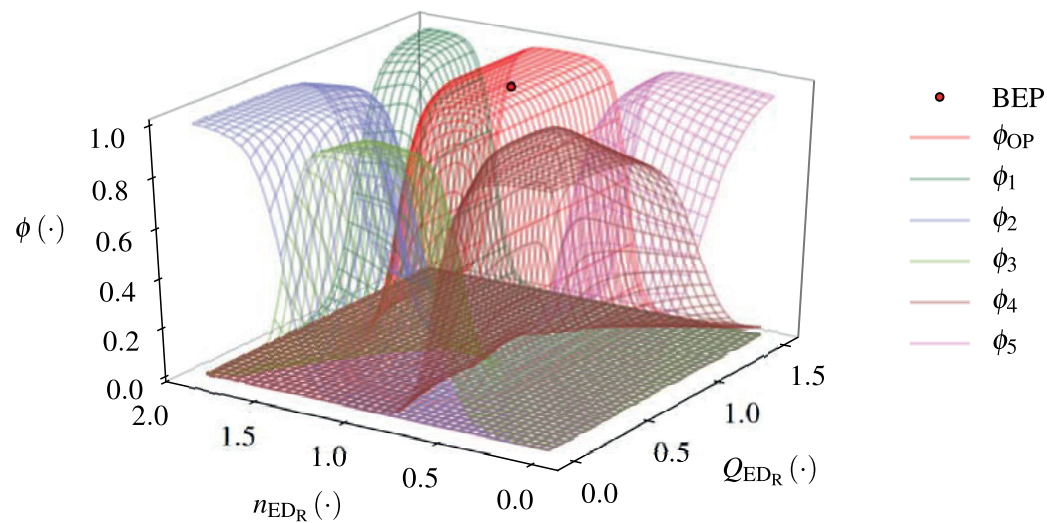
Figure 3.13 – 3-D representation of ϕ_{OP} and the five ϕ_i functions.
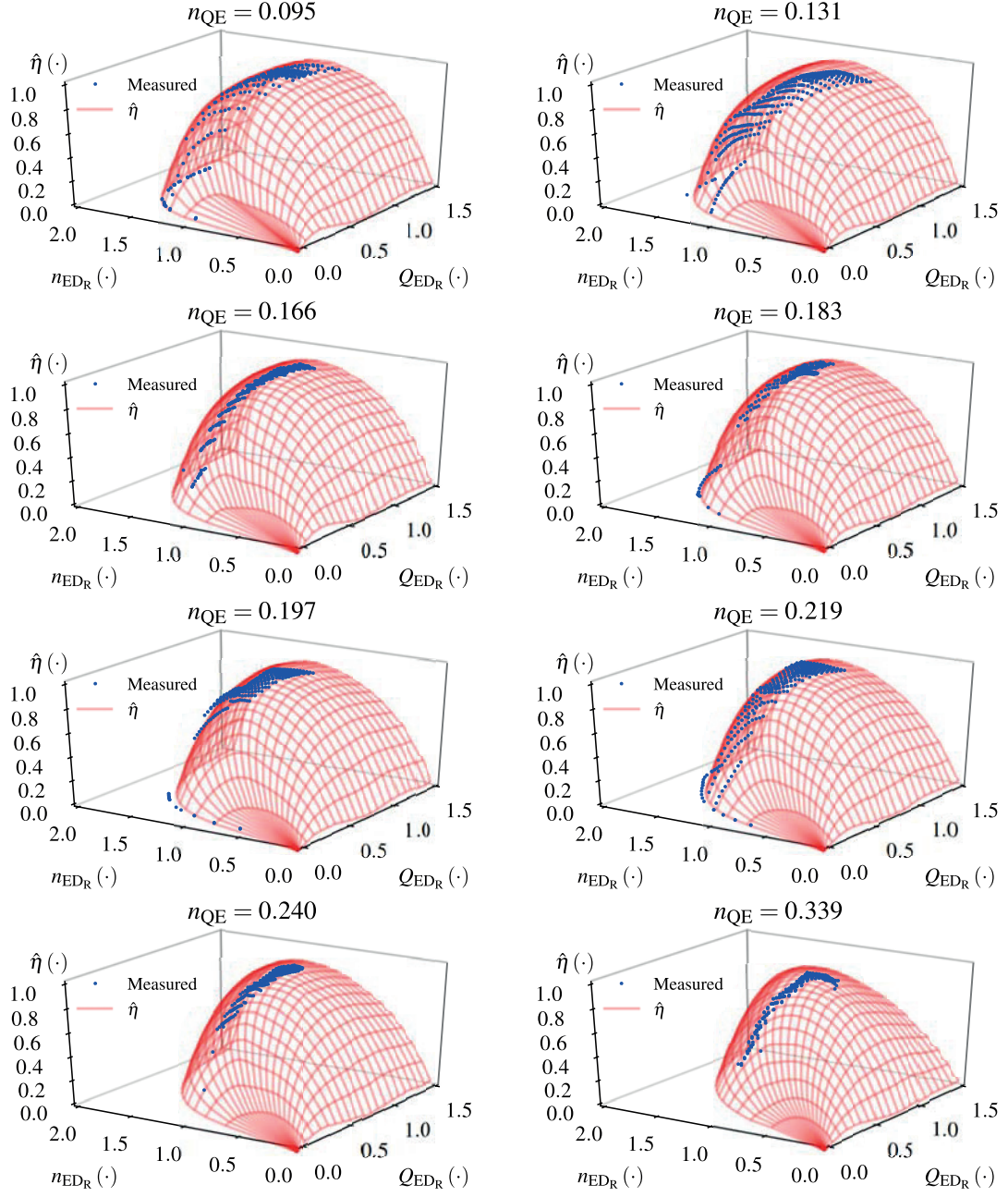
Figure 3.14 – Empirical $\hat{\eta}$ functions generated with input data from eight different turbines with increasing values of n_{QE}.

3.3   Complete characteristic curves estimation model

3.3.1   From the efficiency model to the turbine characteristics

The turbine characteristics is represented by curves of T_{ED} and Q_{ED} values as a function of n_{ED}. These curves correspond to isolines of constant guide vanes opening angle α, as in the example of Figure 3.15.

The previous section provided an estimation of the turbine efficiency for any operating condition where the efficiency is greater than zero. This efficiency is now used to estimate the turbine torque characteristic curves in these conditions. The relation between the turbine efficiency η and the IEC torque factor is:

$$T_{ED} = \frac{\eta}{2 \cdot \pi} \frac{Q_{ED}}{n_{ED}} \tag{3.40}$$

Once the turbine torque is estimated inside the operating range, α or its relative value $\alpha_R = \alpha / \alpha_{BEP}$ is the last variable necessary to construct characteristic curves. In fact, in 1-D numerical simulations, knowing α_R is enough to perform simulations of transient phenomena in time domain.

Making used of the same measurements database used to construct the $\hat{\eta}$ empirical model, an empirical model to predict the relative guide vanes opening angle is constructed. The same procedure applied for the $\hat{n}_{ED_{Run}}$ submodel is applied to generate the $\hat{\alpha}_R$ function of eq. (3.41), providing estimated values of α_R. The mean error between measured and estimated values of α_R is $0.3 \cdot 10^{-2}$ and the standard deviation of the error is $5.9 \cdot 10^{-2}$.

$$\begin{aligned}
\hat{\alpha}_R = \quad & 0.1281 \cdot Q_{ED_R}^{\star\,3} - 0.2832 \cdot Q_{ED_R}^{\star\,2} + 0.5491 \cdot Q_{ED_R}^{\star} + 0.1764 \ldots \\
& + 0.0152 \cdot Q_{ED_R}^{\star} \cdot n_{ED_R}^{\star} + 3.4277 \cdot n_{ED_R}^{\star} + 0.6458 \cdot \exp\left(-0.5431 \cdot n_{ED_R}^{\star}\right)
\end{aligned} \tag{3.41}$$

where:

$$Q_{ED_R}^{\star} = Q_{ED_R} \cdot \left(2.1242 \cdot n_{QE} + 1.0000\right)$$
$$\tag{3.42}$$
$$n_{ED_R}^{\star} = n_{ED_R} \cdot \left(-2.7099 \cdot n_{QE} + 1.0000\right)$$

The $\hat{\alpha}_R$ approximation is only valid for $0.6 \cdot n_{ED_{BEP}} \leq n_{ED} \leq n_{ED_{Run}}$, where measurement samples are available. An example of estimated characteristic curves calculated with $\hat{\eta}$ and $\hat{\alpha}_R$ for a turbine with $n_{QE} = 0.13$ is illustrated in Figure 3.15. The construction of the remaining parts of the complete characteristic curves are discussed in the following subsections.

3.3.2   S-shaped Q_{ED} characteristic curves

Once the turbine enters in the turbine break mode, i.e., an operating condition with $T_{ED} < 0$ and $Q_{ED} > 0$, a quick drop in the turbine discharge is observed for a constant α value. In
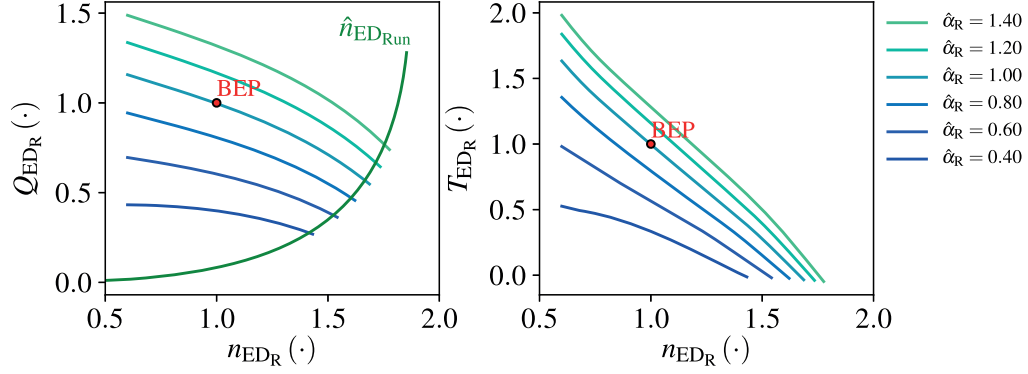
Figure 3.15 – Example of estimated characteristic curves calculated with $\hat{\eta}$ and $\hat{\alpha}_R$.

some cases a S-shaped curve appears in the Q_{ED} characteristic curves and conditions where $\frac{dQ_{ED}}{dn_{ED}} > 0$ are noted. An example of S-shaped characteristic curves is illustrated in Figure 3.16, adapted from the IEC standard [8].
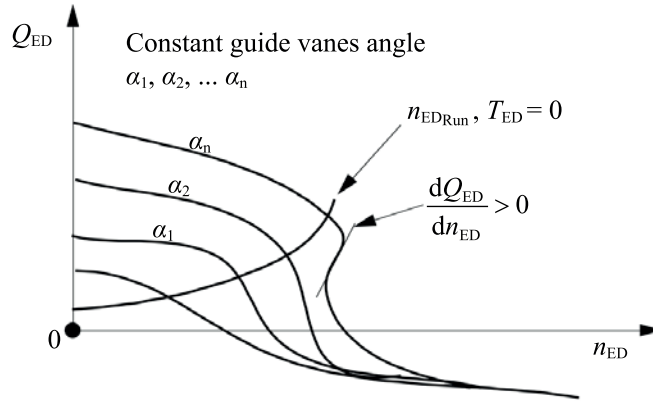
Figure 3.16 – S-shaped curve in a turbine Q_{ED} characteristics, adapted from the IEC standard [8].

The presence of S-shaped characteristic curves depends on many different turbine design choices. Extracted from [83], geometric parameters influencing the S-shaped characteristic curves in pump-turbines are listed in Table 3.4. As a result, knowing the turbine n_{QE} is not enough to estimate the shape of the turbine characteristic curves in this region.

Nevertheless, during preliminary studies, numerical simulations must be performed to evaluate the turbine prototype over-speed or the waterhammer effect in the upstream piping system during transient conditions such as an emergency stop. The presence of S-shaped characteristic curves can alter the outcome of these simulations. For this purpose, different possible characteristic curves —S-shaped or not —can be assumed to assess, for instance, what types of curvatures in the turbine characteristic curves are acceptable for a given power plant generating unit.

Table 3.4 – Runner geometric parameters influencing S-shaped characteristic curves, extracted from [83].

References	Pump-turbine	Investigated geometric parameters and results
Liu et al. [84]	Model for Xianju pumped storage power station (375 MW)	Number of runner blades, wrapping angle of the blade, diameter ratio between outlet and inlet, inlet and outlet blade angles, and the flow channels
Yin et al. [85]	Medium-specific-speed pump-turbine ($n_s = 114$)	Slightly higher D1=D2 and B=D2 values had a stable performance curve
Nielsen et al. [86] & Olimstad et al. [87–89]	Low-specific-speed model pump-turbine	Higher values of diameter and speed of rotation gave steeper characteristic curves; increase the radius of curvature on the pressure side of the leading edge in turbine mode, decrease the inlet radius, increase inlet blade angle, or increase the length of the blade, resulted in a more stable runner
Zhu et al. [90]	Model pump-turbine (corresponding prototype $H_{rated} = 259$ m, $P_{rated} = 255$ MW)	Negative blade lean resulted in a weaker S-shaped characteristics

To provide realistic characteristic curves in this part of the complete turbine characteristics, empirical curves are constructed based on those available in the EPFL database. To construct these curves, a methodology to represent them through a set a parameters is necessary. Making use of a B-spline with four control points, as illustrated in Figure 3.17, all the Q_{ED} characteristic curves inside the EPFL database, for Q_{ED} values inside $Q_{ED_{Run}} \geq Q_{ED} \geq 0$, i.e., in the *turbine break* mode, are accurately approximated. Among these curves, six examples are provided in Figure 3.18. The B-spline approximation is constructed using the NURBS-Python (geomdl) package, described in [91].

Five input values are necessary to construct Q_{ED} characteristic curves as in Figure 3.17: $n_{ED_{Run}}$, $Q_{ED_{Run}}$, θ_{Run}, θ_{80} and θ_{20}, where:

$$\theta_{Run} = \operatorname{atan}\left(\frac{n_{ED80} - n_{ED_{Run}}}{Q_{ED80} - Q_{ED_{Run}}} \right)$$

$$\theta_{80} = \operatorname{atan}\left(\frac{n_{ED20} - n_{ED80}}{Q_{ED20} - Q_{ED80}} \right) \tag{3.43}$$

$$\theta_{20} = \operatorname{atan}\left(\frac{n_{ED0} - n_{ED20}}{n_{ED0} - Q_{ED20}} \right)$$

with $\left(n_{ED80}, Q_{ED80} \right)$, $\left(n_{ED20}, Q_{ED20} \right)$ and $\left(n_{ED0}, Q_{ED0} \right)$ being the coordinates of the B-spline

control points at $Q_{ED} = 0.8 \cdot Q_{ED_{Run}}$, $Q_{ED} = 0.2 \cdot Q_{ED_{Run}}$ and $Q_{ED} = 0$, respectively. For each curve in the available database, the coordinates of the control points are defined as those that minimize the sum of squared errors (SSE) defined as in eq. (3.44).

$$\text{SSE} = \sum_{j}^{N_s} \left[\left({}^{(j)}\hat{n}_{ED_s} - {}^{(j)}n_{ED} \right)^2 + \left({}^{(j)}\hat{Q}_{ED_s} - {}^{(j)}Q_{ED} \right)^2 \right] \tag{3.44}$$

where N_s is the number of measurement samples for a given curve and $\left({}^{(j)}\hat{n}_{ED_s}, {}^{(j)}\hat{Q}_{ED_s} \right)$ is a point in the estimated characteristic curve approximating the measured point $\left({}^{(j)}n_{ED}, {}^{(j)}Q_{ED} \right)$. The angles θ_{Run}, θ_{80} and θ_{20} and the mean squared error (MSE) values, defined as $\text{MSE} = \text{SSE}/N_s$, are also detailed in Figure 3.18 for the six featured examples.
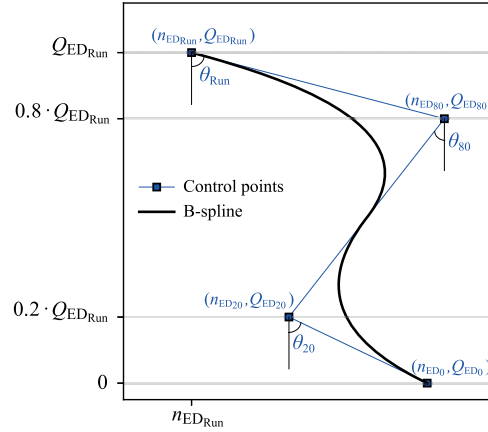
Figure 3.17 – B-spline method to approximate a S-shaped Q_{ED} characteristic curve.

To construct realistic characteristic curves using the B-spline method and based on typical values of θ_{80} and θ_{20}, the procedure illustrated in Figure 3.19 is followed. The variables $\theta_{80_{BEP}}$ and $\theta_{20_{BEP}}$, mentioned in Figure 3.19, correspond to the θ_{80} and θ_{20} values for $\alpha_R = 1$. The procedure consists of the following steps:

1. Making use of the EPFL database, define two empirical approximating functions: i) $f_1\left(\theta_{80_{BEP}}\right) = \frac{\partial\hat{\theta}_{80}(\hat{\alpha}_R=1)}{\partial\hat{\alpha}_R}$, which will help estimating θ_{80} values as α_R varies from $\alpha_R = 1$ and ii) $f_2\left(\theta_{80_{BEP}}\right) = \hat{\theta}_{20_{BEP}}$, providing an empirical relation between $\theta_{80_{BEP}}$ and $\theta_{20_{BEP}}$. Additionally, a value for $\theta_{80_{BEP}}$ is chosen based on realistic values provided by the EPFL database and used in functions f_1 and f_2.

2. Apply the selected $\theta_{80_{BEP}}$ value in the empirical functions f_1 and f_2 to define values of $\frac{\partial\hat{\theta}_{80}(\hat{\alpha}_R=1)}{\partial\hat{\alpha}_R}$ and $\hat{\theta}_{20_{BEP}}$. Use the results in the creation of two new functions: i) $f_3\left(\alpha_R\right)$, able to estimate θ_{80} values for any relative guide vanes opening α_R and ii) $f_4\left(\theta_{80}\right)$, able to estimate θ_{20} values.

3. For a given value of α_R, use function f_3 to calculate the estimated value of θ_{80}, i.e., $\hat{\theta}_{80}$. By introducing $\hat{\theta}_{80}$ in the f_4 function, calculate the estimated θ_{20} value.
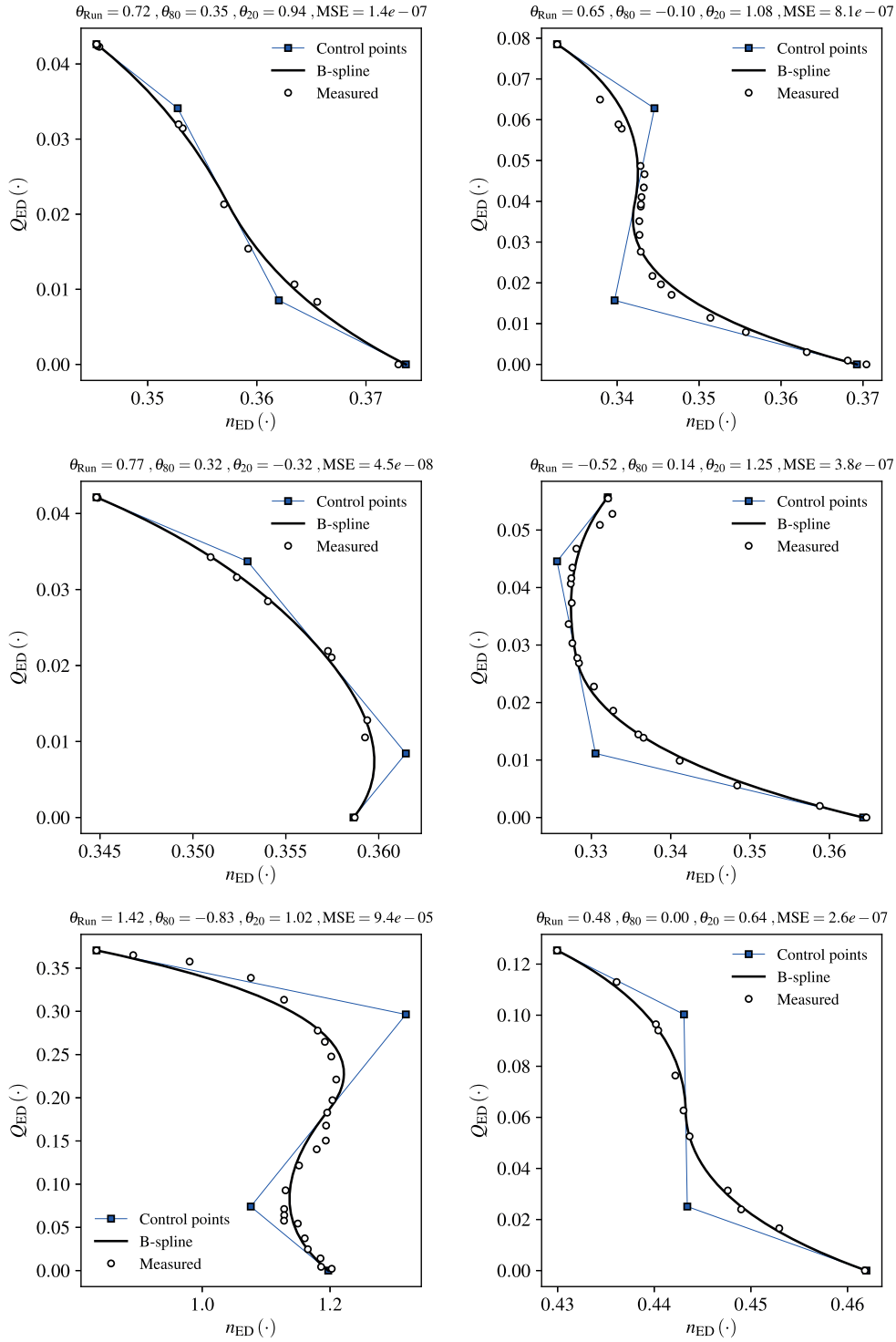
Figure 3.18 – Six examples of curves generated with the B-spline method, approximating measurements available in the EPFL database.

4. Using the $n_{\text{ED}_{\text{Run}}}$ empirical submodel and the $\hat{\alpha}_{\text{R}}$ approximation, define the first control point of the B-spline, $\left(n_{\text{ED}_{\text{Run}}}, Q_{\text{ED}_{\text{Run}}}\right)$, and calculate the angle $\hat{\theta}_{\text{Run}}$. Finally, use the angles $\hat{\theta}_{\text{Run}}$, $\hat{\theta}_{80}$ and $\hat{\theta}_{20}$ to calculate the remaining control points of the B-spline.
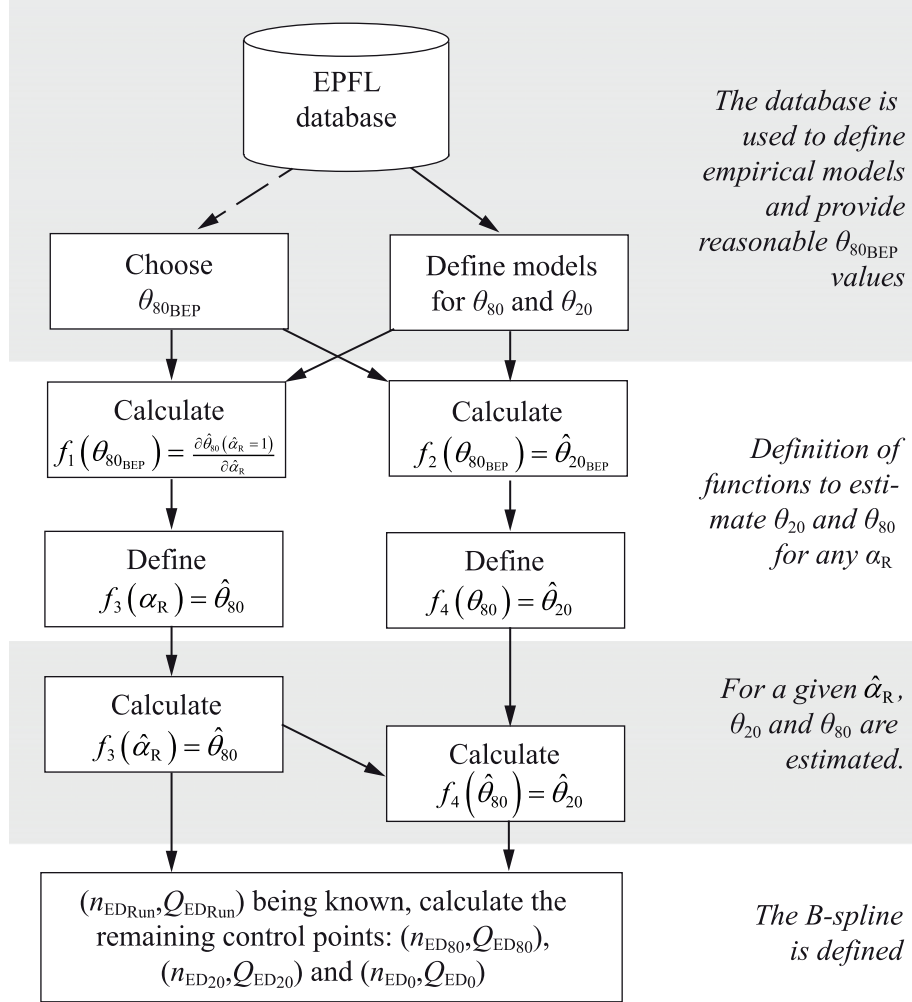
Figure 3.19 – Procedure for the construction of realistic characteristic curves based on the B-spline method.

$\theta_{80_{\text{BEP}}}$ values calculated from measurements for nine different turbines are presented as a function of the turbine n_{QE} in Figure 3.20. The mean measured $\theta_{80_{\text{BEP}}}$ and the mean $\theta_{80_{\text{BEP}}} \pm \sigma_{\text{Std}}$ values are also indicated, where σ_{Std} is the standard deviation of the $\theta_{80_{\text{BEP}}}$ values. Knowing that S-shaped characteristic curves have $\theta_{80} < 0$, the $\theta_{80_{\text{BEP}}}$ values presented in Figure 3.20 confirm that there is no direct relation between n_{QE} and S-shaped characteristic curves, as $\theta_{80_{\text{BEP}}}$ values lower than zero are encountered in turbines with both low and high n_{QE}.

The functions f_1 and f_2 are defined using θ_{80} and θ_{20} values resulting from the application of the B-spline method to approximate the Q_{ED} characteristic curves inside the EPFL database.
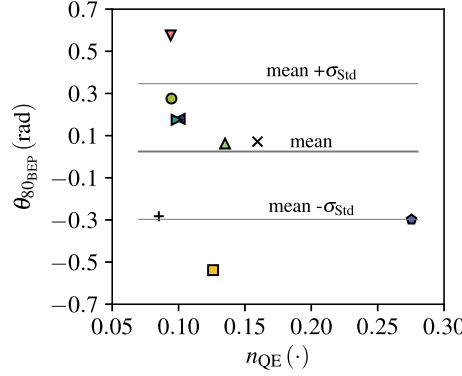
Figure 3.20 – Calculated $\theta_{80_{BEP}}$ values using measurements from nine different turbines. The mean measured θ_{80} and the mean $\theta_{80} \pm \sigma_{Std}$ values are also indicated.

On the left side of Figure 3.21, $\frac{\partial \theta_{80}(\alpha_R=1)}{\partial \alpha_R}$ values — calculated from the points presented in Figure 3.22 — are presented with the resulting approximating function f_1. On the right side of Figure 3.21, $\theta_{20_{BEP}}$ values used to generate the f_2 function are presented. The functions f_1 and f_2 are detailed in eq. (3.45).

$$f_1 \left(\theta_{80_{BEP}} \right) = -1.1248 \cdot \theta_{80_{BEP}}^2 + 1.0913 \cdot \theta_{80_{BEP}} - 0.5754$$

$$f_2 \left(\theta_{80_{BEP}} \right) = -0.5575 \cdot \theta_{80_{BEP}} + 0.8505$$

(3.45)

As the guide vanes relative opening angle α_R becomes small, θ_{80} and θ_{20} values tend to increase, eliminating the eventual S-shaped characteristic at some point. As the Q_{ED} characteristic curves for small α_R values becomes closer to a straight line, it is assumed that for $\alpha_R = 0$ the θ_{80} and θ_{20} values are equal to $\pi/2$. This condition is illustrated by the white squared mark in the two graphs of Figure 3.22 and is taken into account in the definition of the f_3 and the f_4 functions.

The function f_3 is divided in two parts:

$$f_3 \left(\alpha_R \right) = \begin{cases} f_1 \left(\theta_{80_{BEP}} \right) \cdot \left(\alpha_R - 1 \right) + \theta_{80_{BEP}} & \text{if } \alpha_R \geq 0.55 \\ f_3^{\star} \left(\alpha_R \right) & \text{otherwise} \end{cases}$$

(3.46)

where the function $f_3^{\star}$ is a third degree polynomial defined by the boundary conditions:

$$f_3^{\star} \left(\alpha_R = 0.55 \right) = f_3 \left(\alpha_R = 0.55 \right) \qquad f_3^{\star} \left(0 \right) = \pi/2$$

(3.47)

$$\frac{\partial f_3^{\star}(\alpha_R=0.55)}{\partial \alpha_R} = \frac{\partial f_3(\alpha_R=0.55)}{\partial \alpha_R} \qquad \frac{\partial f_3^{\star}(\alpha_R=0)}{\partial \alpha_R} = 0.$$

The f_4 function is defined as:

$$f_4\left(\theta_{80}\right) = \theta_{80} \cdot \left(\frac{f_2\left(\theta_{80_{BEP}}\right) - \pi/2}{\theta_{80_{BEP}} - \pi/2} \right) + \frac{\pi}{2} \left(\frac{\theta_{80_{BEP}} - f_2\left(\theta_{80_{BEP}}\right)}{\theta_{80_{BEP}} - \pi/2} \right) \tag{3.48}$$

which corresponds to a straight line passing through $\left(\theta_{80_{BEP}}, f_2\left(\theta_{80_{BEP}}\right)\right)$ and $\left(\pi/2, \pi/2\right)$.

To illustrated the expected outcome from f_3, in the left side of Figure 3.22 f_3 curves generated with $\frac{\partial \theta_{80}(\alpha_R = 1)}{\partial \alpha_R}$ values taken from measurements, instead of their approximation $f_1\left(\theta_{80_{BEP}}\right)$, are presented. To illustrate the outcome from f_4, in the right side of Figure 3.22 lines representing the f_4 curves generated with values of $\theta_{80_{BEP}}$ and $\theta_{20_{BEP}}$ taken from measurements, instead of their approximation with $f_2\left(\theta_{80_{BEP}}\right)$, are presented.
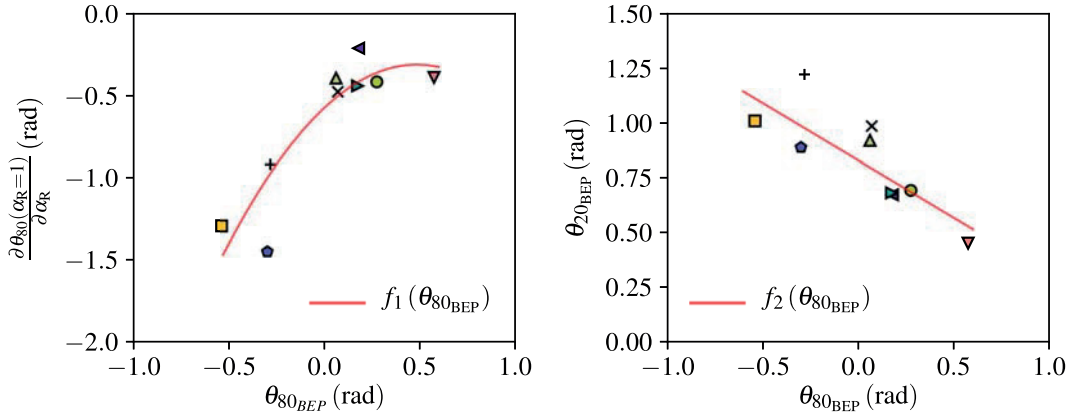
Figure 3.21 – $\frac{\partial \theta_{80}(\alpha_R = 1)}{\partial \alpha_R}$ values obtained from the measurements presented in Figure 3.22, used to define the f_1 function (left side); $\theta_{20_{BEP}}$ values used to generate the f_2 function are also presented (right side).
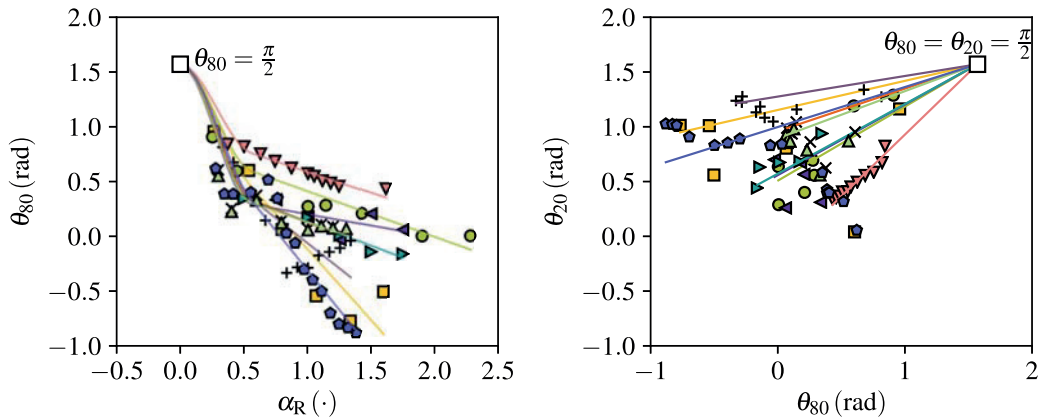
Figure 3.22 – θ_{80} as a function of α_R (left side); θ_{20} as a function of θ_{80} (right side).

63

The proposed procedure is applied to the same empirical characteristic curves of Figure 3.15 to provide Q_{ED} values in the turbine break mode. Three possible Q_{ED} characteristic curves are presented in Figure 3.23, generated by taking the mean value of $\theta_{80_{BEP}}$ and the mean $\theta_{80_{BEP}} \pm \sigma_{Std}$ values (as indicated in Figure 3.20) as an input. As a result, a S-shaped curve is noted when using $\theta_{80} - \sigma_{Std}$, whereas curves closer to a straight line are noted when using $\theta_{80} + \sigma_{Std}$.
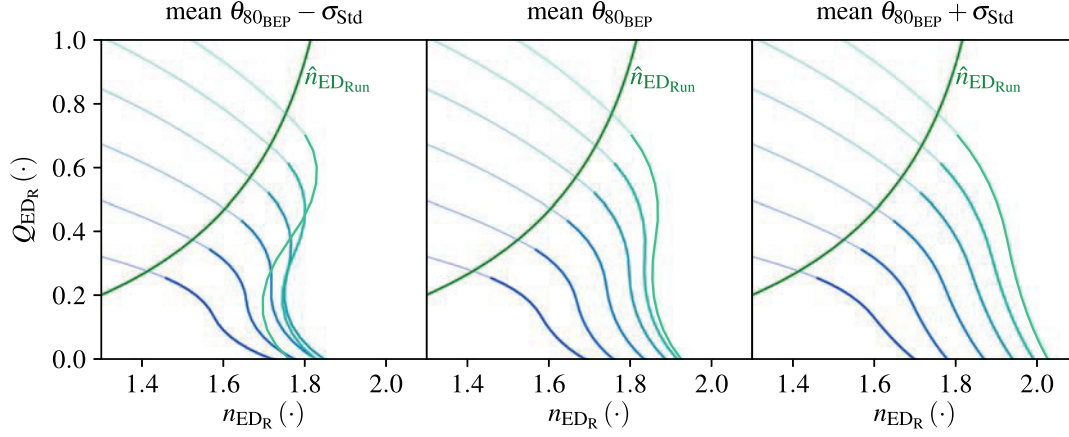
Figure 3.23 – By applying the proposed procedure in the same example as in Figure 3.15, three possible Q_{ED} characteristic curves are generated.

3.3.3 Torque at $Q_{ED} = 0$

To provide realistic T_{ED} characteristic curves in conditions with $n_{ED} > n_{ED_{Run}}$ and Q_{ED} values varying from $Q_{ED_{Run}}$ to zero, an empirical model to estimate T_{ED} values in conditions with zero discharge is generated.

If the guide vanes angle are closed, i.e., $\alpha_R = 0$, the turbine discharge is zero, but viscous forces due to the water recirculating on the shroud, the runner bands and between the runner blades generate a negative torque [92]. As a simplification, the runner can be seen as a disk, and the torque related to disk friction, T_{DF}, in its absolute value is proportional to $n^2 D^5$ (see [93]). As a consequence, the following assumption is made regarding the resulting torque factor due to disk friction $T_{ED_{DF}}$:

$$
\begin{aligned}
&\left| T_{DF} \right| \propto n^2 D^5 \\
&\left| T_{ED_{DF}} \right| \propto n_{ED}^2
\end{aligned}
\tag{3.49}
$$

Discharge values are equal to zero for any n_{ED} value if $\alpha_R = 0$. Nevertheless, for each value of α_R greater than zero, there is an unique n_{ED} value where the runner rotation also leads to zero discharge. In these conditions, the negative torque is not only caused by disk friction, but also by a recirculating flow surrounding the guide vanes and the runner blades. As a result, an empirical formula to estimate T_{ED} values at zero discharge conditions, $T_{ED_{Q=0}}$, must take into
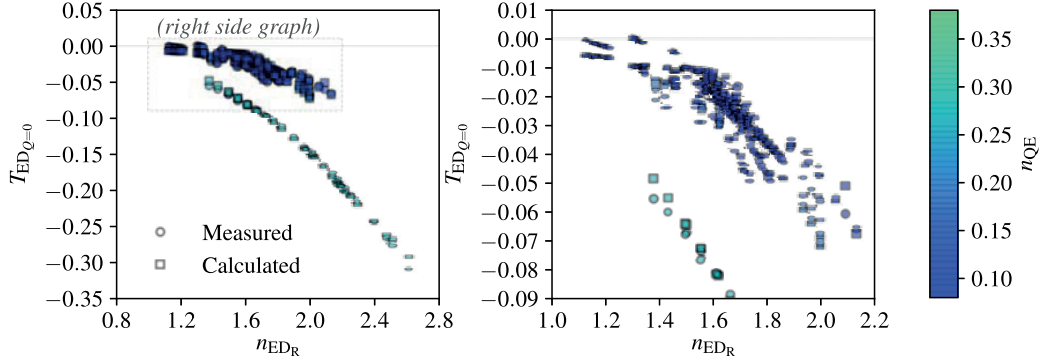
Figure 3.24 – Measured and estimated values of $T_{ED_{Q=0}}$, considering turbines with different n_{QE} values.

account the α_R value. The eq. (3.50) is then proposed to estimate the torque in any condition with $Q = 0$, ensuring: 1) that the torque is zero when $n_{ED} = 0$; 2) that, as $b < 0$, higher α_R values lead to lower $T_{ED_{Q=0}}$ values, as observed in measurements; and 3) that the predicted value is corrected according to the turbine specific speed value.

$$\hat{T}_{ED_{Q=0}} = \left(a \cdot n_{ED}^2 + b \cdot \alpha_R \cdot n_{ED} \right) \cdot \left(n_{QE}{}^c + d \right) \tag{3.50}$$

where the values for the coefficients a, b, c, and d are defined by minimizing the weighted squared error between the estimated values $\hat{T}_{ED_{Q=0}}$ and the measured values $T_{ED_{Q=0}}$ inside the EPFL database. The weights are defined by applying the same methodology as for the $\hat{n}_{ED_{Run}}$ model, i.e., by attributing weight values equal to one divided by the number of measurement samples related to the same turbine. As a result, the empirical approximation of eq. (3.51) is obtained. Measured and estimated values of $T_{ED_{Q=0}}$ are presented in Figure 3.24, considering turbines with different n_{QE} values. The mean error and the standard error of estimate for the points presented in Figure 3.24 are $1.5 \cdot 10^{-4}$ and $4.7 \cdot 10^{-3}$, respectively.

$$\hat{T}_{ED_{Q=0}} = \left(-5.8845 \cdot 10^5 \cdot n_{ED}^2 - 4.6238 \cdot 10^5 \cdot \alpha_R \cdot n_{ED} \right) \cdot \left(n_{QE}{}^{1.2747 \cdot 10} + 9.9950 \cdot 10^{-8} \right) \tag{3.51}$$

Making use of eq. (3.51) to calculate $\hat{T}_{ED_{Q=0}}$, the T_{ED} values in the turbine break mode are estimated as in eq. (3.52). As a result, the estimated T_{ED} characteristic curves for the same turbine illustrated earlier in Figures 3.15 and assuming the same three possibilities as in Figure 3.23 are illustrated in Figure 3.25.

$$\hat{T}_{ED} = -\frac{\hat{T}_{ED_{Q=0}}}{\hat{Q}_{ED_{Run}}} \cdot Q_{ED} + \hat{T}_{ED_{Q=0}} \tag{3.52}$$
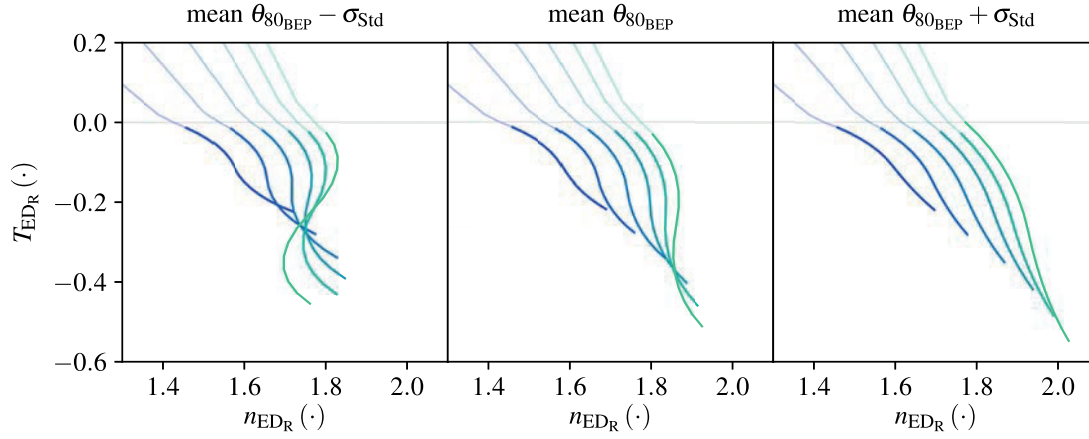
Figure 3.25 – Estimated T_{ED} characteristic curves in the turbine break mode for the same turbine illustrated in Figures 3.15 and assuming the same three possibilities as in Figure 3.23.

3.4 Conclusion

In this Chapter, empirical models to estimate a Francis turbine efficiency and complete characteristic curves are presented. High accuracy in the efficiency estimation is obtained, as detailed in Appendix A.3.

The proposed model for the complete characteristic curves generation incorporates the results from the efficiency model, keeping its high accuracy. It makes use of B-splines to complete the torque and discharge curves at the turbine break mode, being able to construct S-shaped characteristic curves if necessary.

As presented in Chapter 6, the complete characteristic curves generated with the presented empirical models can be used in 1-D numerical simulations in time domain, allowing the estimation of turbine runner overspeed and penstock overpressure values. By comparing simulation results obtained with the empirical turbine characteristic curves to results from measurements and simulations performed with real turbine characteristics, further validation for the presented empirical models is provided in Chapter 6.

4 Part load resonance

This chapter corresponds to the following paper manuscript submitted to the Journal of Mechanical Systems and Signal Processing:

J. Gomes Pereira Jr., A. Favrel, L. Andolfatto, C. Landry, S. Alligné, C. Nicolet, F. Avellan. *Procedure for predicting part load resonance in Francis turbine hydropower units based on swirl number and local cavitation coefficient similitude.*

The present version of the manuscript includes corrections suggested by the reviewers and has been re-submitted to the Journal the 14th of May 2019.

The author's contribution: The author contributed with the post-processing of all the measurements data, the generation of figures, graphs and by writing the paper. He also participated in the measurement campaigns, in the definition of the approximating functions and performed the comparisons between reduced scale model and prototype data.

Abstract

Francis turbines operating at part load conditions develop a cavitation precessing vortex known as a vortex rope in the draft tube cone below the runner outlet. At part load conditions, this vortex precession acts as an excitation source inducing pressure pulsations in the whole hydraulic system at the vortex precession frequency. Simultaneously, the lower pressure levels in the vortex core can lead to cavitation development, increasing the local flow compliance and reducing drastically the pressure wave speed. As a result, the eigenfrequencies of the hydraulic circuit are lowered and may match the vortex rope excitation frequency, leading to undesired resonance conditions. This paper presents a procedure to predict this type of resonance phenomenon in turbine prototypes by performing reduced scale physical turbine model measurements and eigenvalue calculations with linearized system matrices. This new procedure requires the transposition of hydroacoustic parameters from the reduced scale physical model to the prototype scale based on the swirl number and the local cavitation coefficient similarity. The procedure is validated by measurements performed on a turbine

prototype featuring a peak of power swings and pressure pulsations in the predicted operating conditions.

4.1 Introduction

With the increase in power generation from non-dispatchable energy sources, hydropower plants play a key role in providing primary and secondary control for the power transmission grid. Consequently, turbines for hydropower units operate under a large range of head and discharge values, sometimes going into adverse operating conditions. For instance, Francis turbines operating at full load, i.e., with a discharge value higher than that of the best efficiency point (BEP), may enter in an unstable and self-exciting condition, leading to large pressure pulsations and power swings as described in [27, 31, 94, 95]. At the other extreme, Francis turbines operating at very low discharge values, i.e., at deep part load, may present an inter-blade cavitation vortex as described in [66].

Francis turbines operating at part load conditions — i.e., any non-optimal condition where the discharge value is lower than that of the BEP — feature a swirling flow at the runner outlet and draft tube cone. This swirling flow gives rise to a precessing vortex, also known as a vortex rope, with a precession frequency of about one third the rotation frequency of the runner [23]. A vortex rope induces pressure fluctuations that can be decomposed into convective and synchronous components with the same frequency as the precessing frequency, as demonstrated by Nishi in [21] and measured by Arpe in [96]. The synchronous component of these pressure fluctuations acts as a pressure excitation source for the hydraulic system as a whole.

In the vortex rope core the absolute pressure may become lower than the vapor pressure, causing cavitation [58, 60, 97–99]. The cavitating volume increases the flow compliance [100], leading to a lower pressure wave speed and consequently lower hydroacoustic eigenfrequency values of the hydraulic system [50]. With lower hydroacoustic eigenfrequency values comes the risk of resonance with the vortex rope excitation frequency. The pressure pulsations in resonance conditions can lead to power swings [24], increased vibrations and fatigue forcing the plant operator to limit the operating range of the generating unit as described by Guarga et al. in [6].

Reduced scale physical turbine model measurement is a key step to validate the design of a full-scale turbine prototype, to verify its efficiency, and to assess its cavitation operating conditions. These turbine properties are directly transposable from the reduced scale model to the prototype scale, as described in the International Electrotechnical Commission (IEC) standard [8]. However, the system eigenfrequencies and consequently the pressure pulsations amplitude are not directly transposable from model to prototype as they depend not only on the turbine design but also on the contiguous hydraulic system hydroacoustic properties.

A similar issue is raised while attempting to predict pressure fluctuations amplitude on the

turbine prototype by making use of 3-D computational fluid dynamics (CFD) simulations. These simulations of the cavitation vortex rope taking into account only the turbine or the turbine draft tube in their simulation domain — as in [101–103] — can provide accurate estimates of the pressure excitation generated by the vortex. Nevertheless, during experiments the synchronous component of the vortex rope excitation will have its amplitude amplified or damped, depending on the response of the complete piping system where the turbine is installed, as discussed in [104–106]. In case of resonance between the vortex excitation and the system first eigenfrequency, this synchronous component may be amplified considerably.

A new methodology is presented in the HYPERBOLE European project [107] to predict resonance on turbine prototypes operating in part load conditions. For this purpose, additional steps are proposed aside from the typical reduced scale model measurements. These steps include the identification of the pressure wave speed value in the cavitating draft tube cone of the reduced scale model. This value is then transposed to the prototype scale for similar operating conditions, allowing 1-D eigenvalue calculations to estimate the prototype first eigenfrequency.

Following the HYPERBOLE methodology, Landry performed in [108] modal analysis on the reduced scale physical model to make apparent the test rig hydroacoustic eigenfrequencies. Since the cavitation vortex rope is located in the turbine draft tube cone, the hydroacoustic properties of the other components of the turbine and the test rig remain known and unchanged in cavitating conditions. The pressure wave speed in the draft tube cone being the only unknown parameter, Landry performed in [108] eigenvalue calculations of the complete test rig to identify the pressure wave speed value leading to equal values of calculated and measured first eigenfrequency. Landry also proposed methods to transpose this pressure wave speed to the prototype scale, so that eigenvalue calculations of the turbine prototype and its adjacent hydraulic circuit could be performed later to estimate the first hydroacoustic eigenfrequency of the prototype generating unit.

Favrel et al. further applied the HYPERBOLE methodology with results obtained by Landry to a 444 MW prototype test case in [54]. By applying the concept of the swirl number and also transposing the vortex precession frequency using Strouhal number similitude, Favrel et al. were able to predict the occurrence of part load resonance. However, the power output value in which resonance occurred was outside their predicted value uncertainty range.

Favrel et al. considered Thoma number similarity for the transposition of the pressure wave speed value in the cavitating draft tube cone from the reduced scale model value to its equivalent in the prototype scale. This paper demonstrates that the Thoma number is a non-ideal parameter for similarity in terms of cavitation vortex in the draft tube cone. It assumes equivalent energy losses in the draft tube of homologous reduced scale turbine models and prototypes, whereas these energy losses are, in reality, not strictly equivalent.

To improve the accuracy in the prediction of part load resonance in Francis turbine prototypes, this paper considers a local cavitation coefficient as a parameter for similarity. Differently from
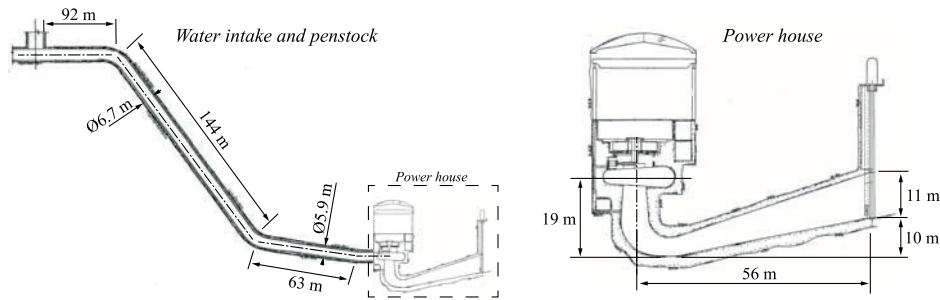
Figure 4.1 – Main dimensions of the turbine prototype and the pressurized pipes composing its hydraulic circuit, courtesy of BC Hydro.

the Thoma number, this coefficient is based on the absolute pressure value measured directly at the wall of the draft tube cone where the vortex is located. Two methods to transpose the wave speed value from model scale to prototype scale are compared: (1) performing a direct transposition based on Froude number, swirl number and local cavitation coefficient similarity; and (2) making use of the non-dimensional wave speed, requiring swirl number and local cavitation coefficient similarity only. Considering the same test case as Favrel et al. with additional prototype measurements, both transposition methods lead to predictions of resonance conditions in part load with greater accuracy than that obtained by Favrel et al.

To describe the test case and exemplify the power and pressure swings observed during part load resonance, prototype measurements are presented in Section 4.2. In Section 4.3, the HYPERBOLE methodology is presented, where previous research works leading to the hydroacoustic characterization of the cavitation vortex rope are introduced, as well as the new transposition methods for the pressure wave speed inside the cavitating draft tube cone. The complete procedure to predict part load resonance in prototypes is detailed in Section 4.4. It is applied to the described test case and its first step, the reduced scale physical model measurements, is presented in Section 4.5. Eigenvalue calculations are performed in Section 4.6, where the prototype first eigenfrequency values are estimated. In Section 4.7, the Strouhal number is used to estimate the vortex rope excitation frequency and the predicted resonance conditions are presented. The measured and predicted resonance conditions are compared, confirming the good agreement between predicted and measured values.

4.2 Prototype part load resonance measurements

The test case turbine is a Francis turbine of IEC specific speed $n_{QE} = 0.131$. The turbine prototype features a runner with external diameter $D_P = 5.4$ m. After synchronization of the generating unit with the power grid, the turbine runner rotates with a constant speed $n_P = 2.143$ Hz. The turbine rated values of power output and net head are $P_{rated} = 444$ MW and $H_{rated} = 170$ m, respectively. The main dimensions of the turbine prototype and the pressurized pipes composing its hydraulic circuit are illustrated in Figure 4.1.
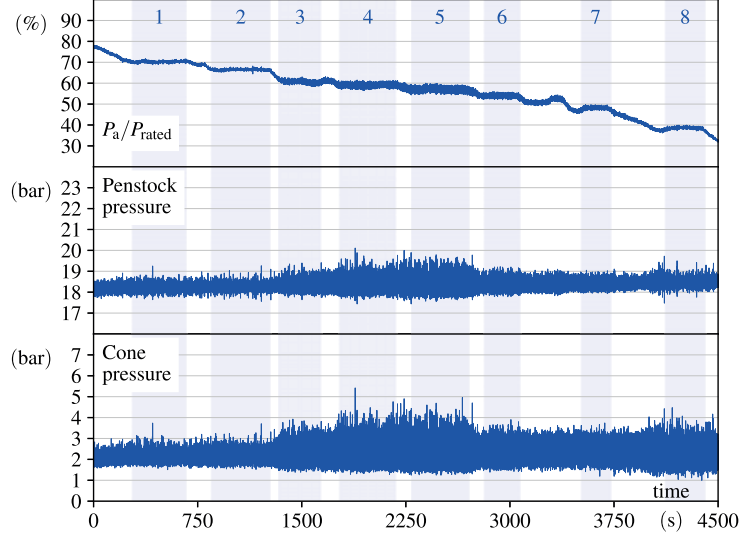
Figure 4.2 – Time history of relative power output, penstock pressure and draft tube cone pressure during measurements at $E = 1759\,\text{J·kg}^{-1}$. Eight time intervals are indicated where the guide vanes opening angle had only minor and slow variations aiming to keep P_a as constant as possible. High power and pressure oscillations are observed at $P_a/P_{rated} \approx 57\%$.

Extensive measurements are performed on the prototype generating unit allowing the detection of part load resonance in two different conditions of specific hydraulic energy $E = gH$ (J·kg^{-1}), where g (m·s^{-2}) is the local gravity acceleration and H (m) the turbine net head. Time history of relative power output P_a/P_{rated} — P_a being the generator active power output — and draft tube cone pressure acquired at $E = 1759\,\text{J·kg}^{-1}$ and $E = 1560\,\text{J·kg}^{-1}$ are presented in Figures 4.2 and 4.3, respectively. For the former, time history of pressure measured at the penstock wall, 35 m away from the spiral case inlet, is also presented. The pressure sensors in the draft tube cone are located at $0.4 \cdot D_P$ distance from the runner outlet. The complete list of sensors installed during the tests at $E = 1759\,\text{J·kg}^{-1}$ is presented in [26] and the procedure to estimate the turbine discharge Q and the net head H is detailed in [109]. The measurements at $E = 1560\,\text{J·kg}^{-1}$ made use of sensors from a monitoring system detailed in [61].

During measurements performed at $E = 1759\,\text{J·kg}^{-1}$, data acquisition in part load conditions is performed during a period of 4500 s with a sampling rate of 256 Hz. During the eight time intervals shown in Figure 4.2, the guide vanes opening angle had only minor and slow variations aiming to keep P_a as constant as possible. For each time interval, the power spectral densities P_{xx} of the active power output P_a, the penstock pressure and the draft tube cone pressure signals are calculated and the results are presented in the three waterfall plots shown in Figure 4.4. An important amplitude peak is observed at 29% of n_P and $P_a/P_{rated} = 57\%$.

The cross power spectral density P_{xy} and the coherence C_{xy} (see [110, 111]) between the draft
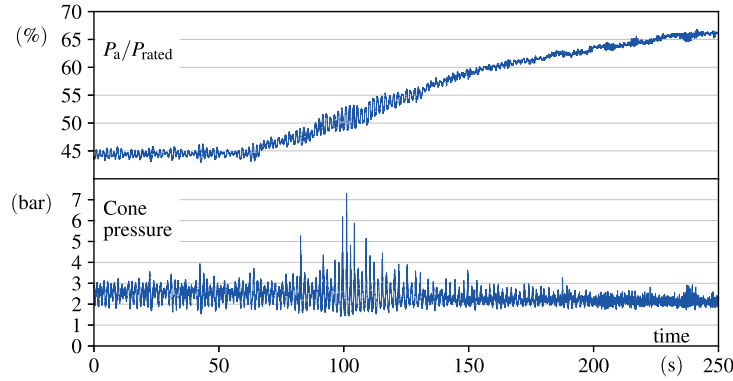
Figure 4.3 – Time history of relative power output and draft tube cone pressure during the power ramp measured at $E = 1560 \ \text{J} \cdot \text{kg}^{-1}$. Higher power and pressure oscillations is noted at time $t \approx 100$ s, corresponding to $P_\text{a}/P_\text{rated} \approx 51\%$.
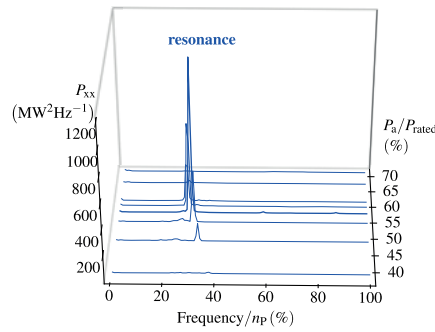
(a) Active power output.
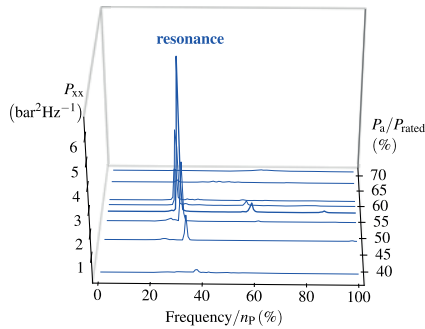
(b) Penstock wall pressure.
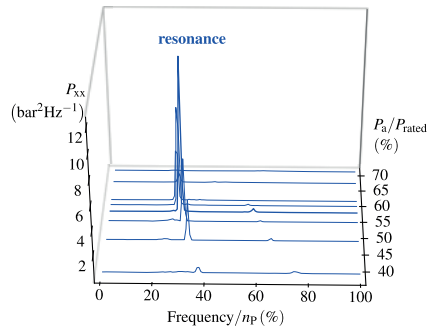
(c) Draft tube cone wall pressure.

Figure 4.4 – Power spectral densities P_xx of (a) the active power output P_a, (b) the penstock wall pressure and (c) the draft tube cone wall pressure. P_xx is calculated for each one of the eight time intervals detailed in Figure 4.2.
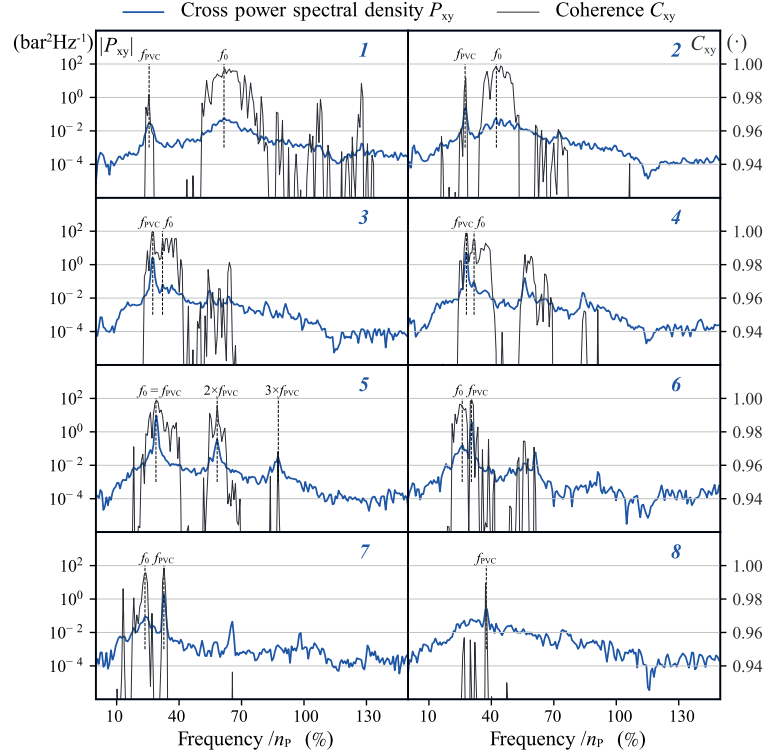
Figure 4.5 – The cross power spectral density P_{xy} and the coherence C_{xy} between the draft tube cone pressure and the penstock pressure signals for the time intervals illustrated in Figure 4.2. By analyzing the peaks in P_{xy} and C_{xy}, the f_{PVC} and f_0 values are identified.

tube cone pressure and the penstock pressure signals are presented in Figure 4.5. By analyzing the peaks in P_{xy} and C_{xy} between these two signals, the vortex rope core precession frequency f_{PVC} (Hz) and the hydroacoustic first eigenfrequency f_0 (Hz) of the prototype hydraulic system are identified. The C_{xy} values close to one confirm the power exchange between the draft tube cone and the penstock for these frequencies. The values presented in Figure 4.5 for f_{PVC} and f_0 are also confirmed by analyzing the pressure signals from two pressure sensors located on opposite sides of the prototype draft tube cone. The procedure to identify f_{PVC} and f_0 using two sensors in the draft tube cone is detailed in [19], where it is applied to reduced scale physical model measurements, and an example is given in Section 4.5.

Consequently, as indicated in Figure 4.5, the first eigenfrequency f_0 decreases as the power decreases, i.e., as the unit goes deeper in part load conditions. The opposite happens to f_{PVC}, as it is slightly increased. During time interval 5, where $P_a/P_{rated} = 57\%$, a condition where f_{PVC} encounters f_0 is observed, resulting in part load resonance. As presented earlier in Figure 4.4, this resonance condition leads to the greater and undesired peak in power and pressure oscillations.

As the turbine operates in part load conditions with $E = 1560$ J·kg^{-1}, a very similar behavior is evidenced during the power ramp. For this power ramp, illustrated in Figure 4.3, a waterfall

(a) Active power output.

(b) Draft tube cone wall pressure.
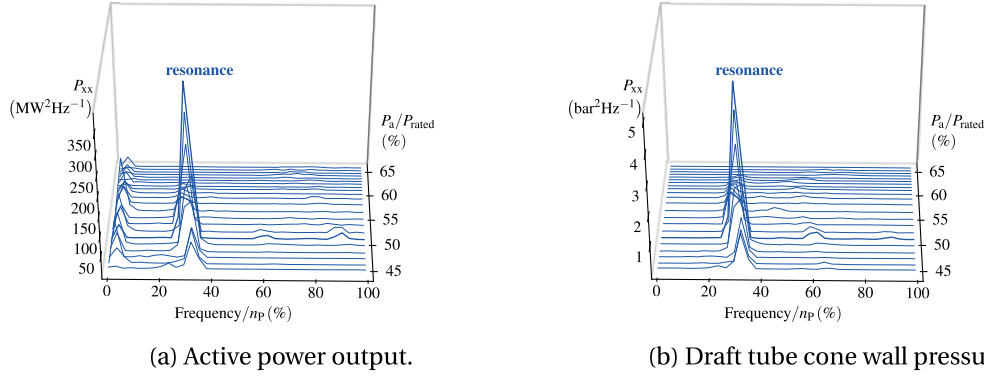
Figure 4.6 – Waterfall plot of power spectral density P_{xx} during the power ramp at $E = 1560$ J·kg^{-1} for (a) the active power output P_a signal and (b) the draft tube cone wall pressure signal.

plot of power spectral densities P_{xx} calculated using 2^{16} samples per segment and 50% overlap are presented in Figure 4.6. During this ramp, data is acquired at a 4096 Hz sampling rate. The resonance peak for this condition is observed at 29.2% of n_P and $P_a/P_{rated} = 51$%, which corresponds to almost the same frequency value and a power output about 11% lower when compared to the measured values at $E = 1759$ J·kg^{-1}.

4.3 The HYPERBOLE methodology

The HYPERBOLE methodology aims to increase the accuracy in predicting pressure surge phenomena related to the part load and full load cavitation vortex. The HYPERBOLE methodology acknowledges that pressure pulsations, such as the ones mentioned in the previous section, cannot be directly transposed from the reduced scale physical model to the prototype, as they depend on the hydroacoustic response of the complete hydraulic system in which the turbine is installed. As illustrated in Figure 4.7, instead of directly transposing measurement results from reduced scale model to prototype, the HYPERBOLE methodology proposes additional steps in which dynamic numerical simulations of both the test rig and the power plant generating unit are performed to increase the accuracy of pressure pulsation predictions.

The part load and the full load vortex in the draft tube cone are a consequence of the swirling flow leaving the runner outlet. Assuming a Francis turbine operating under a given value of specific energy E, there is a unique discharge value Q_0 where $\vec{C}u$, the tangential component of the flow velocity vector $\vec{C}$ at the runner blade trailing edge, has a magnitude close to zero all along the blade. In part load conditions, i.e., when the turbine operates at a discharge $Q < Q_0$, a rotating flow leaves the runner with a $\vec{C}u$ component in the same direction as the runner peripheral velocity vector $\vec{U}$, as illustrated in red in the velocity diagram shown in Figure 4.8a. If the ratio between the axial flux of tangential momentum and the axial flux of axial momentum at the runner outlet is high enough, a precessing vortex rope develops in the

74
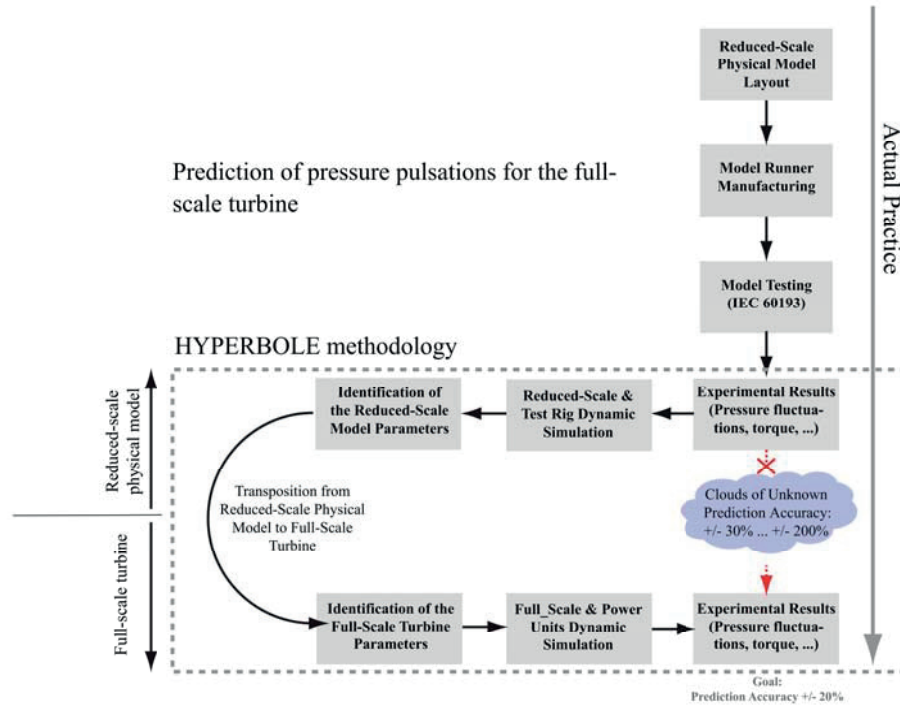
Figure 4.7 – The HYPERBOLE methodology, extracted from [108].

turbine draft tube cone. If the pressure in the vortex rope core becomes lower than the vapor pressure, a cavitating volume such as the one shown in Figure 4.8b takes place.

As a first development inside the HYPERBOLE project, a 1-D mathematical model to represent the hydroacoustic properties of a cavitation vortex rope in a draft tube cone is constructed and presented by Alligné et al. in [39]. This mathematical model is implemented in the SIMSEN software, where similar models based on equations for the flow momentum and mass conservation in hydro-mechanic equipment such as pipes, surge tanks, turbines, and valves are available. Electrical analogy is used to convert the flow variables into their electrical equivalent. The T-shaped electrical analogy of a cavitating draft tube developed by Alligné
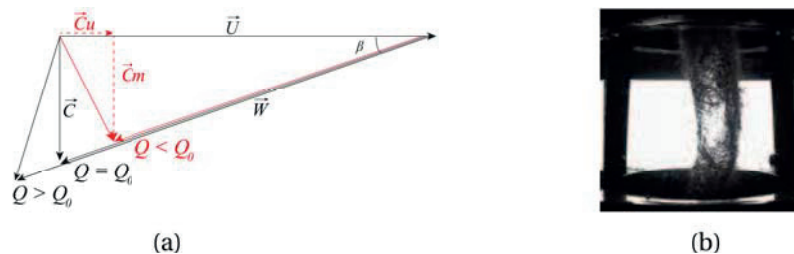
Figure 4.8 – (a) Flow velocity diagram at the runner trailing edge. The part load condition where $Q < Q_0$ is indicated in red. (b) A vortex rope featuring core pressure lower than the vapor pressure. A visible cavitating volume takes place.

75
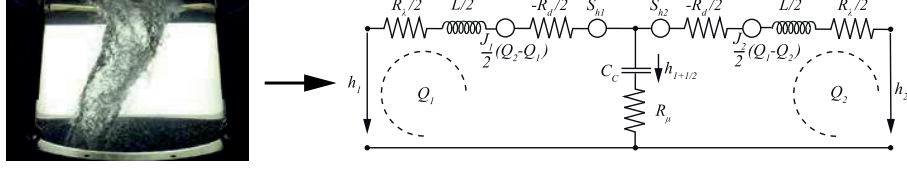
Figure 4.9 – T-shaped electrical analogy of a cavitating draft tube developed by Alligné et al. in [39]

et al. is presented in Figure 4.9. Details on the SIMSEN electrical analogy for other hydro-mechanic components such as surge tanks, pipes and valves are presented in [38]. Once the hydro-mechanic components of a power plant or a test rig are combined in a single SIMSEN model, their integrated dynamic behavior is simulated through a set of first order nonlinear ordinary differential equations. As detailed in [112], the complete system eigenfrequencies are calculated by performing a linear approximation of these equations.

Landry performed reduced scale model measurements and eigenvalue calculations in [108]. Using an excitation system, he identified the test rig first eigenfrequency for different cavitating operating conditions and used SIMSEN simulations to make apparent the draft tube cone cavitation compliance C_c (m^2) by searching for matching values of measured and simulated first eigenfrequencies. The cavitation compliance, introduced by Brennen et al. in [100], is expressed as in Equation 4.1 and is related to the local pressure wave speed a ($m{\cdot}s^{-1}$) as in Equation 4.2 (see [108]).

$$C_c = -\frac{\partial V_c}{\partial h} \tag{4.1}$$

$$a = \sqrt{\frac{gV}{C_c}} \tag{4.2}$$

where V_c (m^3) is the cavitation volume, V (m^3) is the pipe internal volume and h (m) is the local piezometric head.

Favrel et al. performed additional measurements in [19], where the test rig first eigenfrequency could be identified without the need of an excitation system. Notably, similarities regarding the hydroacoustic properties of the vortex rope were identified for operating conditions with the same swirl number S ($\cdot$), defined as the ratio between axial flux of tangential momentum and the axial flux of axial momentum. Favrel et al. also proposed Equation 4.3 to estimate S and demonstrated that operating conditions with the same S have the same Strouhal number St_{PVC} ($\cdot$), defined in Equation 4.4

$$S = n_{ED}\frac{\pi^2}{8}\left(\frac{1}{Q_{ED}} - \frac{1}{Q_{ED_0}}\right) \tag{4.3}$$

$$\text{St}_{\text{PVC}} = \frac{f_{\text{PVC}} D^3}{Q} \tag{4.4}$$

where Q_{ED} and n_{ED} are the non-dimensional discharge and speed factors defined by the IEC standard [8] as in Equation 4.5, and Q_{ED_0} corresponds to the Q_{ED} value at the swirl-free condition, i.e., at discharge $Q = Q_0$.

$$n_{\text{ED}} = \frac{nD}{\sqrt{E}} \qquad Q_{\text{ED}} = \frac{Q}{D^2 \sqrt{E}} \tag{4.5}$$

Following the HYPERBOLE methodology, Favrel et al. presented in [54] a first attempt to predict part load resonance. The identified values of the draft tube cone pressure wave speed in the reduced scale model, a_{M}, were transposed to the prototype scale as in Equation 4.6 proposed by Landry in [108]. Favrel et al. assumed Equation 4.6 to be valid for similar conditions of S, Froude number $\text{Fr} = \sqrt{E/gD}$ (·) and Thoma number σ (·), defined in Equation 4.7.

$$a_{\text{P}} = a_{\text{M}} \cdot \left(\frac{D_{\text{P}}}{D_{\text{M}}} \right) \left(\frac{n_{\text{P}}}{n_{\text{M}}} \right) \tag{4.6}$$

$$\sigma = \frac{NPSE}{E} \tag{4.7}$$

where $NPSE$ (J·kg^{-1}), the net positive suction energy, is defined as:

$$NPSE = \frac{p_{\text{abs}\bar{\text{I}}} - p_{\text{v}}}{\rho} + \frac{C_{\bar{\text{I}}}^2}{2} + g z_{\bar{\text{I}}} - g z_{\text{ref}} \tag{4.8}$$

where the subscript $\bar{\text{I}}$ indicates the draft tube outlet position, C (m·s^{-1}) is the flow velocity, p_{abs} (Pa) is the absolute pressure, p_{v} (Pa) is the vapor pressure, ρ (kg·m^{-3}) is the water density and z (m) is the centerline level. The level z_{ref} is a reference level, usually the spiral casing centerline level.

Using the calculated values of a_{P} in numerical simulations of the prototype generating unit, Favrel et al. were able to predict in [54] the event of part load resonance. Nevertheless, the predicted value of power output P_{a} in resonance conditions was 32.6 MW (7.3% of P_{rated}) higher than the measured value of P_{a}. This deviation is explained by the use of σ as a similitude parameter for the pressure wave speed transposition.

To improve accuracy in the prediction of part load resonance conditions, a local cavitation coefficient χ_{nD} defined in Equation 4.9 is used in this paper to replace σ as a similitude parameter. It takes into account the pressure value measured directly at the draft tube cone wall, p_{cone} (Pa), closer to the vortex rope itself, whereas σ uses the pressure and kinetic energy

at the draft tube outlet. Additionally, in χ_{nD}, the cone pressure is related to $n^2 D^2$, which is proportional to the runner kinetic energy, instead of the available specific energy E. The relation between χ_{nD} and σ is detailed in Equation 4.10. A step-by-step explanation of how Equation 4.10 is obtained is presented in A.6.

$$\chi_{nD} = \frac{p_{\text{cone}} - p_{\text{v}}}{\rho n^2 D^2} \tag{4.9}$$

$$\chi_{nD} = \frac{1}{n_{\text{ED}}^2} \cdot \left(\sigma + \frac{z_{\text{ref}} - z_{\text{cone}}}{\text{Fr}^2 D} + \frac{E_{\text{rd}}}{E} - \frac{Q_{\text{ED}}^2 D^4}{2 A_{\text{cone}}^2} \right) \tag{4.10}$$

where E_{rd} ($\text{J}\cdot\text{kg}^{-1}$) is the energy loss between the draft tube cone and the draft tube outlet cross-sections, which depends on the flow Reynolds number and the friction factor of the draft tube walls. Consequently, a reduced scale turbine model and its homologous prototype operating at the same n_{ED}, Q_{ED}, Fr and σ will not have similar χ_{nD}, as the term $e_{\text{rd}} = E_{\text{rd}}/E$ ($\cdot$) will not be equivalent.

Finally, two methods to calculate prototype a_{P} values from the reduced scale model a_{M} values are tested in the present paper. For the first method, a non-dimensional cavitation compliance $C_{\text{c}}^{\star} = C_{\text{c}}/D^2$ is defined from dimensional analysis. Homologous turbines operating at similar conditions of S, χ_{nD} and Fr are assumed to have the same $C_{\text{c}}^{\star}$. From this assumption, a_{P} is calculated using Equation 4.11. If similar values of Fr and n_{ED} are considered between model and prototype, Equations 4.11 and 4.6 are equivalent.

$$a_{\text{P}} = \left(\frac{g V_{\text{P}}}{C_{\text{c P}}} \right)^{0.5} = \left(\frac{g V_{\text{P}}}{C_{\text{c M}}} \frac{D_{\text{M}}^2}{D_{\text{P}}^2} \right)^{0.5} = \left(a_{\text{M}}^2 \frac{g V_{\text{P}}}{g V_{\text{M}}} \frac{D_{\text{M}}^2}{D_{\text{P}}^2} \right)^{0.5}$$

$$a_{\text{P}} = a_{\text{M}} \left(\frac{D_{\text{P}}}{D_{\text{M}}} \right)^{0.5} \tag{4.11}$$

The second method to transpose pressure wave speed values is also proposed by Landry in [108], by means of a non-dimensional wave speed Π defined in Equation 4.12.

$$\Pi = \frac{\rho a^2}{p_{\text{cone}} - p_{\text{v}}} = \frac{a^2}{\chi_{nD} n^2 D^2} \tag{4.12}$$

As demonstrated in Section 4.6.1, the non-dimensional wave speed Π is a function of S and χ_{nD} only, allowing the equality $\Pi_{\text{P}} = \Pi_{\text{M}}$ between prototype and reduced scale physical model to hold even if they operate under non-similar Fr values. Therefore, the second method to

calculate a_P makes use of Equation 4.13.

$$a_P = n_P D_P \sqrt{\Pi_M \chi_{nD}} \tag{4.13}$$

4.4 Procedure for part load resonance prediction

The procedure to predict part load resonance in hydro-power plants is separated in two parts: (1) the prediction of the turbine prototype f_{PVC} value and (2) the prediction of the complete hydraulic system hydroacoustic first eigenfrequency f_0 value. The prediction of higher order eigenfrequencies, as studied by Nicolet et al. in [113], is outside the scope of this paper.

The prototype f_{PVC} value prediction procedure assumes St_{PVC} similarity between model and prototype. This procedure has already been presented and validated by Favrel et al. in [54] and is presented briefly in this paper.

The diagram in Figure 4.10 summarizes the procedure to predict the prototype f_0 value. The procedure consists of the following steps:

1. Measurements are carried out using a test rig featuring a reduced scale physical turbine model homologous to the turbine prototype, covering a large number of possible part load operating conditions experienced by the prototype. For each operating point:

   - Cross-spectrum analysis of the pressure signal from sensors installed in the draft tube cone is performed to identify the f_0 value. In cases where f_0 can not be detected by cross-spectrum analysis, an excitation system is used (see [50, 51]);

   - By knowing the test rig f_0 value and the hydroacoustic properties of all the remaining parts of the test rig, eigenvalue calculations using SIMSEN software are used to identify the draft tube cone pressure wave speed, a_M, by matching the calculated f_0 to the measured f_0 value. From the identified a_M value, its non-dimensional equivalent Π_M value is calculated. This procedure is detailed in [50, 51].

2. Interpolation functions are generated, allowing estimation of a_M or Π_M in any operating condition of interest;

3. For a given part load operating condition, the interpolation functions are used to define the value for a_M or Π_M. From either a_M or Π_M, the prototype pressure wave speed a_P is estimated using Equation 4.11 or Equation 4.13, respectively;

4. The calculated a_P value is introduced in the prototype generating unit numerical model constructed with SIMSEN software. Eigenvalue calculations are performed, providing the prototype first eigenfrequency f_0.

Finally, for the operating condition being analyzed, the predicted values of prototype f_0 and
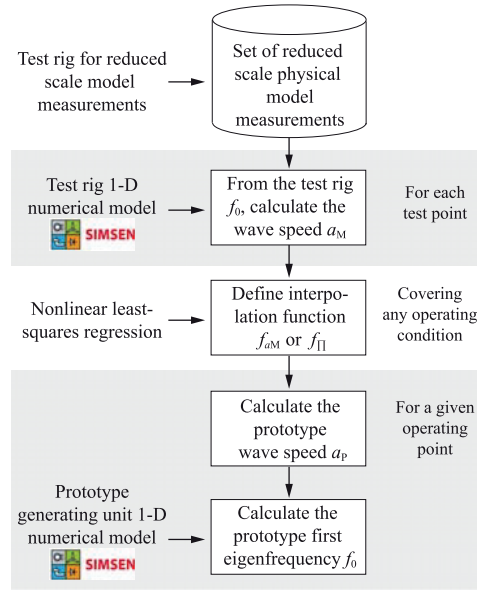
Figure 4.10 – Procedure to predict the prototype generating unit first eigenfrequency f_0.
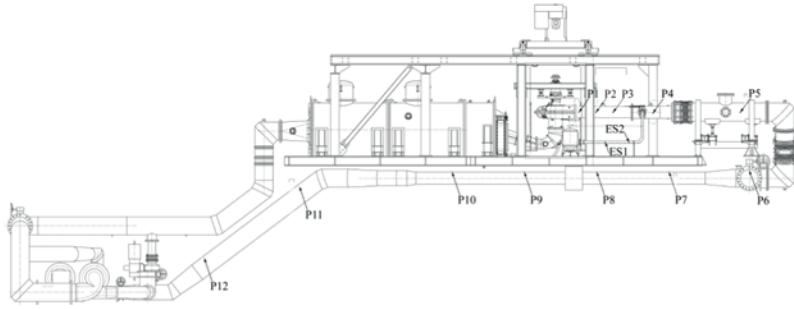
Figure 4.11 – Sketch of the LMH-PF3 test rig.

f_{PVC} are compared. If the uncertainty range of these predicted values overlaps, the operating condition is considered under resonance.

4.5   Reduced scale physical model measurements

The reduced scale physical model of the test case turbine features a runner with external diameter $D_M = 0.35$ m and is installed in the PF3 test rig of the Laboratory for Hydraulic Machines (LMH) at the *École Polytechnique Fédérale de Lausanne* (EPFL), illustrated in Figure 4.11.

Measurements are performed for the operating conditions listed in Table 4.1. Two different Froude numbers, Fr = 8.74 and Fr = 5.52, five different n_{ED} values and Q_{ED} values varying between 0.11 and 0.17 are tested. For the measurements performed at Fr = 8.74, three values of σ are tested: σ_{max}, σ_{rated} and σ_{min}, simulating possible variations of the prototype downstream

Table 4.1 – Operating conditions of the measurements performed on the reduced scale physical model.

Fr	n_{ED}	Q_{ED}	Q_{ED_0}	S	σ_{max}	σ_{rated}	σ_{min}
$(\cdot)$	$(\cdot)$	$(\cdot)$	$(\cdot)$	$(\cdot)$	$(\cdot)$	$(\cdot)$	$(\cdot)$
8.74	0.268	$0.11 \rightarrow 0.16$	0.230	$1.57 \rightarrow 0.63$	0.111	0.095	0.083
8.74	0.277	$0.11 \rightarrow 0.17$	0.236	$1.66 \rightarrow 0.56$	0.119	0.102	0.088
8.74	0.288	$0.11 \rightarrow 0.17$	0.244	$1.78 \rightarrow 0.64$	0.128	0.110	0.095
8.74	0.300	$0.11 \rightarrow 0.17$	0.253	$1.90 \rightarrow 0.71$	0.139	0.119	0.103
8.74	0.317	$0.11 \rightarrow 0.17$	0.265	$2.08 \rightarrow 0.83$	0.156	0.133	0.115
5.52	0.288	$0.11 \rightarrow 0.17$	0.244	$1.78 \rightarrow 0.64$	-	0.110	-

reservoir level.

To calculate the χ_{nD} value in Equation 4.9, the average pressure in the draft tube cone, p_{cone}, is calculated using Equation 4.14.

$$p_{cone} = \frac{1}{N_{sen}} \frac{1}{N_s} \sum_{i=1}^{N_{sen}} \sum_{j=1}^{N_s} p_i^{(j)} \tag{4.14}$$

where N_{sen} is the total number of sensors equally distributed in the same cross-section of the draft tube cone, N_s is the total number of samples acquired during the measurements period, and $p_i^{(j)}$ is the value of the pressure sample j acquired by the sensor i. In this test case, pressure values are acquired by four pressure sensors located in the draft tube cone using a 1000 Hz sampling rate over a period of 200 s for each test point. A sketch of the turbine draft tube with the location of these four pressure sensors — named C1E, C1S, C1W and C1N — is illustrated in Figure 4.12.

By analyzing the cross-spectrum of the pressure signals from these four sensors, the hydraulic circuit first eigenfrequency f_0 and the vortex precession frequency f_{PVC} for each tested operating condition are identified. An example of f_0 and f_{PVC} identification using the pressure signals from two sensors in opposite sides of the draft tube cone cross-section is given in Figure 4.13.

In cases where the amplitude of pressure pulsations at f_0 is small and the f_0 value cannot be identified by analyzing the cross-spectrum of pressure signals from these sensors, an excitation system such as the one presented by Landry et al. in [50] can be used to perform modal analysis and identify f_0. Additionally, using the same type of excitation system as Landry et al. , Favrel et al. proposed in [51] a method based on dynamic modal analysis to decrease the measurement time period required for f_0 identification.

With the f_{PVC} values from the same set of measurements presented in this section, Favrel et al. derived in [19] the following empirical relation between the Strouhal number and the swirl
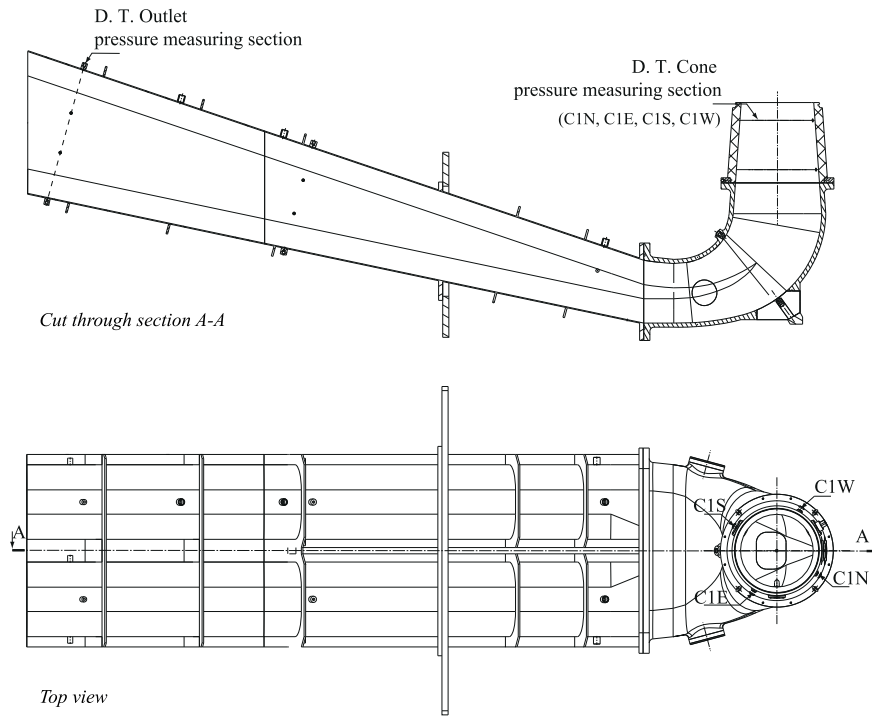
Figure 4.12 – Sketch of the turbine draft tube showing the location of the four pressure sensors for the calculation of χ_{nD}, f_0 and f_{PVC}.
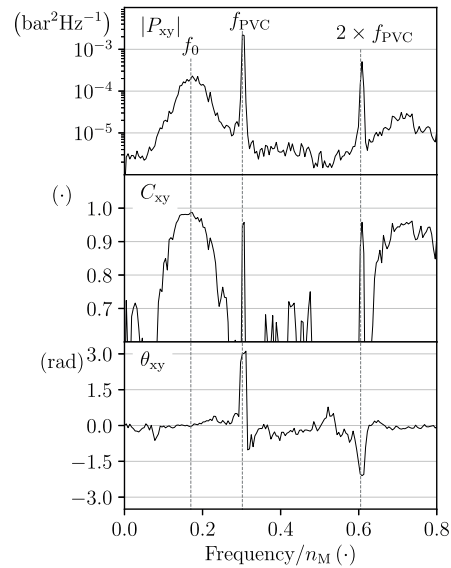
Figure 4.13 – An example of f_0 and f_{PVC} identification using the pressure signals from two sensors in opposite sides of the draft tube cone cross-section.
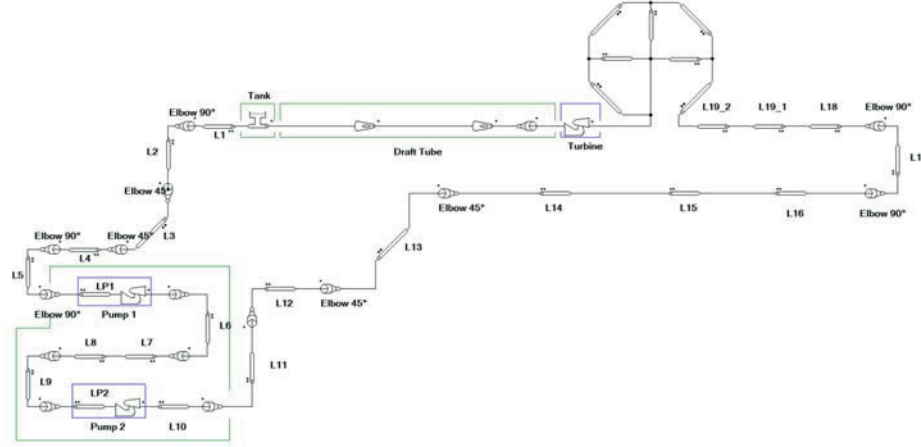
Figure 4.14 – SIMSEN 1-D components to simulate the LMH PF3 test rig dynamic behavior.

number with a standard error of estimate equal to 0.019:

$$\text{St}_{\text{PVC}} \approx 0.429 \cdot S + 0.120 \tag{4.15}$$

4.6 1-D hydroacoustic eigenvalue calculations

4.6.1 Reduced scale physical turbine model

The SIMSEN components to simulate the LMH PF3 test rig dynamic behavior are illustrated in Figure 4.14. Each component contains a set of T-shaped elements similar to the one presented in Figure 4.9 for the draft tube cone. All the hydroacoustic parameters are known and they are not altered by changes in the operating conditions. The unique exception is the pressure wave speed in the draft tube cone a_{M} as it is a function of the cavitation vortex compliance and, consequently, of S, χ_{nD} and Fr. As a result, once the hydroacoustic first eigenfrequency f_0 of the test rig is identified through measurements for a given operating condition, eigenvalue calculations with SIMSEN software are used to identify the unique a_{M} value leading to matching values of measured and calculated f_0. Further details on the a_{M} identification procedure are found in [108].

In the eigenvalue calculations, the pressure wave speed value is assumed to be constant and equal to a_{M} in the 1 m long conical part of the draft tube, just below the runner. This conical part is simulated with a distributed model; its SIMSEN component contains 32 T-shaped elements such as the one shown in Figure 4.9. The remaining part of the draft tube, the diffuser, is represented by three elements with 400 m·s^{-1} wave speed in the first 1.1 m, followed by six elements with 200 m·s^{-1} wave speed in the remaining 2.5 m. These wave speed values for the diffuser are based on measurements performed by Arpe in [96].

The calculated values of a_{M} and the corresponding Π values for all tested operating conditions
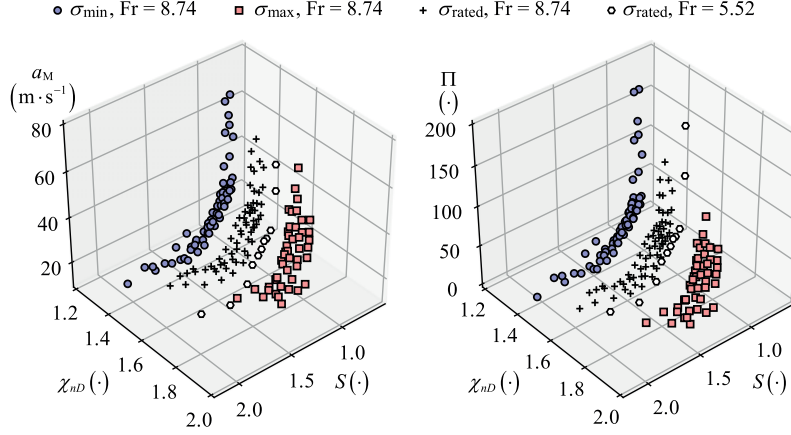
Figure 4.15 – Calculated values of a_M and the corresponding Π values for all tested operating conditions as a function of S and χ_{nD}.
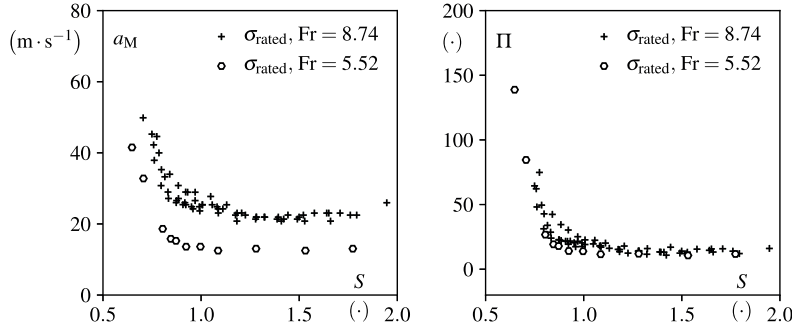
Figure 4.16 – The a_M and Π values for measurements at $\sigma = \sigma_{rated}$, but at two different Fr values are presented. The calculated values of a_M are clearly separated according to the Fr number. The separation disappears when comparing Π values.

described in Table 4.1 are shown in Figure 4.15 as a function of S and χ_{nD}. The a_M and Π values obtained at a similar condition of Thoma number, i.e., $\sigma = \sigma_{rated}$, but at two different conditions of Froude number, are presented in Figure 4.16. The calculated values of a_M are clearly separated according to the Froude number. However, this separation disappears when comparing Π values. As a consequence, a_M is considered as a function of S, χ_{nD} and Fr, while Π is a function of S and χ_{nD} only. The negligible influence of Fr on Π values is also reported by Landry in [108].

An approximation function $f_a\left(S, \chi_{nD}, \text{Fr}\right)$ able to estimate a_M values inside the tested operating range is created using a nonlinear least-squares regression method to define its parameters. The resulting function is detailed in Equation 4.16 and a_M values obtained with f_a assuming Fr = 5.52 and Fr = 8.74 are presented in Figures 4.17 and 4.18, respectively. The resulting
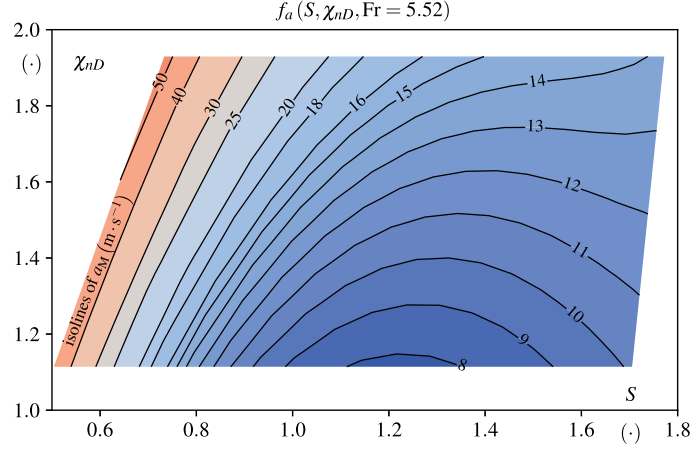
Figure 4.17 – Estimated a_M values calculated with the f_a function for Fr = 5.52.
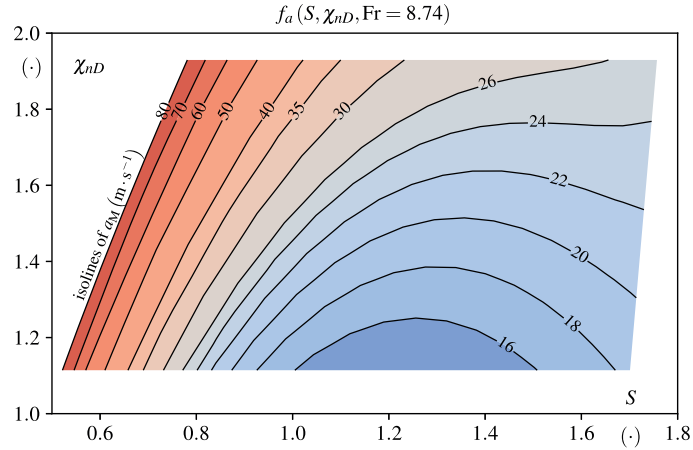
Figure 4.18 – Estimated a_M values calculated with the f_a function for Fr = 8.74.

standard error between measured and approximated values is $\sigma_{\text{Std}fa} = 3.37 \text{ m} \cdot \text{s}^{-1}$.

$$
\begin{aligned}
f_a\left(S, \chi_{nD}, \text{Fr}\right) = \exp\big(\quad & -1.9820 \cdot S^3 + 9.3726 \cdot S^2 - 12.8240 \cdot S \\
& + 2.2583 \cdot \chi_{nD} - 1.0838 \cdot S \cdot \chi_{nD} \\
& + 0.1862 \cdot \text{Fr} + 5.2708 \quad \big)
\end{aligned}
\tag{4.16}
$$

Similar to f_a, an approximation function $f_\Pi\left(S, \chi_{nD}\right)$ able to estimate Π values inside the prototype part load operating range is constructed. The resulting function is detailed in Equation 4.17, and the approximated values of Π calculated with f_Π are presented in Figure 4.19. The proposed f_Π function estimates Π values with a standard error of $\sigma_{\text{Std}f\Pi<40} = 5.21$
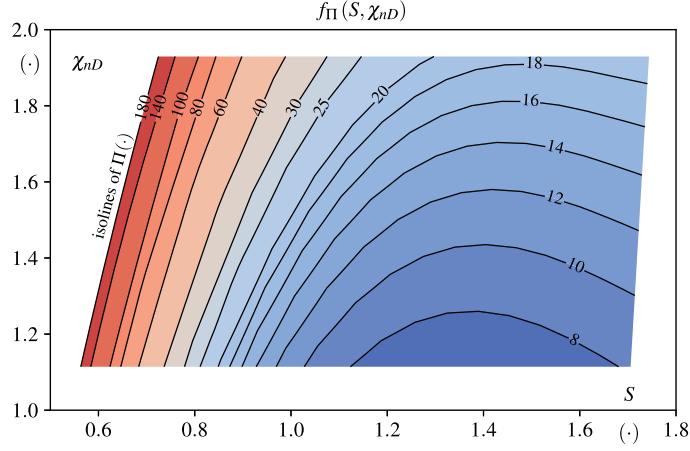
Figure 4.19 – Approximated values of Π calculated with the f_Π function.

for Π values lower than 40 and $\sigma_{\mathrm{Std}f\Pi>40} = 17.09$ for Π values greater than 40.

$$
\begin{aligned}
f_\Pi\left(S, \chi_{nD}\right) = \exp\big(\quad & -3.0298 \cdot S^3 + 15.0806 \cdot S^2 - 23.3895 \cdot S \\
& + 2.2590 \cdot \chi_{nD} - 0.7090 \cdot S \cdot \chi_{nD} \\
& + 11.9863 \quad \big)
\end{aligned}
\tag{4.17}
$$

4.6.2 Turbine prototype

Once the pressure wave speed a_M value for the reduced scale physical model is defined, it is transposed to the prototype scale and eigenvalue calculations of the test case prototype generating unit are performed. For comparison, both methods to transpose wave speed values from the reduced scale model to prototype scale are evaluated, i.e., the direct transposition method of Equation 4.11 or using the non-dimensional wave speed Π in Equation 4.13. As a result, using the approximation functions, a_P may be calculated using either Equation 4.18 or Equation 4.19.

$$
a_\mathrm{P} = f_a\left(S, \chi_{nD}, \mathrm{Fr}\right) \cdot \sqrt{\frac{D_\mathrm{P}}{D_\mathrm{M}}}
\tag{4.18}
$$

$$
a_\mathrm{P} = n_\mathrm{P} D_\mathrm{P} \cdot \sqrt{f_\Pi\left(S, \chi_{nD}\right) \cdot \chi_{nD}}
\tag{4.19}
$$

The resulting values of a_P considering both transposition methods and using the prototype on-site operating conditions in the interpolation functions are illustrated in Figure 4.20. The input values of prototype S, χ_{nD} and Fr required to calculate a_P correspond to the mean values measured during the time intervals indicated by the numbers from 1 to 7 in Figure 4.2. Both
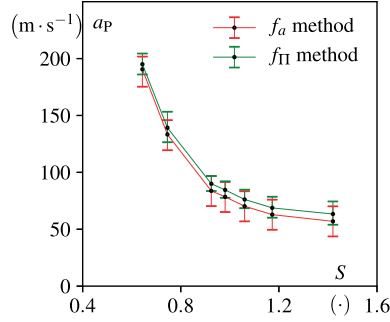
Figure 4.20 – a_P values calculated using both transposition methods and the prototype on-site operating conditions.
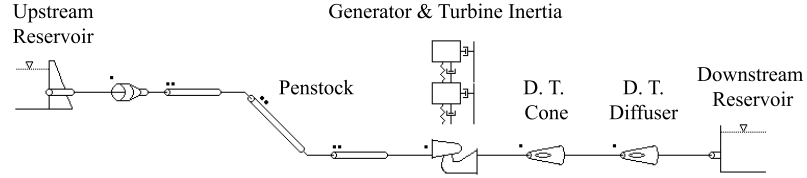
Figure 4.21 – SIMSEN 1-D components to simulate the prototype power plant dynamic behavior and calculate the first eigenfrequency, from [114].

methods to calculate a_P lead to similar values: the maximum deviation between them is 6.4 m·s^{-1}, corresponding to 3.3% of the maximum calculated a_P value equal to 195.0 m·s^{-1}.

The set of SIMSEN components to simulate the prototype generating unit dynamic behavior, designed for this test case by Alligné et al. in [114], is illustrated in Figure 4.21. The calculated a_P values are introduced in the draft tube cone component and the prototype f_0 values calculated. Similar to the eigenvalue calculations of the reduced scale turbine, the pressure wave speed in the draft tube cone of the prototype is assumed to be constant and equal to a_P all along the distributed model. The pressure wave speed in the draft tube diffuser is assumed to be constant and equal to 1000 m·s^{-1}, a wave speed value considered reasonable for a cavitation-free diffuser surrounded by concrete. Also similar to the reduced scale model turbine, the draft tube cone is represented by 32 T-shaped elements.

Comparisons between measured and calculated f_0 values are presented in Figure 4.22 and discussed in further detail in the next section. The uncertainty interval for the calculated a_P and f_0 values are based on the standard error of the interpolating functions f_a and f_Π.

Considering the a_P values lower than 150 m·s^{-1} presented in Figure 4.20 and their corresponding f_0 values obtained through eigenvalue calculations, f_0 values are approximated by assuming $f_0 \approx \hat{f}_0(a_P)$, as in Equation 4.20, leading to a standard error of estimate of only $\sigma_{\hat{f}_0} = 0.010$ Hz. With the help of the approximation functions detailed in Equations 4.15 and 4.20, resonance conditions are calculated by finding the combination of S, χ_{nD} and Q values
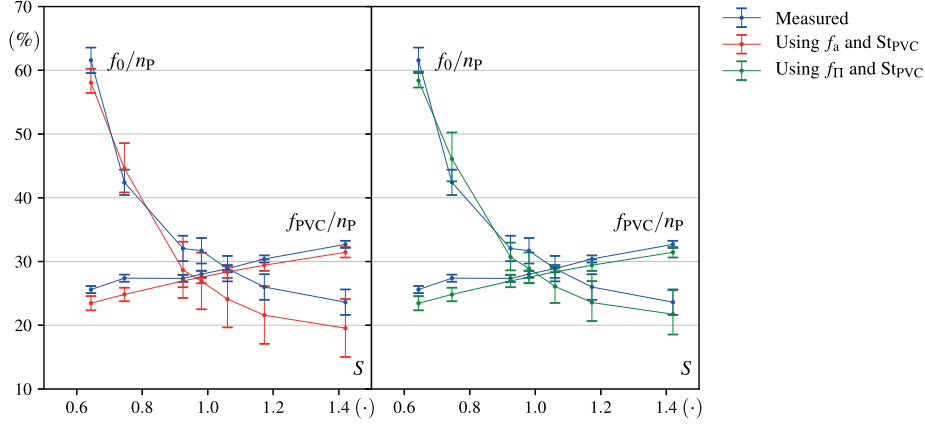
Figure 4.22 – Calculated f_{PVC} and f_0 values, using both a_P estimation methods, as a function of S. Both methods predict resonance in an interval of S values that overlaps the measured S interval.

leading to Equation 4.21.

$$f_0 \approx \hat{f}_0 \left(a_P \right) = 7.246 \cdot 10^{-3} \cdot a_P \tag{4.20}$$

$$\hat{f}_0 = f_{PVC}$$
$$7.246 \cdot 10^{-3} \cdot a_P \left(S, \chi_{nD} \right) = \text{St}_{PVC} \left(S \right) \cdot \frac{Q}{D_P^3} \tag{4.21}$$

where a_P is determined using the f_Π method, i.e., using Equation 4.19.

4.7 Results and validation

Using Equation 4.15 to estimate St_{PVC}, the prototype f_{PVC} values are estimated by calculating $f_{PVC} = \text{St}_{PVC} \cdot Q / D_P^3$, Q being the measured prototype discharge values at $E = 1759 \text{ J} \cdot \text{kg}^{-1}$. The calculated f_{PVC} and the f_0 values resulting from both a_P estimation methods are presented in Figure 4.22 as a function of S. To facilitate comparisons, the measured values of f_{PVC} and f_0 are also presented. The measured and predicted values of S, f_0 and P_a / P_{rated} in resonance conditions are listed in Table 4.2. These values correspond to the crossing point of the curves for f_0 / n_P and f_{PVC} / n_P in the graphs shown in Figure 4.22. The high accuracy of the proposed method to predict P_a and f_0 in resonance conditions is confirmed by the low values of error, also presented in Table 4.2.

Table 4.2 – Measured and predicted values of S, f_0 and P_a/P_{rated} in resonance conditions. The corresponding errors of estimate are also listed.

	Resonance conditions			Error		
	S	f_0/n_P	P_a/P_{rated}	$\|\Delta S\|$	$\|\Delta f_0\|/n_P$	$\|\Delta P_a\|/P_{rated}$
	$(\cdot)$	$(\cdot)$	$(\cdot)$	$(\cdot)$	$(\%)$	$(\%)$
Measured	1.060	0.289	0.57	-	-	-
f_a method	0.965	0.274	0.60	0.095	1.5	2.9
f_{Π} method	1.010	0.279	0.59	0.050	1.0	1.6

By assuming that the prototype χ_{nD} value remains constant, the resulting S value for resonance condition assuming any n_{ED} value inside the prototype operating range is estimated using Equation 4.21. Calculated resonance conditions assuming three possible values of χ_{nD} are illustrated in the hill chart shown in Figure 4.23. They correspond to χ_{nD} values calculated using (1) the draft tube cone pressure $p_{cone,P}$ value measured in resonance conditions at $E = 1759$ J·kg^{-1}, which is taken as a the reference value p_{ref}; (2) $p_{cone,P} = p_{ref} - 0.3$ bar and (3) $p_{cone,P} = p_{ref} + 0.3$ bar. As the reference pressure p_{ref} is measured with a downstream reservoir close to the rated water elevation level, the ± 0.3 bar variation reflects approximately the effect of having maximum or minimum downstream reservoir water levels.

This procedure results in resonance being expected to happen at a quasi-constant S value; a maximum variation of only $\Delta S = 6 \cdot 10^{-3}$ is calculated for a given constant χ_{nD} value. Variations in frequency are also negligible; the frequency deviates by only $4 \cdot 10^{-3}$ Hz for a given χ_{nD} value. These results are in very good agreement with the measurements where resonance with very similar values of S and f_0 values are observed for the two tested E values. In fact, during the prototype measurements a draft tube cone pressure of $p_{cone,P} = 2.5$ bar for $E = 1560$ J·kg^{-1} is measured, a value only 4.7% higher than the one measured at $E = 1759$ J·kg^{-1}, leading to an approximately constant prototype χ_{nD}.

Part load resonance occurring with similar S values for varying values of n_{ED} was previously reported by Favrel et al. in [19] using the reduced scale physical model of the same test case presented in this paper. Similar behavior for the turbine prototype is confirmed by measurements and calculations. Resonance happening with the same S leads to power swings occurring with different mean values of power output, as observed during the site tests. This fact is noted by comparing the isolines of S and the isolines of P_a/P_{rated} in the hill chart shown in Figure 4.23.

4.8 Conclusions

This research paper presented a complete procedure to accurately predict part load resonance between the hydroacoustic first eigenfrequency of a Francis turbine prototype hydraulic circuit and its vortex rope excitation frequency. The procedure requires reduced scale physical model measurements using a test rig and eigenvalue calculations using linearized system
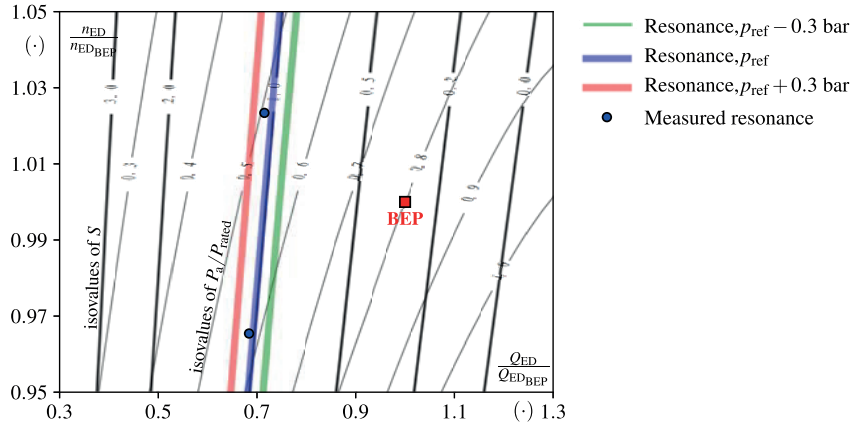
Figure 4.23 – Hill chart featuring the measured and calculated resonance conditions. For the calculated resonance conditions, three possible values for $p_{\mathrm{cone,P}}$ are assumed in the calculation of χ_{nD}. Resonance occurs at approximately constant S values.

matrices. Draft tube cone pressure wave speed values in the reduced scale physical model were calculated and their values transposed to the prototype scale using two different methods, producing similar results. A method based on a non-dimensional wave speed Π presents the advantage of not requiring Froude number similarity between the reduced scale physical model and prototype. Both methods require, however, similarity of swirl number S and local cavitation coefficient χ_{nD}. The coefficient χ_{nD} was proven to be more suitable than the Thoma number σ for this purpose, as χ_{nD} relies on the absolute pressure measured directly at the wall of the turbine draft tube cone.

The procedure to predict resonance in part load conditions is validated by making use of a test case where the predicted conditions of resonance match the measured ones. As demonstrated by calculations and measurements on the prototype, resonance is expected to happen for an approximately constant S value for different E conditions in cases where the draft tube cone pressure remains similar. For these cases, knowing that S and P_{a} values are not completely correlated, the mean power output for resonance conditions is expected to vary.

As demonstrated, part load resonance depends on a large number of factors, including turbine design and power plant layout. The risk of designing a generating unit leading to part load resonance is apparently small, but the possible costs resulting from the damage caused by its high levels of power swings and pressure pulsations or the loss in operation flexibility are not negligible. The presented procedure allows engineers working on the design of a given generating unit to know with accuracy and in advance, i.e., soon after carrying out reduced scale physical model tests, if part load hydroacoustic resonance is expected to occur. If resonance is expected, mitigation mechanisms such as air injection in the draft tube cone can be foreseen. Alternatively, changes in the generating unit design to modify the expected system eigenfrequencies or the vortex rope excitation frequency can also be implemented to

completely avoid this type of resonance.

5 Full load stability

This chapter corresponds to the following paper manuscript submitted to the Journal of Mechanical Systems and Signal Processing:

J. Gomes Pereira Jr., E. Vagnoni, A. Favrel, C. Landry, S. Alligné, C. Nicolet, F. Avellan. *Prediction of unstable full load conditions in a Francis turbine prototype.*

The author's contribution: The author contributed with the post-processing of all the measurements data, the generation of figures, graphs and by writing the paper. He also participated in the measurement campaigns, derived the equations for the mass flow gain factor transposition and performed all the comparisons between reduced scale model and prototype data.

Abstract

Francis turbines operating in full load conditions feature an axisymmetric vortex rotating in the opposite direction of the turbine runner. This vortex rope may enter in an unstable self-exciting process, leading to large pressure pulsations and oscillations in the generating unit power output. In this research work, prototype on-site and reduced scale model test results are presented where the turbine changes from a stable to an unstable full load condition due to an increase in discharge. Measurements are compared in the frequency and time domain, where similarities are evidenced between model and prototype. Using the measurements on the reduced scale model and 1-D numerical models of both the reduced scale model and the turbine prototype, eigenvalue calculations are performed to predict the discharge value of transition from stable to unstable conditions. The transition point on the prototype is then predicted with a small deviation. Transient simulations in the time domain are performed replicating the self-exciting behavior of the unstable full load condition.

5.1   Introduction

In the current energy mix scenario, with the increase of power generation from intermittent energy sources such as wind and solar, the flexibility featured by hydropower units in terms of power generation and its ability to provide ancillary services to the power grid are of great potential value. However, this flexibility requires the hydraulic turbines to operate sometimes in non-optimal conditions. The acceptable operating range of a Francis turbine is limited by the conditions where the turbine efficiency decreases drastically or flow instabilities inducing cavitation and pressure pulsations appear, risking damage and reducing the life span of the unit [60, 58, 95, 98].

When Francis turbines operate with a discharge value higher than the one at the best efficiency point (BEP), the turbine is said to be operating at full load. At this condition, a residual swirl flow rotating in the opposite direction of the runner leaves the runner, leading to an axisymmetric cavitation vortex rope that may enter in self-excitation. Therefore, the full load operating condition can be considered as unstable, when featuring a self-excited vortex, or stable otherwise. The turbine can operate normally at stable full load conditions, with a small decrease of efficiency if compared to the BEP. On the contrary, as the discharge increases and the unit enters in the unstable full load regime, the system experiences unacceptable pressure pulsations and power swings. Example of hydropower plants experiencing full load pressure surges can be found in [27, 30]. A mathematical approach to explain the full load stability and its relation with the swirling flow under the runner can be found in [30, 94, 115]. Numerical simulations of unstable full load conditions can be found in [116, 44, 45, 112].

A large number of factors affect the stability limits in full load operating conditions: the hydraulic system layout, the energy loss coefficients and the cavitating vortex hydro-acoustic properties among others. From a practical point of view, it remains challenging for power plant operators to exactly determine at which operating point the turbine will move from a stable to an unstable condition. This transition point must be known by the plant operators if they attempt to gain in flexibility by operating their turbines in their maximum, but safe, power generation limit.

Research papers such as [30, 94, 115, 112, 116, 44, 45, 48, 117] take into account the cavitation compliance and the mass flow gain factor, the two most important parameters describing the physical mechanism of the cavitating volume, to propose numerical models for the simulation of unstable full load conditions. In [54], Favrel et al. made use of reduced scale physical model measurements and 1-D eigenvalue calculations to identify cavitation compliance values and predict a part load resonance phenomena in a turbine prototype induced by the cavitation vortex rope. Improvements in the methodology undertaken by Favrel et al. are proposed by Gomes Pereira et al. in [118], increasing the prediction accuracy.

In this paper, a new methodology to predict unstable full load conditions on Francis turbine generating units based on reduced scale physical model tests and eigenvalue calculations is proposed. It includes a new procedure to define and transpose values of mass flow gain factor,

a hydro-acoustic parameter leading to full load unstable conditions [28, 30]. This methodology is applied to a turbine test case where the time history of measurements performed on the prototype evidences a clear transition from stable to unstable full load conditions, showing a sudden appearance of high amplitude pressure pulsations and power swings. The same transition is observed in its homologous reduced scale physical model, allowing the construction of a hill chart featuring the limits between the stable and the unstable full load conditions. This hill chart is used to make direct comparisons regarding the stability limits of the reduced scale model and prototype. Additionally, the pressure pulsations measured in the reduced scale model and in the prototype are analyzed and compared in both frequency and time domain.

Knowing that direct comparisons do not take into account all hydro-acoustic parameters acting on the full load stability limits, the transition from stable to unstable conditions is also analyzed through 1-D eigenvalue calculations. Reduced scale model and prototype being homologous, the hydro-acoustic parameters are first identified for the reduced scale model and then transposed to the prototype, according to the on-site operating conditions. The eigenvalue calculations are then able to predict a transition from stable to unstable conditions on the prototype, although the transition occurred with a discharge value slightly greater than the predicted value.

Finally, 1-D numerical simulations are performed in time domain for the prototype generating unit, considering a stable full load condition and an unstable full load condition. In these simulations, the system nonlinearities are taken into account, and values for the draft tube cone pressure wave speed and energy loss coefficient are updated according to the calculated instantaneous wall pressure. Pressure pulsations originated by a temporary excitation source are either totally damped or amplified entering in a self-exciting mode, replicating the dynamic behavior of the real turbine in stable and unstable conditions, respectively.

Greek characters

α ($^\circ$)   guide vanes opening angle

β ($\cdot$)   void fraction

η ($\cdot$)   turbine efficiency

λ_0 first eigenvalue

μ' (Pa·s)   pressurized pipes bulk viscosity coefficient

μ'' (Pa·s)   cavitation volume bulk viscosity coefficient

Π ($\cdot$)   dimensionless pressure wave speed

ρ (kg·m^{-3})   liquid water density

σ ($\cdot$)   Thoma number

χ (s)   mass flow gain factor

Abbreviations

BEP	Best Efficiency Point
LMH	Laboratory for Hydraulic Machines
NPSE ($J \cdot kg^{-1}$)	Net Positive Suction Energy

Subscripts

cone	at the draft tube cone
h	hysteresis
M	reduced scale model value
P	prototype value
rated	rated value
ref	reference value
v	vapor

5.2 Turbine prototype measurements

The test case is a Francis turbine with IEC specific speed $n_{QE} = 0.131$, defined as in eq. (5.1), and featuring a runner with $D = 5.4$ m of external diameter.

$$n_{QE} = n \cdot \frac{Q^{1/2}}{E^{3/4}} \tag{5.1}$$

The turbine prototype rated power, rotational speed and rated net head are $P_{rated} = 444$ MW, $n = 2.143$ Hz and $H_{rated} = 170$ m, respectively. Main dimensions of the power plant penstock and the turbine prototype are illustrated in Figure 5.1. The on-site tests are performed at $\sigma = 0.122$ and net head $H = 177$ m, where σ (·) is the Thoma number defined as in eq. (5.2), according to the IEC standard [8].

$$\sigma = \frac{NPSE}{E} \tag{5.2}$$

Extensive measurements are performed on the prototype — detailed description is provided in [27, 61, 26] — including measurements of guide vanes opening angle α (°) and generator active power output P_a (MW). The values of the turbine discharge Q, net head H and turbine efficiency η are estimated by using α and P_a as an input for interpolation functions generated with results from the reduced scale physical model measurements. The complete description of the procedure to estimate Q, H and η through interpolation functions are presented in [109].
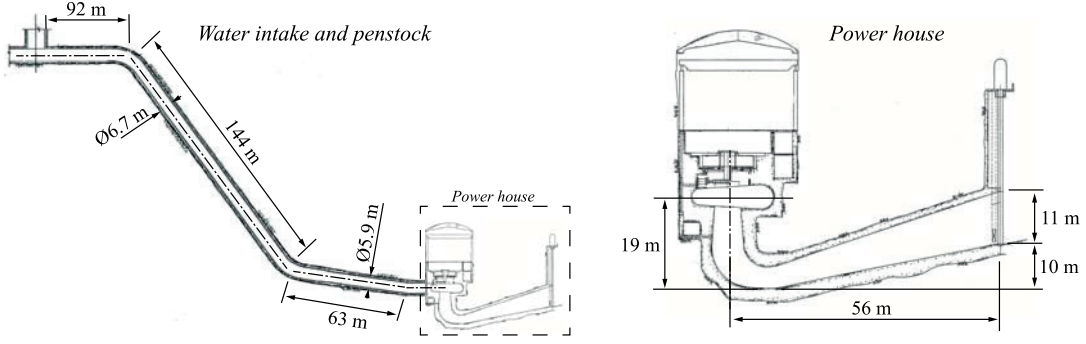
Figure 5.1 – Main dimensions of the penstock and the turbine prototype, courtesy of BC Hydro.

Dynamic wall pressure measurements are performed in the draft tube cone with two sensors located at $0.4 \times D$ distance below the runner outlet, at $90°$ and $270°$ of the upstream reservoir direction. The time history of prototype guide vane opening angle α, pressure in the draft tube cone, c_p coefficient calculated as in eq. (5.3) and active power output P_a of the generating unit are presented in Figure 5.2.

$$c_\mathrm{p} = \frac{\bar{p}(t) - p_\mathrm{ref}}{\rho E} \qquad p_\mathrm{ref} = \frac{1}{T_\mathrm{aq}} \int_{t=0}^{T_\mathrm{aq}} \bar{p}(t)\, dt \qquad (5.3)$$

where $\bar{p}$ (Pa) is the instantaneous mean pressure measured by the two pressure sensors in the draft tube cone and p_ref (Pa) is a reference pressure, equal to the mean value of $\bar{p}$ over the whole measurements acquisition period T_aq (s).

As a general rule for all figures in this paper, the stable operating conditions are represented in green and the unstable conditions in red. In Figure 5.2, four instants of time are indicated by letters which refer to the onset of the following phenomena:

ⓐ The prototype leaves the rope-free zone according to what is observed in the reduced scale physical model, as discussed later in Section 5.3;

ⓑ The unstable full-load condition triggers;

ⓒ The measured guide vanes opening angle reaches its maximum value. At this condition, power oscillations of about $\Delta P_\mathrm{a} = 40$ MW magnitude are observed;

ⓓ The large power and pressure oscillations stop, as the guide vanes opening angle is decreased and the unit is back to stable condition.

A small hysteresis effect is noticed as the unit becomes unstable at $\alpha = 26.3°$ at the instant ⓑ, and comes back to the stable condition at $\alpha = 25.9°$ at instant ⓓ, leading to $\Delta \alpha_\mathrm{h} = 0.4°$.
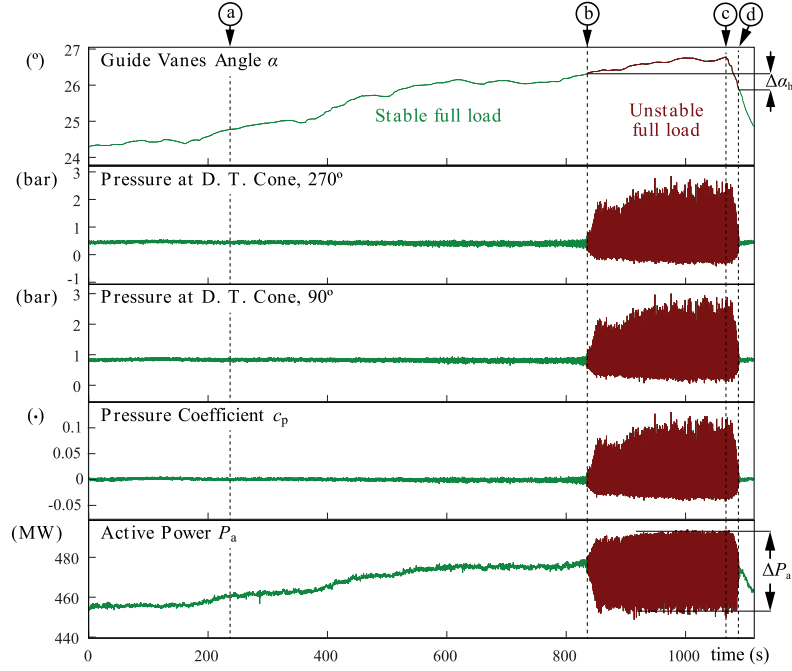
Figure 5.2 – Time history of the prototype guide vanes opening angle α, pressure at the draft tube cone at $270°$ and $90°$, pressure coefficient c_p and active power P_a, respectively. Four different instants of the signal time history are indicated: ⓐ end of the rope-free zone according to the reduced scale physical model, ⓑ start of the unstable full-load conditions, ⓒ peak guide vanes opening value and ⓓ end of power and pressure oscillations.

5.3   Reduced scale physical model measurements

The homologous reduced scale physical model of the turbine prototype features a runner with $D = 0.35$ m external diameter and is installed in the LMH-PF3 closed-loop test rig, as illustrated in Figure 5.3. This test rig features two 400 kW axial pumps that can supply a maximum head of 100 m. All the measurements are performed according to the IEC standard [8].

Measurements are carried out to create the efficiency hill chart of the turbine presented in Figure 5.4. The performed measurements are interpolated and presented as a function of the IEC non-dimensional speed factor n_{ED} and discharge factor Q_{ED} defined as in eq. (5.4).

$$Q_{ED} = \frac{Q}{D^2\sqrt{E}} \qquad n_{ED} = \frac{nD}{\sqrt{E}} \tag{5.4}$$

Test points where measurements are performed and isolines of interpolated values of guide vanes opening angle α, turbine efficiency η and mechanical power P_m are shown in Figure 5.4. The presented η and P_m values are already transposed to the prototype scale by following the
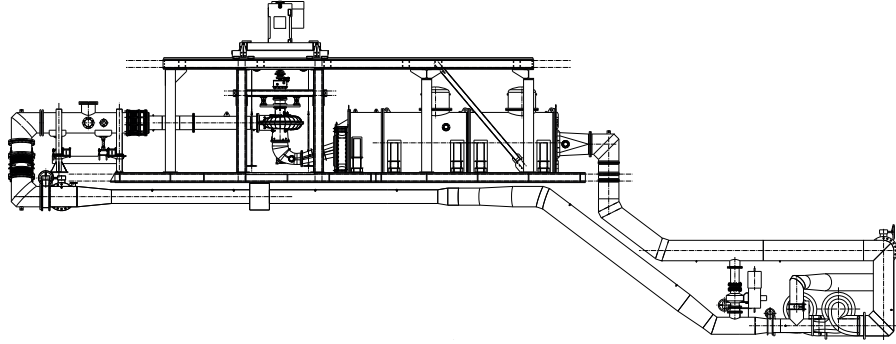
Figure 5.3 – LMH-PF3 closed-loop test rig, featuring two axial pumps and complying with the IEC 60153 standard for reduced scale physical turbine model tests [8].

Table 5.1 – Operating conditions tested on the reduced scale physical model. The Q_{ED} values for the stability limit are also presented.

n_{ED}	Q_{ED} - measured range	Q_{ED} - stability limit	σ	N
$(\cdot)$	$(\cdot)$	$(\cdot)$	$(\cdot)$	$\left(\text{min}^{-1}\right)$
0.268	[0.233, 0.250]	0.241	0.095	744
0.277	[0.243, 0.272]	0.249	0.101	770
0.288	[0.251, 0.278]	0.254	0.109	800
0.300	[0.258, 0.278]	0.264	0.119	833

procedure described in the IEC Standard [8]. The rope-free zone, where no swirling flow under the runner is experienced, is represented by the blue area in the hill chart shown in Figure 5.4.

Four pressure sensors are installed in the draft tube cone of the reduced scale physical model to investigate the turbine stability in full load conditions. They are equally spaced in a horizontal cross-section located at $0.4 \times D$ distance from the runner outlet, similarly to the prototype. An example of time history of pressure values and resulting c_p values for one stable and one unstable full load condition with $n_{ED} = 0.277$ is presented in Figure 5.5. In this example the clear difference between a stable and an unstable full load condition is illustrated, with a difference in Q_{ED} values of 0.019. The pressure oscillations recorded by the sensors have the same phase, evidencing the synchronous nature of the pressure oscillations in unstable conditions.

Additional measurements to determine the full load stability limits are performed at four different n_{ED} values, as listed in Table 5.1. For each n_{ED}, the range of tested Q_{ED} values starts at stable full load conditions, close to the rope-free zone, and ends at unstable conditions. The Q_{ED} values for the stability limit, the Thoma number σ and the rotational speed of the model $N = 60 \times n$ (min^{-1}) are listed in Table 5.1. The n_{ED} and σ values simulate possible variations of available specific energy on the prototype, assuming a rated downstream reservoir level. The Froude number, defined as $\text{Fr} = \sqrt{E/gD}$ $(\cdot)$, is kept constant and equal to 8.73.
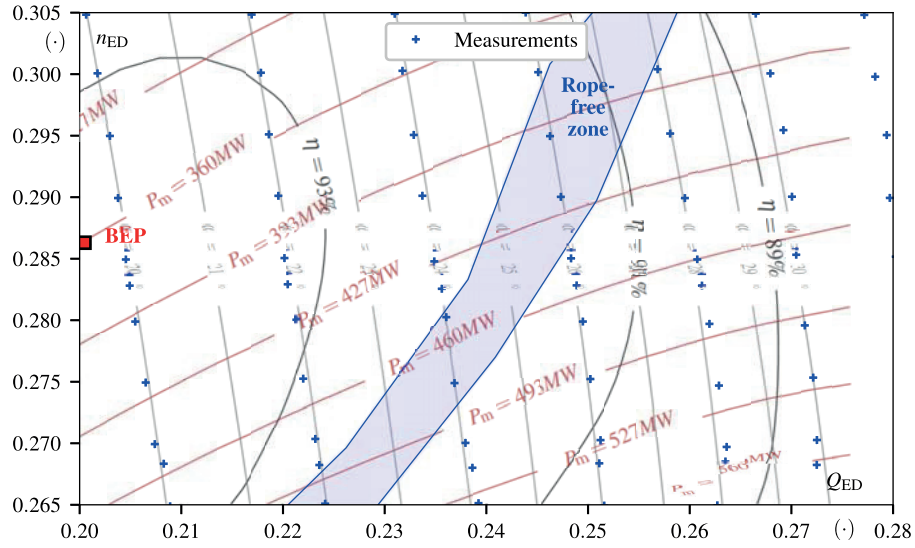
Figure 5.4 – Standard turbine hill chart as a function of Q_{ED} and n_{ED}. Test points where measurements are performed are presented and isolines of interpolated values of α, η and P_m are provided, all values transposed to the prototype scale. The rope-free zone is represented in blue.
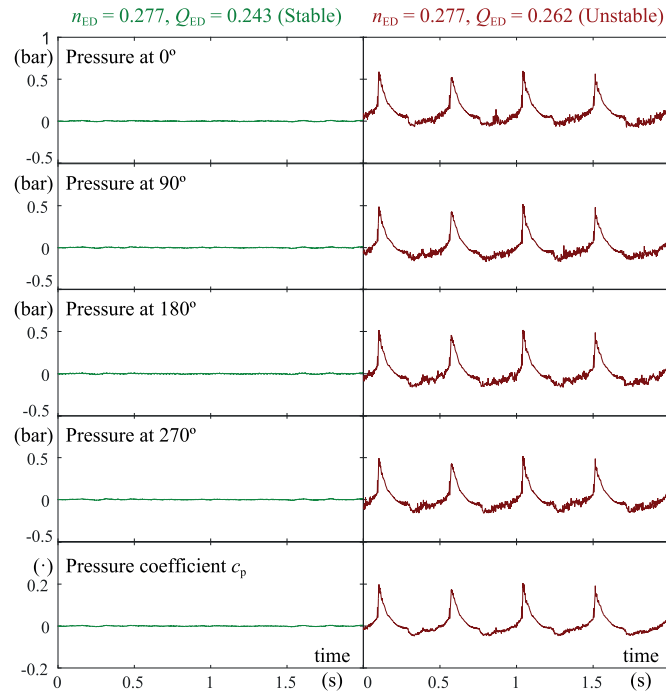
Figure 5.5 – Time history of pressure and pressure coefficient c_p values for one stable and one unstable full load condition with the same n_{ED}. The two conditions have only a small difference in Q_{ED} value, i.e., $\Delta Q_{ED} = 0.019$.
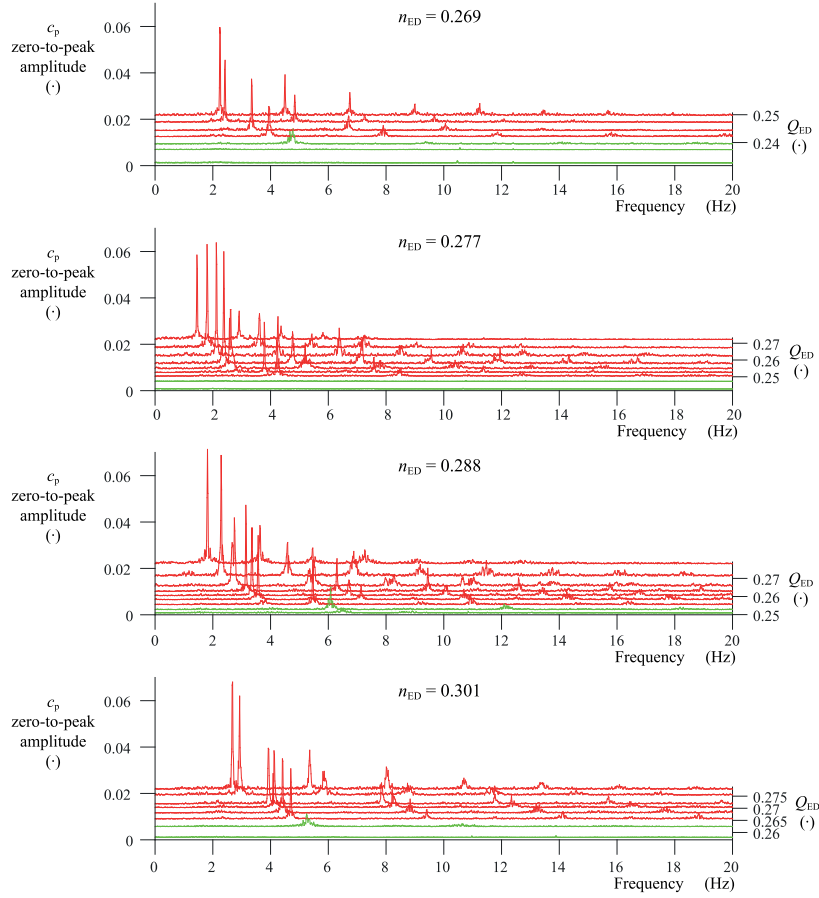
Figure 5.6 – Waterfall plots of c_p for all the tested operating conditions on the reduced scale physical model. The maximum zero-to-peak amplitude for each Q_{ED} value is also indicated.

Waterfall plots of zero-to-peak amplitudes of c_p in the frequency domain as a function of Q_{ED} for all the tested operating conditions are presented in Figure 5.6. The maximum zero-to-peak amplitude for each combination of n_{ED} and Q_{ED} values is also detailed in Figure 5.7a. Similarly, the frequency values at which the maximum zero-to-peak amplitude is calculated are detailed in Figure 5.7b, making evident the decrease in the pulsation frequency as Q_{ED} increases. Due to the self-excited nature of the vortex rope in unstable conditions, the pressure pulsation frequency values shown in 5.7b are also the first eigenfrequency, f_0, values of the complete hydraulic system. A decrease in f_0 indicate an increase in cavitation volume, as discussed in [50].

As indicated in Figure 5.7a, this paper considers as unstable full load conditions the operating conditions where the c_p signal contains in its spectrum a maximum zero-to-peak amplitude greater than 0.01, regardless of the frequency value. This amplitude value corresponds to about 20 % of the maximum zero-to-peak amplitude registered in the measurements campaign and, once this criteria is attained, the change in behavior of the c_p signal is clear as demonstrated by the example presented in Figure 5.5. Although it is possible that the real transition to
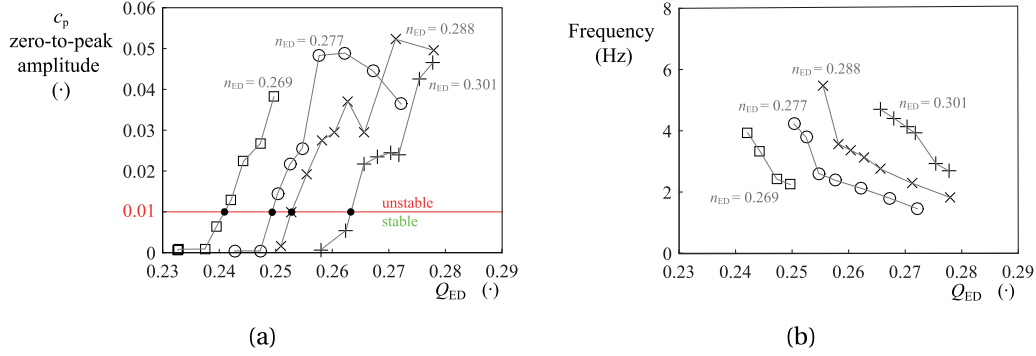
Figure 5.7 – (a) Maximum zero-to-peak amplitude value of the c_p spectrum for each tested combination of Q_{ED} and n_{ED} values, as a function of Q_{ED}. (b) Frequency at which the maximum amplitude is observed, considering only the points inside the unstable full load zone.
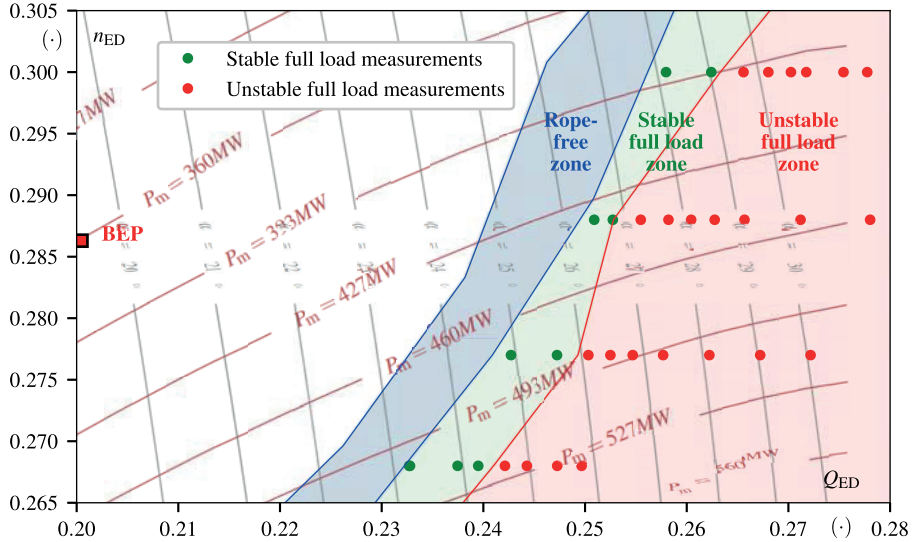
Figure 5.8 – Turbine hill chart featuring the set of measurements on the reduced scale model performed to identify the stable and the unstable full load operating conditions. Based on these measurements, zones of expected stable and unstable conditions are defined.

unstable conditions happens at a slightly lower Q_{ED} value, distinguishing the full load pressure pulsations from other types of disturbances and noise could be problematic, specially in prototype site tests.

The tested operating points described in table 5.1 are presented in the hill chart of Figure 5.8, where the isolines of P_m and α defined previously are also shown. The zones of expected stable and unstable operating conditions defined by the interpolation of the measured stability limits are presented in this new hill chart.
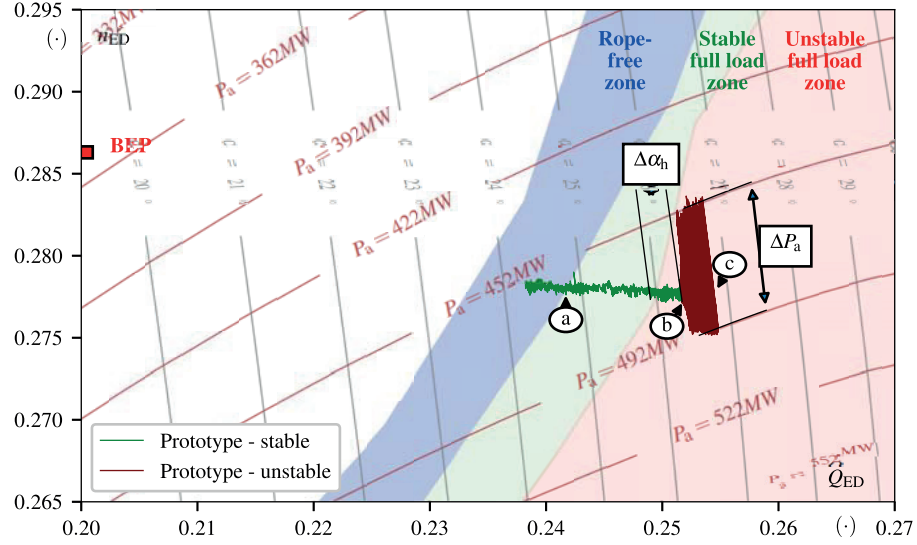
Figure 5.9 – Measured values of α and P_a on the prototype are used to locate the prototype operating conditions inside the hill chart. Only measurements in the ascending trend of guide vanes opening angle are presented, i.e., from the beginning of the time series to the instant ©.

5.4 Comparisons between reduced scale physical model and prototype

In Figure 5.9, the measured values of α and P_a on the prototype are used to locate the prototype operating conditions inside the hill chart constructed with measurements on the reduced scale physical model (see [109]). In Figure 5.9, only the measurements acquired from time $t = 0$ s to the instant indicated by © in Figure 5.2, corresponding to an ascending trend of guide vanes opening angle, are presented. Those acquired from instant © to the end of the time series, corresponding to a descending trend of guide vanes opening angle, are presented in Figure 5.10.

The prototype becomes unstable at $Q_{ED_b} = 0.252$, close to the value defined by the reduced scale physical model measurements, and comes back to a stable condition at $Q_{ED_d} = 0.249$, as illustrated in Figures 5.9 and 5.10. The difference between Q_{ED_b} and Q_{ED_d} is only $\Delta Q_{ED_h} = 0.003$. Therefore, the observed hysteresis can be considered negligible and the transition to unstable conditions, in practical terms, can be said to happen at $Q_{ED} \approx 0.251$, almost the same value measured in the reduced scale model.

The waterfall plot presented in Figure 5.11 features four spectra of the c_p measurements in the reduced scale physical model at $n_{ED} = 0.277$, together with one spectrum in the prototype with $n_{ED} = 0.278$ and $Q_{ED} \approx 0.254$. In the x-axis, the frequency values are made relative by the runner rotation frequency: $n = 2.14$ Hz for the prototype and $n = 12.83$ Hz for the reduced scale physical model. As the excited frequency values are also the eigenfrequencies of the
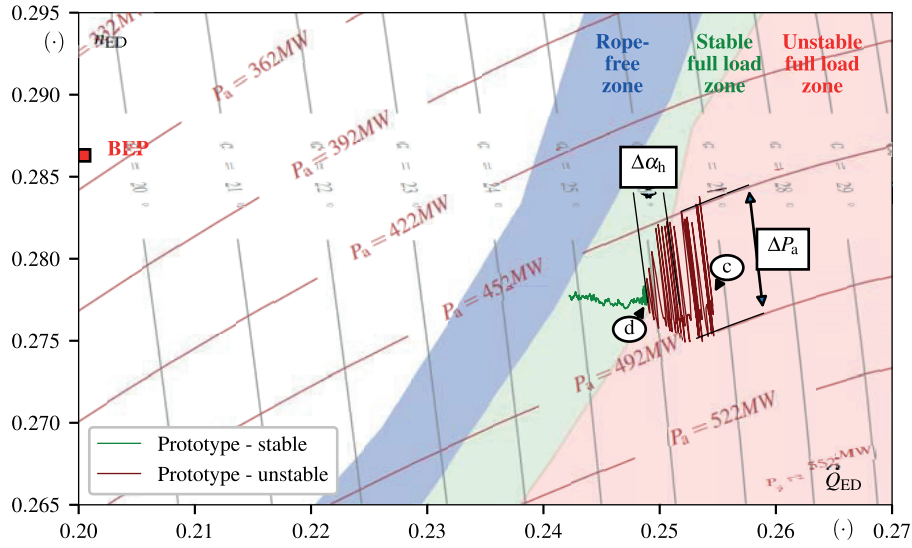
Figure 5.10 – Measured values of α and P_a on the prototype are used to locate the prototype operating conditions inside the hill chart. Only the measurements in the descending trend of guide vanes opening angle are presented, i.e., from the instant ⓒ to the end of the time series.
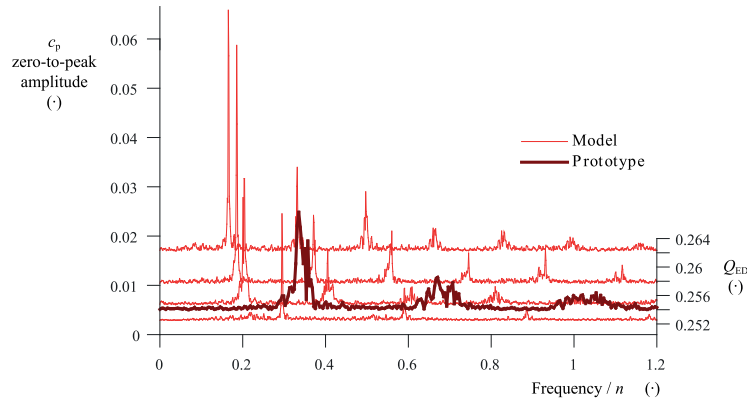
Figure 5.11 – Waterfall plot featuring the spectrum of four reduced scale model c_p measurements at $n_{ED} = 0.277$ and one spectrum from the prototype measurements at similar conditions. The excited frequencies on the prototype and on the reduced scale physical model are different.

complete hydraulic circuit, the values for the reduced scale model and for the prototype are completely different, even in relative terms.

The time history of c_p using the time divided by the pulsation period in the x-axis is presented in Figure 5.12, featuring both model and prototype measurements at approximately the same full load operating conditions, i.e., $n_{ED} \approx 0.277$ and $Q_{ED} \approx 0.254$. A similar behavior of c_p is observed when the time is made relative by the pulsation period. The c_p signals of both

Figure 5.12 – Time history of c_p for both model and prototype measurements at approximately the same operating conditions. A very similar behavior is observed when time is made relative by the pulsation period.

model and prototype feature a similar peak, followed by a second smaller peak and noise-like oscillations close to the trough. These peaks and noise-like pressure oscillations are studied in detail by A. Müller et al. in [119], where they are associated to the behavior of the cavitation vortex rope and blade cavitation through high-speed camera acquisition. The evolution of c_p in an unstable full load condition and the associated images extracted from [119] are presented in Figure 5.13.

5.5 Predicting unstable full load conditions from 1-D eigenvalue calculations

As presented in the previous section, the transition from stable to unstable full load operating conditions in the turbine prototype occurred as predicted by the reduced scale physical model in this specific test case. Nevertheless, previous research works such as [32, 120] reported other test cases where stability limits are unequal when comparing reduced scale models and prototypes. These differences can be explained by the large number of parameters affecting the full load stability limits, including for instance the geometry and the hydro-acoustic properties of the complete hydraulic circuit, which are never homologous between reduced scale model and prototype. In this section, the parameters acting on the full load stability limits are discussed and an attempt to predict the prototype full load instability by taking into account all these parameters is presented.

To identify the hydro-acoustic parameters of the cavitation vortex rope, a 1-D numerical model of the LMH PF3 test rig and the reduced scale turbine model is required. For this purpose, this paper makes use of the SIMSEN software in which mass and momentum conservation equations are modeled according to their electrical equivalent, as presented in [38, 121]. The SIMSEN components to simulate the LMH PF3 test rig proposed by Landry et al. in [50] are illustrated in Figure 5.15. The integrated dynamic behavior of the whole test rig is then simulated in time domain through a set of first order nonlinear ordinary differential equations. As detailed in [112], the eigenvalues of the complete system are calculated by performing a
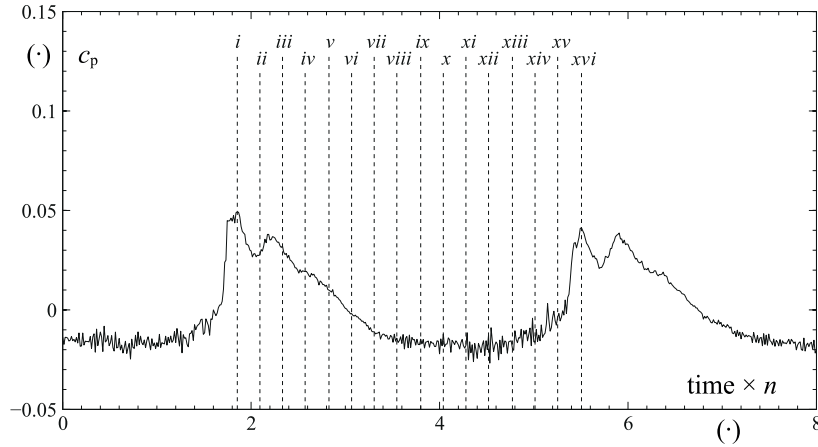
(a) Evolution of c_p as a function of time times the runner rotation frequency n
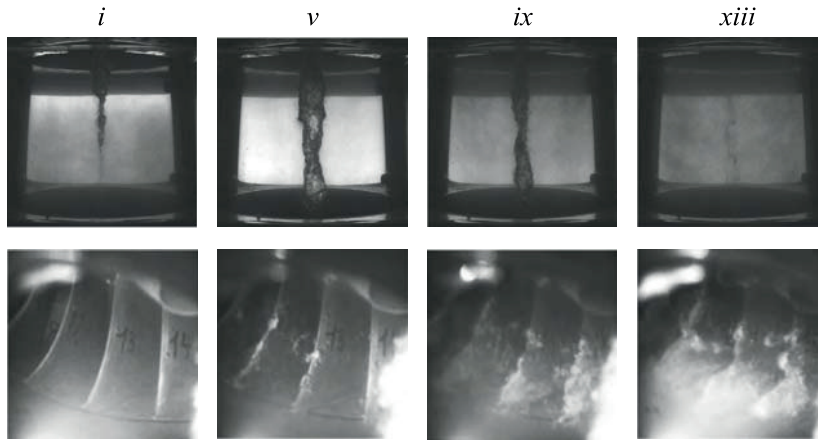
(b) Images of the draft tube cone and the runner outlet recorded with a high-speed camera.

Figure 5.13 – The evolution of c_p associated trhough imagines to the behavior of the cavitation vortex rope and blade cavitation. Research presented by Müller et al. in [119].

linear approximation of these equations.

The 1-D SIMSEN hydro-acoustic model of a cavitating draft tube cone is presented by Alligné et al. in [39]. Its T-shaped electrical equivalent is presented in Figure 5.14. In [50], Landry et al. make use of this model to calculate the eigenvalues of the LMH PF3 complete hydraulic circuit during part load conditions and extract the hydro-acoustic parameters of the cavitating vortex rope. In [54, 118], these hydro-acoustic parameters are transposed and applied in eigenvalue calculations of the prototype generating unit to predict the occurrence of pressure pulsations caused by resonance in part load conditions.

For both the reduced scale model and the turbine prototype 1-D numerical models, the draft tube is divided in two parts: the first part corresponds to the cone and the elbow, and the
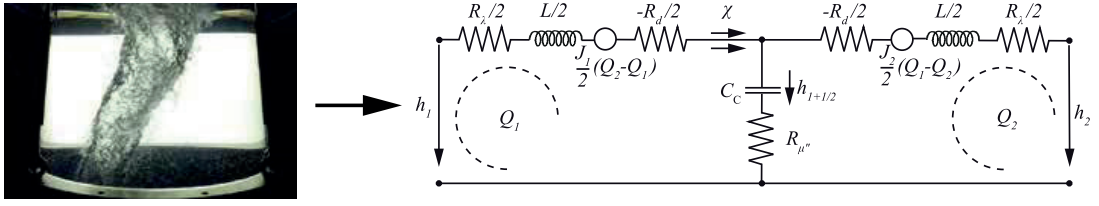
Figure 5.14 – SIMSEN hydro-acoustic model of a cavitating draft tube cone, presented by Alligné et al. in [39].
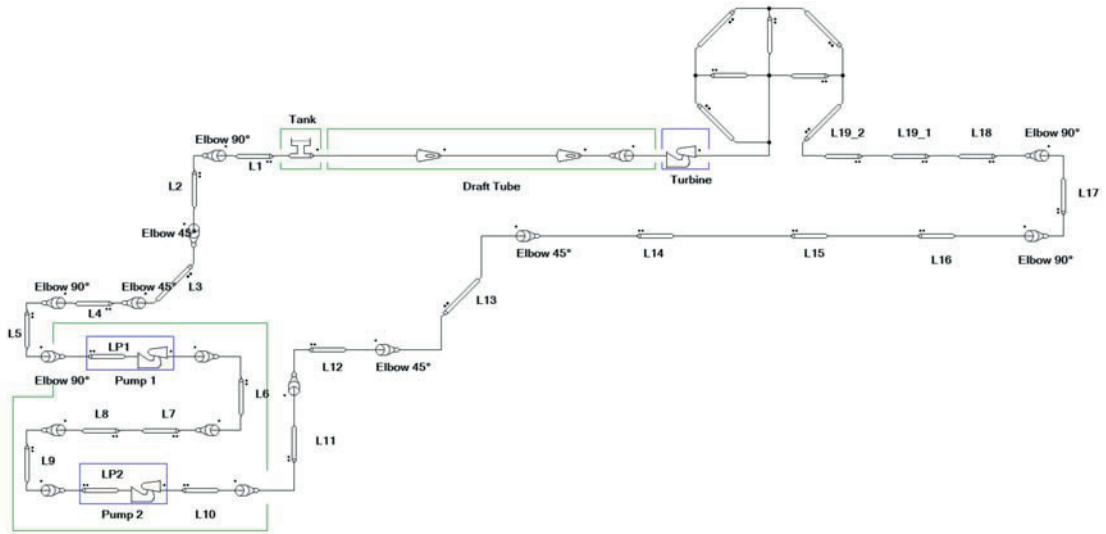
Figure 5.15 – The SIMSEN components to simulate the LMH PF3 test rig proposed by Landry et al. in [50].

second part corresponds to the diffuser. All the parameters affected by the cavitating vortex rope are assumed to be located in the first part of the draft tube, which is $2.86 \cdot D$ (m) long and is represented by 32 elements like the one in Figure 5.14.

To calculate the stability limits in full load conditions, a number of hydro-acoustic variables have to be quantified. The most relevant variables affecting the system stability and the procedures to estimate their values are summarized in Table 5.2.

Considering cavitation-free pressurized pipes, a parameter defining the energy dissipation due to volume changes is the bulk viscosity coefficient μ' (Pa·s) (see [123, 124]), combining the viscoelastic damping effects of both the fluid and the pipe wall. The bulk viscosity coefficient μ' is implemented in the SIMSEN software pipe component as described in [125]. As a reminder, the bulk viscosity is sometimes mistaken by the second coefficient of fluid viscosity, as discussed in [126, 127]. The bulk viscosity μ' is a frequency-dependent parameter (see [128, 122]) and, according to the measurement results presented by Dörfler in [122] for a given

107

Table 5.2 – Estimation procedure to define values for the most relevant hydro-acoustic variables of the SIMSEN components.

component type	variable	estimated according to
cavitation-free pressurized pipes	pressure wave speed $$a_{\mathrm{pipe}} = \left(\frac{\rho}{E_w} + \frac{\rho D_{\mathrm{pipe}}}{eE_{\mathrm{pipe}}} \right)^{-2}$$	Nicolet in [38], taking into account the pipe thickness e, the Young modulus E_{pipe}, and the water bulk modulus E_{w}.
	friction factor for distributed energy losses	measurements of pressure drop on the hydraulic circuit.
	bulk viscosity coefficient $$\mu^{I} = 2.17 \cdot 10^{6} \cdot f^{-8.79 \cdot 10^{-1}}$$	empirical relation obtained by Dörfler in [122] to estimate values of μ^{I} (Pa·s), the bulk viscosity coefficient for pressurized pipes.
draft tube cone featuring a cavitation vortex	pressure wave speed $$a_{\mathrm{cone}} = \sqrt{\frac{g V_{\mathrm{cone}}}{C_{\mathrm{c}}}}$$ $$C_{\mathrm{c}} = -\frac{\partial V_{\mathrm{c}}}{\partial h}$$ $$\Pi = \frac{\rho}{p_{\mathrm{cone}} - p_{\mathrm{v}}} \cdot a_{\mathrm{cone}}^{2}$$	reduced scale model measurements presented in the present paper and calculation procedures proposed by Landry et al. in [50].
	bulk viscosity coefficient $$\mu^{II} = M^{II} \cdot \frac{p_{\mathrm{cone}} - p_{\mathrm{v}}}{f_{0}}$$ $$M^{II} = \Pi^{2} \cdot (1 - \beta)^{2} \cdot \frac{p_{\mathrm{v}}}{\rho}$$ $$\beta = \Pi^{-1} \cdot 0.6201^{1.1585}$$	measurements, calculation results and empirical relations obtained for the same reduced scale model test case of the present paper, at part load operating conditions, presented in [50, 108].
	mass flow gain factor $$\chi = -\frac{\partial V_{\mathrm{c}}}{Q_{1}}$$	a new procedure proposed in the present paper.

test case, the bulk viscosity can be estimated as:

$$\mu^{I} = 2.17 \cdot 10^{6} \cdot f^{-8.79 \cdot 10^{-1}} \qquad (\text{Pa} \cdot \text{s}) \tag{5.5}$$

where f (Hz) is the excitation frequency.

Similarly to the damping effect related to μ^{I} in non-cavitating pressurized pipes, variations in the cavitation volume inside the cavitating draft tube cone are also expected to dissipate energy. To simulate this energy loss, a bulk viscosity coefficient for the cavitation volume, μ^{II} (Pa·s), is defined [39, 50]. The bulk viscosity coefficients μ^{I} and μ^{II} are used in the definition of the resistance located in the center of the T-shaped element — presented in Figure 5.14, for the cavitating draft tube component — as detailed in eq. (5.6) and eq. (5.7), respectively.

$$R_{\mu I} = \frac{\mu^{I}}{\rho g \, dx A_{\text{pipe}}} \qquad \text{for pressurized pipes} \tag{5.6}$$

$$R_{\mu II} = \frac{\mu^{II}}{\rho g \, dx A_{\text{cone}}} \qquad \text{for the cavitation vortex in the draft tube cone} \tag{5.7}$$

where dx (m) is the length of the SIMSEN element, A_{pipe} is the pipe element cross-section area and A_{cone} is the cone element cross-section area.

The capacitance term present in the center of the T-shaped element of the cavitating draft tube, equal to C_{c} (m^2) and known as the cavitation compliance, is related to the local pressure wave speed a as in eq. (5.8).

$$C_{\text{c}} = -\frac{\partial V_{\text{c}}}{\partial h} = \frac{g \, dx A_{\text{cone}}}{a^2} \tag{5.8}$$

where V_{c} (m^3) is the cavitation volume and h (m) is the local piezometric head.

Landry et al. presented in [50] a procedure to determine μ^{II} and a in part load conditions, for the same test case discussed in this paper. A faster procedure to identify a in reduced scale physical models through dynamic modal analysis of the test rig is presented by Favrel et al. in [51]. Landry et al. also proposed non-dimensional numbers for these two parameters, defined as in eq. (5.9), and a relation between these two numbers expressed in eq. (5.10). An empirical relation between β and Π is proposed by Landry et al. as in eq. (5.11)

$$\text{M}^{II} = \frac{\mu^{II} f_0}{p_{\text{cone}} - p_{\text{v}}} \qquad \Pi = \frac{\rho a^2}{p_{\text{cone}} - p_{\text{v}}} \tag{5.9}$$

$$\text{M}^{II} = \Pi^2 \cdot (1 - \beta)^2 \cdot \frac{\rho_{\text{v}}}{\rho} \tag{5.10}$$
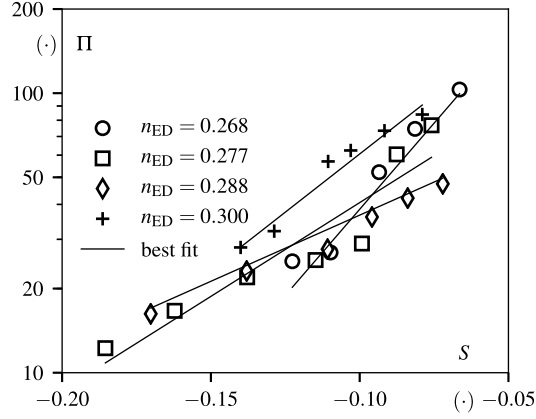
Figure 5.16 – Π values obtained from measurements on the reduced scale physical model. The best fit functions are detailed in A.7.

$$\beta = \frac{0.6201^{1.1585}}{\Pi} \tag{5.11}$$

As presented in [50], by matching measured and calculated values of f_0, the pressure wave speed a in the cavitating draft tube cone is identified. From the calculated a value, values of Π, β and μ'' are determined making use of equations (5.9), (5.10) and (5.11). The the obtained Π values are presented in Figure 5.16 as a function of the swirl number S. They are approximated by exponential equations detailed in A.7 and obtained through a best fit procedure. The swirl number S, defined first by Gupta et al. in [18] as the ratio between the axial flux of angular momentum and the axial flux of axial momentum, is calculated as in eq. (5.12) proposed by Favrel et al. in [19].

$$S = n_{\mathrm{ED}} \frac{\pi^2}{8} \left(\frac{1}{Q_{\mathrm{ED}}} - \frac{1}{Q_{\mathrm{ED}_0}} \right) \tag{5.12}$$

where Q_{ED_0} is the Q_{ED} value at the rope-free condition for the same n_{ED} value at which S is being calculated.

The mass flow gain factor χ (s) is defined as in eq. (5.13) (see [28, 44]). While the bulk viscosity contributes to the energy dissipation and the system stability, χ acts as a destabilizing factor in full load conditions [129]. A new procedure to define values for χ and transpose it to other operating conditions or from the reduced scale model to the prototype scale is presented in the following sections. Additionally, making use of the hydroacoustic variables mentioned in Table 5.2, eigenvalue calculations are used to predict unstable full load operating conditions

on the reduced scale model and on the prototype.

$$\chi = -\frac{\partial V_{\mathrm{c}}}{\partial Q_1} \tag{5.13}$$

where Q_1 is the discharge at the turbine runner outlet.

5.5.1 Predicting unstable conditions on the reduced scale physical model

Eigenvalue calculations are performed for the reduced scale physical model and the transition from stable to unstable conditions is given by the real part of the first eigenvalue, $\mathrm{Re}\left(\lambda_0\right)$. The operating conditions with $\mathrm{Re}\left(\lambda_0\right) > 0$ have a positive modal damping and are, consequently, unstable whereas those with $\mathrm{Re}\left(\lambda_0\right) < 0$ are stable (see [112]). Π values are calculated according to the best fit approximations shown in Figure 5.16 and detailed in A.7, leading to the pressure wave speed a. The void fraction β is calculated as in eq. (5.11). After a first eigenvalue calculation assuming $\mu' = \mu'' = 0$, the obtained f_0 value is used to update the μ' value according to eq. (5.5) and the μ'' value is obtained by isolating μ'' in eq. (5.9). With the updated values of μ' and μ'', the system eigenvalues are recalculated. Complete convergence is assumed when the difference between consecutive calculated values of $f_0 = \mathrm{Im}\left(\lambda_0\right)/2\pi$ is lower than 0.1 Hz, as illustrated in the flowchart of Figure 5.17.
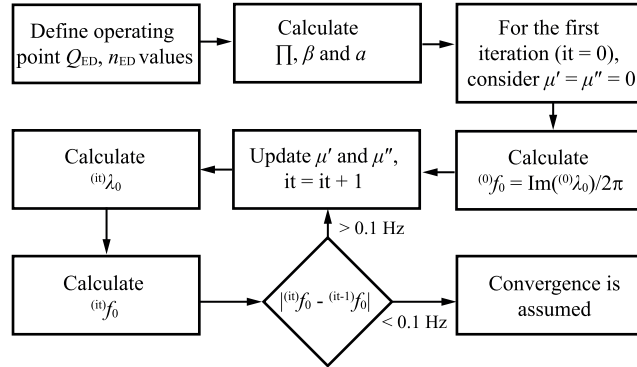
Figure 5.17 – Procedure flowchart for the calculation of λ_0 and f_0. Complete convergence is assumed when the difference between consecutive calculated values of f_0 is lower than 0.1 Hz.

A reference value of mass flow gain factor is defined: $\chi = \chi_{\mathrm{M_{ref}}} = -4.15 \cdot 10^{-4}$ s. The $\chi_{\mathrm{M_{ref}}}$ value corresponds to the χ value leading to a similar measured and calculated Q_{ED} value of transition from stable to unstable full load conditions on the reduced scale model at $n_{\mathrm{ED}} = 0.277$, the n_{ED} value closest to that of the prototype during the on-site tests. From $\chi_{\mathrm{M_{ref}}}$, other values of χ for the reduced scale physical model at different Q_{ED} and n_{ED} conditions are calculated as in eq. (5.14). The eq. (5.14) is derived by assuming a cavitation vortex in a straight pipe, as detailed in A.8.

$$\chi_{\mathrm{M}} = \chi_{\mathrm{M_{ref}}} \cdot \left(\frac{U_{\mathrm{M_{ref}}}}{U_{\mathrm{M}}}\right)^3 \cdot \frac{\left(p_{\mathrm{cone}} - p_{\mathrm{v}}\right)_{\mathrm{M}}}{\left(p_{\mathrm{cone}} - p_{\mathrm{v}}\right)_{\mathrm{M_{ref}}}} \cdot \exp\left(K_{\mathrm{M}} - K_{\mathrm{M_{ref}}}\right) \tag{5.14}$$
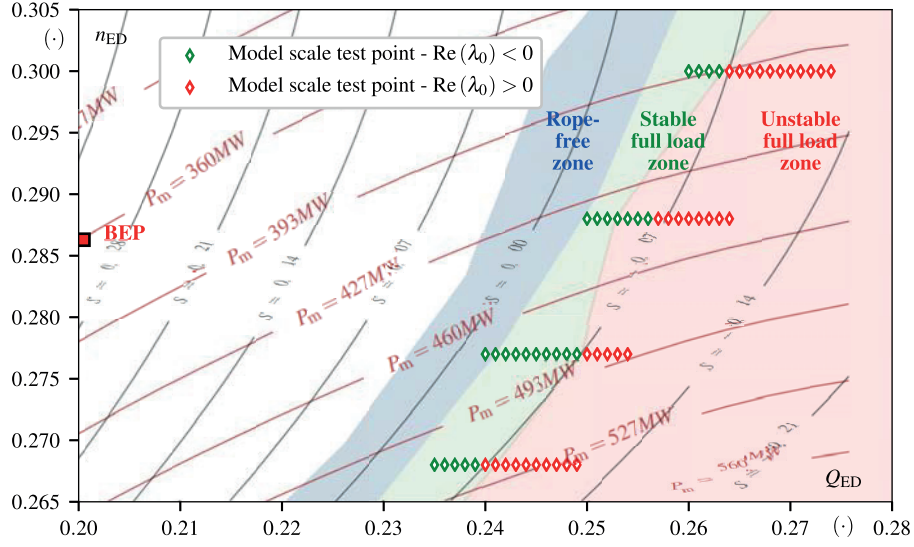
Figure 5.18 – Hill chart featuring the stable and unstable full load operating zones, defined by the measurements on the reduced scale model, and the test points where eigenvalue calculations are performed.

where $U = \pi n D$ (m·s^{-1}) is the runner peripheral speed, the subscript $_M$ refers to values for the reduced scale model and K (·) is calculated as:

$$K = \frac{2}{Cu^2} \cdot \frac{(p_v - p_{cone})}{\rho} \tag{5.15}$$

where Cu (m·s^{-1}) is the tangential flow velocity, which value is discussed in A.8.

A hill chart featuring the stable and unstable full load operating zones defined by the measurements on the reduced scale model, together with the test points where eigenvalue calculations are performed are presented in Fig 5.18. A good agreement between measured and calculated stability limits is obtained, the highest deviation being $\Delta Q_{ED} = 6 \cdot 10^{-3}$ at $n_{ED} = 0.288$. As indicated by the isolines of constant swirl number S, the transition from stable to unstable conditions is expected to occur at an approximately constant S value.

The real and imaginary parts of the first and the second eigenvalues, λ_0 and λ_1, respectively, calculated for the reduced scale physical model at $n_{ED} = 0.277$ and Q_{ED} values between 0.240 and 0.254 are presented in Figure 5.19. The Re(λ_0) value increases as the Q_{ED} increases, until unstable conditions are reached at $Q_{ED} = 0.250$, matching the experiments.

5.5.2 Predicting unstable conditions on the prototype

By following a similar procedure, χ values are transposed from the model scale, χ_M, to the prototype scale, χ_P, as in eq. 5.16. Kinematic similitude between model and prototype is
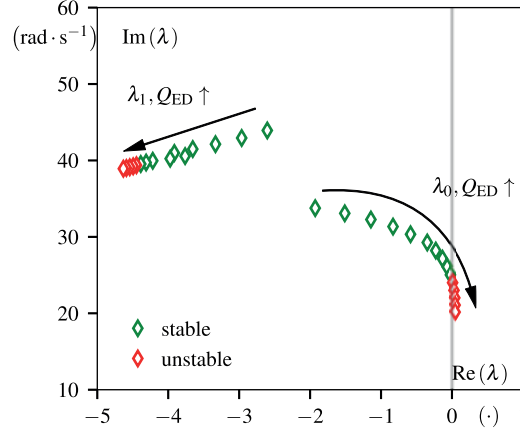
Figure 5.19 – The real and imaginary parts of the first and second eigenvalues, λ_0 and λ_1, respectively, calculated for the reduced scale physical model at $n_{ED} = 0.277$ and Q_{ED} values between 0.240 and 0.254.

considered, leading to a constant ratio Cu/U, as discussed in A.8.

$$\chi_P = \chi_M \cdot \frac{D_P}{D_M} \frac{(p_{cone} - p_v)_P}{(p_{cone} - p_v)_M} \cdot \left(\frac{U_M}{U_P}\right)^3 \cdot \exp\left(K_P - K_M\right) \tag{5.16}$$

The measured absolute pressure in the reduced scale model draft tube cone wall and the calculated values of χ_M for the reduced scale model and χ_P for the prototype on-site conditions are presented in Figure 5.20. The wall pressure of the prototype draft tube cone remained approximately constant and equal to 1.99 bar during the tests.

The prototype eigenvalues are initially calculated by following the same procedure applied for the reduced scale model to determine a, μ' and μ'' and by making use of the SIMSEN components illustrated in Figure 5.21. The results lead to a predicted transition to unstable conditions at $Q_{ED} = 0.242$, a value 3.2% lower than the measured value. By assuming $\mu' = 4 \cdot \mu'_0$, where μ'_0 is the value obtained with eq. (5.5), the calculated transition from stable to unstable condition occurs at $Q_{ED} = 0.245$, a value 2% lower than the measured value. This greater bulk viscosity coefficient value corresponds to the upper uncertainty limit for eq. (5.5), predicted by Dörfler in [122]. As the results obtained assuming $\mu' = 4 \cdot \mu'_0$ on the prototype are more accurate, this value is considered in the following eigenvalue calculations and numerical simulations presented in this paper.

The real and imaginary parts of the calculated first and second eigenvalues, λ_0 and λ_1, of the prototype for Q_{ED} values between 0.240 and 0.254 are presented in Figure 5.22. The calculated stable and unstable test points for the prototype generating unit are presented in the hill chart of Figure 5.23, together with the measurements performed in a descending trend of guide vanes opening angle.
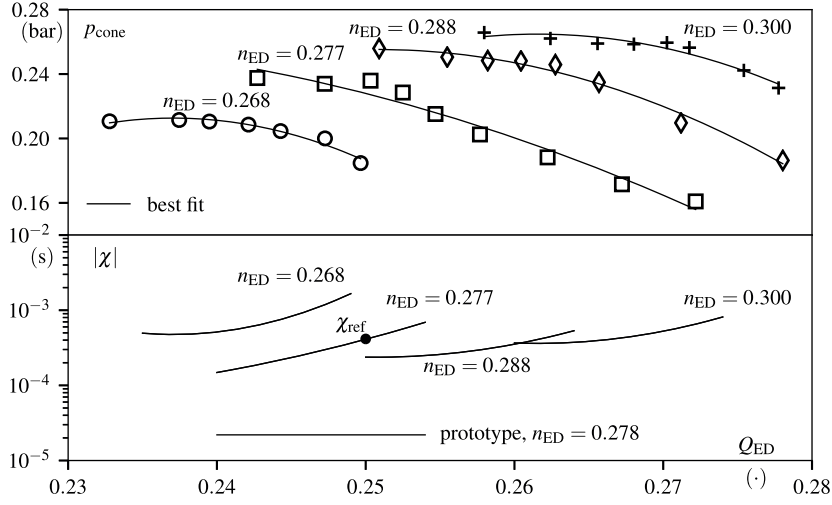
Figure 5.20 – Absolute pressure in the draft tube cone of the reduced scale model (top) and calculated values of $|\chi|$ for the model and prototype (bottom), for each tested n_{ED} value.
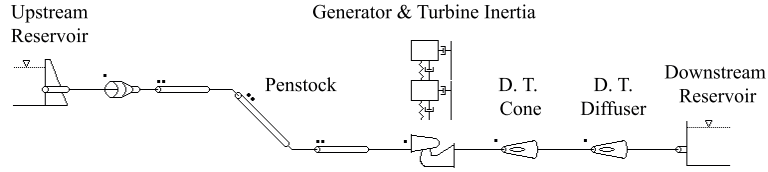
Figure 5.21 – SIMSEN components to calculate the eigenvalues of the prototype generating unit.

5.6   1-D transient numerical simulations

Simulations of the prototype are performed in the time domain to verify the capability of the 1-D numerical model to simulate the self-excited behavior of unstable full load conditions and to estimate the pressure pulsations amplitude. Therefore, the non-linear behavior of the pressure wave speed in the draft tube cone a and the bulk viscosity coefficient μ'' are taken into account: a and μ'' values are adjusted every time step $\Delta t = 10^{-3}$ s according to the calculated local pressure variation, as detailed in eq. (5.17) and eq. (5.18).

$$a(t) = \left[\frac{\Pi}{\rho} \cdot \left(\bar{p}_{\text{cone}} + \Delta p(t) - p_{\text{v}} \right) \right]^{0.5} \tag{5.17}$$

$$\mu''(t) = \text{M}'' \cdot \frac{\bar{p}_{\text{cone}} + \Delta p(t) - p_{\text{v}}}{f_0} \tag{5.18}$$

114

where $\bar{p}_{\mathrm{cone}}$ (Pa) is the mean pressure measured in the prototype draft tube cone wall and $\Delta p(t)$ (Pa) is the pressure variation calculated during the transient simulation. Π is calculated with the best fit equation for $n_{\mathrm{ED}} = 0.277$ detailed in A.7 and M'' is calculated with eq. (5.10).

To create a small disturbance and excite the first eigenmode of the prototype, an excitation pressure head $S_{\mathrm{h}}(t)$ (m) is introduced for a few seconds in the last element of the draft tube
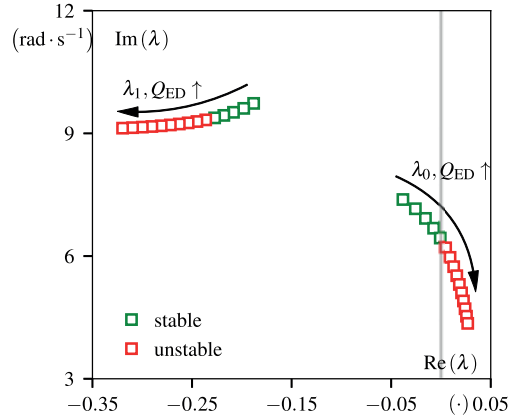
Figure 5.22 – Real and imaginary parts of the calculated first and second eigenvalues, λ_0 and λ_1, of the prototype for Q_{ED} values between 0.240 and 0.254. The transition to unstable conditions occurs at $Q_{\mathrm{ED}} = 0.245$.
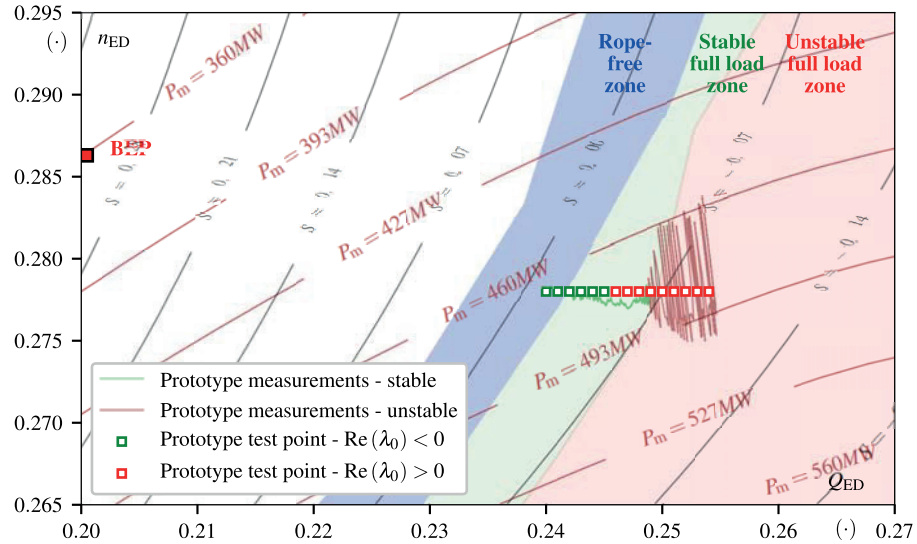
Figure 5.23 – Calculated stable and unstable test points for the prototype generating unit. Measurements on the prototype with a descending trend of guide vanes opening angle are also illustrated.
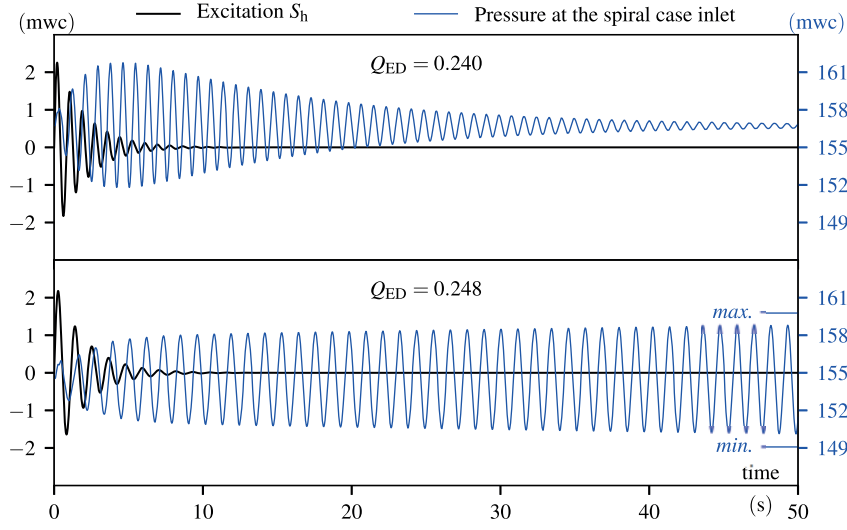
Figure 5.24 – Time history of the temporary excitation and of the calculated pressure head at the prototype spiral case inlet during the transient simulations. Results are presented for a stable and an unstable Q_{ED} value at $n_{ED} = 0.278$.

elbow, as expressed as in eq. (5.19).

$$S_h(t) = 2.5 \cdot e^{-0.5t} \cdot \sin(2\pi f_0 t) \tag{5.19}$$

The time history of S_h and of the calculated pressure head at the spiral case inlet during the transient simulations are presented in Figure 5.24. For the transient simulation at $Q_{ED} = 0.240$, the excitation source excites the system first eigenmode, but the pressure oscillations are quickly damped due to the energy losses. For the simulation at $Q_{ED} = 0.248$, the pressure oscillations slowly increases with time and enters in a self-exciting behavior, as observed in the unstable full load measurements. After time $t \approx 200$ s, a constant pressure oscillations amplitude is reached, as indicated by the maximum and minimum pressure values shown for $Q_{ED} = 0.248$ in Figure 5.24.

The discharge factor Q_{ED} equal to 0.248 is chosen for the transient simulation as its difference from the calculated Q_{ED} value of transition from stable to unstable conditions is $\Delta Q_{ED} = 0.003$. It is the same ΔQ_{ED} value measured on the prototype at the instant indicated by ⓒ in Figure 5.2. The calculated maximum pressure pulsations amplitude at the spiral case inlet during the transient simulations at $Q_{ED} = 0.248$ is 10.7 m. The pressure pulsations measured on the prototype at ⓒ have approximately 14 m of peak-to-peak amplitude.

5.7 Conclusions

To accommodate new renewable energy sources such as solar and wind, growing attention has been given to the possibility of extending the operating range of hydropower plant generating units. However, there are safety limits while extending the operating range of Francis turbines: in full load conditions the generating unit may move from a stable to an unstable condition, resulting in large power swings and pressure oscillations. For a given test case, this paper presented measurements on both the reduced scale physical model and the turbine prototype to compare their operating conditions of transition from stable to unstable full load conditions. Additionally, a procedure to predict this transition while taking into account all the relevant hydro-acoustic parameters defining the system stability is presented. The procedure requires measurements on the reduced scale physical turbine model and 1-D eigenvalue calculations.

A first set of measurements on the reduced scale model is used to construct a standard hill chart where values of efficiency, mechanical power and guide vanes angle are presented as a function of non-dimensional speed and discharge factors. A second set of measurements defines the limits at which the turbine operating condition moves from stable to unstable full load condition, for given values of σ and Froude number. The combination of these two sets of measurement results allows drawing a new hill chart featuring zones of stable and unstable full load operating conditions on the reduced scale model. The transition to unstable conditions is noted to occur at an approximately constant swirl number value.

For a similar n_{ED} value, comparisons in time and in frequency domain between the draft tube cone pressure coefficient signal recorded in unstable conditions on the model and on the prototype are presented. The behavior of their pressure coefficient signal inside each pressure pulsation period is similar, giving a clear indication that the reduced scale physical model properly reproduces the physical mechanisms behind the full load instability observed on prototypes.

The transition from a stable to an unstable full load condition on the prototype occurs as predicted by the measurements on the reduced scale model. However, stability limits in full load condition are a function of a large number of factors, such as the hydraulic circuit layout, the overall energy losses and the pressure wave speed values. These differences may lead to different stability limits when comparing reduced scale model and prototype in another turbine test case. Eigenvalue calculations are then performed to, firstly, identify the hydro-acoustic parameters for the reduced scale physical model. These parameters are transposed to the prototype scale, allowing eigenvalue calculations of the prototype generating unit. These calculations lead to a correct prediction of change from stable to unstable conditions on the prototype. However, the predicted discharge value for the transition is slightly smaller than the measured value.

Transient numerical simulations are performed to estimate the pressure pulsations amplitude on the prototype generating unit. During the transient simulations, a quasi-static approach is used to recalculate the pressure wave speed value and bulk viscosity in the cavitating draft

tube cone at each time step. After a small excitation of the system first eigenfrequency, the calculated pressure oscillations in hydraulic system are totally damped when the real part of the first eigenvalue is negative at $t = 0$. In case the real part is positive at $t = 0$, they increase with time until pressure oscillations with constant amplitude are reached. The simulations are then able to replicate the behavior of the prototype in stable and in unstable conditions, respectively. The simulation in unstable full load condition lead to a maximum pressure pulsations amplitude similar to that measured on the prototype.

As a proposal for future research works, improvements can be foreseen in the accurate calculation of:

- the bulk viscosity coefficient for cavitation-free pressurized pipes, as it requires further research to better take into account different possibilities of pipe diameters and materials;

- the bulk viscosity for the cavitating volume, as the values applied in this research work were determined in part load conditions;

- the mass flow gain factor, as it can be currently defined only at the full load stability limit and by assuming that all other variables are known and defined with accuracy.

Nevertheless, the results presented in this paper are encouraging. By increasing the accuracy in the determination of the aforementioned hydro-acoustic parameters, hill charts featuring the prototype stability limits and adaptable to any condition of Froude or Thoma number can be foreseen. These hill charts can help plant operators to define the safe operation limits of their turbines according to their current on-site conditions.

Acknowledgements and Funding

6 Performance Prediction

6.1 Introduction

As discussed in the previous chapters, the overall performance of a Francis turbine is mainly affected by two aspects: (1) the turbine complete characteristics of torque and discharge, comprising the turbine efficiency and (2) the occurrence of large power and pressure swings, caused by either part load resonance of full load instability, limiting the turbine operating range. The following items provide a short summary of how the research work presented in the previous chapters can be applied during the early specification stage of a Francis generating unit to predict its performance:

1. in *Chapter 3* an empirical model to estimate the turbine efficiency and complete characteristics is presented. In the early specification stage, this estimated efficiency allows accurate estimations of the amount of energy harnessed by the turbine in typical operating conditions. The complete characteristics can be used in transient simulations to predict overpressure and overspeed values, as detailed in Section 6.2;

2. in *Chapter 4* a methodology to accurately predict part load resonance is presented. This methodology can be applied as soon as the turbine reduced scale physical model is available, i.e., usually years before the turbine prototype commissioning. The obtained results can be further explored to assess what are the power plant designs that lead to a higher risk of presenting this type of resonance. If the risk is detected, changes in the unit preliminary design can be foreseen. This analysis is detailed in Section 6.3;

3. in *Chapter 5* a methodology to predict unstable full load conditions on the prototype is presented. Even though future research works are necessary to more accurately quantify the values for parameters such as the mass flow gain factor and the bulk viscosity, the presented methodology can be applied to evaluate the risk of the occurrence of unstable full load conditions in future projects.

The timeline illustrated in Figure 6.1 presents the stages of a hydropower plant project where
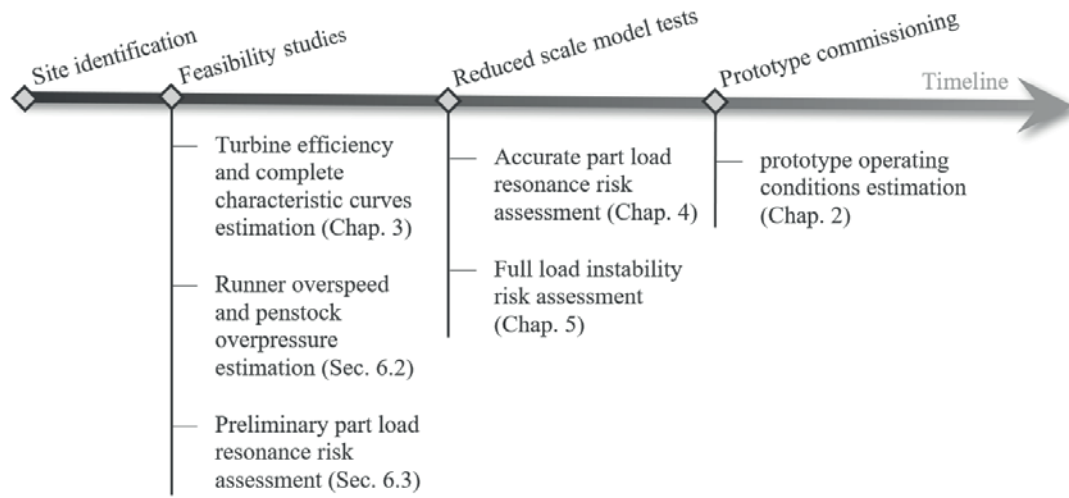
Figure 6.1 – Timeline of a hydropower plant project and applications of this thesis research work.

each chapter or section of this thesis research work is applied.

6.2 Turbine performance in emergency shut-down simulations

6.2.1 Emergency shut-down of a Francis generatin unit

An emergency shut-down consists of a sudden disconnection of the generating unit from the power grid while it operates with a given generator active power output, P_a. To illustrate the effects of an emergency shut-down on the runner blades and the complete hydraulic circuit, Trivedi et al. present in [130] measurements acquired during emergency shut-down tests performed in a reduced scale physical turbine model. Simulations of emergency shut-down on prototypes are found in [131, 132].

Once the generator is disconnected, the hydraulic energy recovered by the turbine increases the kinetic energy of the rotating parts of the generating unit. These rotating parts accelerate until a maximum speed value defined as the turbine overspeed. Simultaneously to the generator disconnection from the grid, the turbine guide vanes starts a closing procedure to avoid overspeed values that may damage the unit.

The closing procedure of the turbine guide vanes during an emergency shut-down has a secondary effect: part of the water kinetic energy in the penstock is transformed into pressure potential energy, leading to a water hammer effect [133]. The amount of overpressure generated by the water hammer effect is strictly related to the pressure wave speed in the penstock, the guide vanes closing rate and the turbine characteristics. Penstocks are designed to withstand a certain amount of water hammer overpressure, so parameters such as the

guide vanes closing rate must be chosen carefully, for instance, with the aid of 1-D numerical transient simulations.

The results from these numerical simulations are of great impact in estimating the manufacturing costs of the generating unit equipment. Overpressure values resulting from these numerical simulations will help defining the thickness of the penstock pipe walls. The estimated overspeed value becomes an input for the mechanical calculations ensuring that the rotating parts can withstand the centrifugal forces, limiting the design choices. Hydrogenerators in large hydropower units are designed to provide a certain amount of inertia for the rotating parts to keep the overspeed value inside an acceptable range. Additionally, the emergency shut-down simulations may prove the need for a surge tank, drastically increasing the costs in civil works.

Consequently, a proper estimation of the turbine characteristics is of great use in the early stage of a generating unit design. In the following sections, emergency shut-down simulations are performed making use of turbine characteristics generated with the empirical model. The results are compared either with actual prototype measurements, or with simulations performed using real turbine characteristics, obtained through measurements in the reduced scale physical model. They demonstrate that accurate predictions of overspeed and overpressure values can be obtained still during the power plant early specification stage.

6.2.2   444MW test case: validation through measurements

An emergency shut-down test is performed on the 444 MW generating unit presented previously as a test case in Chapters 1, 3 and 4. Transient simulations are performed making use of either an empirical turbine characteristics or the real turbine characteristics, obtained through reduced scale model measurements, and compared to the measurements acquired during the prototype on-site test. General information on the turbine prototype taken as an input to generate the empirical characteristic curves is presented in Table 6.1. The estimated and measured peak efficiency values are also presented.

Table 6.1 – Turbine prototype data used to generate the empirical characteristic curves.

Runner diameter	D_P	5.4 m
Runner rated rotation speed	N_rated	128.6 min^{-1}
Year of commissioning	y	1975
Turbine head at BEP	H_BEP	160 mwc
IEC speed factor at BEP	$n_\mathrm{ED_{BEP}}$	0.290 $(\cdot)$
IEC discharge factor at BEP	$Q_\mathrm{ED_{BEP}}$	0.204 $(\cdot)$
IEC specific speed	n_QE	0.131 $(\cdot)$
Estimated peak efficiency	$\hat{\eta}_\mathrm{BEP}$	95.20 %
Measured peak efficiency	η_BEP	94.19 %

The initial conditions for the present test case are listed in Table 6.2. In Figure 6.2, the time

Table 6.2 – Prototype initial conditions before the emergency shut-down.

Active power output	P_a	434 MW
Upstream researvoir level	Z_B	752.8 masl
Downstream reservoir level	$Z_{\bar{B}}$	572.4 masl
Guide vanes opening angle	α	22.4 °
Relative guide vanes opening	$\alpha_R = \alpha / \alpha_{BEP}$	1.13 ($\cdot$)
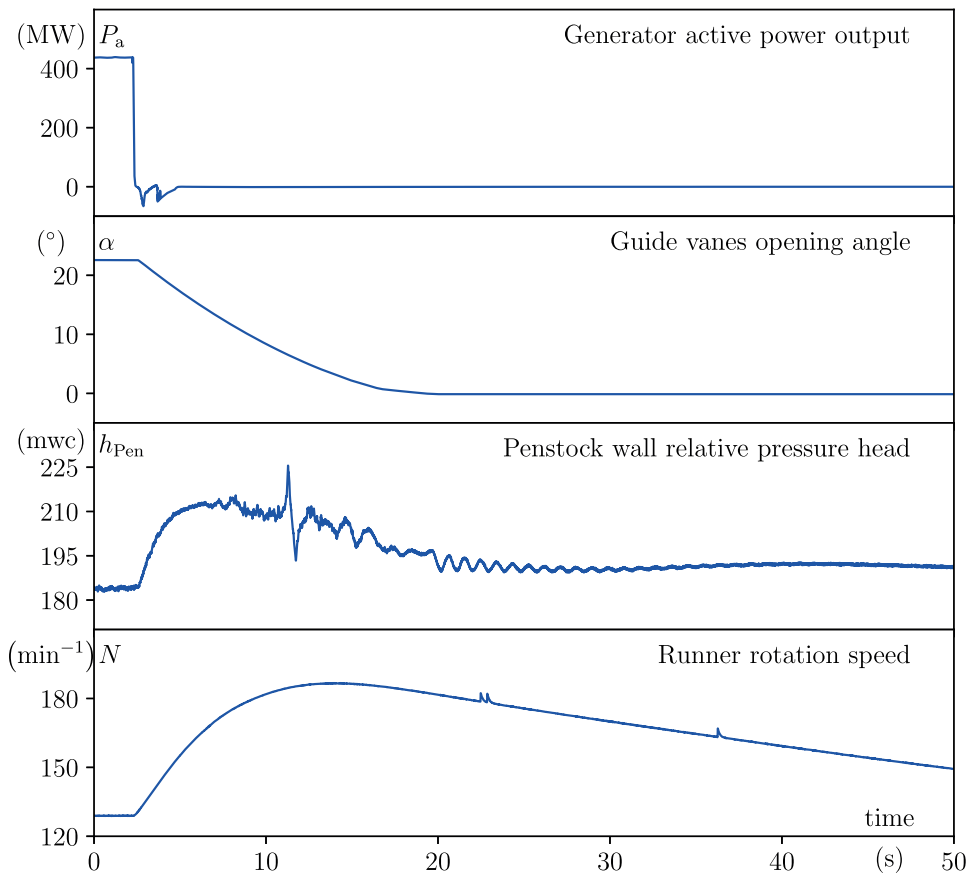
Figure 6.2 – Time history of active power output, guide vanes opening angle, penstock pressure and the runner rotation speed.

history of the active power output P_a, guide vanes opening angle α, penstock wall relative pressure head h_{Pen} and runner rotation speed N are presented. The penstock pressure is measured at 13.7 m distance to the spiral case inlet.

The 1-D SIMSEN components used for the transient simulations performed in this section are presented in Figure 6.3. Detailed information on each SIMSEN component is presented in the Appendix A.5. The initial conditions are adjusted to have the same initial P_a value as the prototype measurements. Additionally, the same closing time for the guide vanes opening

angle is imposed in the transient simulation.

The time history of measured and calculated values of penstock pressure and runner overspeed during the emergency shut-down test are presented in Figure 6.4. The time instant where the peak in the runner overspeed value is observed has a delay smaller than 2 s between the measured and the simulated values. The maximum values of penstock wall pressure and runner overspeed and the relative error between measured and calculated values are listed in Table 6.3. The low values of relative error indicate good accuracy for simulations performed using either the empirical or the real turbine characteristics.

Figure 6.3 – 1-D SIMSEN components for the transient simulations.
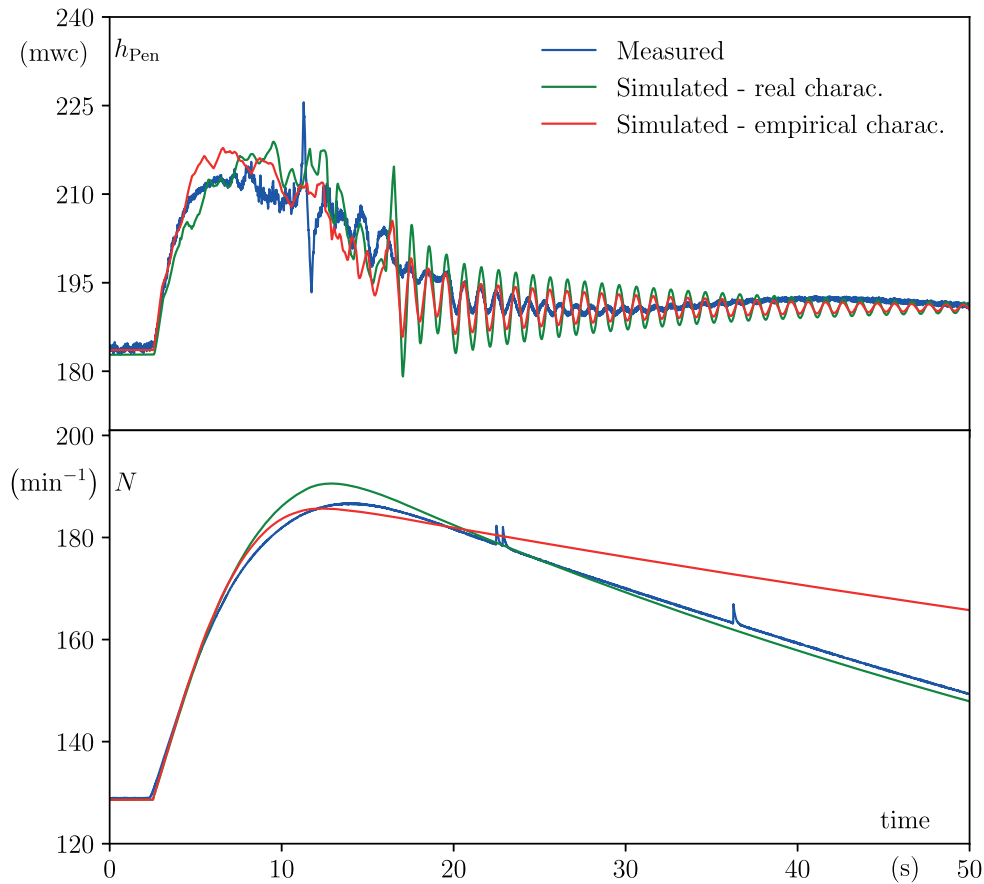
Figure 6.4 – Simulated and measured values of penstock pressure and runner rotation speed.

Table 6.3 – Measured and calculated values of maximum penstock pressure and overspeed.

	Measured	Calculated (emp. charac.)	Calculated (real charac.)
Max. penstock pressure h_{Pen}	225.6 mwc	217.8 mwc	218.9 mwc
Relative error $\Delta h_{Pen}/H_{BEP}$	-	4.9%	4.2%
Max. runner overspeed N	186.6 min^{-1}	185.7 min^{-1}	190.6 min^{-1}
Relative error $\Delta N/N_{rated}$	-	0.7%	-3.1%

The empirical turbine characteristics applied in the simulations are generated assuming $\theta_{80_{BEP}}$ equal to the mean $\theta_{80_{BEP}}$ value among those in the LMH database, as described in Section 3.3.2. A slightly different curvature is noted between empirical and real characteristic curves in the turbine break zone is noted, with the real characteristics being more curved at low guide vanes opening values.

In Figure 6.5, the empirical and the real turbine characteristics of Q_{ED} and T_{ED} are presented. The path of Q_{ED} and T_{ED} values calculated during the transient simulation is also indicated and good similarity between them is noted.
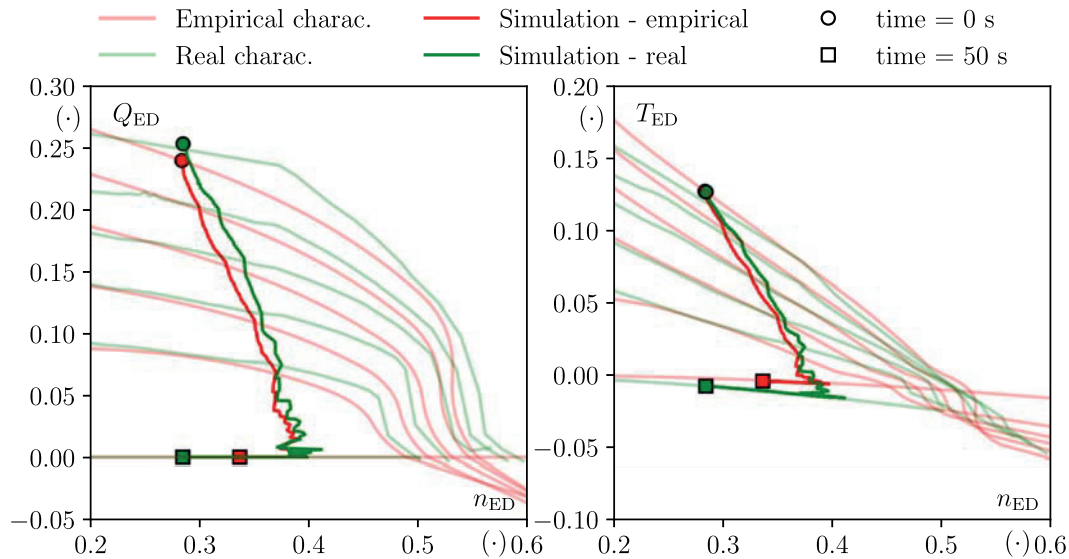
Figure 6.5 – Empirical and real turbine characteristics and the path of calculated n_{ED} and Q_{ED} values during the transient simulation.

6.2.3 Test cases with varying n_{QE} values

To validate the method for empirical turbine characteristics generation in a wide range of n_{QE} values, emergency shut-down simulations are performed for nine different real test cases. As in the previous section, simulations making use of either the empirical characteristics or the

real turbine characteristics are performed. The turbine mechanical power and net head in the best efficiency conditions are listed in Table 6.4, along with the turbine specific speed, the penstock length and the penstock diameter. Whether or not the hydraulic circuit of the test case power plant presents a surge tank is also indicated in Table 6.4. Test cases are ordered with ascending values of n_{QE}.

The test case number 4 is the same generating unit presented in the previous section, but operating under different initial conditions. All the other test cases feature Francis turbines that are not part of the LMH database and were not used in the construction of the empirical model.

Table 6.4 – Turbine power and net head in the BEP, along with the turbine specific speed and general information on the generating unit hydraulic circuit.

Test number	n_{QE} (·)	$P_{m_{BEP}}$ (MW)	H_{BEP} (mwc)	D_{Pen} (m)	L_{Pen} (m)	Surge tank?
1	0.094	72	270	3.5	310	yes
2	0.105	5	105	3.0	400	yes
3	0.110	18	100	5.0	360	yes
4	0.132	340	160	6.7	350	no
5	0.138	12	80	0.8	1500	no
6	0.145	25	100	5.0	360	yes
7	0.157	8	80	1.5	160	yes
8	0.187	16	85	2.4	260	yes
9	0.260	80	60	6.6	180	no

The time history of calculated relative turbine net head H/H_{BEP} and guide vanes opening angle α/α_{BEP} values during the emergency shut-down simulations are presented in Figure 6.6. Knowing that the downstream reservoir water level is constant, the turbine H reflects the pressure in the penstock outlet. During the guide vanes closing procedure, a very similar time history of H values is noted between simulations with the real and the empirical characteristics. Only test case number 8 presented a noticeable higher overpressure in the first seconds of the guide vanes closing time. During the final moments of the guide vanes closing procedure, simulations with the real characteristics for test cases number 1, 5 and 8 present a peak in H values, followed by high amplitude oscillations after the guide vanes are closed. This peak and the pressure oscillations can be a result of an insufficient number of available characteristic curves with low α values in the real characteristics. However, this hypothesis cannot be verified at the moment.

The time history of calculated relative runner rotation N/N_{rated} and guide vanes opening angle α/α_{BEP} values during the emergency shut-down simulations are presented in Figure 6.7. Considering all the nine test cases, the maximum difference of peak N/N_{rated} values between the empirical and the real characteristics is 5.1%. After the peak in runner rotation, runner rotation values obtained using empirical characteristic curves are often overestimated. This is explained by a possible overestimation in T_{ED} values once the guide vanes are closed.
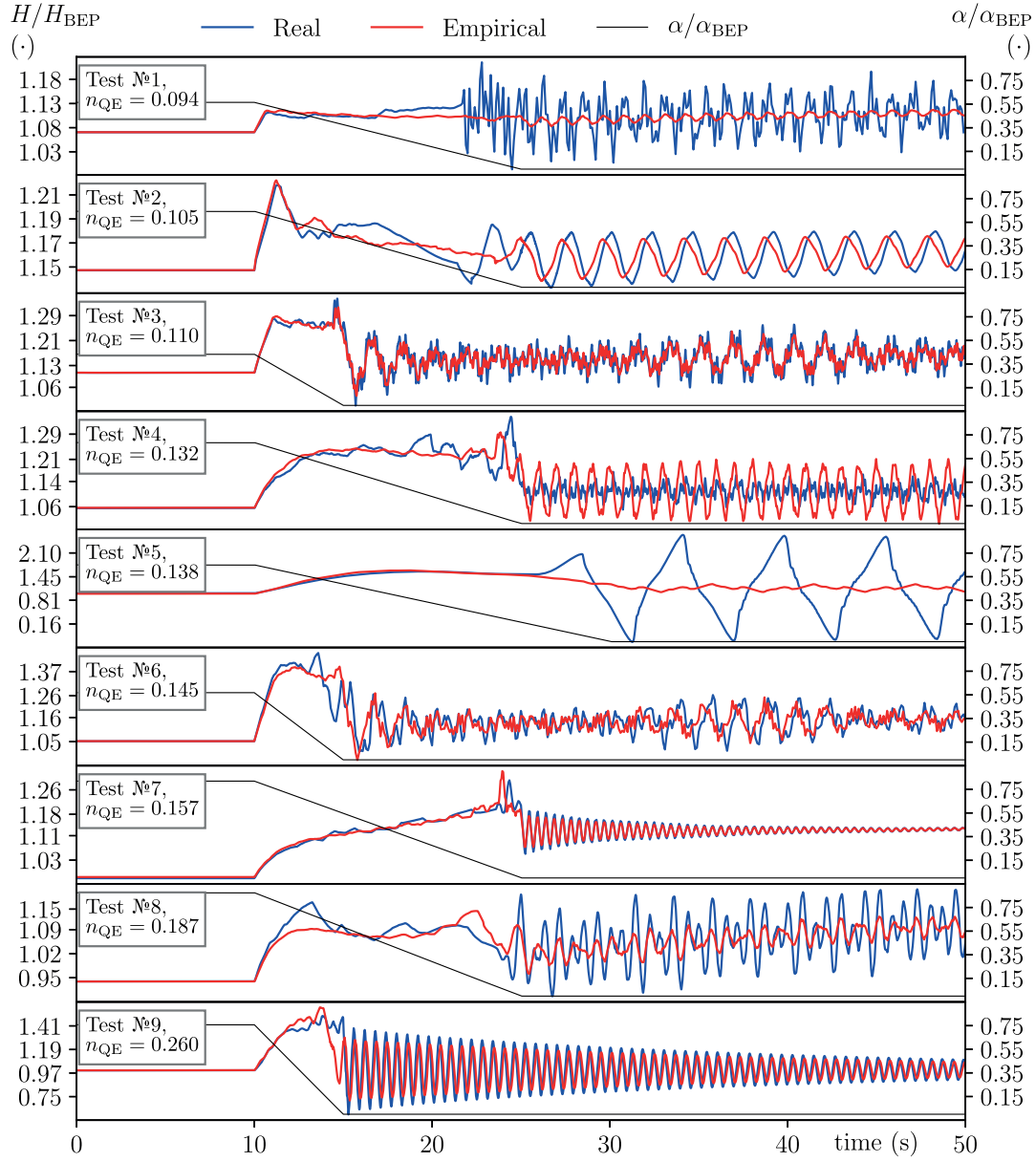
Figure 6.6 – Time history of H/H_{BEP} and α/α_{BEP} values during an emergency shut-down for the nine test cases described in Table 6.4
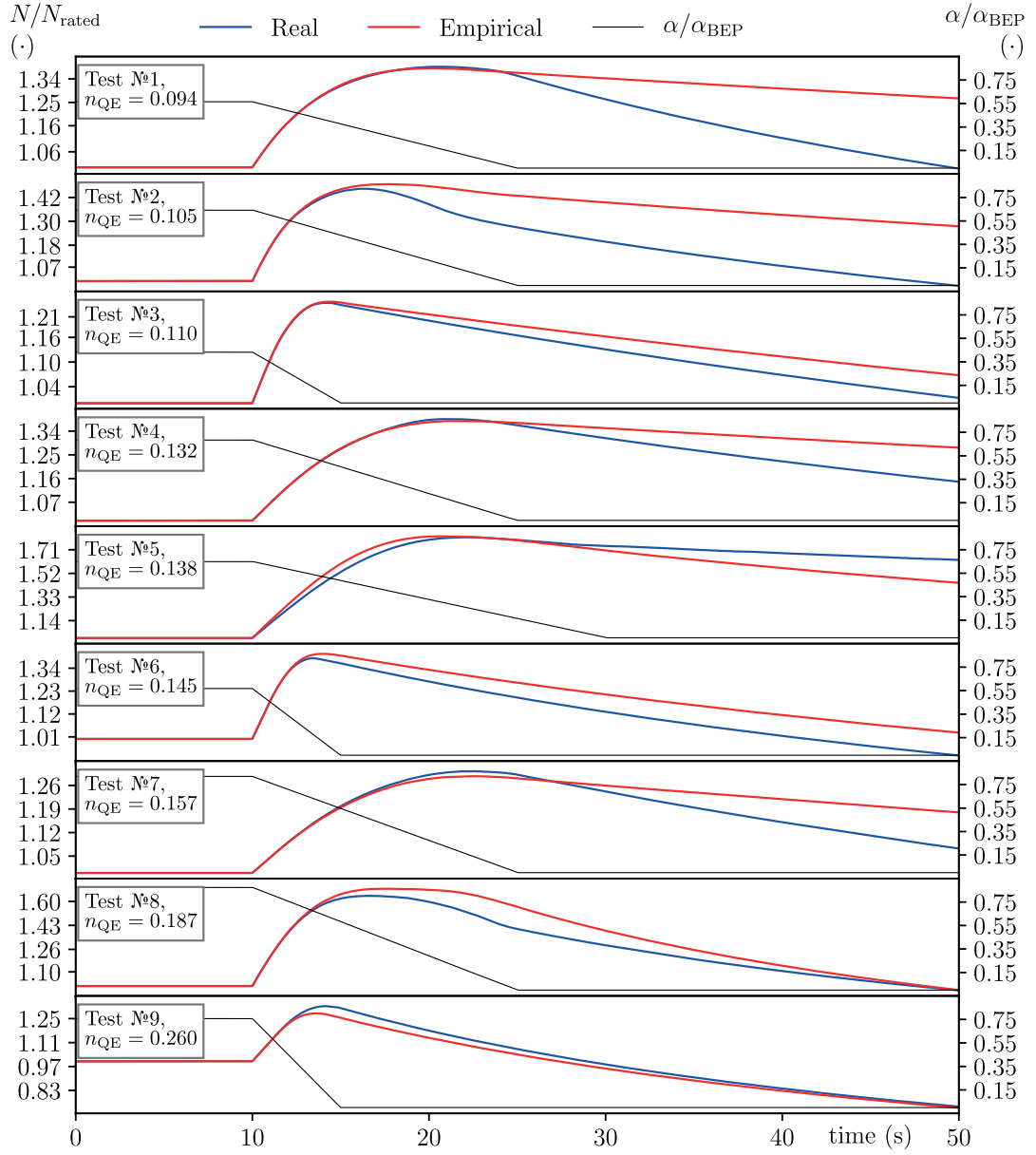
Figure 6.7 – Time history of N/N_{rated} and α/α_{BEP} values during an emergency shut-down for the nine test cases described in Table 6.4

6.3 Assessing the risk of part load resonance

6.3.1 Introduction

This section contains excerpts from the paper *Part Load Resonance Risk Assessment of Francis Hydropower Units* presented at the 13th European Turbomachinery Conference in Lausanne-Switzerland, having this thesis author as its first author.

A complete methodology to accurately predict resonance phenomena between the excitation generated by the part load vortex rope core precession movement and the hydraulic circuit first eigenfrequency of a given power plant generating unit was presented in Chapter 3. The same methodology can be applied to other test cases, but it requires first the design definition of the Francis turbine, followed by the manufacturing and testing of its reduced scale physical model.

During preliminary studies of a hydropower plant project, neither the design nor the reduced scale physical turbine model are available. Usually, decisions are taken regarding the Francis turbine design and the generating unit hydraulic circuit without a proper risk assessment of the possibility of hydro-acoustic resonances. One example of this type of assessment is performed by Nicolet et al. in [113].

This section proposes a procedure to estimate what are the hydropower projects that have a higher risk of presenting part load resonance phenomenon. For this purpose, the hydroacoustic properties of the cavitating vortex rope obtained from the measurements presented previously in Chapter 3 are taken as a reference. These reference values are assumed to be representative to any Francis turbine design. They are then transposed and applied to a large number of power plant configurations where typical values of turbine runner diameter and rotation speed are derived [134].

Two possibilities for the penstock are assumed: a long penstock with low wave speed and a short penstock with high wave speed, as the hydroacoustic properties of most power plants fall in between these two cases. Finally, eigenvalue calculations are performed assuming different discharge values in part load conditions. In case the first eigenfrequency can match the vortex rope excitation frequency, the hypothetical power plant project is identified as having a higher risk of resonance.

The final aim of this study is to help engineers working in the early specification stage of a given hydropower plant project to assess if a part load resonance phenomenon is likely to occur. A given range of turbine rated head and rated discharge values is identified as having higher risk of presenting part load resonance. If a given turbine design falls inside this range, the present study may justify the investment in further investigations — such as the one performed in Chapter 3 — once detailed information on the hydraulic circuit and the final turbine design are available. Detecting and mitigating the risk of resonance in the early specification stage may reduce future operational costs, as it can avoid a reduction in the turbine operating range

or the necessity of air injection.

6.3.2 Pressure wave speed and C_c values

As demonstrated by Nicolet in [38], the pressure wave speed inside a cavitation-free pressurized pipe is calculated as:

$$a = \left(\frac{\rho}{E_{\text{water}}} + \frac{\rho D}{e E_{\text{pipe}}} \right)^{-0.5} \tag{6.1}$$

where E_{water} is the water bulk modulus, D is the pipe diameter, e is the pipe thickness and E_{pipe} is the pipe material Young modulus. Typical values of pressure wave speed in steel-lined penstocks are between 1000 m·s^{-1} and 1300 m·s^{-1} (see [135]), but lower values such as 400 m·s^{-1} are possible notably in penstocks made of polymeric material (see [136]).

Once cavitation occurs, typical wave speed values are much lower. As presented in Chapter 3, in cavitation conditions the pressure wave speed in the draft tube cone of the reduced scale model reaches values such as 15 m·s^{-1}. For the prototype, pressure wave speed values such as 60 m·s^{-1} are calculated. In these conditions, the influence of the pipe elasticity and the water bulk modulus is negligible and the pressure wave speed equation is simplified as:

$$a = \sqrt{\frac{gAL}{C_c}} \qquad C_c = -\frac{\partial V_c}{\partial h} \;\; (\text{m}^2) \tag{6.2}$$

In Chapter 3, wave speed values in the cavitating draft tube cone of the reduced scale physical model are presented as a function of χ_{nD}, S and Fr. In Figure 6.8, the corresponding values of C_c for the wave speed values at $n_{\text{ED}} = 0.288 \approx n_{\text{ED}_{\text{BEP}}}$ are presented as a function of σ, S and Fr. The presented C_c values correspond to the total cavitation compliance in the one meter long draft tube cone of the reduced scale physical turbine model.

$$\hat{f}_C = \left(-0.74291 \times S^4 + 4.46758 \times S^3 + -10.33367 \times S^2 + 10.77484 \times S + -3.67842 \right) * \exp\left(-30.98655 \times \sigma + -0.02472 \times \text{Fr}^2 \right)$$
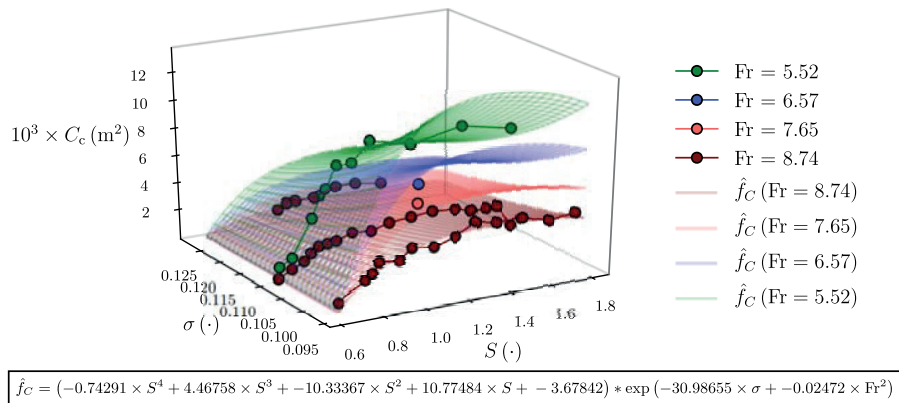
Figure 6.8 – C_c values for the cavitating draft tube cone of the reduced scale physical model at $n_{\text{ED}} \approx n_{\text{ED}_{\text{BEP}}}$

Using a non-linear least-squares method, a best fit interpolation function $\hat{f}_C(\sigma, S, \text{Fr})$ is derived from the performed measurements to estimate C_c at any operating condition in part load. The resulting $\hat{f}_C$ function shown in Figure 6.8 approximates the measured C_c values with a resulting standard error of $0.46 \cdot 10^{-3}$ m^2.

By using dimensional analysis and considering two homologous Francis turbines operating at the same conditions of Fr, S and σ, the transposition of C_c values from model to prototype scale is performed as in eq. (6.3).

$$C_{c_P} = C_{c_M} \cdot \left(\frac{D_P}{D_M}\right)^2 \approx f_C(\sigma, S, \text{Fr}) \cdot \left(\frac{D_P}{D_M}\right)^2 \tag{6.3}$$

where $f_C(\sigma, S, \text{Fr}) = \max\left[\hat{f}_C(\sigma, S, \text{Fr}), 0\right]$ in order to have $C_{c_P} = 0$ in cases where $0 < S < 0.63$, the part load S values in which no cavitation is observed. Once the cavitation compliance becomes low, the pressure wave speed is once again calculated as in eq. (6.1), which can result in a maximum pressure wave speed value equal to the speed of sound in an unbounded water medium, i.e., 1480 m$\cdot$s^{-1} approximately.

6.3.3 Procedure for risk assessment of part load resonance

Once the turbine rated head value is defined for a given generating unit, Francis turbines manufactures tend to design turbines with very similar n_{QE} value. As a consequence, other design variables such as σ_{rated} and K_u, defined as in eq. (6.4), can also be estimated empirically. Using a large database of Francis turbines, the relations between H_{rated}, n_{QE}, σ_{rated} and K_u obtained by Lugaresi and Massa [134] are presented in Figure 6.9.

$$K_u = \frac{\pi D_P N_P}{60 \left(2 g H_{\text{rated}}\right)^{0.5}} = \frac{\pi}{\sqrt{2}} n_{ED_{\text{rated}}} \tag{6.4}$$

Also according to [134], the turbine diameter D_P is properly estimated by eq. (6.5).

$$D_P = 0.44 \cdot \left(\frac{Q_{\text{rated}}}{H_{\text{rated}}^{0.1}}\right)^{0.5} \tag{6.5}$$

As a result, by knowing only H_{rated} and Q_{rated} of the Francis turbine generating unit, values of σ_{rated}, Fr_{rated} and S at part load conditions can be estimated.

By knowing that Francis turbines have very similar geometric and kinematic properties, it is assumed that the C_c values obtained with the reference test case, illustrated in Figure 6.8, are representative and can be applied to other turbines operating in the same conditions of S, σ and Fr. This assumption allows the use of eq. (6.3) to estimate the prototype cavitation compliance, C_{c_P}, in other test cases as a first approximation.

The following procedure is then applied to estimate what are the hydropower plant configurations and Francis turbine design choices that present a higher risk of resonance between
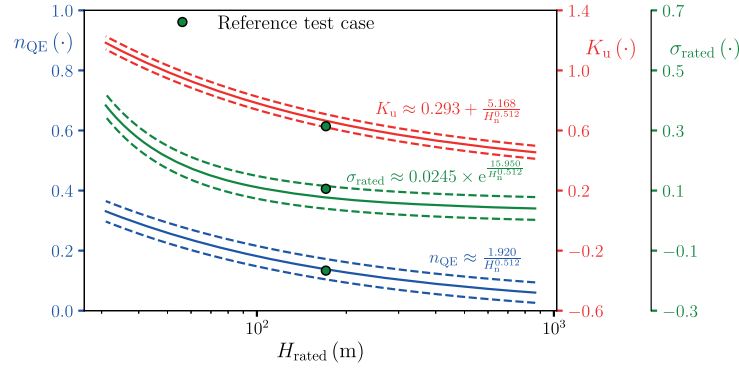
Figure 6.9 – Relations between H_{rated}, N_{q}, σ_{rated} and K_{u} obtained by [134].

the first eigenfrequency of the plant hydraulic circuit, f_0, and the excitation frequency of the vortex rope, f_{PVC}:

1. From H_{rated} and Q_{rated}, use the empirical relations proposed by Lugaresi and Massa [134] to define σ_{rated} and Fr_{rated} values. S values in part load conditions are defined by assuming Q values in the interval $\left[0.5 \cdot Q_{\text{rated}}, 0.9 \cdot Q_{\text{rated}}\right]$ and Q_{rated} equal to the swirl-free discharge;

2. Calculate $C_{\text{c}_{\text{p}}}$ using σ_{rated}, Fr_{rated}, D_{P} and the part load S values in eq. (6.3). Some extrapolation in terms of Fr and σ of the measurements range used to generate eq. (6.3) is necessary, but those are usually conditions with high Fr_{rated} or high σ_{rated} values, both leading to small C_{c} values, as captured by eq. (6.3). Operating conditions with S values greater than 1.77 are ignored as beyond this value the cavitation volume of the vortex rope becomes very unstable and incoherent, as discussed in [19]. This limitation in S values only affects a small number of high H_{rated} turbines;

3. Use the data from the previous steps in the SIMSEN 1-D components of the simplified hydropower plant hydraulic circuit, illustrated in Figure 6.10, and calculate the first eigenfrequency of the hydraulic system, f_0, for each S value;

4. Assume the vortex precessing frequency as $f_{\text{PVC}} = 0.3 \cdot N_{\text{P}}/60$. If there is a possibility of having $f_0 = f_{\text{PVC}}$, risk of resonance is predicted for this hydropower plant test case.

The length of the hydropower plant penstock has a direct impact on f_0, notably in cavitation-free conditions. Knowing that most of the plants feature penstock length values between $L = H_{\text{rated}}$ and $L = 3 \cdot H_{\text{rated}}$, these two extreme possibilities are assumed for the eigenvalue calculations. The same reasoning is applied to the pressure wave speed: the wave speed in the short version of the penstock is fixed at $a = 1480 \text{ m} \cdot \text{s}^{-1}$, equal to the wave speed in water at $20\,^{\circ}\text{C}$, while the long version of the penstock is fixed at $a = 700 \text{ m} \cdot \text{s}^{-1}$. Consequently, the short penstock case with high wave speed features greater values of f_0 than the long penstock
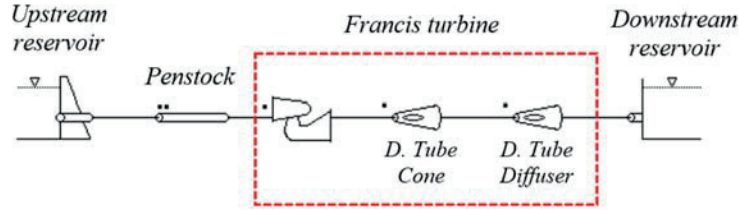
Figure 6.10 – Numerical simulation of the simplified hydropower plant hydraulic circuit.

case. In both cases, the penstock diameter is calculated as in eq. (6.6) (see [137]).

$$D = 3.55 \cdot \left(\frac{Q_{rated}^2}{2 g H_{rated}} \right)^{0.25} \quad \text{Sarkaria's equation, or}$$

$$D = \sqrt{\frac{4 \cdot Q_{rated}}{3 \cdot \pi}} \quad \text{based on a flow velocity of 3 m·s}^{-1} \tag{6.6}$$

where the lesser of the two values is taken.

In case the cavitation compliance in the draft tube cone becomes $C_{c_p} \approx 0$, the maximum value of wave speed inside the draft tube cone is assumed to be $a = 1000 \, \text{m} \cdot \text{s}^{-1}$. In the remaining parts of the draft tube where no cavitation is expected, i.e., the elbow and the diffuser, the wave speed is assumed to have a constant value of $a = 1000 \, \text{m} \cdot \text{s}^{-1}$. The turbine itself being a small part of the whole hydraulic circuit, the assumed wave speed values in non-cavitating conditions inside the turbine parts are expected to have only a small impact in the final results.

6.3.4   Risk assessment results and discussions

The described procedure is applied to a large interval of possible H_{rated} and Q_{rated} values containing all the values in which Francis turbines are normally designed. To better illustrate the results, typical f_0 curves for the short penstock case and the long penstock case as a function of Q are shown in Figure 6.11a and Figure 6.11b. The results are separated in five groups according to the position of the f_{PVC} and the f_0 curves:

- **(1)** The estimated f_{PVC} values are higher than any calculated f_0 value, for both short and long penstock cases. No risk of resonance with the first hydraulic system eigenfrequency is possible, but higher-order eigenfrequencies may be excited. These cases are outside the scope of this research work;

- **(2)** The f_{PVC} curve crosses the f_0 curve in the short penstock case only, indicating risk of resonance in this case;

- **(3)** The f_{PVC} curve crosses the f_0 curves of the short and the long penstock cases, indicating risk of resonance in both.

- **(4)** The f_{PVC} curve remains below the f_0 curve for both short and long penstock cases,

so no resonance is possible.

- **(5)** The f_{PVC} curve remains above the f_0 curve for the long penstock case and below the f_0 curve for the short penstock case. The vortex rope causes only a negligible change in the system eigenfrequencies, reducing the likelihood of a resonance phenomenon.

The interval of H_{rated} and Q_{rated} values for the five groups aforementioned are presented in Figure 6.11c. The interval in which the risk of resonance is predicted is larger for the short penstock case, as it combines the intervals indicated by (2) and (3), than the interval for the long penstock case, indicated by (3). The higher risk of resonance for the short penstock case is explained by the larger decrease in f_0 values from a cavitation-free to a cavitation condition.

Although not indicated in Figure 6.11, an interval of H_{rated} and Q_{rated} values where resonance only in the long penstock case is predicted is also theoretically possible. Nevertheless, this condition was not observed in the chosen test cases as it would represent a very small interval between groups (3) and (4).

In Figure 6.11c, the values of H_{rated} and Q_{rated} for the reference test case are illustrated, together with the H_{rated} and Q_{rated} values of three other cases described in [138, 139, 25], where part load resonance is equally observed in the prototype. These three additional cases fall inside the predicted range of risk of resonance, confirming the accuracy of the presented methodology. It is important to remind that resonant part load conditions may sometimes not lead to harmful power and pressure swings, as it depends on the intensity of the excitation source and the energy dissipation in the hydraulic circuit.

To verify the sensitivity of the results presented in Figure 6.11c to a variation in the assumed f_{PVC} value, the same calculation procedure is performed assuming $f_{PVC} = 0.2 \cdot N_P/60$ and $f_{PVC} = 0.4 \cdot N_P/60$. Only a small number of points are affected by this variation, as shown in Figure 6.12, where the test points featuring risk of resonance for the short penstock case are presented.

The following conclusions are drawn from the presented results:

1. Resonance is likely to occur in hydropower projects containing turbines designed within a certain range of rated head and rated discharge values. This range corresponds to rated head values where the turbine draft tube C_{c_p} values in part load conditions are the highest, causing *large variations of eigenfrequency values*;

2. Hydropower plants featuring a *short penstock* present a higher risk of resonance than those with long penstocks;

3. Francis units with the highest rated head values feature a part load vortex rope with precession frequency higher than the first hydraulic system eigenfrequency. *Resonance with eigenfrequencies of a higher order can occur* in these cases, but this aspect is not considered in this research work;

4. Turbines featuring a larger diameter lead to higher C_{c_p} values, causing higher variations of f_0 and increasing the risk of resonance.

It must be emphasized that the presented procedure cannot predict with certainty the occurrence of resonance in a given hydropower plant. For this purpose, the same methodology presented in Chapter 3 has to be applied for the specific test case being analyzed, including the generation of a detailed 1-D numerical model of the Francis turbine generating unit and the accurate definition of cavitation compliance values. However, performing this type of measurements is expensive and time consuming, but can be justified in case the risk of resonance is predicted. That would be the case for the three generating units with rated head and rated discharge values within the predicted range of risk mentioned in Figure 6.11c. The results presented in this section can then be seen as a guideline, showing the cases where further investigations are worth the investment.

(a)

(b)

(c)
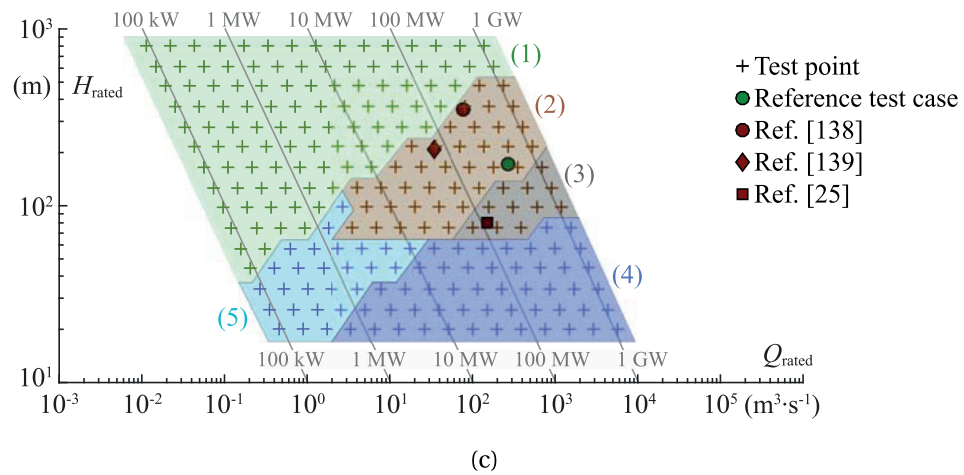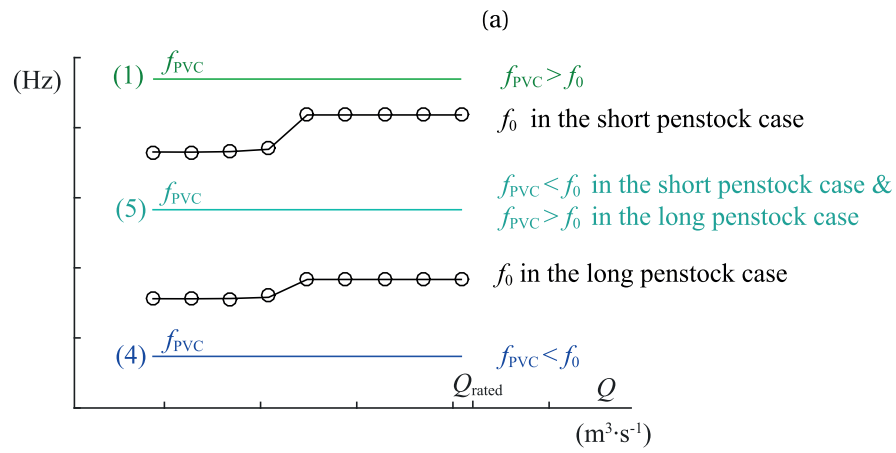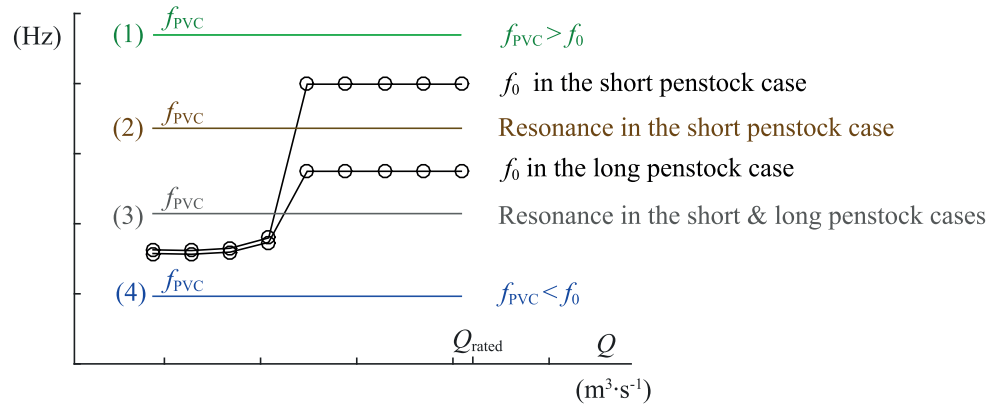
Figure 6.11 – a) Typical f_0 curves for the short penstock case and the long penstock case, as a function of Q in part load conditions. Four groups are indicated according to the position of f_{PVC} with respect to the f_0. b) H_{rated} and Q_{rated} test point values where the procedure is applied. Real cases where part load resonance conditions were detected are also indicated.
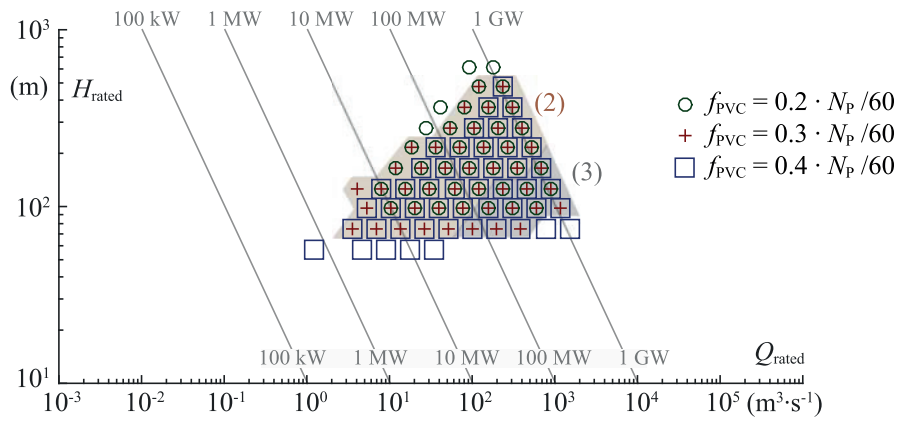
Figure 6.12 – Test points featuring risk of resonance, for the short penstock case, assuming three possible f_{PVC} values. The interval corresponding to groups (2) and (3), for $f_{PVC} = 0.3 \cdot N_P$, is also indicated.

7 Conclusions and Perspectives

7.1 Conclusions

Each hydropower plant has its own particular site conditions that define the range of specific energy and discharge values available for its turbines. As a consequence, Francis turbines are designed to be as efficient as possible for these specific site conditions, making each turbine design unique.

This particularity in Francis turbines poses a difficulty for engineers working on a power plant project: the process of designing, testing and validating the dynamic properties of a Francis turbine is time consuming and only justified after the decision to construct the power plant is already taken. However, the greater the amount of knowledge on these dynamic properties are available, the lesser are the risks involved in the power plant project itself, for reasons such as:

- the amount of energy produced and sold to the grid operator over the year can be calculated more accurately if the turbine efficiency is also known with accuracy;

- overpressure values in the conduits and the turbine overspeed can be calculated more accurately, allowing a proper calculation of wall thickness for the pipes and of required inertia for the rotating parts, notably the generator inertia;

- issues regarding power swings and pressure pulsations can be completely avoided or attenuated.

Therefore, by knowing these dynamic properties in advance, the power plant project itself can be optimized, avoiding risks and increasing the return on investments. This thesis objective is then to provide methods to predict the dynamic behavior of Francis turbine prototypes in the early stages of a power plant project. These methods are presented in four chapters and a fifth chapter is dedicated to present practical applications.

In **Chapter 2** the methodology to construct surrogate functions based on a combination of Hermite Polynomials is presented. This chapter consists of a research paper published in the

Journal of Flow Measurement and Instrumentation, where these surrogate functions are used to estimate a Francis prototype operating conditions during on-site measurements. These surrogate functions are then the basis required for the empirical model for turbine efficiency estimation, presented in the next chapter.

In **Chapter 3** empirical models able to estimate Francis turbines efficiency values from a small number of data input such as the turbine diameter, specific speed and year of commissioning are presented. A procedure to generate the turbine complete characteristics of torque and discharge is also presented, allowing the calculation of overspeed and overpressure values still in a very early stage of the hydropower plant project. The peak efficiency of Francis turbines is predicted with a standard error of estimate lower than 1%.

In **Chapter 4** a procedure to predict the occurrence of resonance between the vortex rope excitation frequency and the system first eigenfrequency in part load conditions is presented. It allows accurate predictions of the operating conditions where resonance will be encountered on the prototype. These predictions can be made long time before the prototype is manufactured, i.e., soon after reduced scale model measurements are performed. If resonance is predicted, it can still be avoided by performing modifications in the turbine design, changing the vortex rope excitation frequency or the system eigenfrequencies.

In **Chapter 5** a complete methodology to predict unstable, i.e., self-excited, full load operating conditions on the prototype is presented. It is applied to the same turbine test case described in Chapters 2 and 4 and unstable conditions are predicted by reduced scale model measurements and 1-D eigenvalue calculations. Hydro-acoustic parameters such as the bulk viscosity coefficient for pressurized pipes and for the cavitation vortex are estimated based on results presented by other authors: for pipes, the coefficient is calculated using measurements performed in another test case, while the vortex rope bulk viscosity coefficient is based on results obtained at part load. Even if a higher level of uncertainty regarding these parameters is expected, the results obtained are still impressive. Further improvements are expected in future works, allowing even more accurate estimations of the stability limits in Francis turbine prototypes operating in full load.

In **Chapter 6** predictions of the dynamic behavior of Francis turbine prototypes are performed and validated. This chapter focuses on calculations that can be performed even before the reduced scale model testing. Firstly, 1-D transient numerical simulation results of an emergency stop making use of predicted turbine characteristics are compared to on-site measurements and to simulations making use of the real, i.e., measured, turbine characteristics. Secondly, cavitation compliance values obtained from the reference test case are adapted to different turbine designs, in varying operating conditions, and used in eigenvalue calculations of a large number of possible hydropower plant layouts. As a result, typical power plant projects leading to a higher risk of resonance in part load conditions are identified.

This thesis work presented empirical models and new procedures to predict the dynamic behavior of Francis turbine prototypes with high accuracy. In times when a large number

of new projects of hydropower plant projects — and the rehabilitation of old ones — are expected, as one of the many measures to tackle CO_2 emissions, the models and procedures presented in this thesis may lower the risk levels involved in these projects, allow optimization procedures and increase the final return on investments.

7.2 Perspectives

In future research projects, the empirical models and methodologies proposed in this thesis research work can receive further improvements. Suggestions for new research possibilities are discussed in the following paragraphs.

Turbine efficiency and complete characteristics — The presented methodology to construct empirical models to predict a Francis turbine efficiency and complete characteristics can be applied to other types of turbines, such as Pelton, Kaplan or pump-turbines. As more reduced scale model measurements are performed and the amount of training data for the empirical models increase, additional parameters can be considered to increase the model accuracy without the risk of overfitting.

Part load resonance — The presented procedure to predict part load resonance has been validated in a given test case where high accuracy is obtained. Ideally, this procedure should be tested in other test cases to confirm its accuracy in any turbine design and power plant layout. By performing additional measurements with different turbines, the standard deviation of cavitation compliance values obtained at the same swirl number and local cavitation coefficient conditions can be assessed. If the standard deviation value is confirmed to be small, the accuracy of the risk assessment presented in Section 6.3 is further confirmed.

Full load stability — While eigenfrequency values in hydraulic circuits are mostly related to values of pressure wave speed and inertia of the water volume inside the pressurized pipes, the modal damping coefficient defining the system stability depends, among others, on: 1) the energy losses related to the bulk viscosity of the water and the pressurized pipes wall material, 2) the bulk viscosity of the cavitation volume and 3) the cavitation volume mass flow gain factor. These three hydro-acoustic parameters makes the full load instability prediction much more challenging than predicting part load resonance. In future research works, these parameters can be determined with higher accuracy in reduced scale model testing through the following procedure:

- in a cavitation-free and vortex rope-free condition, the bulk viscosity coefficient for the test rig pressurized pipes can be determined by applying an external excitation and analysing the system response. Making use of the 1-D SIMSEN model of the test rig, the

viscosity coefficient is then determined by matching the calculated and the measured system response;

- in a stable full load condition, where no pressure pulsation is induced by the vortex rope, the bulk viscosity coefficient of the cavitation volume can be determined by applying an external excitation and analysing the system response. At this point, the viscosity coefficient of the pressurized pipes is considered in the 1-D SIMSEN model, and the cavitation volume bulk viscosity coefficient of the cavitation volume is then determined by matching the calculated and the measured system response;

- the mass flow gain factor can be determined following the same procedure presented in Chapter 5, i.e., by identifying the operating condition of transition from stable to unstable full load and using the 1-D SIMSEN model to perform eigenvalue calculations and quantify the mass flow gain factor leading to the same transition point. As the mass flow gain factor value depends on the assumed bulk viscosity values, more accurate values of bulk viscosity lead to more accuracy in the mass flow gain factor determination.

A Appendix

A.1 Turbine specific speed

From the equation for the turbine power output 1.1, the following equality can be assumed for two different turbines associated to the indexes $_1$ and $_2$:

$$\frac{P_1}{P_2} = \frac{\eta_1 \rho_1 Q_1 E_1}{\eta_2 \rho_2 Q_2 E_2} \tag{A.1}$$

Assuming that these two turbines were designed to maximize their efficiency for their respective specific conditions of Q and E, $\eta_1 \approx \eta_2$ can be considered. Also considering similar values of ρ, Equation A.1 becomes:

$$\frac{P_1}{P_2} = \frac{Q_1 E_1}{Q_2 E_2} \tag{A.2}$$

By using dimensional analysis, the turbine power P can be assumed as proportional to $\rho D^2 E^{1.5}$. With this assumption, Equation A.3 becomes:

$$\frac{\rho D_1^2 E_1^{1.5}}{\rho D_2^2 E_2^{1.5}} = \frac{Q_1 E_1}{Q_2 E_2} \longrightarrow \frac{D_1^2 E_1^{0.5}}{Q_1} = \frac{D_2^2 E_2^{0.5}}{Q_2} \tag{A.3}$$

The ratio between the peripheral runner velocity U and the flow velocity C at the runner outlet can be assumed to be the same for two similar turbines. Knowing that $U = \pi n D$ and $C = Q A^{-1}$ leads to:

$$\frac{U_1}{C_1} = \frac{U_2}{C_2} \longrightarrow \frac{n_1 D_1^3}{Q_1} = \frac{n_2 D_2^3}{Q_2} \tag{A.4}$$

By combining Equations A.3 and A.4, the influence of the turbine diamaters can be removed:

$$\frac{n_1 Q_1^{0.5}}{E_1^{0.75}} = \frac{n_2 Q_2^{0.5}}{E_2^{0.75}} \tag{A.5}$$

The constant value obtained using the equation above is known as the IEC specific speed n_{QE}, as it is defined in the IEC standard [8]. To calculate n_{QE}, values at the BEP are taken:

$$n_{\mathrm{QE}} = \frac{n_{\mathrm{BEP}} Q_{\mathrm{BEP}}^{0.5}}{E_{\mathrm{BEP}}^{0.75}} = n_{\mathrm{ED}_{\mathrm{BEP}}} Q_{\mathrm{ED}_{\mathrm{BEP}}}^{0.5} \tag{A.6}$$

A.2 Equations for the efficiency and the complete characteristics estimation

A.2.1 Efficiency estimation submodels

Sub-model	Formulae	Expected error of estimate
Peak efficiency	$\hat{\eta}_{\text{BEP}} = 98.65\% - \Delta\epsilon_{\text{year}} - \Delta\epsilon_{n_{\text{QE}}} + \Delta\epsilon_{\text{size}}$ $\Delta\epsilon_{\text{year}} = 1 - \dfrac{1}{1+\exp\left\{\left[-1117\cdot(y-1746)\cdot10^{-5}\right]\right\}}$ $\Delta\epsilon_{n_{\text{QE}}} = \left[\left(\dfrac{n_{\text{q}}-42}{338}\right)^2\right]^{1.017}$ $\Delta\epsilon_{\text{size}} = \left(1 - 98.65\cdot10^{-2} + \Delta\epsilon_{\text{year}} + \Delta\epsilon_{n_{\text{QE}}}\right)\ldots$ $\cdot\left(1 - 78.90\cdot10^{-2}\cdot D^{-0.2}\right)$ *new projects* : y = year of commissioning *rehabilitation projects* : $y = \dfrac{\left(\text{year of 1}^{\text{st}}\text{ commissioning}\right) + 2\cdot\left(\text{year of rehabilitation}\right)}{3}$	Mean error $\bar{\epsilon}_{\eta_{\text{BEP}}}$ 0.00% Std. deviation $\sigma\left(\epsilon_{\eta_{\text{BEP}}}\right)$ 0.78%
Relative efficiency first approx.	$\hat{\eta}_{\text{R}} = \sum\limits_{p=0}^{9} \lambda_p \text{He}_p\left(\mathbf{X}\right)$ $\mathbf{X} = g_{\text{T}_0}\left(\left[Q_{\text{ED}_{\text{R}}}, n_{\text{ED}_{\text{R}}}\right]^T\right)$ $g_{\text{T}_0} = \begin{bmatrix} a_0 & 0 \\ b_0 & c_0 \end{bmatrix}\begin{bmatrix} Q_{\text{ED}_{\text{R}}} - 1.00329 \\ n_{\text{ED}_{\text{R}}} - 0.96269 \end{bmatrix} = \begin{bmatrix} X_1 \\ X_2 \end{bmatrix}$ $a_0 = 3.96864$ $b_0 = 0.30232$ $c_0 = -9.34478$ $[\lambda_0,\ldots,\lambda_9] = \big[9.52045\cdot10^{-1}, 1.65858\cdot10^{-2}, 1.02415\cdot10^{-2},$ $-3.13746\cdot10^{-2}, -7.95964\cdot10^{-3}, -1.49667\cdot10^{-2},$ $3.84278\cdot10^{-3}, 2.58181\cdot10^{-3}, 1.92860\cdot10^{-3},$ $-2.04906\cdot10^{-4}\big]$	See Section A.3

Appendix A. Appendix

Sub-model	Formulae	Expected error of estimate
Relative efficiency log. version	$$\hat{\eta}_{\mathrm{R}} = \sum_{p=0}^{9} \lambda_p \mathrm{He}_p\left(\mathbf{X}\right)$$ $$\mathbf{X} = g_{\mathrm{T}}\left(\left[Q_{\mathrm{ED_R}}, n_{\mathrm{ED_R}}\right]^T, n_{\mathrm{QE}}\right)$$ $$g_{\mathrm{T}} = \begin{bmatrix} a & 0 \\ b & c \end{bmatrix} \begin{bmatrix} Q_{\mathrm{ED_R}} - 1.00329 \\ n_{\mathrm{ED_R}} - 0.96269 \end{bmatrix} = \begin{bmatrix} X_1 \\ X_2 \end{bmatrix}$$ $$a = 3.96864 \cdot \left[0.50311 \cdot \log_{10}\left(n_{\mathrm{QE}}\right) + 1\right]$$ $$b = 0.30232 \cdot \left[13.9565 \cdot \log_{10}\left(n_{\mathrm{QE}}\right) + 1\right]$$ $$c = -9.34478 \cdot \left[-0.10838 \cdot \log_{10}\left(n_{\mathrm{QE}}\right) + 1\right]$$ $$\begin{aligned}\left[\lambda_0, ..., \lambda_9\right] = &\left[8.60095 \cdot 10^{-1}, 9.09185 \cdot 10^{-2}, 1.79605 \cdot 10^{-2},\right. \\ &-1.68465 \cdot 10^{-1}, -4.67051 \cdot 10^{-2}, \\ &-1.35925 \cdot 10^{-2}, 5.39519 \cdot 10^{-2}, 1.39829 \cdot 10^{-2}, \\ &\left.3.56701 \cdot 10^{-3}, 1.89355 \cdot 10^{-4}\right]\end{aligned}$$	See Section A.3
Relative efficiency linear version	$$\hat{\eta}_{\mathrm{R}} = \sum_{p=0}^{9} \lambda_p \mathrm{He}_p\left(\mathbf{X}\right)$$ $$\mathbf{X} = g_{\mathrm{T}}\left(\left[Q_{\mathrm{ED_R}}, n_{\mathrm{ED_R}}\right]^T, n_{\mathrm{QE}}\right)$$ $$g_{\mathrm{T}} = \begin{bmatrix} a & 0 \\ b & c \end{bmatrix} \begin{bmatrix} Q_{\mathrm{ED_R}} - 1.00329 \\ n_{\mathrm{ED_R}} - 0.96269 \end{bmatrix} = \begin{bmatrix} X_1 \\ X_2 \end{bmatrix}$$ $$a = 3.96864 \cdot \left(3.10954 \cdot n_{\mathrm{QE}} + 1\right)$$ $$b = 0.30232 \cdot \left(85.18272 \cdot n_{\mathrm{QE}} + 1\right)$$ $$c = -9.34478 \cdot \left(0.09583 \cdot n_{\mathrm{QE}} + 1\right)$$ $$\begin{aligned}\left[\lambda_0, ..., \lambda_9\right] = &\left[9.67107 \cdot 10^{-1}, 1.95013 \cdot 10^{-3}, 7.69154 \cdot 10^{-3},\right. \\ &-1.55947 \cdot 10^{-2}, 7.61258 \cdot 10^{-3}, \\ &-1.55227 \cdot 10^{-2}, 1.99402 \cdot 10^{-3}, \\ &\left.-9.66331 \cdot 10^{-4}, 1.01063 \cdot 10^{-3}, 4.84562 \cdot 10^{-4}\right]\end{aligned}$$	See Section A.3

Sub-model	Formulae	Expected error of estimate
Relative Runaway n_{ED}	$$\frac{\hat{n}_{ED_{Run}}}{n_{ED_{BEP}}} = \frac{Q^c_{ED_R}}{a \cdot Q_{ED_R} + b}$$ $a = 1.3748 \cdot n_{QE} + 0.1501$ $b = 0.2794 \cdot n_{QE} + 0.0861$ $c = -0.2627 \cdot n_{QE} + 0.4628$	Mean error $\bar{\epsilon}_{Run}$ $5.26 \cdot 10^{-3}$ Std. deviation $\sigma(\epsilon_{Run})$ $6.41 \cdot 10^{-2}$
Relative guide vanes opening angle	$\hat{\alpha}_R = \;\; 0.1281 \cdot Q^{\star\,3}_{ED_R} - 0.2832 \cdot Q^{\star\,2}_{ED_R} + 0.5491 \cdot Q^{\star}_{ED_R} \cdots$ $+ 0.1764 + 0.0152 \cdot Q^{\star}_{ED_R} \cdot n^{\star}_{ED_R} + 3.4277 \cdot n^{\star}_{ED_R} \cdots$ $+ 0.6458 \cdot \exp\left(-0.5431 \cdot n^{\star}_{ED_R}\right)$	Mean error $\bar{\epsilon}_\alpha$ $0.3 \cdot 10^{-2}$ Std. deviation $\sigma(\epsilon_\alpha)$ $5.9 \cdot 10^{-2}$

145

A.3 η_R **estimation error**

As the distribution in terms of (n_{ED}, Q_{ED}) values of the measurement samples available for different turbines is never the same, the mean error between the estimated values of η_R and the measured values vary depending on the interval of Q_{ED_R} and n_{ED_R} values, ΔQ_{ED_R} and Δn_{ED_R} respectively, that is being analyzed. Additionally, the deviations tend to increase as regions further away from the BEP are analyzed.

To provide more accurate information about the expected error in the η_R value estimations, the number of samples N_s, the mean error $\bar\epsilon$ as in Equation A.8 and the standard deviation of the error $\sigma(\epsilon)$ as in Equation A.9 are calculated inside specific intervals of ΔQ_{ED_R} and Δn_{ED_R}.

$$^{(j)}\epsilon = {}^{(j)}\eta_R - {}^{(j)}\hat\eta_R \tag{A.7}$$

$$\bar\epsilon = \frac{1}{N_s} \sum_{j=1}^{N_s} {}^{(j)}\epsilon \tag{A.8}$$

$$\sigma(\epsilon) = \sqrt{\frac{1}{N_s - 1} \sum_{j=1}^{N_s} \left({}^{(j)}\epsilon - \bar\epsilon\right)^2} \tag{A.9}$$

where N_s is the number of available samples inside the chosen interval.

The number of samples N_s per interval $\Delta Q_{ED_R} = 0.130$ and $\Delta n_{ED_R} = 0.094$ is presented in Figure A.1. The mean error and the standard deviation of the error for the first approximation, for the adaptive submodel using the logarithmic coefficients a, b and c, and for the adaptive submodel using linear coefficients a, b and c are presented in the following subsections.
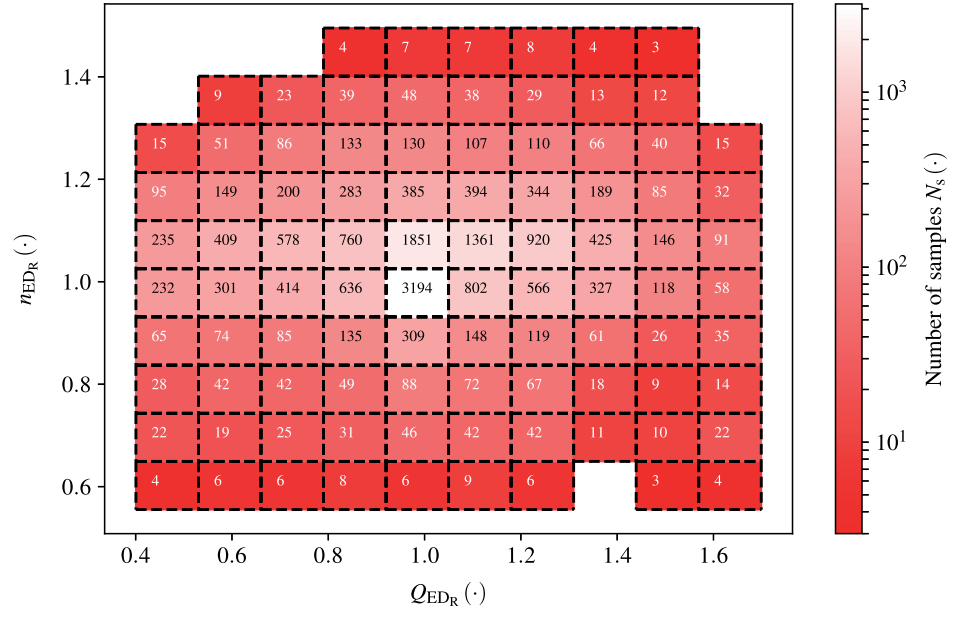
Figure A.1 – Number of samples per interval $\Delta Q_{ED_R} = 0.130$ and $\Delta n_{ED_R} = 0.094$.

A.3.1 First approximation
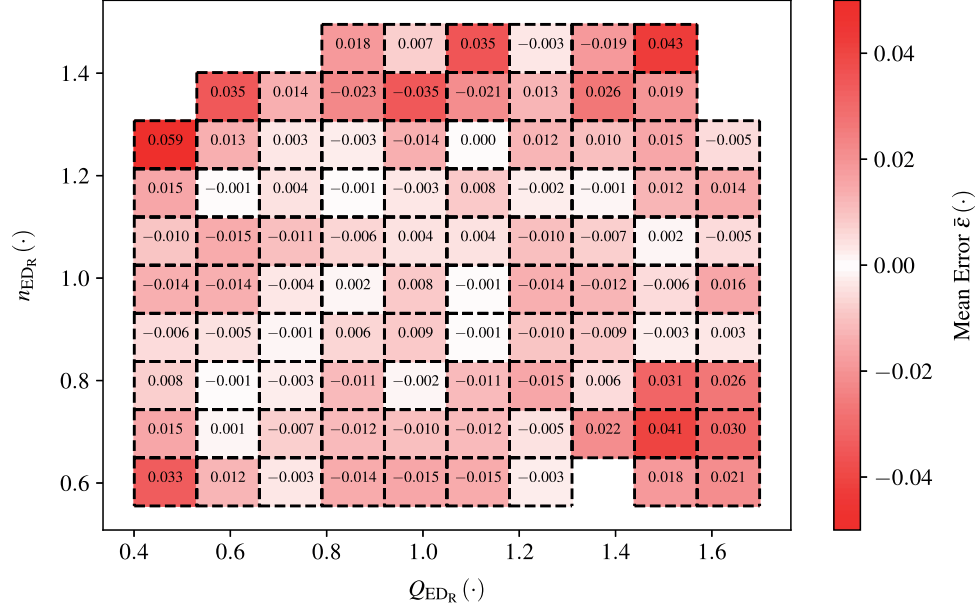
Figure A.2 – Mean error using the first approximation to estimate η_R.
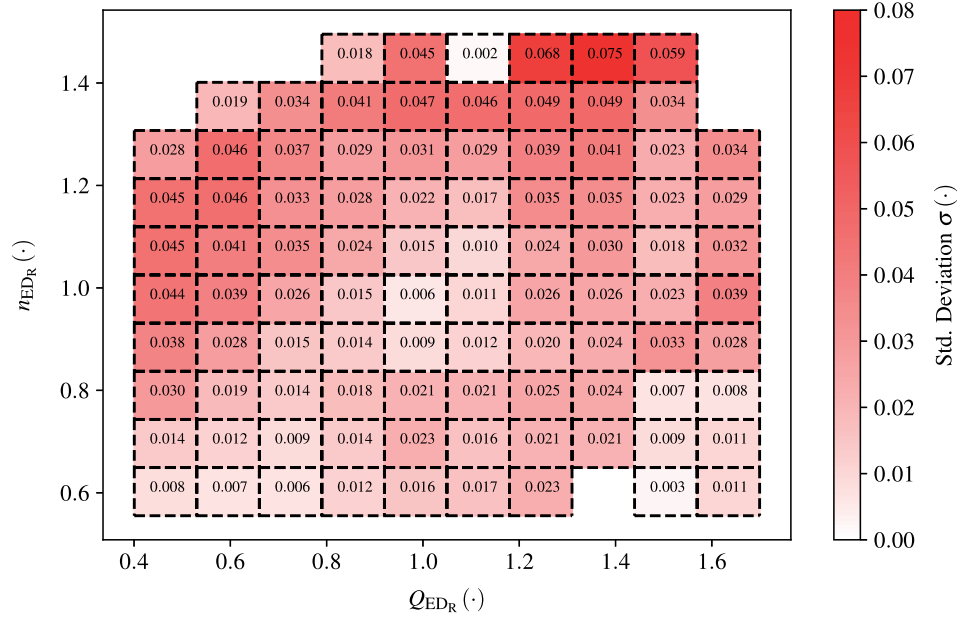
Figure A.3 – Standard deviation of the error using the first approximation to estimate η_R.

A.3.2 Logarithmic submodel
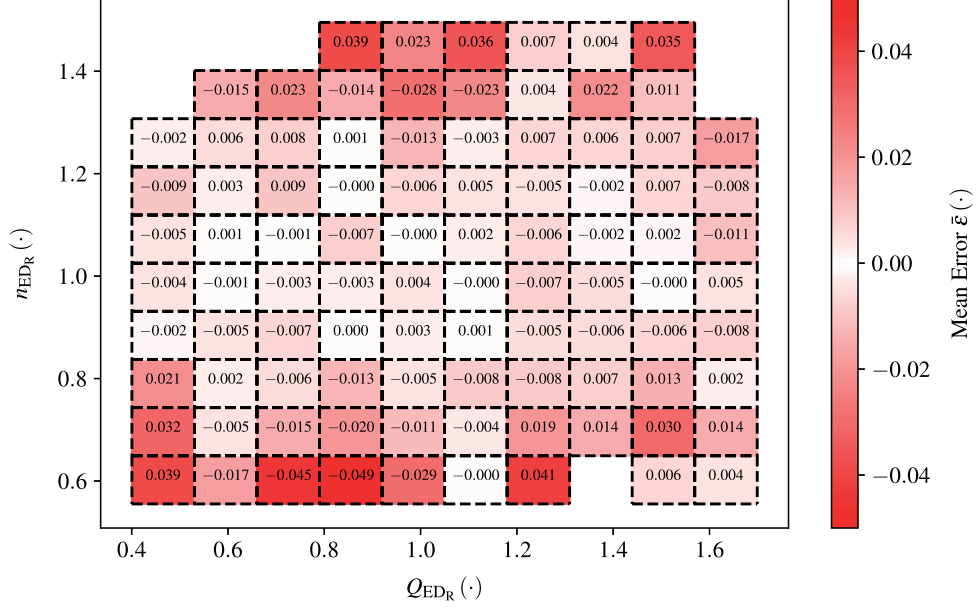
Figure A.4 – Mean error using the logarithmic submodel to estimate η_{R}.
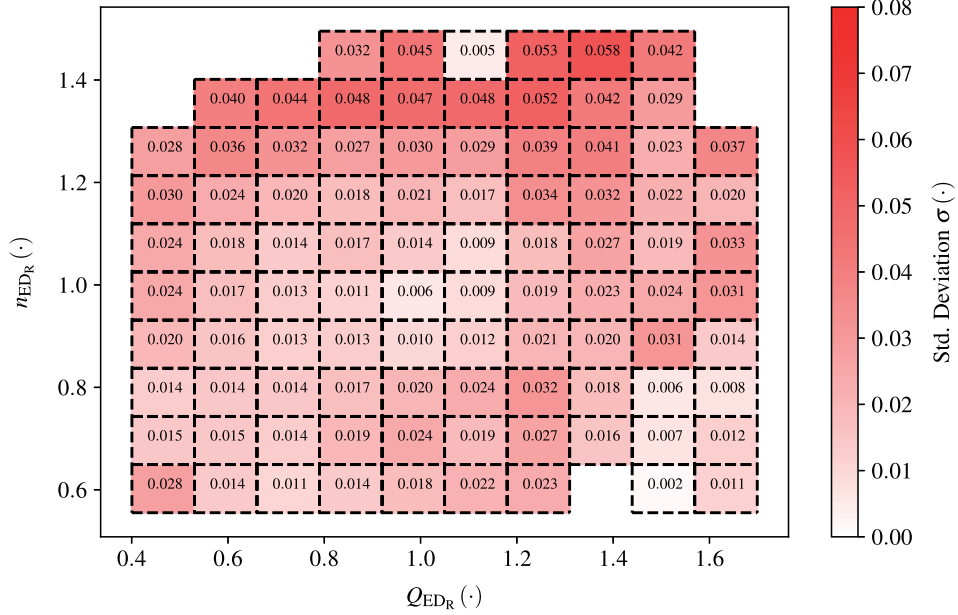
Figure A.5 – Standard deviation of the error using the logarithmic submodel to estimate η_{R}.

A.3.3 Linear submodel
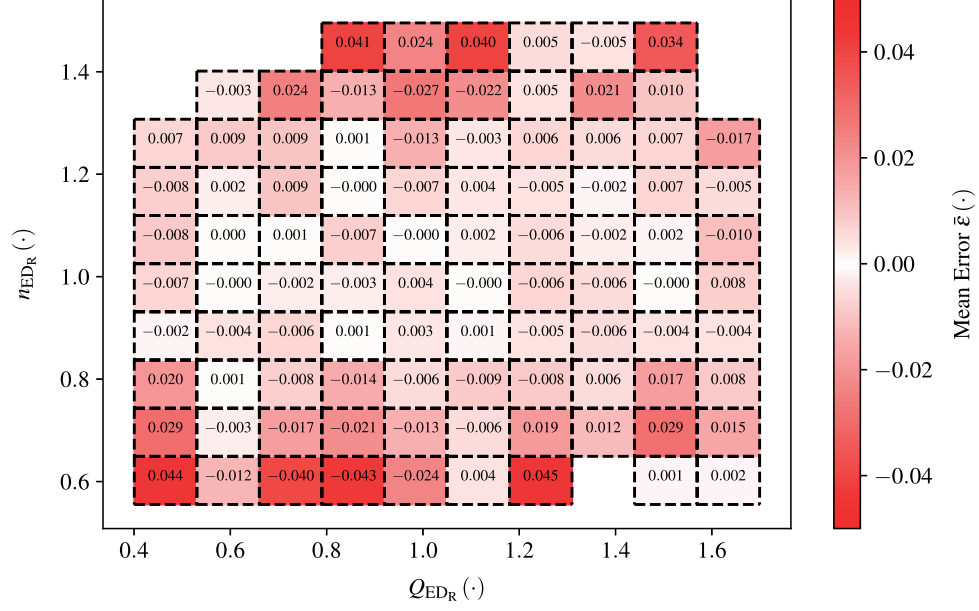
Figure A.6 – Mean error using the linear submodel to estimate η_R.
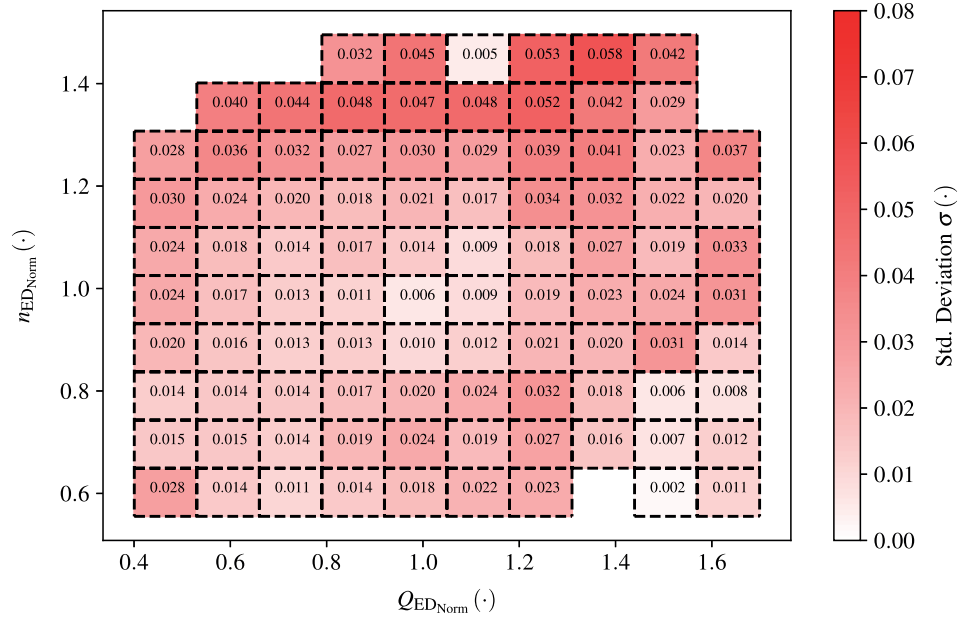
Figure A.7 – Standard deviation of the error using the linear submodel to estimate η_R.

A.4   Least squares method for approximations by blending functions

This Appendix details the procedure to apply the least squares method to define the modal strengths in the polynomial approximation used in the construction of the $\hat{\eta}_{TR}$ function. The Equation for $\hat{\eta}_{TR}$ is defined as:

$$\hat{\eta}_{TR} = \sum_{i=1}^{N_\phi} \phi_{TR,i} \cdot \sum_{j=0}^{p_{max}} \lambda_{j,i} He_j \tag{A.10}$$

When applying the least squares method, the modal strengths $\lambda_{j,i}$ are defined as those leading to a minimum value of L defined as:

$$L = \sum_{k=1}^{N_{TR}} \left({}^{(k)}\hat{\eta}_{TR} - {}^{(k)}\eta_{TR} \right)^2$$

$$L = \sum_{k=1}^{N_{TR}} \left({}^{(k)}\hat{\eta}_{TR} - \sum_{i=1}^{N_\phi} {}^{(k)}\phi_{TR,i} \cdot \sum_{j=0}^{p_{max}} \lambda_{j,i} \cdot {}^{(k)}He_j \right)^2$$

$$L = \sum_{k=1}^{N_{TR}} \left[\sum_{i=1}^{N_\phi} {}^{(k)}\phi_{TR,i} \underbrace{\left({}^{(k)}\hat{\eta}_{TR} - \sum_{j=0}^{p_{max}} \lambda_{j,i} \cdot {}^{(k)}He_j \right)}_{{}^{(k)}\epsilon_i} \right]^2 \tag{A.11}$$

$$L = \sum_{k=1}^{N_{TR}} \left[\sum_{i=1}^{N_\phi} {}^{(k)}\phi_{TR,i} \cdot {}^{(k)}\epsilon_i \right]^2$$

$$L = \sum_{i=1}^{N_\phi} \sum_{k=1}^{N_{TR}} {}^{(k)}\phi_{TR,i}^2 \cdot {}^{(k)}\epsilon_i^2 + 2 \cdot \sum_{i=1}^{N_\phi - 1} \sum_{l=i+1}^{N_\phi} \sum_{k=1}^{N_{TR}} {}^{(k)}\phi_{TR,i} \cdot {}^{(k)}\epsilon_i \cdot {}^{(k)}\phi_{TR,l} \cdot {}^{(k)}\epsilon_l$$

The equation for L can be written in the matrix form as:

$$L = \sum_{i=1}^{N_\phi} \vec{\epsilon}_i^T \overline{\overline{\phi_i \phi_i}} \vec{\epsilon}_i + 2 \cdot \sum_{i=1}^{N_\phi - 1} \sum_{l=i+1}^{N_\phi} \vec{\epsilon}_i^T \overline{\overline{\phi_i \phi_l}} \vec{\epsilon}_l \tag{A.12}$$

where:

$$\vec{\epsilon}_i = \vec{\eta}_{TR} - \mathbf{He}\vec{\lambda}_i$$

$$\vec{\eta}_{TR} = \left[{}^{(1)}\eta_{TR}, {}^{(2)}\eta_{TR}, ..., {}^{(N_{TR})}\eta_{TR} \right]^T \tag{A.13}$$

$$\vec{\lambda}_i = \left[\lambda_{0,i}, \lambda_{1,i}, ..., \lambda_{p_{max},i} \right]^T$$

The matrix **He** is defined as in Equation 2.10 and $\overline{\overline{\phi_i\phi_l}}$ is a diagonal matrix with $^{(k)}\phi_i \cdot {}^{(k)}\phi_j$ in its diagonal line. To find the minimum value for L, each derivative $\partial L/\partial\vec{\lambda}_x$ can be defined as zero, $\forall x \in [0,1,...,p_{max}]$. As a result:

$$\frac{\partial L}{\partial\vec{\lambda}_x} = \frac{\partial}{\partial\vec{\lambda}_x}\left(\sum_{i=1}^{N_\phi}\vec{\epsilon}_i^T\overline{\overline{\phi_i\phi_i}}\vec{\epsilon}_i + 2\cdot\sum_{i=1}^{N_\phi-1}\sum_{l=i+1}^{N_\phi}\vec{\epsilon}_i^T\overline{\overline{\phi_i\phi_l}}\vec{\epsilon}_l\right)$$

$$0 = -2\cdot\mathbf{He}\overline{\overline{\phi_x\phi_x}}\vec{\epsilon}_x - 2\cdot\sum_{i=1,i\neq x}^{N_\phi}\mathbf{He}\overline{\overline{\phi_i\phi_x}}\vec{\epsilon}_x$$

$$0 = \sum_{i=1}^{N_\phi}\mathbf{He}\overline{\overline{\phi_i\phi_x}}\vec{\epsilon}_x \tag{A.14}$$

$$0 = \sum_{i=1}^{N_\phi}\mathbf{He}\overline{\overline{\phi_i\phi_x}}\left(\vec{\eta}_{TR} - \mathbf{He}\vec{\lambda}_x\right)$$

$$\sum_{i=1}^{N_\phi}\mathbf{He}\overline{\overline{\phi_i\phi_x}}\vec{\eta}_{TR} = \sum_{i=1}^{N_\phi}\mathbf{He}\overline{\overline{\phi_i\phi_x}}\mathbf{He}\vec{\lambda}_x$$

By combining all the possible values of x in the equation above into a single expression, the linear system of Equation A.15 can be constructed. The solution of this linear system provides the values for each possible $\vec{\lambda}_x$.

$$\begin{bmatrix} \mathbf{He}^T\overline{\overline{\phi_1\phi_1}}\mathbf{He} & \mathbf{He}^T\overline{\overline{\phi_1\phi_2}}\mathbf{He} & \cdots & \mathbf{He}^T\overline{\overline{\phi_1\phi_{N_\phi}}}\mathbf{He} \\ \mathbf{He}^T\overline{\overline{\phi_2\phi_1}}\mathbf{He} & \mathbf{He}^T\overline{\overline{\phi_2\phi_2}}\mathbf{He} & \cdots & \mathbf{He}^T\overline{\overline{\phi_2\phi_{N_\phi}}}\mathbf{He} \\ \vdots & \vdots & \ddots & \vdots \\ \mathbf{He}^T\overline{\overline{\phi_{N_\phi}\phi_1}}\mathbf{He} & \mathbf{He}^T\overline{\overline{\phi_{N_\phi}\phi_2}}\mathbf{He} & \cdots & \mathbf{He}^T\overline{\overline{\phi_{N_\phi}\phi_{N_\phi}}}\mathbf{He} \end{bmatrix}\begin{bmatrix} \vec{\lambda}_1 \\ \vec{\lambda}_2 \\ \vdots \\ \vec{\lambda}_{N_\phi} \end{bmatrix} = \begin{bmatrix} \sum_{i=1}^{N_\phi}\mathbf{He}^T\overline{\overline{\phi_1\phi_i}}\vec{\eta}_{TR} \\ \sum_{i=1}^{N_\phi}\mathbf{He}^T\overline{\overline{\phi_2\phi_i}}\vec{\eta}_{TR} \\ \vdots \\ \sum_{i=1}^{N_\phi}\mathbf{He}^T\overline{\overline{\phi_{N_\phi}\phi_i}}\vec{\eta}_{TR} \end{bmatrix} \tag{A.15}$$

A.5 Parameters of the SIMSEN components for the emergency shut-down simulation

RESU

H [m] = 7.52761100000000E+002   g [m/s2] = 9.81000000000000E+000
Rho [kg/m3] = 1.00000000000000E+003

DLU2

K [1] = 2.19000000000000E-001   g [m/s2] = 9.81000000000000E+000
Aref [m2] = 3.52600000000000E+001
Rho [kg/m3] = 1.00000000000000E+003

PIPE21

Nb. of elements = 8   Lambda [1] = 6.00000000000000E-003
Zin [m] = 6.89760000000000E+002   Ksi [1] = 1.00000000000000E+000
Zout [m] = 6.89760000000000E+002   Mu [Pa.s] = 1.00000000000000E+005
L [m] = 9.89300000000000E+001   Rho [kg/m3] = 1.00000000000000E+003
D [m] = 6.70000000000000E+000   g [m/s2] = 9.81000000000000E+000
a [m/s] = 1.25486000000000E+003

PIPE22

Nb. of elements = 11   Lambda [1] = 6.00000000000000E-003
Zin [m] = 6.89760000000000E+002   Ksi [1] = 1.00000000000000E+000
Zout [m] = 5.80171600000000E+002   Mu [Pa.s] = 1.00000000000000E+005
L [m] = 1.34490000000000E+002   Rho [kg/m3] = 1.00000000000000E+003
D [m] = 6.70000000000000E+000   g [m/s2] = 9.81000000000000E+000
a [m/s] = 1.25486000000000E+003

PIPE23

Nb. of elements = 2   Lambda [1] = 6.00000000000000E-003
Zin [m] = 5.80170000000000E+002   Ksi [1] = 1.00000000000000E+000
Zout [m] = 5.70900000000000E+002   Mu [Pa.s] = 1.00000000000000E+005
L [m] = 2.65400000000000E+001   Rho [kg/m3] = 1.00000000000000E+003
D [m] = 6.70000000000000E+000   g [m/s2] = 9.81000000000000E+000
a [m/s] = 1.21660000000000E+003

PIPE24

Nb. of elements = 4

Zin [m] = 5.70900000000000E+002

Zout [m] = 5.64490000000000E+002

L [m] = 5.72900000000000E+001

D [m] = 5.94000000000000E+000

a [m/s] = 1.33880000000000E+003

Lambda [1] = 6.00000000000000E-003

Ksi [1] = 1.00000000000000E+000

Mu [Pa.s] = 1.00000000000000E+005

Rho [kg/m3] = 1.00000000000000E+003

g [m/s2] = 9.81000000000000E+000

BS

Nb. of elements = 3

Zin [m] = 5.64489600000000E+002

Zout [m] = 5.64489600000000E+002

L [m] = 3.56370000000000E+001

D [m] = 3.96000000000000E+000

a [m/s] = 1.27067000000000E+003

Lambda [1] = 6.00000000000000E-003

Ksi [1] = 1.00000000000000E+000

Mu [Pa.s] = 1.00000000000000E+005

Rho [kg/m3] = 1.00000000000000E+003

g [m/s2] = 9.81000000000000E+000

TURB2

N [rpm] = 1.28600000000000E+002

y [1] = 1.13000000000000E+000

Dref [m] = 5.40000000000000E+000

Lequ [m] = 4.00000000000000E+001

Amean [m2] = 2.30000000000000E+001

Rho [kg/m3] = 1.00000000000000E+003

g [m/s2] = 9.81000000000000E+000

RTURB1

J [kgm2] = 6.50000000000000E+005

RSM1

J [kgm2] = 2.83262724000000E+007

K [Nm/rad] = 2.39445662665000E+009

DLOSSIN

K [1] = 1.00000000000000E+000

Aref [m2] = 2.29000000000000E+001

Rho [kg/m3] = 1.00000000000000E+003

g [m/s2] = 9.81000000000000E+000

154

DTUBE21

Nb. of elements = 32

Zin [m] = 5.62656600000000E+002

Zout [m] = 5.48440000000000E+002

L [m] = 1.54800000000000E+001

D [m] = 6.75000000000000E+000

a [m/s] = 1.00000000000000E+002

Lambda [1] = 6.00000000000000E-003

Ksi [1] = 1.00000000000000E+000

Mu [Pa.s] = 1.00000000000000E+005

Rho [kg/m3] = 1.00000000000000E+003

g [m/s2] = 9.81000000000000E+000

DTUBE22

Nb. of elements = 9

Zin [m] = 5.48440000000000E+002

Zout [m] = 5.60680000000000E+002

L [m] = 5.60670000000000E+001

D [m] = 1.05100000000000E+001

a [m/s] = 4.00000000000000E+002

Lambda [1] = 1.14600000000000E-002

Ksi [1] = 1.00000000000000E+000

Rho [kg/m3] = 1.00000000000000E+003

g [m/s2] = 9.81000000000000E+000

RESD1

H [m] = 5.72400000000000E+002

Rho [kg/m3] = 1.00000000000000E+003

g [m/s2] = 9.81000000000000E+000

A.6 Relation between χ_{nD} and σ

This appendix details how the relation between χ_{nD} and σ expressed in Equation 4.10 is obtained.

For any cross-section x of the turbine draft tube, the average specific energy E_x can be written as:

$$E_x = \frac{p_{\mathrm{abs}\,x}}{\rho} + \frac{C_x^2}{2} + g z_x \tag{A.16}$$

Making use of the specific energy at the draft tube outlet $E_{\bar{1}}$, the expression for σ presented in Equation 4.7 is rewritten as:

$$\sigma = \frac{1}{E} \cdot \left(E_{\bar{1}} - \frac{p_{\mathrm{v}}}{\rho} - g z_{\mathrm{ref}} \right) \tag{A.17}$$

Knowing that E_{rb} is the energy loss between the cone and the outlet cross-sections, Equation A.17 can be rewritten as:

$$\sigma = \frac{1}{E} \cdot \left(E_{\mathrm{cone}} - E_{\mathrm{rb}} - \frac{p_{\mathrm{v}}}{\rho} - g z_{\mathrm{ref}} \right)$$

$$\sigma = \frac{1}{E} \cdot \left(\frac{p_{\mathrm{cone}} - p_{\mathrm{v}}}{\rho} + \frac{C_{\mathrm{cone}}^2}{2} + g z_{\mathrm{cone}} - g z_{\mathrm{ref}} - E_{\mathrm{rd}} \right) \tag{A.18}$$

Multiplying Equation A.18 by $E \cdot (nD)^{-2}$ and rearranging it, the expression relating χ_{nD} and σ is obtained:

$$\frac{p_{\mathrm{cone}} - p_{\mathrm{v}}}{\rho n^2 D^2} = \frac{E}{n^2 D^2} \cdot \left(\sigma + \frac{g z_{\mathrm{ref}} - g z_{\mathrm{cone}}}{E} + \frac{E_{\mathrm{rd}}}{E} - \frac{C_{\mathrm{cone}}^2}{2E} \right)$$

$$\chi_{nD} = \frac{1}{n_{\mathrm{ED}}^2} \cdot \left(\sigma + \frac{g z_{\mathrm{ref}} - g z_{\mathrm{cone}}}{\mathrm{Fr}^2 D} + \frac{E_{\mathrm{rd}}}{E} - \frac{Q^2}{2 A_{\mathrm{cone}}^2 E} \right)$$

$$\chi_{nD} = \frac{1}{n_{\mathrm{ED}}^2} \cdot \left(\sigma + \frac{g z_{\mathrm{ref}} - g z_{\mathrm{cone}}}{\mathrm{Fr}^2 D} + \frac{E_{\mathrm{rd}}}{E} - \frac{D^4 Q_{\mathrm{ED}}^2}{2 A_{\mathrm{cone}}^2} \right) \tag{A.19}$$

A.7 Best fit approximations in Fig. 5.16 and Fig. 5.20

n_{ED} $(\cdot)$	Pressure at the draft tube cone wall (bar)	non-dimensional pressure wave speed $(\cdot)$
0.268	$p_{\mathrm{cone}} = -1.594 \cdot 10^7 \cdot Q_{\mathrm{ED}}^2 + 7.556 \cdot 10^6 \cdot Q_{\mathrm{ED}} - 8.745 \cdot 10^5$	$\Pi = 656.038 \cdot \exp(28.376 \cdot S)$
0.277	$p_{\mathrm{cone}} = -4.048 \cdot 10^6 \cdot Q_{\mathrm{ED}}^2 + 1.789 \cdot 10^6 \cdot Q_{\mathrm{ED}} - 1.714 \cdot 10^5$	$\Pi = 190.314 \cdot \exp(15.450 \cdot S)$
0.288	$p_{\mathrm{cone}} = -9.472 \cdot 10^6 \cdot Q_{\mathrm{ED}}^2 + 4.749 \cdot 10^6 \cdot Q_{\mathrm{ED}} - 5.696 \cdot 10^5$	$\Pi = 108.920 \cdot \exp(10.901 \cdot S)$
0.300	$p_{\mathrm{cone}} = -1.181 \cdot 10^7 \cdot Q_{\mathrm{ED}}^2 + 6.179 \cdot 10^6 \cdot Q_{\mathrm{ED}} - 7.816 \cdot 10^5$	$\Pi = 412.371 \cdot \exp(19.176 \cdot S)$

A.8 χ transposition

A procedure to estimate χ_M values for Q_ED conditions surrounding that of the transition from stable to unstable in the reduced scale model, and also to estimate the prototype mass flow gain factor for similar conditions, χ_P, is presented in this appendix. The draft tube cone is simplified as a straight pipe with cross-section $A_\mathrm{p} = \pi R_\mathrm{p}^2 = V_\mathrm{Cone}/L_\mathrm{Cone}$, where V_Cone and L_Cone are the cone volume and length, respectively. Constant tangential and axial flow velocities are assumed, being equal to Cu and Cm, respectively. The radial flow velocity is assumed as zero.

From the simplification of the momentum conservation equation in the radial direction, eq. (A.20) is obtained.

$$\frac{Cu^2}{r} = \frac{1}{\rho}\frac{\partial\rho}{\partial r} \tag{A.20}$$

Assuming that the axisymmetric cavitation vortex rope features a radius equal to R_c, the integration of eq. (A.20) from the cavitating radius to the pipe radius leads to:

$$\int_{R_\mathrm{c}}^{R_\mathrm{p}} \frac{Cu^2}{r}\,dr = \frac{p(R_\mathrm{p}) - p(R_\mathrm{c})}{\rho}$$

$$C_u{}^2 \ln\left(\frac{R_p}{R_c}\right) = \frac{p_\mathrm{p} - p_\mathrm{v}}{\rho} \tag{A.21}$$

where p_p and p_v are the pipe wall pressure and the water vapor pressure, respectively. By isolating R_c in eq. (A.21), the cavitating cross section $A_\mathrm{c} = \pi R_\mathrm{c}^2$ is obtained as in eq. A.22.

$$A_\mathrm{c} = A_\mathrm{p} \cdot \exp\left(2 \cdot \frac{p_\mathrm{v} - p_\mathrm{p}}{\rho Cu^2}\right) \tag{A.22}$$

By applying eq. (A.22) in the definition of the mass flow gain factor, $\chi = -\partial V_\mathrm{c}/\partial Q$, eq. (A.23) is obtained:

$$\chi = -\frac{\partial V_\mathrm{c}}{\partial Q} = -\frac{L_\mathrm{p}}{A} \cdot \frac{\partial A_\mathrm{c}}{\partial Cm}$$

$$\chi = \frac{4V_\mathrm{p}}{A}\left(\frac{p_\mathrm{v} - p_\mathrm{p}}{Cu^3\rho}\right) \cdot \exp\left(2 \cdot \frac{p_\mathrm{v} - p_\mathrm{p}}{Cu^2\rho}\right) \cdot \frac{\partial Cu}{\partial Cm} \tag{A.23}$$

where p_p and V_p are assumed to be equivalent to the draft tube cone wall pressure p_cone and volume V_cone.

Considering the velocity triangle at the runner outlet, the partial derivative $\frac{\partial Cu}{\partial Cm}$ is assumed as equal to $-\frac{U}{Cm_0}$, where U is the runner peripheral velocity and the index $_0$ indicates the no-swirl condition, i.e., the condition which $Cu = 0$. The eq. (A.23) becomes:

$$\chi = -\frac{4V_\mathrm{cone}U}{Q_0}\left(\frac{p_\mathrm{v} - p_\mathrm{cone}}{Cu^3\rho}\right) \cdot \exp\left(2 \cdot \frac{p_\mathrm{v} - p_\mathrm{cone}}{Cu^2\rho}\right) \tag{A.24}$$
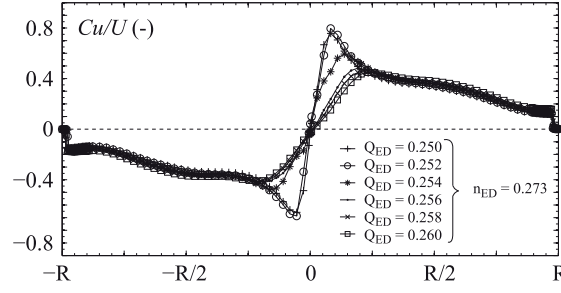
Figure A.8 – Cu velocity profile for different Q_{ED} values, extracted from [140].

The measurements on the reduced scale physical model lead to a transition from a stable to an unstable full load condition at $n_{\mathrm{ED}} = 0.277$ and $Q_{\mathrm{ED}} = 0.250$. Eigenvalue calculations are performed to define a χ value leading to a transition from stable to unstable condition at the same measured Q_{ED} value. This χ value is taken as a reference value, $\chi_{\mathrm{Mref}} = -4.1 \cdot 10^{-4}$ s, from which $Cu_{\mathrm{Mref}} = -0.13 \cdot U_{\mathrm{Mref}} = -1.88$ m·s^{-1} is obtained numerically making use of eq. (A.24).

From eq. (A.24), χ_{M} values in similar conditions of S, but with different p_{cone} and n_{ED} conditions are estimated as in eq. (A.25). For small variations of S values, the tangential flow velocity Cu is assumed to remain constant. This assumption is corroborated by the flow velocity profile measurements performed by Müller in [140] and illustrated in Figure A.8, where Cu values are only varying at the center of the vortex. The velocity profile is measured at $0.39 \cdot D$ distance from the runner outlet.

$$\chi_{\mathrm{M}} = \chi_{\mathrm{Mref}} \cdot \left(\frac{U_{\mathrm{Mref}}}{U_{\mathrm{M}}} \right)^3 \cdot \frac{(p_{\mathrm{v}} - p_{\mathrm{cone}})_{\mathrm{M}}}{(p_{\mathrm{v}} - p_{\mathrm{cone}})_{\mathrm{Mref}}} \cdot \exp\left(K_{\mathrm{M}} - K_{\mathrm{Mref}} \right) \tag{A.25}$$

where K is calculated as:

$$K = \frac{2}{Cu^2} \left(\frac{p_{\mathrm{v}} - p_{\mathrm{p}}}{\rho} \right) \tag{A.26}$$

Considering operating conditions with constant ratios Cu/U and Cm/U between the reduced scale model and the turbine prototype, eq. (A.24) is used to derive an equation to transpose χ values from the model scale, χ_{M}, to the prototype scale, χ_{P}, as in:

$$\chi_{\mathrm{P}} = \chi_{\mathrm{M}} \cdot \frac{D_{\mathrm{P}}}{D_{\mathrm{M}}} \frac{(p_{\mathrm{v}} - p_{\mathrm{p}})_{\mathrm{P}}}{(p_{\mathrm{v}} - p_{\mathrm{p}})_{\mathrm{M}}} \cdot \left(\frac{U_{\mathrm{M}}}{U_{\mathrm{P}}} \right)^3 \cdot \exp\left(K_{\mathrm{P}} - K_{\mathrm{M}} \right) \tag{A.27}$$

Bibliography

[1] AIE, Energy Technology Perspectives 2012: Pathways to a Clean Energy System, Éditions OCDE, Paris, 2012 (2012). `doi:https://doi.org/https://doi.org/10.1787/energy_tech-2012-en`.
URL https://www.oecd-ilibrary.org/content/publication/energy_tech-2012-en

[2] GE, General Electrics Renewable Energy, Francis Hydro Turbine (Accessed: 2019-01-24).
URL https://www.gerenewableenergy.com/hydro-power/large-hydropower-solutions/hydro-turbines/francis-turbine

[3] A. T. Favrel, Dynamics of the cavitation precessing vortex rope for francis turbines at part load operating conditions, Ph.D. thesis, Lausanne (2016). `doi:10.5075/epfl-thesis-6880`.
URL http://infoscience.epfl.ch/record/215867

[4] C. Nicolet, F. Avellan, P. Allenbach, A. Sapin, J. J. Simond, J. J. Herou, Transient phenomena in francis turbine power plants : Interaction with the power network, 11th International Meeting of the IAHR Work Group on the Behavior of Hydraulic Machinery under Steady Oscillatory Conditions (2003).
URL http://infoscience.epfl.ch/record/59040

[5] A. Bergant, B. Karney, S. Pejović, J. Mazij, Treatise on water hammer in hydropower standards and guidelines, in: IOP Conference Series: Earth and Environmental Science, Vol. 22, IOP Publishing, 2014, p. 042007 (2014).

[6] R. Guarga, G. Hiriart, J. Torres, Oscillatory problems at mexico's la angostura plant, Water Power and Dam Construction 35 (1983) 33–6 (1983).

[7] Andritz Hydro , pdf file presentation (Accessed: 2019-06-03).
URL www.hdc.si/wp-content/uploads/hy-andritz-hydro-en.pdf

[8] I. E. Commission, et al., Hydraulic turbines, storage pumps and pump-turbines —model acceptance tests, Standard No. IEC 60193, International Electrotechnical Commission, 1999 (1999).

[9] LMH, LMH website (Accessed: 2019-06-03).
URL https://lmh.epfl.ch/scientific-services/facilities/hydraulic-machine-experimental-test-rigs/

[10] J.-F. Cyr, M. Landry, Y. Gagnon, Methodology for the large-scale assessment of small hydroelectric potential: Application to the province of new brunswick (canada), Renewable energy 36 (11) (2011) 2940–2950 (2011).

Bibliography

[11] P. P. Gohil, R. Saini, Cfd: Numerical analysis and performance prediction in francis turbine, in: 1st International Conference on Non Conventional Energy (ICONCE), 2014, IEEE, 2014, pp. 94–97 (2014).

[12] J. Wu, K. Shimmei, K. Tani, K. Niikura, J. Sato, Cfd-based design optimization for hydro turbines, Journal of Fluids Engineering 129 (2) (2007) 159–168 (2007).

[13] H.-J. Choi, M. A. Zullah, H.-W. Roh, P.-S. Ha, S.-Y. Oh, Y.-H. Lee, Cfd validation of performance improvement of a 500 kw francis turbine, Renewable Energy 54 (2013) 111 – 123, aFORE 2011 (Asia-Pacific Forum of Renewable Energy 2011) (2013). `doi:https://doi.org/10.1016/j.renene.2012.08.049`.
URL http://www.sciencedirect.com/science/article/pii/S0960148112005198

[14] T. M. Arispe, W. de Oliveira, R. G. Ramirez, Francis turbine draft tube parameterization and analysis of performance characteristics using cfd techniques, Renewable Energy 127 (2018) 114–124 (2018).

[15] Z. Zhang, M. Titzschkau, Self-validated calculation of characteristics of a francis turbine and the mechanism of the s-shape operational instability, in: IOP Conference Series: Earth and Environmental Science, Vol. 15, IOP Publishing, 2012, p. 032036 (2012).

[16] T. K. Nielsen, Simulation model for francis and reversible pump turbines, 27th IAHR Symposium on Hydraulic Machinery and Systems, September 4, Montreal, Canada 8 (3) (2015) 169–182 (2015).

[17] J. Gordon, Hydraulic turbine efficiency, Canadian Journal of Civil Engineering 28 (2) (2001) 238–253 (2001).

[18] A. K. Gupta, a. G. Lilley, N. Syred, Swirl flows, Tunbridge Wells, Kent, England, Abacus Press, 1984, 488 p. (1984).

[19] A. Favrel, J. Gomes Pereira Jr., C. Landry, A. Müller, C. Nicolet, F. Avellan, New insight in francis turbine cavitation vortex rope: role of the runner outlet flow swirl number, Journal of Hydraulic Research 56 (3) (2018) 367–379 (2018).

[20] S. Skripkin, M. Tsoy, P. Kuibin, S. Shtork, Swirling flow in a hydraulic turbine discharge cone at different speeds and discharge conditions, Experimental Thermal and Fluid Science 100 (2019) 349 – 359 (2019). `doi:https://doi.org/10.1016/j.expthermflusci.2018.09.015`.
URL http://www.sciencedirect.com/science/article/pii/S0894177718309245

[21] M. NISHI, Surging characteristics of conical and elbow type draft tubes, Proc. 12th IAHR Symposium on Hydraulic Machinery and System, Stirling, 1984 (1984) 272–283 (1984).
URL https://ci.nii.ac.jp/naid/80002469683/en/

[22] J. Arpe, C. Nicolet, F. Avellan, Experimental evidence of hydroacoustic pressure waves in a francis turbine elbow draft tube for low discharge conditions, Journal of Fluids Engineering Vol. 131 (2009). `doi:10.1115/1.3155944`.
URL http://infoscience.epfl.ch/record/139297

[23] P. Dériaz, A contribution to the understanding of flow in draft tubes of francis turbines, IAHR Section Hydraulic Machinery, Equipment, and Cavitation, 1st Symposium (Nice, 1960), paper B-1, 1960 (1960).

[24] W. Rheingans, Power swings in hydroelectric power plants, Trans. ASME 62 (3) (1940) 171–184 (1940).

[25] T. Jacob, Evaluation sur modèle réduit et prédiction de la stabilité de fonctionnement des turbines francis (1993) 226 (1993).

[26] A. Presas, D. Valentin, E. Egusquiza, C. Valero, Detection and analysis of part load and full load instabilities in a real francis turbine prototype, Hyperbole Conf. Porto, Port. Febr. 2-3, 2017 813 (2017) 012038 (04 2017). $doi:10.1088/1742-6596/813/1/012038$.

[27] D. Valentín, A. Presas, E. Egusquiza, C. Valero, M. Egusquiza, M. Bossio, Power swing generated in francis turbines by part load and overload instabilities, Energies 10 (12) (2017) 2124 (2017).

[28] C. Brennen, A. Acosta, The dynamic transfer function for a cavitating inducer, Journal of Fluids engineering 98 (2) (1976) 182–191 (1976).

[29] J. Koutnik, L. Pulpitel, Modeling of the francis turbine full-load surge, 1996 (1996).

[30] J. Koutnik, C. Nicolet, G. A. Schohl, F. Avellan, Overload surge event in a pumped-storage power plant, Proceedings of the 23rd IAHR Symposium on Hydraulic Machinery and Systems, Yokohama, Japan 1 (2006) 14. 1–14 (2006).

[31] A. Müller, A. Favrel, C. Landry, K. Yamamoto, F. Avellan, Experimental hydro-mechanical characterization of full load pressure surge in francis turbines, Hyperbole Conf. Porto, Port. Febr. 2-3, 2017 813 (1) (2017) 012018 (2017).
URL http://stacks.iop.org/1742-6596/813/i=1/a=012018

[32] T. Jacob, J. E. Prenat, G. Vullioud, B. Lopez Araguas, Surging of 140 mw francis turbines at high load, analysis and solution, in: Proceedings of the16th IAHR Symposium, section on hydraulic machinery and cavitation: Large and medium size hydraulic machinery and installations from planning to operation, São Paulo, Brésil, 14th to 18th September, no. LMH-CONF-1992-004, 1992 (1992).

[33] M. Nishi, S. Liu, An outlook on the draft-tube-surge study, International Journal of Fluid Machinery and Systems 6 (1) (2013) 33–48 (2013).

[34] A. Ruprecht, T. Helmrich, T. Aschenbrenner, T. Scherer, Simulation of pressure surge in a hydro power plant caused by an elbow draft tube, in: 10th International Meeting of the work group on the behaviour of hydraulic machinery under steady oscillatory condition, Trondheim, Norway, Citeseer, 2001 (2001).

[35] J. L. Kueny, M. Lourenco, J. L. Ballester, Transient flow analysis linked to fast pressure disturbance monitored in pipe systems, 26th IAHR Symposium on Hydraulic Machinery and Systems, August 19-23, 2012, Beijing, China 15 (4) (2012) 042021 (nov 2012). $doi:10.1088/1755-1315/15/4/042021$.
URL https://doi.org/10.1088%2F1755-1315%2F15%2F4%2F042021

[36] M. Manderla, K. Kiniger, J. Koutnik, Improved pump turbine transient behaviour prediction using a thoma number-dependent hillchart model, 27th IAHR Symposium on Hydraulic Machinery and Systems, September 22-26, 2014, Montreal, Canada 22 (3) (2014) 032039 (2014).

[37] S. Riedelbauch, C. Stens, Pump to turbine transient for a pump-turbine in a model test circuit and a real size power plant, 29th IAHR Symposium on Hydraulic Machinery and Systems, September 16-21, 2018, Kyoto, Japan 240 (2019) 072039 (mar 2019). `doi:10.1088/1755-1315/240/7/072039`.
URL https://doi.org/10.1088%2F1755-1315%2F240%2F7%2F072039

[38] C. Nicolet, Hydroacoustic modelling and numerical simulation of unsteady operation of hydro-electric systems, Ph.D. thesis, Lausanne (2007).

[39] S. Alligné, C. Nicolet, Y. Tsujimoto, F. Avellan, Cavitation surge modelling in francis turbine draft tube, Journal of Hydraulic Research 52 (3) (2014) 399–411 (2014). `arXiv:https://doi.org/10.1080/00221686.2013.854847, doi:10.1080/00221686.2013.854847`.
URL https://doi.org/10.1080/00221686.2013.854847

[40] P. Dörfler, System dynamics of the francis turbine half load surge, in: Proceedings of the 11th IAHR Symposium on Hydraulic Machinery and Systems, 1982, pp. 441–453 (1982).

[41] M. Couston, R. Philibert, Partial load modelling of gaseous francis turbine rope, in: Proceedings of the III Conference on Modelling, Testing and Monitoring for Hydro Power Plants, 1998, pp. 5–7 (1998).

[42] D. Chirkov, A. Avdyushenko, L. Panov, D. Bannikov, S. Cherny, V. Skorospelov, I. Pylev, Cfd simulation of pressure and discharge surge in francis turbine at off-design conditions, in: IOP Conference Series: Earth and Environmental Science, Vol. 15, IOP Publishing, 2012, p. 032038 (2012).

[43] F. Flemming, J. Foust, J. Koutnik, R. K. Fisher, Overload surge investigation using cfd data, International Journal of Fluid Machinery and Systems 2 (4) (2009) 315–323 (2009).

[44] P. Dörfler, M. Keller, O. Braun, Francis full-load surge mechanism identified by unsteady 2-phase cfd, in: IOP Conference Series: Earth and Environmental Science, Vol. 12, IOP Publishing, 2010, p. 012026 (2010).

[45] J. Wack, S. Riedelbauch, Two-phase simulations of the full load surge in francis turbines, in: IOP Conference Series: Earth and Environmental Science, Vol. 49, IOP Publishing, 2016, p. 092004 (2016).

[46] S. Alligné, C. Nicolet, N. Ruchonnet, V. Hasmatuchi, P. Maruzewski, F. Avellan, Numerical simulation of nonlinear self oscillations of a full load vortex rope, in: Vol. 2, 3rd Meeting of the IAHR Workgroup on Cavitation and Dynamic Problems in Hydraulic Machinery and Systems, Brno, Czech Republic, 2009, pp. 325–338 (2009).

[47] S. Pasche, F. Avellan, F. Gallaire, Part load vortex rope as a global unstable mode, Journal of Fluids Engineering 139 (5) (2017) 051102 (2017).

[48] J. Decaix, A. Müller, A. Favrel, F. Avellan, C. Münch, Urans models for the simulation of full load pressure surge in francis turbines validated by particle image velocimetry, Journal of Fluids Engineering 139 (12) (2017) 121103 (2017).

[49] C. Landry, A. Favrel, A. Müller, K. Yamamoto, S. Alligné, F. Avellan, Experimental investigation of the mass flow gain factor in a draft tube with cavitation vortex rope, Journal of Physics: Conference Series 813 (1) (2017).
URL http://stacks.iop.org/1742-6596/813/i=1/a=012022

[50] C. Landry, A. Favrel, A. Müller, C. Nicolet, F. Avellan, Local wave speed and bulk flow viscosity in francis turbines at part load operation, Journal of Hydraulic Research 54 (2) (2016) 185–196 (2016). `arXiv:https://doi.org/10.1080/00221686.2015.1131204, doi:10.1080/00221686.2015.1131204`.
URL https://doi.org/%10.1080/00221686.2015.1131204

[51] A. Favrel, J. Gomes Pereira Jr., C. Landry, A. Müller, K. Yamaishi, F. Avellan, Dynamic modal analysis during reduced scale model tests of hydraulic turbines for hydro-acoustic characterization of cavitation flows, Mechanical Systems and Signal Processing 117 (2019) 81 – 96 (2019). `doi:https://doi.org/10.1016/j.ymssp.2018.07.053`.
URL http://www.sciencedirect.com/science/article/pii/S0888327018304564

[52] G. Blommaert, Etude du comportement dynamique des turbines francis contrôle actif de leur stabilité de fonctionnement, Ph.D. thesis, Lausanne (2000).

[53] A. Favrel, A. Müller, C. Landry, K. Yamamoto, F. Avellan, Study of the vortex-induced pressure excitation source in a francis turbine draft tube by particle image velocimetry, Experiments in Fluids 56 (12) (2015) 215 (Nov 2015). `doi:10.1007/s00348-015-2085-5`.
URL https://doi.org/10.1007/s00348-015-2085-5

[54] A. Favrel, J. Gomes Pereira Jr, C. Landry, S. Alligné, L. Andolfatto, C. Nicolet, A. Avellan, Prediction of hydro-acoustic resonances in hydropower plants by a new approach based on the concept of swirl number, Journal of Hydraulic Research 0 (0) (2019) 1–18 (2019). `arXiv:https://doi.org/10.1080/00221686.2018.1555556, doi:10.1080/00221686.2018.1555556`.
URL https://doi.org/10.1080/00221686.2018.1555556

[55] A. Favrel, A. Müller, C. Landry, J. Gomes Pereira Jr., K. Yamamoto, F. Avellan, Dynamics of the precessing vortex rope and its interaction with the system at francis turbines part load operating conditions, Journal of Physics: Conference Series 813 (1) (2017) 012023 (2017).
URL http://stacks.iop.org/1742-6596/813/i=1/a=012023

[56] U. Dorji, R. Ghomashchi, Hydro turbine failure mechanisms: An overview, Engineering Failure Analysis 44 (2014) 136 – 147 (2014). `doi:https://doi.org/10.1016/j.engfailanal.2014.04.013`.
URL http://www.sciencedirect.com/science/article/pii/S1350630714001277

[57] X. Liu, Y. Luo, Z. Wang, A review on fatigue damage mechanism in hydro turbines, Renewable and Sustainable Energy Reviews 54 (2016) 1–14 (2016).

[58] F. Avellan, Introduction to cavitation in hydraulic machinery, in: The 6th International Conference on Hydraulic Machinery and Hydrodynamics, Timisoara, Romania, 2004 (2004).

[59] R. Goyal, B. K. Gandhi, Review of hydrodynamics instabilities in francis turbine during off-design and transient operations, Renewable Energy 116 (2018) 697–709 (2018).

[60] P. Kumar, R. Saini, Study of cavitation in hydro turbines—a review, Renewable and Sustainable Energy Reviews 14 (1) (2010) 374–383 (2010).

[61] C. Valero, E. Egusquiza, A. Presas, D. Valentin, M. Egusquiza, M. Bossio, Condition monitoring of a prototype turbine. description of the system and main results, in: Hyperbole Conf. Porto, Port. Febr. 2-3, 2017, Vol. 813, IOP Publishing, 2017, p. 012041 (2017).

[62] E. C. Bortoni, G. S. Bastos, T. M. Abreu, B. Kawkabani, Online optimal power distribution between units of a hydro power plant, Renewable Energy 75 (2015) 30–36 (2015). `doi:https://doi.org/10.1016/j.renene.2014.09.009`.
URL http://www.sciencedirect.com/science/article/pii/S096014811400559X

[63] M. Ak, E. Kentel, S. Savasaneril, Operating policies for energy generation and revenue management in single-reservoir hydropower systems, Renewable and Sustainable Energy Reviews 78 (2017) 1253–1261 (2017).

[64] Y. Shang, S. Lu, J. Gong, R. Liu, X. Li, Q. Fan, Improved genetic algorithm for economic load dispatch in hydropower plants and comprehensive performance comparison with dynamic programming method, Journal of Hydrology 554 (2017) 306–316 (2017).

[65] I. E. Commission, et al., Hydraulic machines, radial and axial – Performance conversion method from model to prototype, Standard No. IEC 62097, International Electrotechnical Commission, 2009 (2009).

[66] K. Yamamoto, A. Müller, A. Favrel, F. Avellan, Experimental evidence of inter-blade cavitation vortex development in francis turbines at deep part load condition, Experiments in Fluids 58 (10) (2017) 142 (Sep 2017). `doi:10.1007/s00348-017-2421-z`.
URL https://doi.org/10.1007/s00348-017-2421-z

[67] M. H. Stone, The generalized weierstrass approximation theorem, Mathematics Magazine 21 (5) (1948) 237–254 (1948).

[68] C. Hermite, Sur un nouveau développement en série des fonctions, Mallet-Bachelier, 1864 (1864).

[69] L. Andolfatto, J. Delgado, E. Vagnoni, C. Münch-Alligné, F. Avellan, Analytical hill chart towards the maximisation of energy recovery in water utility networks with counter-rotating runners micro-turbine, in: E-proceeding of the 36th IAHR World Congress 2015, The Hague, The Netherlands, 2015, p. 12 (2015).
URL http://infoscience.epfl.ch/record/253055

[70] H. Akaike, Problems of control and information, in: 2nd International Symposium on Information Theory, Budapest: Akademiai Kaido, 1973, pp. 267–281 (1973).

[71] C. M. Hurvich, C.-L. Tsai, Regression and time series model selection in small samples, Biometrika 76 (2) (1989) 297–307 (1989).

[72] I. E. Commission, et al., Field Acceptance Tests to Determine the Hudraulic Performance of Hydraulic Turbines, Storage Pumps and Pump-turbines, Standard No. IEC 60041, International Electrotechnical Commission, 1991 (1991).

[73] I. E. Commission, et al., Rotating electrical machines–Part 2-1: Standard methods for determining losses and efficiency from tests (excluding machines for traction vehicles), Standard No. IEC 60034-2-1, International Electrotechnical Commission, 2014 (2014).

[74] F. Avellan, Lecture notes on hydraulic turbomachines (August 2018).

[75] P. Drtina, M. Sallaberger, Hydraulic turbines—basic principles and state-of-the-art computational fluid dynamics applications, Proceedings of the Institution of Mechanical Engineers, Part C: Journal of Mechanical Engineering Science 213 (1) (1999) 85–102 (1999).

[76] K. Patel, J. Desai, V. Chauhan, S. Charnia, Development of francis turbine using computational fluid dynamics, in: 11st Asian International Conference on Fluid Machinery and 3rd Fluid Power Technology Exhibition, 2011, pp. 1–3 (2011).

[77] P. Maruzewski, V. Hasmatuchi, H.-P. Mombelli, D. Burggraeve, J. Iosfin, P. Finnegan, F. Avellan, Surface roughness impact on francis turbine performances and prediction of efficiency step up, International Journal of Fluid Machinery and Systems 2 (4) (2009) 353–362 (2009).

[78] D. Čelič, H. Ondráčka, The influence of disc friction losses and labyrinth losses on efficiency of high head francis turbine, in: Journal of Physics: Conference Series, Vol. 579, IOP Publishing, 2015, p. 012007 (2015).

[79] X. Liu, Y. Luo, B. W. Karney, W. Wang, A selected literature review of efficiency improvements in hydraulic turbines, Renewable and Sustainable Energy Reviews 51 (2015) 18–28 (2015).

[80] W. Huang, K. Yang, X. Guo, J. Ma, J. Wang, J. Li, Prediction method for the complete characteristic curves of a francis pump-turbine, Water 10 (2) (2018) 205 (2018).

[81] W. Zeng, J. Yang, Y. Cheng, Construction of pump-turbine characteristics at any specific speed by domain-partitioned transformation, Journal of Fluids Engineering 137 (3) (2015) 031103 (2015).

[82] J. Manness, J. Doering, An improved model for predicting the efficiency of hydraulic propeller turbines, Canadian Journal of Civil Engineering 32 (5) (2005) 789–795 (2005).

[83] Z. Zuo, S-shaped characteristics on the performance curves of pump-turbines in turbine mode – a review, Renewable and Sustainable Energy Reviews 60 (2016) 836–851 (07 2016). `doi:10.1016/j.rser.2015.12.312`.

[84] W. Liu, J. Zheng, J. Chen, Q. Shi, Optimization of the s-shaped characteristics of the pump-turbine of xianju pumped storage power station, in: Proceedings on the Engineering Construction of Pumped Storage Power Stations [in Chinese], 2013, pp. 148–152 (2013).

[85] J. Yin, D. Wang, X. Wei, L. Wang, Hydraulic improvement to eliminate s-shaped curve in pump turbine, Journal of Fluids Engineering 135 (7) (2013) 071105 (2013). `doi:10.1115/1.4023851`. URL http://dx.doi.org/10.1115/1.4023851

[86] G. Nielsen TK, Olimstad, Dynamic behaviour of reversible pump-turbines in turbine mode of operation, in: Proceedings of the 13th international symposium on transport phenomena and dynamics of rotating machine: Honolulu, HI, 2010, pp. 74–78 (2010).

[87] G. Olimstad, B. Børresen, T. Nielsen, A two dimensional model for pump-turbine instability investigation, in: 14th International Symposium on Transport Phenomena and Dynamics of Rotating Machine, Honolulu, HI, 2012 (2012).

[88] G. Olimstad, B. Børresen, T. Nielsen, Geometry impact on pump-turbine characteristics, in: 14th International Symposium on Transport Phenomena and Dynamics of Rotating Machine, Honolulu, HI, 2012 (2012).

[89] G. Olimstad, T. Nielsen, B. Børresen, Dependency on runner geometry for reversible-pump turbine characteristics in turbine mode of operation, Journal of Fluids Engineering 134 (12) (2012) 121102 (2012).

[90] B. Zhu, X. Wang, L. Tan, D. Zhou, Y. Zhao, S. Cao, Optimization design of a reversible pump–turbine runner with high efficiency and stability, Renewable Energy 81 (2015) 366–376 (2015).

[91] O. R. Bingol, A. Krishnamurthy, Nurbs-python: An open-source object-oriented nurbs modeling framework in python, SoftwareX 9 (2019) 85 – 94 (2019). `doi:https://doi.org/10.1016/j.softx.2018.12.005`.
URL http://www.sciencedirect.com/science/article/pii/S2352711018301778

[92] J. F. Gülich, Disk friction losses of closed turbomachine impellers, Forschung im Ingenieurwesen 68 (2) (2003) 87–95 (Dec 2003). `doi:10.1007/s10010-003-0111-x`.
URL https://doi.org/10.1007/s10010-003-0111-x

[93] A. Nemdili, D. H. Hellmann, Investigations on fluid friction of rotational disks with and without modified outlet sections in real centrifugalpump casings, Forschung im Ingenieurwesen 71 (1) (2007) 59–67 (Mar 2007). `doi:10.1007/s10010-006-0045-1`.
URL https://doi.org/10.1007/s10010-006-0045-1

[94] C. Chen, C. Nicolet, K. Yonezawa, M. Farhat, F. Avellan, Y. Tsujimoto, One-dimensional analysis of full load draft tube surge, Journal of Fluids Engineering 130 (4) (2008) 041106 (2008).

[95] C. Trivedi, P. J. Gogstad, O. G. Dahlhaug, Investigation of the unsteady pressure pulsations in the prototype francis turbines – part 1: Steady state operating conditions, Mechanical Systems and Signal Processing 108 (2018) 188 – 202 (2018). `doi:https://doi.org/10.1016/j.ymssp.2018.02.007`.
URL http://www.sciencedirect.com/science/article/pii/S0888327018300578

[96] J. Arpe, Analyse du champ de pression pariétale d'un diffuseur coudé de turbine francis, Ph.D. thesis, Lausanne (2003).

[97] C. Brennen, A review of the dynamics of cavitating pumps, Journal Of Fluids Engineering-Transactions Of The Asme 135 (6) (2013). `doi:http://dx.doi.org/10.1115/1.4023663`.

[98] X. Escaler, E. Egusquiza, M. Farhat, F. Avellan, M. Coussirat, Detection of cavitation in hydraulic turbines, Mechanical Systems and Signal Processing 20 (4) (2006) 983 – 1007 (2006). `doi:https://doi.org/10.1016/j.ymssp.2004.08.006`.
URL http://www.sciencedirect.com/science/article/pii/S0888327004001475

[99] X. wu LUO, B. JI, Y. TSUJIMOTO, A review of cavitation in hydraulic machinery, Journal of Hydrodynamics, Ser. B 28 (3) (2016) 335 – 358 (2016). `doi:https://doi.org/10.1016/S1001-6058(16)60638-8`.
URL http://www.sciencedirect.com/science/article/pii/S1001605816606388

[100] C. Brennen, A. Acosta, Theoretical, quasi-static analysis of cavitation compliance in turbopumps., Journal of Spacecraft and Rockets 10 (3) (1973) 175–180 (1973). `doi:https://doi.org/10.2514/3.27748`.

[101] A. KC, Y. H. Lee, B. Thapa, Cfd study on prediction of vortex shedding in draft tube of francis turbine and vortex control techniques, Renewable Energy 86 (2016) 1406 – 1421 (2016). `doi:https://doi.org/10.1016/j.renene.2015.09.041`.
URL http://www.sciencedirect.com/science/article/pii/S0960148115303207

[102] B. Ji, J. Wang, X. Luo, K. Miyagawa, L. Z. Xiao, X. Long, Y. Tsujimoto, Numerical simulation of cavitation surge and vortical flows in a diffuser with swirling flow, Journal of Mechanical Science and Technology 30 (6) (2016) 2507–2514 (Jun 2016). `doi:10.1007/s12206-016-0511-0`.
URL https://doi.org/10.1007/s12206-016-0511-0

[103] X. Luo, A. Yu, B. Ji, Y. Wu, Y. Tsujimoto, Unsteady vortical flow simulation in a francis turbine with special emphasis on vortex rope behavior and pressure fluctuation alleviation, Proceedings of the Institution of Mechanical Engineers, Part A: Journal of Power and Energy 231 (3) (2017) 215–226 (2017). `arXiv:https://doi.org/10.1177/0957650917692153`, `doi:10.1177/0957650917692153`.
URL https://doi.org/10.1177/0957650917692153

[104] H. Falvey, A primer on draft tube surging, Hydro Review; (United States).

[105] S. Alligné, P. Silva, A. Béguin, B. Kawkabani, P. Allenbach, C. Nicolet, F. Avellan, Forced response analysis of hydroelectric systems, Proceedings of the 27th IAHR Symposium on Hydraulic Machinery and Systems 1 (2014) 14. 1–14 (2014).
URL http://infoscience.epfl.ch/record/255343

[106] S. Alligné, C. Nicolet, A. Béguin, C. Landry, J. Gomes Pereira, F. Avellan, Hydroelectric system response to part load vortex rope excitation, Proceedings of the 28th IAHR symposium on Hydraulic Machinery and Systems 49 (2016) 8. 1–8 (2016). `doi:10.1088/1755-1315/49/5/052002`.
URL http://infoscience.epfl.ch/record/231255

[107] HYPERBOLE: HYdropower plants PERformance and flexiBle Operation towards Lean integration of new renewable Energies (Accessed: 1st of May 2019).
URL https://hyperbole.epfl.ch

[108] C. Landry, Hydroacoustic modeling of a cavitation vortex rope for a francis turbine, Ph.D. thesis, Lausanne (2015).

[109] J. Gomes Pereira Jr., L. Andolfatto, F. Avellan, Monitoring a francis turbine operating conditions, Flow Measurement and Instrumentation (2018). `doi:https://doi.org/10.1016/j.flowmeasinst.2018.07.007`.
URL http://www.sciencedirect.com/science/article/pii/S0955598618302395

[110] J. CHARLEY, F. CARTA, Application of the auto- and cross-power spectra to hydro- and aeroacoustics, Mechanical Systems and Signal Processing 15 (2) (2001) 399 − 417 (2001). `doi:https://doi.org/10.1006/mssp.2000.1332`.
URL http://www.sciencedirect.com/science/article/pii/S0888327000913323

[111] K. Lou, P. Sherman, D. Lyon, System identification and coherence analysis in the presence of a harmonic signal, Mechanical Systems and Signal Processing 7 (1) (1993) 13 − 27 (1993). `doi:https://doi.org/10.1016/0888-3270(93)90002-E`.
URL http://www.sciencedirect.com/science/article/pii/088832709390002E

[112] S. Alligné, C. Nicolet, P. Allenbach, B. Kawkabani, J.-J. Simond, F. Avellan, Influence of the francis turbine location under vortex rope excitation on the hydraulic system stability, International Journal of Fluid Machinery and Systems 2 (4) (2009) 286–294 (2009).

[113] C. Nicolet, J.-J. Herou, B. Greiveldinger, P. Allenbach, J.-J. Simond, F. Avellan, Methodology for risk assessment of part load resonance in francis turbine power plant, in: Proceedings IAHR Int. Meeting of Working Group on Cavitation and Dynamic Problems in Hydraulic Machinery and Systems, no. LMH-CONF-2007-004, 2006 (2006).

[114] S. Alligné, C. Nicolet, A. Bégum, C. Landry, J. Gomes Pereira Jr., F. Avellan, Hydroelectric system response to part load vortex rope excitation, 28th IAHR symposium on Hydraulic Machinery and Systems (IAHR2016) 49 (5) (2016) 052002 (2016).
URL http://stacks.iop.org/1755-1315/49/i=5/a=052002

[115] C. Chen, C. Nicolet, K. Yonezawa, M. Farhat, F. Avellan, Y. Tsujimoto, One-dimensional analysis of full load draft tube surge considering the finite sound velocity in the penstock, International Journal of Fluid Machinery and Systems 2 (3) (2009) 260–268 (2009).

[116] D. Chirkov, S. Cherny, P. Scherbakov, A. Zakharov, Evaluation of range of stable operation of hydraulic turbine based on 1d-3d model of full load pulsations, in: Proc. of the 6th IAHR Int. Meeting of the Workgroup on Cavitation and Dynamic Problems in Hydraulic Machinery and Systems, 2015 (2015).

[117] A. Favrel, J. Gomes Pereira Jr., C. Landry, S. Alligné, C. Nicolet, F. Avellan, Reduced scale model testing for prediction of eigenfrequencies and hydro-acoustic resonances in hydropower plants operating in off-design conditions, in: Proceedings of the 29th IAHR Symposium on Hydraulic Machinery and Systems, 2018 (2018).

[118] J. Gomes Pereira Jr, A. Favrel, L. Andolfatto, C. Landry, S. Alligné, C. Nicolet, A. Avellan, Procedure for predicting part load resonance in francis turbines hydropower units based on swirl number and local cavitation coefficient similitude, manuscript submitted for publication in Journal of Mechanical Systems and Signal Processing (2019).

[119] A. Müller, A. Favrel, C. Landry, F. Avellan, Fluid–structure interaction mechanisms leading to dangerous power swings in francis turbines at full load, Journal of Fluids and Structures 69 (2017) 56–71 (2017).

[120] R. K. Fisher Jr., P. Ulith, Comparison of draft tube surging of homologous scale models and prototype francis turbines., Voith Research and Construction 28 (1982) 7. 1–21 (1982).

[121] C. Nicolet, F. Avellan, P. Allenbach, A. Sapin, J.-J. Simond, New tool for the simulation of transient phenomena in francis turbine power plants, in: Proceedings of the Hydraulic Machinery and Systems 21st IAHR Symposium September 9-12, 2002, Lausanne, 2002 (2002).

[122] P. K. Dörfler, Pressure wave propagation and damping in a long penstock, in: 4th International Meeting on Cavitation and Dynamic Problems in Hydraulic and Systems, Serbia, 2011 (2011).

[123] L. Liebermann, The second viscosity of liquids, Physical Review 75 (9) (1949) 1415 (1949).

[124] M. Mitosek, R. Szymkiewicz, Wave damping and smoothing in the unsteady pipe flow, Journal of Hydraulic Engineering 138 (7) (2012) 619–628 (2012).

[125] C. Landry, C. Nicolet, A. Bergant, A. Müller, F. Avellan, Modeling of unsteady friction and viscoelastic damping in piping systems, Proceedings of the 26th IAHR Symposium on Hydraulic Machinery and Systems 1 (2012) 9. 1–9 (2012). `doi:10.1088/1755-1315/15/5/052030`.
URL http://infoscience.epfl.ch/record/181459

[126] M. Gad-el Hak, P. R. Bandyopadhyay, Questions in fluid mechanics, Journal of Fluids Engineering 117 (3) (1995) 5 (1995).

[127] A. S. Dukhin, P. J. Goetz, Bulk viscosity and compressibility measurement using acoustic spectroscopy, The Journal of chemical physics 130 (12) (2009) 124519 (2009).

[128] J. Kůrečka, V. Habán, D. Himr, Bulk viscosity of water in acoustic modal analysis and experiment, in: EPJ Web of Conferences, Vol. 180, EDP Sciences, 2018, p. 02049 (2018).

[129] C. Brennen, The unsteady, dynamic characterization of hydraulic systems with emphasis on cavitation and turbomachines, Proceedings: Joint Symposium on Design and Operation of Fluid Machinery, June 12-14, 1978, Colorado State University, Fort Collins, Colorado 1 (1978) 99–107 (1978).

[130] C. Trivedi, M. J. Cervantes, B. Gandhi, O. G. Dahlhaug, Transient pressure measurements on a high head model francis turbine during emergency shutdown, total load rejection, and runaway, Journal of Fluids Engineering 136 (12) (2014) 121107 (2014).

[131] C. Nicolet, F. Avellan, P. Allenbach, A. Sapin, J.-J. Simond, S. Kvicinsky, M. Crahan, Simulation of transient phenomena in francis turbine power plants: Hydroelectric interaction, Waterpower XIII (2003).

[132] P. Pennacchi, S. Chatterton, A. Vania, Modeling of the dynamic response of a francis turbine, Mechanical Systems and Signal Processing 29 (2012) 107–119 (2012).

[133] M. S. Ghidaoui, M. Zhao, D. A. McInnis, D. H. Axworthy, A review of water hammer theory and practice, Applied Mechanics Reviews 58 (1) (2005) 49–76 (2005).

[134] A. Lugaresi, A. Massa, Designing francis turbines: trends in the last decade, International Water Power and Dam Construction IWPCDM 39 (11) (1987).

[135] F. Hachem, A. Schleiss, A review of wave celerity in frictionless and axisymmetrical steel-lined pressure tunnels, Journal of Fluids and Structures 27 (2) (2011) 311–328 (2011).

[136] A. Triki, Water-hammer control in pressurized-pipe flow using a branched polymeric penstock, Journal of Pipeline Systems Engineering and Practice 8 (4) (2017) 04017024 (2017).

[137] A. H. E. Center, Standards/manuals/guidelines for small hydro development (2012).

[138] P. C. Silva, C. Nicolet, P. Grillot, J.-L. Drommi, B. Kawkabani, Assessment of power swings in hydropower plants through high-order modeling and eigenanalysis, IEEE Transactions on Industry Applications 53 (4) (2017) 3345–3354 (2017).

[139] P. Gautam, J. Gummer, J. Pott, Local penstock resonance resulting from turbine operation, in: Proc. of the IAHR Symposium (Montréal,), 2014 (2014).

[140] A. Müller, Physical mechanisms governing self-excited pressure oscillations in francis turbines, Ph.D. thesis, Lausanne (2014). `doi:10.5075/epfl-thesis-6206`.
URL http://infoscience.epfl.ch/record/199130

João Gomes Pereira Jr.

Curriculum Vitae

Rue de l'Industrie 18
1023-Crissier, VD, Switzerland
✆ *+41 76 603 09 23*
✉ *joaogpjr@gmail.com*
Brazilian, married, 36 y.o.

Summary of Qualifications

More than 8 years of professional and academic experience in hydropower generation;

Field experience in testing and diagnosing turbines and generators;

International experience;

Knowledge on numerical methods, programming languages and measurement techniques;

Master and bachelor from highly ranked universities, PhD candidate;

Always looking for new challenges, experiences and personal growth;

Education

May 2015 - Sept. 2019 (expected)
École Polytechnique Fédérale de Lausanne, *Ph.D*, Energy Doctoral School, Lausanne - Switzerland.
Title: Predicting the dynamic behavior of Francis turbine generating units;
Objective: Be able to predict with accuracy the turbine efficiency inside its operating range, its behavior in transient conditions such as an emergency stop, and also resonance issues in part load conditions or unstable conditions in full load that may lead to large pressure pulsations and power swings.

Sept. 2008 - July 2010
École Polytechnique Fédérale de Lausanne, *M.Sc.*, Mechanical Engineering, Lausanne - Switzerland.
Master thesis: Open-Channel Flow Numerical Modeling;
Two times semester projects: Preliminary design of a tidal stream turbine.

Feb. 2002 - Dec. 2007
State University of Campinas, *B.Sc.*, Mechanical Engineering, Campinas - Brazil.
Bachelor thesis: Modal analysis of a concrete foundation for electron microscope installation;
Extracurricular activities: Participation in two editions of the SAE Aerodesign competition; Research work on stainless steel welding at the Brazilian Synchrotron Light Laboratory (LNLS).

Aug. 2005 - July 2006
École Nationale Supérieure d'Ingénieurs du Mans (ENSIM), *bac +4*, Exchange student, Le Mans - France.
One year as an exchange student at the ENSIM, an engineering school specialized in acoustic and vibrations.

Work Experience

2015–present
Teaching Assistant, *Laboratory for Hydraulic Turbines - EPFL*, Lausanne - Switzerland.
Work as a teacher assistant for the courses on *Hydraulic Turbines* and *Acoustic Hydrodynamics*, and as an adviser providing guidance for master and bachelor students in their projects.

Oct. 2010 - April 2015
On-site Measurements Engineer , *Alstom Hydropower*, Taubaté - Brazil.
Main activities: Planning and performing on-site measurements on hydro turbines and generators to confirm contractual guarantees; Diagnose any unexpected behavior of the generating unit and provide feedback to project managers or expert engineers; Develop data analysis and report generation tools; Write and present technical papers.

Oct. 2007 - July 2008	**Mechanical Design Engineer**, *Alstom Hydropower*, Taubaté - Brazil. Participation in a training program focused on the basic design and mechanical calculations of the three main equipment manufactured at Alstom Hydro Taubaté: hydraulic turbines, generators and gates.
March 2010 - May 2010	**Internship**, *Alstom's Generator Technology Center*, Birr - Switzerland. Internship on the mechanical and electrical design of hydro-generators.

Achievements

July 2018	**Hyperloop Pod Competition**, Space-X Headquarters, Los Angeles, USA. Member of the EPFLoop Team, working mostly on the design of the pod's battery packs. While participating for the first time, the EPFLoop team finished third place in a competition that started with more than 5000 candidates. (`https://hyperloop.epfl.ch/`)
2015 - 2018	**Swiss Government Excellence Scholarship for Foreign Scholars**, Switzerland. Allowing me to pursue my Ph.D studies at the École Polytechnique Fédérale de Lausanne.
2008 - 2010	**Alstom Talents Scholarship**, Brazil & Switzerland. Allowing me to pursue my M.Sc. studies at the École Polytechnique Fédérale de Lausanne.

Software and Programming Skills

Programming	**Labview** (certified by National Instruments, Core I and II), **Diadem** (certified by National Instruments, basic and advanced modules), **Matlab**, **Python**, **Visual Basic**
Simulation	**SIMSEN**, **Ansys**
CAD	**Pro/Engineer**, **Autocad**, **Autodesk Fusion 360**, **Solid Works**

Language Skills

French (fluent oral and written), **English** (fluent oral and written), **Portuguese** (native), **Spanish** (intermediate), **German** (beginner).

Publications

J. Gomes Pereira Jr., E. Vagnoni, A. Favrel, C. Landry, S. Alligné, C. Nicolet, F. Avellan, *Prediction of unstable full load conditions in a Francis turbine prototype*, submitted to the Journal of Mechanical Systems and Signal Processing in 2019.

J. Gomes Pereira Jr., A. Favrel, L. Andolfatto, C. Landry, S. Alligné, C. Nicolet, F. Avellan, *Procedure for predicting part load resonance in Francis turbine hydropower units based on swirl number and local cavitation coefficient similitude*, submitted to the Journal of Mechanical Systems and Signal Processing in 2019.

A. Favrel, J. Gomes Pereira Jr., C. Landry, S. Alligné, L. Andolfatto, C. Nicolet, A. Avellan, *Prediction of hydro-acoustic resonances in hydropower plants by a new approach based on the concept of swirl number*, Journal of Hydraulic Research 0 (0) (2019) 1–18 (2019), `https://doi.org/10.1080/00221686.2018.1555556`

A. Favrel, J. Gomes Pereira Jr., C. Landry, A. Müller, K. Yamaishi, F. Avellan, *Dynamic modal analysis during reduced scale model tests of hydraulic turbines for hydro-acoustic characterization of cavitation flows*, Mechanical Systems and Signal Processing 117 (2019) 81 − 96 (2019), `https://doi.org/10.1016/j.ymssp.2018.07.053`

J. Gomes Pereira Jr., L. Andolfatto, F. Avellan, *Monitoring a Francis turbine operating conditions*, Flow Measurement and Instrumentation, Vol. 63, Oct. 2018, Pages 37-46 doi: `https://doi.org/10.1016/j.flowmeasinst.2018.07.007`

C. Landry, C. Nicolet, J. Gomes Pereira Jr., L. Andolfatto, C. Todde, F. Avellan, *Renovation of hydraulic power plant: how to select the best technical options?*, Hydro 2018, Gdansk, Poland, October 15-17, 2018

A. Favrel, J. Gomes Pereira Jr., C. Landry, S. Alligné, C. Nicolet, F. Avellan, *Reduced scale model testing for prediction of eigenfrequencies and hydro-acoustic resonances in hydropower plants operating in off-design conditions*, 29th IAHR Symposium on Hydraulic Machinery and Systems, Kyoto, Japan, Sep. 17 - 21, 2018

J. Gomes Pereira Jr.,A. Favrel, C. Landry,C. Nicolet, F. Avellan, *Measurements of Cavitation Compliance in the Draft Tube Cone of a Reduced Scale Francis Turbine Operating at Part Load*, 10th International Cavitation Symposium (cav2018), Baltimore, USA, May 14 – 16, 2018, `http://infoscience.epfl.ch/record/255597`

A. Favrel, J. Gomes Pereira Jr., C. Landry, A. Müller, C. Nicolet, F. Avellan, *New insight in Francis turbine cavitation vortex rope: role of the runner outlet flow swirl number*, Journal of Hydraulic Research 56 (3) (2018) 367–379 (2018)

J. Gomes Pereira Jr., A. Favrel, C. Landry, C. Nicolet, F. Avellan, *Transposition of Francis turbine cavitation compliance at partial load to different operating conditions*, HYPERBOLE Conference, Porto, Portugal, February 2-3, 2017. p. 012030. DOI : 10.1088/1742-6596/813/1/012030.

S. Alligné, C. Nicolet, A. Béguin, C. Landry, J. Gomes Pereira Jr., F. Avellan, *Prediction of Francis Turbine Prototype Part Load Pressure and Output Power Fluctuations with Hydroelectric Model*, HYPERBOLE Conference, Porto, Portugal, February 2-3, 2017. p. 012016. DOI : 10.1088/1742-6596/813/1/012016.

A. Favrel, A. Müller, C. Landry, J. Gomes Pereira Jr., K. Yamamoto, F. Avellan, *Dynamics of the precessing vortex rope and its interaction with the system at Francis turbines part load operating conditions*, HYPERBOLE Conference, Porto, Portugal, February 2-3, 2017, DOI : 10.1088/1742-6596/813/1/012023.

S. Alligné, C. Nicolet, A. Béguin, C. Landry, J. Gomes Pereira Jr., F. Avellan, *Hydroelectric System Response to Part Load Vortex Rope Excitation*, 28th IAHR Symposium on Hydraulic Machinery and Systems, Grenoble, France, July 4-8, 2016. p. 1-8. DOI : 10.1088/1755-1315/49/5/052002.

C. Munch, M. Vonlanthen, J. Gomes Pereira Jr., R. Luquet, P. Guinard, F. Avellan, *Design and Performance Assessment of a Tidal Ducted Turbine*, 3rd IAHR International Meeting of the Workgroup on Cavitation and Dynamic Problems in Hydraulic Machinery and Systems, Brno, Czech Republic, October 14-16, 2009.